Winter 12-15-2015

Novel Applications of Electrostatic Precipitators in Coal - Biomass Combustion Systems

He Jing
Washington University in St. Louis

WASHINGTON UNIVERSITY IN ST. LOUIS

School of Engineering and Applied Science
Department of Energy, Environmental and Chemical Engineering

Dissertation Examination Committee:
Pratim Biswas, Chair
Richard Axelbaum
John Gleaves
Jung-Tsung Shen
Brent Williams
Ye Zhuang

Novel Applications of Electrostatic Precipitators in Coal - Biomass Combustion Systems

By

He Jing

A dissertation presented to the
Graduate School of Arts & Sciences
of Washington University in
partial fulfillment of the
requirements for the degree
of Doctor of Philosophy

December 2015
St. Louis, Missouri

Contents

LIST OF FIGURES

LIST OF TABLES

ACKNOWLEDGMENTS

I would like to express my deepest and most sincere gratitude to Professor Pratim Biswas, my PhD advisor, for his great guidance and endless support on my research. Professor Biswas always tries to inspire me, which helps me come up with good research ideas. He gives me a lot of freedom and lets me explore new possibilities in research, but also keeps a close eye on me to make sure I am in the right direction. What I appreciate most is that Professor Biswas is extremely considerate and ready to help me anytime, which makes the research work much easier and also fun. Professor Biswas is a role model to me. I am sure that my entire life will benefit a lot from what I learned from him.

I also would like to thank other committee members for serving on my dissertation committee and providing important and valuable comments and suggestions to improve this dissertation. Especially, I want to thank Professor Axelbaum for providing me suggestions, not only from a point of view of scientific research, but also from a point of view of practical coal combustion in the industry. I would like to thank Professor Gleaves for helping me find key scientific questions in my research, Professor Shen for teaching me how to justify the importance of my study, and Professor Williams for the valuable discussion, as well as guidance and support on using the measuring techniques such as AMS. Additionally, I would like to thank Dr. Zhuang (from Beijing Guodian Longyuan Environmental Engineering Co.) for sharing with me his experiences in performing the coal combustion study and his industrial experiences.

Also I would like to express my gratitude to Professor Da-Ren Chen for bringing me into the field of aerosol science and technology, and teaching me how to do aerosol research. I thank

Professor Kumfer on his suggestion and the valuable discussion on my research, and his great help on our ACERF test and pressurized ESP study.

I want to thank the funding agency Consortium for Clean Coal Utilization (CCCU) for supporting me to do the coal combustion and ESP research. I also appreciate the support from ENVIRSAN Scholarship from EECE Department.

I want to thank my colleagues in the Aerosol & Air Quality Research Laboratory for providing their help and assistance, and most importantly a super great work environment. Special thanks go to my collaborators on the coal projects: Dr. Wei-Ning Wang and Dr. Xiaofei Wang for the help and guidance, especially in the period when I started the coal combustion study. I thank Zhichao, Yang, and Yuqi for their collaboration and tremendous help on the coal projects.

I also want to thank LACER members for the collaboration and help on the ACERF test. Especially I would like to thank Dr. Dhungel for the support of our test and George for the great help on the setup and ESP design. I also would like to thank colleagues in ACT lab for the help on aerosol measurements, especially Dhruv, for his coordination and help on the ozone measurement, and Michael, for his help on the AMS analysis. I also want to thank former Particle Lab members for their help, in particularly, Dr. He, Dr. Ou, and Dr. Hsiao, in the sampler study.

I would like to thank Jim from the Chemistry Department machine shop for building the sampler and Todd from the Physics Department machine shop for building the pressurized ESP. I would also like to thank Mr. Ballard from the Engineering Communication Center for helping with my manuscript editing.

Finally, many thanks also go to my friends and staff in the EECE department.

He Jing

Washington University in St. Louis

December 2015

ABSTRACT OF THE DISSERTATION

Novel Applications of Electrostatic Precipitators in Coal - Biomass Combustion Systems

by

He Jing

Doctor of Philosophy in Energy, Environmental & Chemical Engineering

Washington University in St. Louis, 2015

Professor Pratim Biswas, Chair

Pulverized coal combustion is an important source of electricity production worldwide. However, it is also a primary air pollution emission (particulate matters, mercury, etc.) source. Electrostatic precipitators (ESPs) are widely used in coal-fired power plants to control particulate matters. This dissertation contributes in the study of the pollution formation from coal combustion processes and pollution control based on ESPs in the following three aspects: (1) explore novel applications of ESPs in particulate matters and mercury removal; (2) develop and evaluate an compact electrostatic precipitator for sampling purpose, which can support offline fly ash particle analysis; (3) study the submicrometer particle formation during co-firing of coal with sawdust.

Part.1. Three new topics in flue gas treatment using ESPs were studied: (1) elemental mercury (Hg^0) oxidation by a soft X-ray irradiation enhanced ESP; (2) secondary aerosol formation in the ESP during flue gas treatment; (3) submicrometer particle capture by a pressurized ESP.

In the first study, *in-situ* soft X-rays were coupled to a DC (direct current) corona-based (ESP). The device showed Hg^0 oxidation efficiency of 49.0% without soft X-rays and soft X-rays could enhance the oxidation to an efficiency of 65.6%. Hg^0 was oxidized by the oxidizing radicals

formed due to corona discharge and soft X-ray irradiation. Detailed mechanisms of radical formations and Hg^0 oxidation were proposed and discussed based on ozone generation measurements and Hg^0 oxidation behavior observations in single gas environments (O_2, N_2, and CO_2). The effects of flue gas compositions and particulate matters on the performance of the studied device were also evaluated.

The second study reported the new aerosol formation (or secondary aerosol formation) in the ESP during flue gas treatment for the first time. The size distributions and chemical compositions of the secondary aerosols were characterized. It is very likely that they were H_2O-H_2SO_4 aerosols with a unimodal size distribution and a peak diameter around 20 nm. They were formed through the following pathway: (1) SO_2 in the flue gas was oxidized by the oxidizing radicals, reacted with H_2O in the ESP, and eventually formed H_2SO_4 (vapor); (2) H_2O-H_2SO_4 SAs were firstly formed through ion-induced nucleation; (3) SAs grew through condensation and nucleation. During the particle formation, organics were also absorbed on SAs. The effects of SO_2 concentration, water content in the flue gas, ESP voltage, and flow rate through the ESP on the new aerosol formation were also evaluated.

In the third study, the performance of the pressurized ESP, a promising particle control solution for pressurized coal combustion, was studied. The ESP was operated under 1 atm, 2 atms, and 3 atms, respectively. Current-voltage characteristics of the ESP show that ionization was more difficult with higher gas pressure. Under the same ESP voltage, higher gas pressure resulted in less particle capture due to insufficient particle charging. However, under the same ESP current, the ESP with higher gas pressure worked better. A modified Deutsche-Anderson (D-A) equation was developed and the experimental data fitted well with the estimated particle capture efficiencies from the modified D-A equation. The capture of fly ash particles by the pressurized

ESP was also studied. The charging status of fly ash particles greatly influenced the capture efficiencies.

Part.2. In order to characterize the fly ash particles, proper particle sampling is needed. In this part, an electrostatic nanoparticle sampler was developed. It is a two-stage ESP. A parametric study was first performed to identify the optimal operating condition of the sampler. Under the optimized conditions, the sampler achieved a collection efficiency of more than 90% for particles ranging from 50 to 500 nm, and 57% to 78% of the particles were collected on the SEM stub in the sampler. The collection efficiencies of oleic acid particles were lower than those of NaCl particles in the size range from 50 to 150 nm, due to lower charging efficiencies of oleic acid particles.

Part.3. Co-firing of coal with biomass for electricity generation has economic and environmental benefits, which makes it a promising alternative of coal combustion. To better understand this process, submicrometer particle formation during co-firing of coal with sawdust was studied in this part. Particle size distributions, elemental compositions, and organic compositions of particles were analyzed in detail. Coal contributed more than sawdust in submicrometer particle formation and the formation of organic part of the particles was closely related with the formation of inorganic part. Higher sulfur content in coal and higher combustion temperature resulted in higher concentrations of submicrometer particles and organics. Higher moisture content resulted in lower overall particle concentrations but higher particle concentrations in the size range between 80 nm to 500 nm and more organics in the particles.

CHAPTER 1. INTRODUCTION

1.1 Electricity generation based on coal combustion and pollutant emission from coal combustion

Pulverized coal combustion is a major source of electricity generation in the world. 40% of the world's electricity is provided by coal combustion (EIA 2009). This number varies among different countries. In developing countries such as India and China, greater than 70% of the electricity was produced by coal combustion (Biswas et al., 2011). However, even in developed country such as U.S., coal combustion also provides 45% of the electricity. It is estimated that in 2030, coal combustion will still be the most important source of electricity and it will account for 43% of the global electricity generation then (EIA 2009). Although the shale gas revolution resulted in an increased natural gas usage in electricity generation (providing 30% electricity in U.S., EIA 2015), the important role of coal in electricity generation did not change. It is projected that even in 2040 natural gas will still account for 30% of U.S. electricity generation, which is still lower than the percentage of the contribution of coal combustion (EIA 2015). Several factors have important influence on the roles of coal and gas in electricity production, such as the price volatility of natural gas (Macmillan et al., 2013).

Environmental consideration is another affecting factor of coal's role in power generation. Coal combustion is a major source of many air pollutants, including particulate matters (fly ash), SO_2, NO_x, mercury, etc. Recently, CO_2 became considered as a type of pollutant as well because it is major greenhouse gas. Coal combustion is the most important provider of the CO_2 emission.

To control those air pollutions, stricter air emission regulations for coal-fired power plants are being set all over the world. U.S. is at the leading place to restrict the power plant emission. USEPA has recently finalized several air emission regulations and is on the way to establish other new regulation. Cross-State Air Pollution Rule (CSAPR) aims to reduce SO_2 emissions by

73% and NO_x emissions by 54% from 2005 levels in the CSAPR region, and Mercury and Air Toxics Standards (MATS), which will result in reducing 90% of mercury emissions, 88% of acid gas emissions, 41% of SO_2 emissions beyond the reductions expected from CSAPR, as well as reduction of non-mercury metals and dioxins and furans emissions. In order to reduce the CO_2 emissions, currently EPA is also developing carbon pollution standards for power plants under the Clean Air Act. To meet these regulations and reduce the pollution from coal-fired power plant, new flue gas treatment technologies are urgently needed for a cost-effective and reliable pollution reduction.

At the same time, the advanced combustion technologies are under study and some of them have the advantage in reducing pollution from the pulverized coal combustion. To name a few, oxy-combustion results in a higher concentration of CO_2 in the exhaust from the combustion, which benefits the following carbon capture process, besides, without N_2 in the system, less NO_x will be generated (Chen et al., 2012); pressurized combustion is more effective than the atmosphere pressure coal combustion due to recoverable latent heat, which means less pollution emission for the same amount of power generation (Gopan et al., 2014); co-firing of coal with biomass generates less pollution than the dedicated coal combustion because biomass has lower contents of nitrogen, sulfur, mercury than coal (Sami et al., 2001; Wooldridge 2001; Saidur et al., 2011; Williams et al., 2012).

In this thesis, the emphasis is put on the particulate matter and mercury control. Thus, these two topics are discussed below in detail.

1.1.1 Particle formation during coal combustion process and control technologies

The coal combustion is one of the major sources of the airborne particulate matters all over the world. For example, the electric utility coal combustion accounted for 570,000 tons per year of $PM_{2.5}$ emission in the U.S. in 2001 (Davidson et al., 2005). In China the PM emission from coal-fired power plants totals 3.81 million tons per year, accounting for 44.6% of the total PM (Yao et al., 2010).

The particulate matters primarily originated from the mineral matter in coal, including included minerals (intimately associated with coal matrix, eg. organically-bound element) and excluded minerals (little or no association with carbonaceous materials). The major processes governing ash particles formation have been summarized by Xu et al. (2011) and are shown in Figure 1.1. The particles can be classified into two categories: residual ash particles (typically larger particles) and vaporized particles (typically smaller particles). The residual particles are formed through particles fragmentation and mineral coalescence, while the vaporized particles are formed from the inorganic vapor through nucleation, coagulation, and agglomeration (Xu et al., 2011). Beside the formation of particles from minerals, which is a dominate particle formation pathway in coal combustion, there are also other pathways. For example, the soot particles can be formed from tar during the coal combustion (Olmez et al., 1988; Bond et al., 2004; Cho et al., 2009).

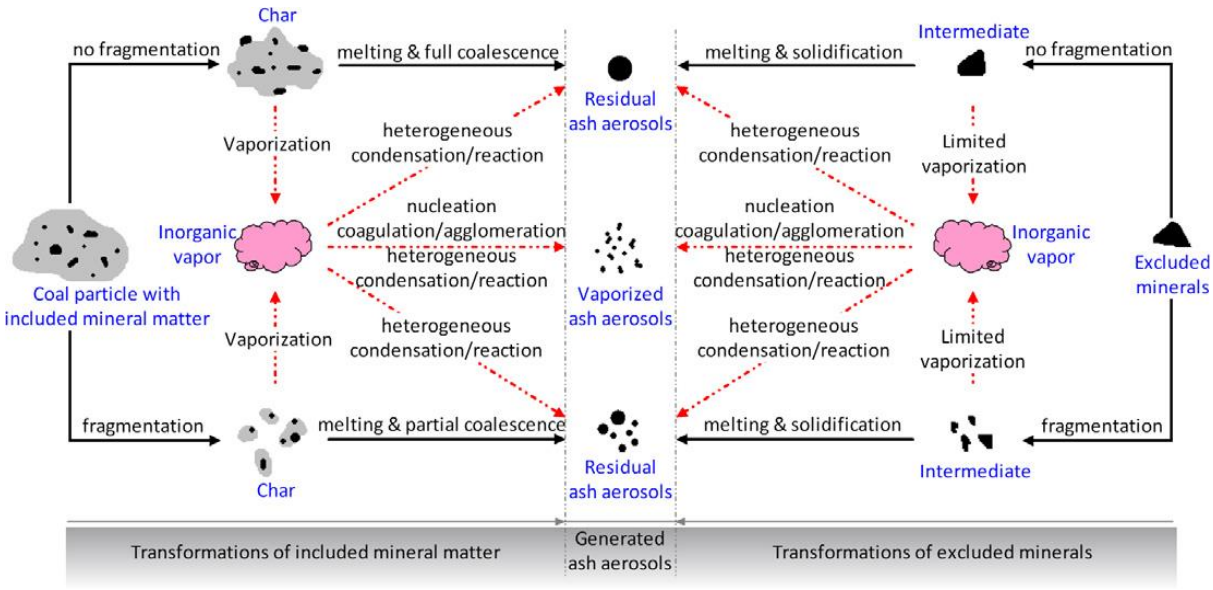

Figure 1.1 Major ash particle formation mechanisms during coal combustion (adopted from Xu et. al., 2011)

Among all the particles, the submicrometer particles are of special interest because they can penetrate into the alveolar regions of the lungs upon inhalation cause more adverse health problems (Biswas and Wu, 2005). As discussed in the previous paragraph, they are mainly formed from inorganic through nucleation, condensation and coagulation. The general formation pathway has been well developed (Quann and Sarofim, 1982; Quann et al., 1982; Linak and Wendt, 1994; Biswas and Wu 1998). Beside the general formation pathway, submicrometer soot particles may also been produced from tar during the coal combustion. Tar vapors from coal pyrolysis may lose H and O atoms to form soot (Olmez et al., 1988; Bond et al., 2004; Cho et al., 2009). Thus, the main composition of submicrometer particles is inorganic substance, including SiO_2, MgO, Fe_2O_3, elemental carbon, and trace species, such as Pb, Hg and Se (Linak and Wendt, 1994).

At the same time, the coal fly ash particles also contain organic matters. Zhang et al. (2008) analyzed the chemical composition of particulate matter from both industrial boilers and residential stoves, and found that the main components of the organic part were alkanes, aliphatic acids, aromatic acids, and PAHs. Wang et al. (2013, 2015) has proposed the pathway of the formation of organic part of the coal fly ash particles, as shown in Figure 1.2. The organic species from coal pyrolysis condensed on the inorganic particles during its growth and form the organic part.

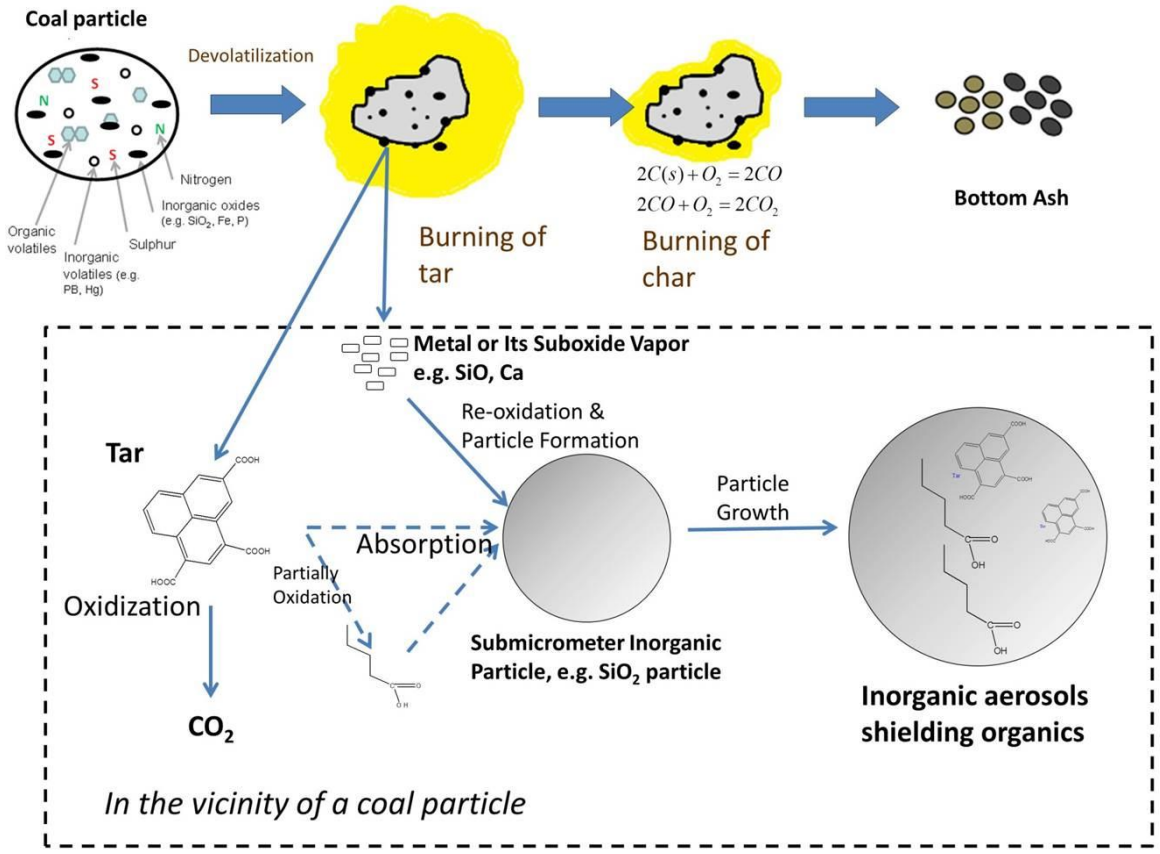

Figure 1.2 Proposed formation mechanisms of organic aerosols from coal combustion (adopted from Wang et al., 2013)

The most widely used particle control systems in coal-fired power plants are electrostatic precipitators (ESPs) and fabric filters. They are both reliable and with high particle capture efficiencies (exceed 99%) (Huang and Chen, 2002; Moretti et al., 2012). ESPs electrically charge fly ash particles and then collect and remove them in an electrical field. They have the advantages of low pressure drop through the system, resistance to high moisture and temperature, and low maintenance (Robinson 1971). Fabric filters collects the dry particulate matter as the flue gas passes through the filter material, and the main mechanisms include inertial impaction, diffusion, and direct interception. The advantages of fabric filters include high collection

efficiency throughout the particle size range, little impact of ash chemical constituents on performance, and resistance to flow changes (Moretti 2012). Wet scrubbers in coal-fired power plants are primarily for SO_2 and other acid gas removal. However, they also contribute in particle removal, relying on direct and irreversible contact of a liquid (droplets, foam, or bubbles) with the PM.

1.1.2 Mercury emission from coal combustion and control technologies

Coal combustion is also a dominant source of anthropogenic mercury emission. In U.S., 50% of the anthropogenic mercury emission is from coal-fired power plants (Senior et al., 2000a and 2000b). In the flue gas, there are four types of mercury compounds, Hg^0, $Hg^{2+}X$ (X can be O, Cl_2, SO_4, etc), $Hg_2^{2+}X$, and CH_3Hg. Among them, $Hg_2^{2+}X$ is usually unstable, and the amount of CH_3Hg is little. Thus, the dominant species are $Hg^0(g)$, $HgCl_2(g)$, $HgO(s,g)$, and $HgSO_4(s)$ (Galbreath and Zygarlicke, 1996). In other words, mercury is usually present in three forms: (a) $Hg^0(g)$; (b) $Hg^{2+}(g)$; (c) Hg(s). $Hg^{2+}(g)$ can be absorbed by water, so they can be easily removed by wet scrubber; while Hg(s) can be removed by fabric filters or ESPs along the particles (Zhuang et al., 2004). The main challenge of mercury control is to remove $Hg^0(g)$ (Pavlish et al., 2003) and previous measurements show that the amount of $Hg^0(g)$ is significant, which usually took up around 50% of the total mercury (Galbreath and Zygarlicke, 1996). There are two strategies: (a) directly capture $Hg^0(g)$ or (b) oxidize it into Hg^{2+}.

Several methods have been developed to control $Hg^0(g)$. The most widely used methods are: activated carbon injection (ACI) and halogen injection. Besides, SCR (selective catalytic reaction), which was first developed to control NO_x, also contributes a lot in $Hg^0(g)$ oxidation. In

addition, recently, hot injection of sorbent has also been used to control mercury (Biswas and Wu, 1998).

During ACI, the powdered activated carbon particles (usually several to around fifty micrometer) are injected into the flue gas ductwork and absorb the Hg^0 and the activated carbon particles are then removed by particle control units. Usually a 5,000-100,000:1 carbon mercury (mass based) ratio is needed to reach a removal efficiency over 90% (His et al, 1998; Pavlish et al., 2003). The disadvantage of ACI is the high cost. Besides, the collected fly ash can be reused as cement replacement, and the carbon in the fly ash will adversely affect the quality of the cement replacement (Pflughoeft-Hassett et al., 2009).

During halogen injection, the halogen can oxidize the $Hg^0(g)$ to Hg^{2+}, which leads to a better mercury removal. Bromine is the most widely used halogen (Liu et al., 2007). At the same time, chlorine (Senior et al., 2000b) and iodine can also oxidize $Hg^0(g)$ (Li et al., 2009a). The disadvantage of halogen injection is that it may cause corrosion of the equipment (Zhuang et al. 2009). The mechanism of the SCR on mercury removal is catalytic oxidation of $Hg^0(g)$. The detailed mechanisms of various catalysts have been extensively studied (Gao et al., 2013).

Hot injection of sorbent is a technique to reduce the toxic metal emissions from coal combustion (Gale and Wendt, 2005; Yoo et al., 2005; Wendt and Lee, 2010). Submicrometer particles containing toxic metal may penetrate through particle control device and are emitted from stack. However, with sorbent injected into the furnace, toxic metal tends to go through the nucleation, condensation, and coagulation process together with the vapor of sorbent and form larger particles, which can be easily captured by the particle control device. As a result, the emission of toxic metal decreases. Experiments show that TiO_2 (Suriyawong et al., 2009), V_2O_5, CuO, and

Fe_2O_3 sorbents can capture mercury. Among them, V_2O_5 worked best, which may be due to the additional catalytic effect (Wang 2014).

1.2 Applications of electrostatic precipitators and other corona discharged based technologies for exhaust gas treatment in coal combustion systems

1.2.1 Electrostatic precipitators

Electrostatic precipitators are the most widely used particle control systems in coal-fired power plants because of its economic and performance advantages. Its working mechanism can be summarized into the following steps: (1) ion generation due to DC (direct current) corona discharge, which is mainly caused by collisions of electrons and gas molecules and the "electron avalanche"; (2) fly ash particles charging by the ions through diffusion charging (dominant mechanism for small particles) and field charging (dominant mechanism for large particles); (3) charged particles migrate following the electric field and eventually collected on the collection electrode (Robinson 1971).

The submicrometer particle capture capability of ESPs have been specifically studied on both bench-scale ESPs with synthetic particles (Yoo et al., 1997; Zhuang et al., 2000; Huang and Chen, 2002; Jing et al., 2013) and ESPs with particles and flue gas from real combustion systems ((McCain et al., 1975; Ylätalo and Hautanen, 1998; Suriyawong et al., 2006; Li et al., 2009b). Two phenomena were observed. Firstly, there was minimum collection efficiency in the 0.1-1 μm size range, which was due to the combination effect of diffusion charging and field charging. Secondly, the collection efficiency became lower as the size was smaller in the ultrafine size

range. One of the reasons was that the particle charging efficiency decreased dramatically as the particle size became smaller.

1.2.2 Treatment of other pollutants with corona discharge technologies

Other than DC corona discharge, which is the key mechanism of electrostatic precipitators, there are also other types of corona discharge, including AC (alternative current) corona discharge and pulsed corona discharge. All of them have been applied into treatment of other pollutants from coal combustion. Rather than utilizing the electric properties of the ions generated from corona discharge, the mechanism here is chemical reaction. During the corona discharge, oxidizing radicals, for instance, ·O, ·OH, O_3, are formed in the reactor and can oxidize the pollutants, which leads to the removal of those pollutants (Yan 2001; Kim 2004).

It has been reported that corona discharge can oxidize SO_2 to SO_3, and eventually formed H_2SO_4 particles. The H_2SO_4 particles were then charged and collected in the corona discharge particles. As a result, some of the SO_2 was removed from flue gas (Matteson et al., 1972; Kuroki et al., 2002; Mok and Nam, 2002; Dong et al., 2003). Similarly, NO_x can be removed in the form of HNO_3 particles or NH_4NO_3 particles with the presence of NH_3 in the flue gas (Kuroki et al., 2002; Mok and Nam, 2002). Corona discharge can also oxidize Hg^0(g) and contribute in mercury removal (Urabe et al., 1988; Chen et al., 2006; Ko et al., 2008; Wang et al., 2011). In addition, the corona discharge technology can also be applied in VOCs degradation (Marotta et al., 2007; Schiorlin et al., 2009). Most of the above are still in the lab study phase, and only few pilot studies have been done (Chang et al., 2003).

1.2.3 Soft X-ray enhanced electrostatic precipitation technology

Soft X-ray irradiation is firstly introduced to enhance the performance of ESP in 2002 (Kulkarni et al., 2002). Soft X-rays interact with particles, electrodes, and gas molecules to emit electrons, thereby generating positively charged particles and ions (as shown in Figure 1.3). As a result, the particle changing is enhanced and this helps increase the submicrometer particle capture efficiency of ESP (Kulkarni et al., 2002; Hogan et al., 2004). The effectiveness of soft X-ray enhanced electrostatic precipitation on fly ash particles capture has been verified on a pilot-scale coal combustion system (Li et al., 2009b). The soft X-rays irradiation can also enhance the performance of DC corona discharge on toluene oxidation (Namiki et al., 2005).

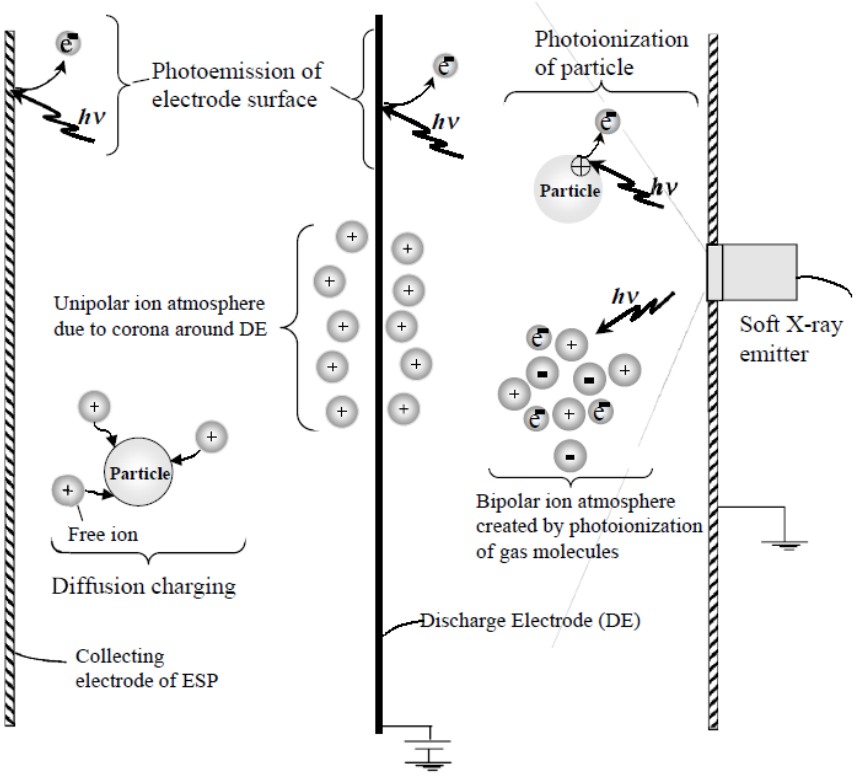

Figure 1.3 Principle of operation of the soft X-ray enhanced ESP for particle charging and capture (adapted from Kulkarni et al., 2002)

1.3 Particle sampler based on electrostatic precipitation

As discussed above, electrostatic precipitation is an efficient method for particle collection. Thus, it has also been extensively utilized as an approach of particle sampling. Many particle samplers have been developed based on electrostatic precipitation (Dixkens and Fissan, 1999; Fierz et al., 2007; Li et al., 2010; Miller et al., 2010). They are made to support offline analysis of particles, such as analyses of particle morphology, chemical composition, and biological properties. However, the current samples still have some shortcomings, including low collection efficiencies (Fierz et al., 2007), requiring external charging component (Li et al., 2010), and possible damage of particles by corona discharge (Miller et al., 2010).

1.4 Dissertation outlines

This dissertation has three main objectives:

1) To investigate several novel applications of electrostatic precipitators in particulate matters and mercury control from coal combustion exhaust and understand the mechanisms (Chapters 2-4);

2) To develop an electrostatic particle sampler (a two-stage electrostatic precipitator) and investigate the submicrometer particle charging and collection process in the sampler (Chapter 5); and

3) To investigate the submicrometer particle formation during co-firing of coal with sawdust (Chapter 6).

The three objectives are studied and described in five chapters (Chapters 2-6) of the dissertation. This dissertation is organized such that each chapter is self-contained with an introduction, experimental section, results, discussion, and conclusions. Chapter 2 reports the study of mercury removal using a new technology, ESP enhanced with soft X-ray irradiations. Chapter 3 elucidates the secondary particle formation in the ESP during flue gas treatment, which is previously observed but unclear problem. Chapter 4 studies the performance of a pressurized ESP on submicrometer particle capture. In Chapter 5, an electrostatic precipitator for particle sampling was developed and evaluated. The mechanism submicrometer particle charging and collection is also discussed in detail. Chapter 6 provides a systematic study of the characteristics of submicrometer particles from co-firing of coal with sawdust. At last, Chapter 7 concludes the dissertation.

1.5 Reference

Biswas, P., W.-N. Wang, and W.-J. An. 2011. The energy-environment nexus: aerosol science and technology enabling solutions. *Front. Environ. Sci. En.* 5(3):299-312.

Biswas, P., and C.-Y. Wu. 2005. Nanoparticles and the environment. *J. Air Waste Manage.* 55(6):708-746.

Biswas, P., and C.-Y. Wu. 1998. Control of toxic metal emissions from combustors using sorbents: a review. *J. Air Waste Manage.* 48(2):113-127.

Bond, T.C., D.G. Streets, K.F. Yarber, S.M. Nelson, J.H. Woo, and Z. Klimont. 2004. A technology−based global inventory of black and organic carbon emissions from combustion. *J. Geophys. Res-Atmos* 109(D14).

Chang, J.-S., K. Urashima, Y.X. Tong, W.P. Liu, H.Y. Wei, F.M. Yang, and X.J. Liu. 2003. Simultaneous removal of NO_x and SO_2 from coal boiler flue gases by DC corona discharge ammonia radical shower systems: pilot plant tests. *J. Electrostat.* 57(3):313-323.

Chen, L., S.Z. Yong, and A.F. Ghoniem. 2012. Oxy-fuel combustion of pulverized coal: Characterization, fundamentals, stabilization and CFD modeling. *Prog. Energ. Combust.* 38(2):156-214.

Chen, Z., D.P. Mannava, and V.K. Mathur. 2006. Mercury oxidization in dielectric barrier discharge plasma system. *Ind. Eng. Chem. Res.* 45(17):6050-6055.

Cho, S.-H., J.-I. Yoo, A.T. Turley, C.A. Miller, W.P. Linak, J.O.L. Wendt, F.E. Huggins, and M.I. Gilmour. 2009. Relationships between composition and pulmonary toxicity of prototype

particles from coal combustion and pyrolysis. *P. Combust. Inst.* 32(2):2717-2725.

Davidson, C.I., R.F. Phalen, and P.A. Solomon. 2005. Airborne particulate matter and human health: a review. *Aerosol Science and Technology* 39(8):737-749.

Dixkens, J., and H. Fissan. 1999. Development of an electrostatic precipitator for off-line particle analysis. *Aerosol Sci. Tech.* 30(5):438-453.

Dong, L.M., Z. Wu, J.X. Yang, and X.C. Chi. 2003. Chemical kinetics model for sulfur dioxide removal in flue gas using corona discharge. Paper presented at Conference on Electrical Insulation and Dielectric Phenomena, Albuquerque, NM, USA, October 19-22, 2003.

EIA. 2009. International Energy Outlook. Washington, DC: DOE.

EIA. 2015. Annual Energy Outlook. Washington, DC: DOE.

Fierz, M., R. Kaegi, and H. Burtscher. 2007. Theoretical and experimental evaluation of a portable electrostatic TEM sampler. *Aerosol Sci. Tech.* 41(5):520-528.

Galbreath, K.C., and C.J. Zygarlicke. 1996. Mercury speciation in coal combustion and gasification flue gases. *Environ. Sci. Tech.* 30(8):2421-2426.

Gale, T.K, and J.O.L. Wendt. 2005. In-furnace capture of cadmium and other semi-volatile metals by sorbents. *P. Combust. Inst.* 30(2):2999-3007.

Gao, Y., Z. Zhang, J. Wu, L. Duan, A. Umar, L. Sun, Z. Guo, and Q. Wang. 2013. A critical review on the heterogeneous catalytic oxidation of elemental mercury in flue gases. *Environ. Sci. Tech.* 47(19):10813-10823.

Gopan, A., B.M. Kumfer, J. Phillips, D. Thimsen, R. Smith, and R.L. Axelbaum. 2014. Process

design and performance analysis of a Staged, Pressurized Oxy-Combustion (SPOC) power plant for carbon capture. *Appl. Energ.* 125:179-188.

Hogan, C.J., M.-H. Lee, and P. Biswas. 2004. Capture of viral particles in soft X-raye-nhanced corona systems: charge distribution and transport characteristics. *Aerosol Sci. Tech.* 38(5):475-486.

Hsi, H.-C., S. Chen, M Rostam-Abadi, M.J. Rood, C.F. Richardson, T.R. Carey, and R. Chang. 1998. Preparation and evaluation of coal-derived activated carbons for removal of mercury vapor from simulated coal combustion flue gases. *Energ. Fuels* 12(6):1061-1070.

Huang, S.-H., and C.-C. Chen. 2002. Ultrafine aerosol penetration through electrostatic precipitators. *Environ. Sci. Tech.* 36(21):4625-4632.

Jing, H., S. He, Q. Ou, T.-C. Hsiao, and D.-R. Chen. 2013. Development of a Compact Electrostatic Nanoparticle Sampler for Offline Aerosol Characterization. *Mapan-J. Metrol. Soc. I.* 28(3):217-226.

Kim, H.−H. 2004. Nonthermal plasma processing for air−pollution control: a historical review, current issues, and future prospects. *Plasma Process. Polym.* 1(2):91-110.

Ko, K.B., Y. Byun, M. Cho, W. Namkung, I.P. Hamilton, D.N. Shin, D.J. Koh, and K.T. Kim. 2008. Pulsed corona discharge for oxidation of gaseous elemental mercury. *Appl. Phys. Lett.* 92(25):251503.

Kulkarni, P., N. Namiki, Y. Otani, and P. Biswas. 2002. Charging of particles in unipolar coronas irradiated by in-situ soft X-rays: Enhancement of Capture Efficiency of Ultrafine

Particles. *J. Aerosol Sci.* 33(9):1279-1296.

Kuroki, T., M. Takahashi, M. Okubo, and T. Yamamoto. 2002. Single-stage plasma-chemical process for particulates, NO_x, and SO_x simultaneous removal. *IEEE T. Ind. Appl.* 38(5):1204-1209.

Li, C., S. Liu, and Y. Zhu. 2010. Determining ultrafine particle collection efficiency in a nanometer aerosol sampler. *Aerosol Sci. Tech.* 44(11):1027-1041.

Li, Y., Michael D., A. Suriyawong, and P. Biswas. 2009a. Mercury emissions control in coal combustion systems using potassium iodide: bench-scale and pilot-scale studies. *Energ. Fuels* 23 (1):236-243.

Li, Y., A. Suriyawong, M. Daukoru, Y. Zhuang, and P. Biswas. 2009b. Measurement and capture of fine and ultrafine particles from a pilot-scale pulverized coal combustor with an electrostatic precipitator. *J. Air Waste Manag.* 59(5):553.

Linak, W.P., and J.O.L. Wendt. 1994. Trace metal transformation mechanisms during coal combustion. *Fuel Processing Tech.* 39 (1):173-198.

Liu, S.-H., N.-Q. Yan, Z.-R. Liu, Z. Qu, H.P. Wang, S.-G. Chang, and C. Miller. 2007. Using bromine gas to enhance mercury removal from flue gas of coal-fired power plants. *Environ. Sci. Tech.* 41(4):1405-1412.

Macmillan, S., Antonyuk, A., Schwind, H. 2013. Gas to Coal Competition in the U.S. Power Sector. *IEA Insights Series 2013*. Paris, France: International Energy Agency.

Marotta, E., A. Callea, M. Rea, and C. Paradisi. 2007. DC corona electric discharges for air pollution control. Part 1. Efficiency and products of hydrocarbon processing. *Environ.*

Sci. Tech. 41(16):5862-5868.

Matteson, M.J, H.L. Stringer, and W.L. Busbee. 1972. Corona discharge oxidation of sulfur dioxide. *Environ. Sci. Tech.* 6(10):895-901.

McCain, J.D., J.P. Gooch, and W.B. Smith. 1975. Results of field measurements of industrial particulate sources and electrostatic precipitator performance. *JAPCA J. Air Waste Ma.* 25(2):117-121.

Miller, A., G. Frey, G. King, and C. Sunderman. 2010. A handheld electrostatic precipitator for sampling airborne particles and nanoparticles. *Aerosol Science and Technology* 44(6):417-427.

Mok, Y.S., and I.-S. Nam. 2002. Modeling of pulsed corona discharge process for the removal of nitric oxide and sulfur dioxide. *Chem. Eng. J.* 85(1):87-97.

Moretti, A.L., C.S. Jones. 2012. Advanced Emissions Control Technologies for Coal-Fired Power Plants. Babcock & Wilcox Power Generation Group, BR-1886.

Namiki, N., K. Cho, P. Fraundorf, and P. Biswas. 2005. Tubular reactor synthesis of doped nanostructured titanium dioxide and its enhanced activation by coronas and soft X-rays. *Ind. Eng. Chem. Res.* 44(14):5213-5220.

EC/R Incorporated. 1998. Stationary Source Control Techniques Document for Fine Particulate Matter. EPA Contract No. 68-D-98-026.

Olmez, I., A.E. Sheffield, G.E. Gordon, J.E. Houck, L.C. Pritchett, J.A. Cooper, T.G. Dzubay, and R.L. Bennett. 1988. Compositions of particles from selected sources in Philadelphia for receptor modeling applications. *JAPCA J. Air Waste Ma.* 38 (11):1392-1402.

Pavlish, J.H., E.A. Sondreal, M.D. Mann, E.S. Olson, K.C. Galbreath, D.L. Laudal, and S.A. Benson. 2003. Status review of mercury control options for coal-fired power plants. *Fuel Processing Tech.* 82(2):89-165.

Pflughoeft-Hassett, D.F., D.J. Hassett, T.D. Buckley, L.V. Heebink, and J.H. Pavlish. 2009. Activated carbon for mercury control: Implications for fly ash management. *Fuel Processing Tech.* 90(11):1430-1434.

Quann, R.J., M. Neville, M. Janghorbani, C.A. Mims, and A.F. Sarofim. 1982. Mineral matter and trace-element vaporization in a laboratory-pulverized coal combustion system. *Environ. Sci. Tech.* 16(11):776-781.

Quann, R.J., and A.F. Sarofim. 1982. Vaporization of refractory oxides during pulverized coal combustion. Paper presented at 19th Symposium (international) on combustion, Pittsburgh, PA, USA.

Robinson, M. 1971. Electrostatic precipitation. In *Air pollution control*. New York: John Wiley.

Saidur, R., E.A. Abdelaziz, A. Demirbas, M.S. Hossain, and S. Mekhilef. 2011. A review on biomass as a fuel for boilers. *Renew. Sust. Energ. Rev.* 15(5):2262-2289.

Sami, M., K. Annamalai, and M. Wooldridge. 2001. Co-firing of coal and biomass fuel blends. *Prog. Energ. Combust.* 27(2):171-214.

Schiorlin, M., E. Marotta, M. Rea, and C. Paradisi. 2009. Comparison of toluene removal in air at atmospheric conditions by different corona discharges. *Environ. Sci. Tech.* 43(24):9386-9392.

Senior, C.L., J.J. Helble, and A.F. Sarofim. 2000a. Emissions of mercury, trace elements, and

fine particles from stationary combustion sources. *Fuel Processing Tech*. 65:263-288.

Senior, C.L., A.F. Sarofim, T. Zeng, J.J. Helble, and R. Mamani-Paco. 2000b. Gas-phase transformations of mercury in coal-fired power plants. *Fuel Processing Tech*. 63(2):197-213.

Suriyawong, A., M. Gamble, M.-H. Lee, R. Axelbaum, and P. Biswas. 2006. Submicrometer particle formation and mercury speciation under O_2-CO_2 coal combustion. *Energ. Fuels* 20(6):2357-2363.

Suriyawong, A., M. Smallwood, Y. Li, Y. Zhuang, and P. Biswas. 2009. Mercury capture by nano-structured titanium dioxide sorbent during coal combustion: lab-scale to pilot-scale studies. *Aerosol Air Qual. Res.* 9(4):394-403.

Urabe, T., Y. Wu, T. Nagawa, and S. Masuda. 1988. Study on Hg, NO_x, SO_x behavior in municipal refuse incinerator furnace and removal of those by pulse corona discharge. *Seiso Giho* 13:12-29.

Wang, M., T. Zhu, H. Luo, H. Wang, and W. Fan. 2011. Effects of reaction conditions on elemental mercury oxidation in simulated flue gas by DC nonthermal plasma. *Ind. Eng. Chem. Res.* 50 (10):5914-5919.

Wang, X., B.J. Williams, Y. Tang, Y. Huang, L. Kong, X. Yang, and P. Biswas. 2013. Characterization of organic aerosol produced during pulverized coal combustion in a drop tube furnace. *Atmos. Chem. Phys.* 13(21):10919-10932.

Wang, X.. 2014. Fine Particle and Mercury Formation and Control during Coal Combustion. Ph.D. Thesis, Washington University in St. Louis, USA.

Wang, X., E. Cotter, K.N. Iyer, J. Fang, B.J. Williams, and P. Biswas. 2015. Relationship between pyrolysis products and organic aerosols formed during coal combustion. *P. Combust. Inst.* 35(2):2347-2354.

Wendt, J.O.L., and S.J. Lee. 2010. High-temperature sorbents for Hg, Cd, Pb, and other trace metals: Mechanisms and applications. *Fuel* 89(4):894-903.

Williams, A, J.M. Jones, L. Ma, and M. Pourkashanian. 2012. Pollutants from the combustion of solid biomass fuels. *Prog. Energ. Combust* 38(2):113-137.

Xu, M., D. Yu, H. Yao, X. Liu, and Y. Qiao. 2011. Coal combustion-generated aerosols: Formation and properties. *P. Combust. Inst.* 33(1):1681-1697.

Yan, K. 2001. Corona plasma generation. Ph.D. Thesis, Technische Universiteit Eindhoven, Netherlands

Yao, Q., S.-Q. Li, H.-W. Xu, J.-K. Zhuo, and Q. Song. 2010. Reprint of: Studies on formation and control of combustion particulate matter in China: A review. *Energy* 35(11):4480-4493.

Ylätalo, S.I., and J.Hautanen. 1998. Electrostatic precipitator penetration function for pulverized coal combustion. *Aerosol Sci. Tech.* 29(1):17-30.

Yoo, J.-I., T. Shinagawa, J.P. Wood, W.P. Linak, D.A. Santoianni, C.J. King, Y.-C. Seo, and J.O.L. Wendt. 2005. High-temperature sorption of cesium and strontium on dispersed kaolinite powders. *Environ. Sci. Tech.* 39(13):5087-5094.

Yoo, K.H., J.S.Lee, and M.D. Oh. 1997. Charging and collection of submicron particles in two-stage parallel-plate electrostatic precipitators. *Aerosol Sci. Tech.* 27(3):308-323.

Zhang, Y., J.J. Schauer, Y. Zhang, L. Zeng, Y. Wei, Y. Liu, and M. Shao. 2008. Characteristics of particulate carbon emissions from real-world Chinese coal combustion. *Environ. Sci. Tech.* 42(14):5068-5073.

Zhuang, Y., C. Chen, R. Timpe, and J. Pavlish. 2009. Investigations on bromine corrosion associated with mercury control technologies in coal flue gas. *Fuel* 88(9):1692-1697.

Zhuang, Y., Y.J. Kim, T.G. Lee, and P. Biswas. 2000. Experimental and theoretical studies of ultra-fine particle behavior in electrostatic precipitators. *J Electrostat* 48(3):245-260.

Zhuang, Y., J.S. Thompson, C.J. Zygarlicke, and J.H. Pavlish. 2004. Development of a mercury transformation model in coal combustion flue gas. *Environ. Sci. Tech.* 38(21):5803-5808.

CHAPTER 2. ELEMENTAL MERCURY OXIDATION IN AN ELECTROSTATIC PRECIPITATOR WITH IN SITU SOFT X-RAY IRRADIATION

The results of this chapter has been published in Jing, H.; Wang, X.; Wang, W.-N.; Biswas, P., Elemental Mercury Oxidation in an Electrostatic Precipitator Enhanced with In Situ Soft X-ray Irradiation. Journal of the Air & Waste Management Association, 2015, 65, 455-465

Supplementary materials are available in Appendix I

Abstract

Corona discharge based techniques are promising approaches for oxidizing elemental mercury (Hg^0) in flue gas from coal combustion. In this study, in-situ soft X-rays were coupled to a DC (direct current) corona-based electrostatic precipitator (ESP). The soft X-rays significantly enhanced Hg^0 oxidation, due to generation of ion-electron pairs from photoionization of gas molecules and the ESP electrode materials. This coupling technique worked better in the positive corona discharge mode because more electrons were in the high energy region near the electrode. Detailed mechanisms of Hg^0 oxidation are proposed and discussed based on ozone generation measurements and Hg^0 oxidation behavior observations in single gas environments (O_2, N_2, and CO_2). The effect of O_2 concentration in flue gas, as well as the effects of particles (SiO_2, TiO_2, and KI) was also evaluated. In addition, the performance of a soft X-ray coupled ESP in Hg^0 oxidations was investigated in a lab-scale coal combustion system. With the ESP voltage at +10 kV, soft X-ray enhancement, and KI addition, mercury oxidation was maximized.

2.1 Introduction

Mercury (Hg) pollution is arousing increasing attention due to its toxicity. Coal-fired power plants are the primary emission sources of anthropogenic releases of mercury, and accounted for 53% of the total mercury emission in United States in 2005 (U.S. Environmental Protection Agency, EPA, 2011). In 2011, the EPA finalized the first U.S. national standards to regulate mercury emission from coal-fired power plants.

In flue gas from coal-fired power plants, mercury is usually present in ionic, particulate, and elemental states (Korpiel and Vidic, 1997; Fujiwara et al., 2002). Due to its high solubility in water, the ionic state of mercury can be removed by treatments such as wet scrubbers. Particulate mercury can be removed by particle treatment facilities such as electrostatic precipitators (ESPs) or a fabric filter baghouse. However, elemental mercury (Hg^0) that is present as vapor is hard to capture.

Several types of approaches have been proposed to treat Hg^0 in flue gas, including activated carbon injection (ACI) (Sjostrom et al., 2010), non-carbon sorbent injection (Worathanakul et al., 2008; Suriyawong et al., 2009), addition of oxidizing chemicals, like chlorine (Richardson et al., 2003), and selective catalytic reaction (SCR) (Gao et al., 2013). Among them, ACI and SCR are already commercially available. ACI is the most commonly used technique, but it has limitations, such as high cost and a low applicable temperature range. The activated carbon also affects the reuse of the fly ash. The oxidation effect of SCR was quite variable and appears to be coal-specific and catalyst-specific (Feeley et al., 2003).

Corona discharge has been proven to oxidize Hg^0 (Urabe et al., 1988), and its operation cost is much lower than that of ACI. There are three types of corona discharge: alternating current (AC),

direct current (DC), and pulsed. Dielectric barrier discharge (DBD), a type of AC corona discharge, has been well studied as a Hg^0 oxidation technique (Chen et al., 2006; Jeong and Jurng, 2007; Byun et al., 2008; Ko et al., 2008a; Lin et al., 2010; Wang et al., 2010; Byun et al., 2011a; Byun et al., 2011b; Jiang et al., 2012). Similarly, DC corona discharge (Liang et al., 2002; Wang et al., 2009; Wang et al., 2011a; Wang et al., 2013a) and pulsed corona discharge (Liang et al., 1998; Ko et al., 2008b; Ko et al., 2008c; Xu et al., 2009) have also been used to oxidize Hg^0. Notably corona discharge has additional beneficial effects other than Hg^0 oxidation. DBD, pulsed corona discharge, and the system based on DC corona discharge by Wang et al. (2013a) can also oxidize NO_x and SO_x. The corona-based ESP developed by Liang et al. (2002) can remove both Hg^0 and zinc-rich fly ash particles.

Although the process of Hg^0 oxidation by corona discharge has been studied for years, its role in Hg^0 oxidation by DC-energized ESPs in practical flue gas treatment is not clear. Hg^0 could be captured and partially oxidized in ESPs at coal-fired power plants. In pilot-scale and full-scale ESPs, 8%-58% Hg^0 concentration reductions have been reported (Xie et al., 2002; Wang et al., 2008; Hu et al., 2009; Yang et al., 2013). However, the Hg^0 oxidation in such processes was attributed to oxidizing compounds in the flue gas, such as hydrogen chloride (HCl). The effect of corona discharge was not investigated.

Soft X-ray radiation has been coupled with ESP to enhance its ability to collect particulate matter (Kulkarni et al., 2002; Hogan et al., 2004; Kettleson et al., 2009; Li et al., 2009a; Kettleson et al., 2013). Collection efficiency is enhanced when X-rays interact with particles, electrodes, and gas molecules to emit electrons, thereby generating positively charged particles and ions, which then increase particle charging. Considering this, soft X-ray radiation may also be able to enhance

Hg^0 oxidation in ESPs, based on the higher ionization environment in ESPs and also the potential interactions between soft X-rays and Hg atoms.

This study first evaluated the effect of a DC corona discharge-based ESP with *in situ* soft X-ray irradiation on mercury oxidation, considering both DC corona discharge alone and the combined effect of corona discharge and soft X-rays. In addition, the effects of flue gas compositions and representative fly ash and sorbent particles in flue gas were evaluated in synthetic flue gas. Finally, mercury oxidation by ESP and soft X-rays was tested in a flue gas from coal combustion in a drop-tube furnace.

2.2 Experimental Section

2.2.1 Experimental Setup

A cylinder-wire ESP was used in this study. The configuration of the ESP and the coupling of the ESP and the photoionizer are shown in Figure A1.1 of the supplemental materials. A DC power supply (Glassman High Voltage Inc., series EL) provided the voltage. The current through the ESP was monitored with a microamp meter (Nishizawa, U-120, class 1.5). The soft X-rays were generated by a photoionizer (Hamamatsu Photonics Ltd., Japan, Model C7114-01, 3.5-9.5 keV).

Two experimental systems were used. In the simulated flue gas system (Figure 2.1a), flue gas was obtained by mixing different types of gases (O_2, CO_2, and N_2). Their flow rates were regulated by mass flow controllers (OMEGA; FMA 5510, FMA 5512). The total flow rate was kept at 1 lpm. Mercury was generated at 12 ng/min by a mercury permeation tube (Dynacal, Valco Instruments Co. Inc. and VICI AG, Houston, Texas, USA). The effects of silicon dioxide

(SiO_2, Snowtex-o, Nissan Chemical), titanium dioxide (TiO_2, Aerodisp-W740X, Evonic industries), and potassium iodide (KI, Mallinckrodt Chemicals) particles were studied. Particles were generated by an atomizer (TSI model 3076). Gases and particles were mixed in a clean quartz tube (61.0 cm L, 1.9 cm ID). The ESP was set downstream of the tube. Hg^0 concentration and submicron particle size distribution were measured by a mercury analyzer (Nippon Instruments Corporation, Japan, WA-4) and scanning mobility particle sizer (SMPS, TSI, model 3080), respectively. The ozone concentration was measured by an ozone analyzer (Thermo, Model 49i). An EPA method using a sampling train was used to measure both Hg^0 and Hg^{2+} concentrations (Hedrick et al., 2001).

In the second system (Figure 2.1b), coal was combusted in a drop-tube furnace (ThermoElectronCorp., USA, Lindberg/Blue) (Zhuang and Biswas, 2001; Suriyawong et al., 2006; Wang et al., 2013b). Pulverized PRB (Powder River Basin) sub-bituminous coal (supplied by Ameren UE, St. Louis, MO) was used in the experiment without KI addition, while Chinese S03 coal was used in the KI addition case. The composition of the coals used is in Table A1.1. They were fed by a coal feeder (Quann et al., 1982) at 1 g/hr. The coal was carried by a 0.5 lpm air flow, and another 0.5 lpm air flow was directly injected into the ceramic tube. The ESP was again set downstream of the furnace, and the same measurements were taken as in the simulated flue gas system. A cascade impactor (Pollution Control Systems Corp., Seattle, WA, Mark III) was set before the SMPS to remove particles larger than 1 μm.

(a)

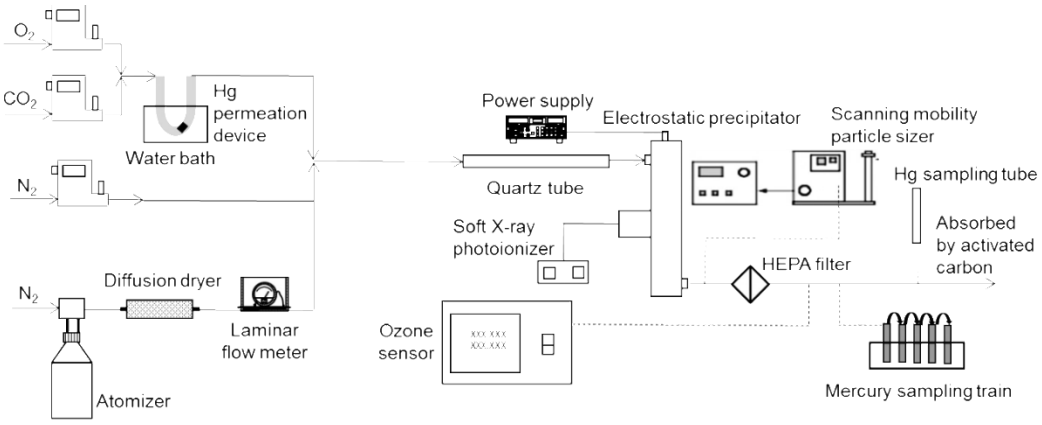

(b)

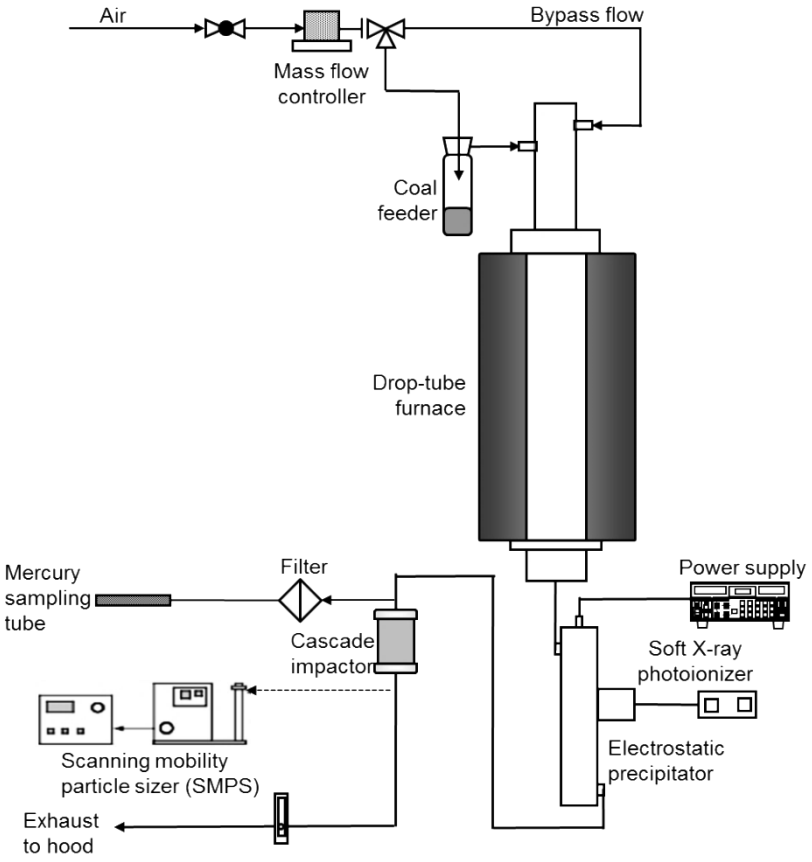

Figure 2.1 (a) Simulated flue gas experimental system (for experiments Set I to III). (b) Drop-tube furnace experimental system (for experiments Set IV)

2.2.2 Experimental design

The experimental plan is summarized in Table 2.1. The effects of corona discharge and X-rays on elemental mercury oxidation were first evaluated (in Set I). Then, the effects of two factors on this process were evaluated, namely (1) the flue gas composition effect (pure O_2, CO_2, and N_2, in Set II) and (2) the particle effect (in Set III). Finally, in Set IV the effects of corona discharge and X-rays on elemental mercury oxidation were tested on practical flue gas from coal combustion.

Table 2.1 Test plan

Set	Purpose	Particle	ESP operation	Gas composition
I	Test effects of corona discharge and soft X-ray	No particles	Corona -10kV, -8kV, +8kV, +10kV, soft X-ray off; Corona -10kV, -8kV, 0kV, +8kV, +10kV, soft X-ray on	4%O_2-12%CO_2-84%N_2
II	Test effects of O_2, CO_2, and N_2 in the flue gas	No particles	Corona +10kV, soft X-ray off and on	100%CO_2, 100%N_2, and 100%O_2, respectively
III	Test effect of particles in flue gas	SiO_2 particles; TiO_2 particles; KI particles	Corona +10kV, soft X-ray off and on	4%O_2-12%CO_2-84%N_2
IV	Test mercury oxidation by ESP and soft X-ray in flue gas from coal combustion	Fly ash particles from drop tube furnace; particles removed by HEPA filter; fly ash particles from drop tube furnace with KI addition	Corona +10kV, soft X-ray off and on	Gas from drop tube furnace

2.3 Results and Discussion

2.3.1 Effects of corona discharge and soft X-rays

Based on previous studies (Kulkarni et al., 2002; Namiki et al., 2005; Suriyawong et al., 2008) and industrial ESP operation (Parker, 2003), -10 kV, -8 kV, 0 kV, +8 kV, and +10 kV were selected as the test conditions. Hg^0 conversion was used as the indicator of mercury oxidation. The conversion efficiency was calculated using the following equation:

$$Hg^0 \text{ conversion efficiency} = (1 - \frac{C_{Hg0,on}}{C_{Hg0,off}}) \times 100\% \quad (2.1)$$

Figure 2.2 shows that at +10 kV, conversion efficiencies of 49.0% without soft X-rays and 65.6% with soft X-rays were reached; while at -10 kV, the conversion efficiencies were lower, 24.1% and 31.5% for ESP and ESP with soft X-rays. In contrast to the +10 kV and -10 kV cases, the conversion was not significant (below 4.8%) under other applied voltages, due to low electron concentrations in the ESP, which can be inferred from current-voltage characteristics (Figure A1.2). The phenomenon of higher Hg^0 conversion at +10 kV than that at -10 kV could be explained by the electron density distribution, which will be modeled in a following section.

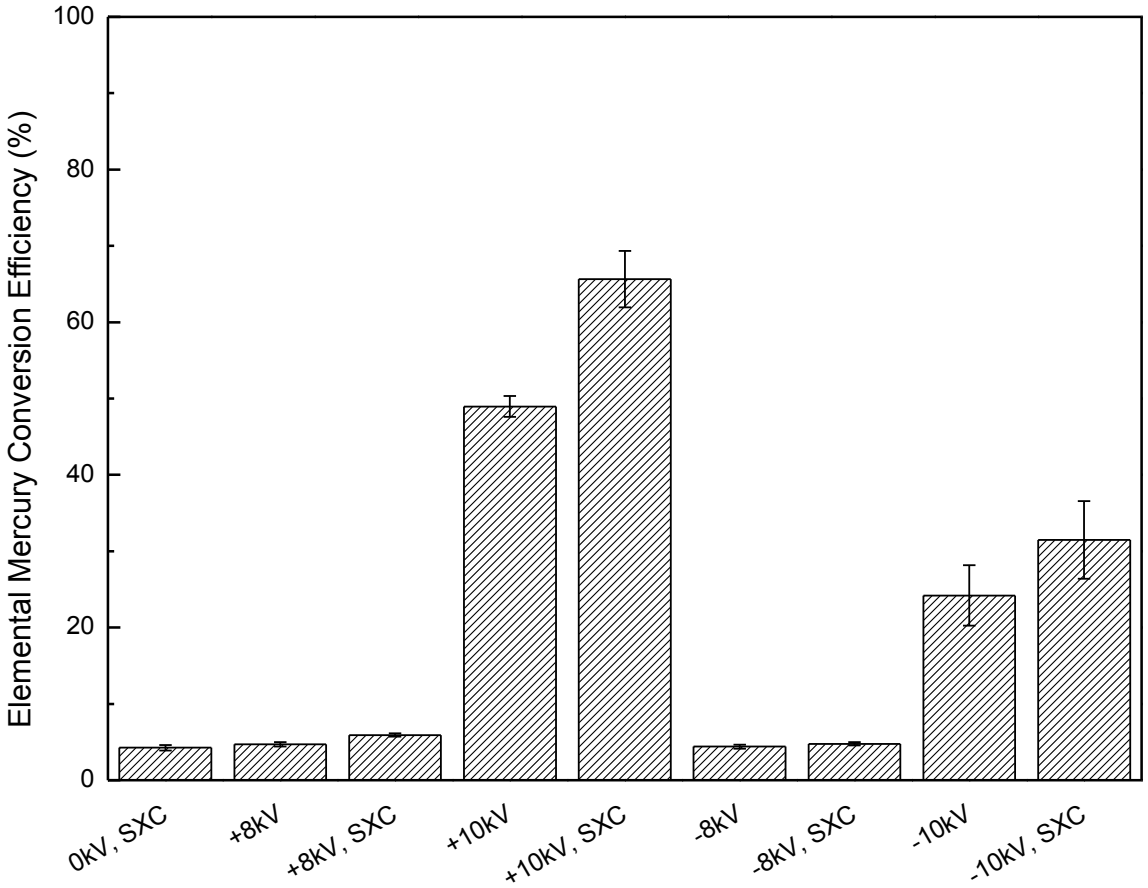

Figure 2.2 Elemental mercury conversion efficiencies under various ESP voltages, with soft X-ray corona (SXC) off and on (gas combination: 0.04 lpm O_2, 0.12 lpm CO_2, 0.84 lpm N_2)

2.3.2 Possible Mercury Oxidation Mechanisms

In the soft X-ray coupled ESP, a possible Hg^0 oxidation mechanism can be summarized in four steps. In step 1, energetic photons from corona discharges and soft X-rays (if applied) ionize gas molecules or electrodes in the ESP and form positive ion-electron pairs (Goldman et al., 1985; Chen, 2002; Kulkarni et al., 2002). In step 2, the newly generated high energy electrons collide with gas molecules and the electrodes, which may result in four outcomes: a) a gas molecule absorbs energy from the collision and dissociates into a positive ion and a new electron, b) a new

electron is released from the electrode after the collision between an electron and the electrode, c) the gas molecule absorbs energy from the collision and dissociates into atoms, and d) the gas molecule absorbs energy from the collision and transforms to the excited state. As a result of processes a) and b), a great number of electrons are generated, and they initiate more collisions. The processes occurring in steps 1 and 2 are summarized in Figure 3. The positive voltage case (Figure 2.3a) and negative case (Figure 2.3b) have two major differences: the drifting directions of ions are opposite between the two cases, so are the drifting direction of electrons; and the process 2b) just happens in the negative voltage case. In step 3, non-electron species generated in step 2 take part in further chemical reactions. The detailed reactions and produced species depend on the gas composition in the ESP, will be discussed in later sections. In step 4, the oxidizing radicals generated in steps 2 and 3 react with and oxidize Hg^0. For example, oxygen atoms (O) and ozone molecules (O_3) oxidize Hg^0 in the following pathways (Van Veldhuizen, 2000; Wang et al., 2009):

$$Hg + O \rightarrow HgO \tag{2.2}$$

$$Hg + O_3 \rightarrow HgO + O_2 \tag{2.3}$$

Production of Hg^{2+} was confirmed with mercury speciation measurement (Figure A1.3).

Applying soft X-rays resulted in more electron production in step 1, which promoted the electron impact reactions and chemical reactions in steps 2 and 3. Consequently, more radicals were formed and resulted in a high Hg^0 oxidation rate. However, under soft X-rays alone only an insignificant amount of Hg^0 was oxidized, as shown in Figure 2.2. There are two possible reasons. First, without an electric field in the ESP, the energy of electrons generated by photoionization due to X-rays was too low to initiate the chain reactions, and finally could not

oxidize Hg^0. Second, when the electric field was off, there was no force driving electrons to move. Therefore, the possibility of collisions between electrons and gas molecules was much lower than when the ESP was on, which resulted in fewer reactions. For these reasons, soft X-ray alone was not used as a test condition in the experiments discussed in the following sections.

(a)

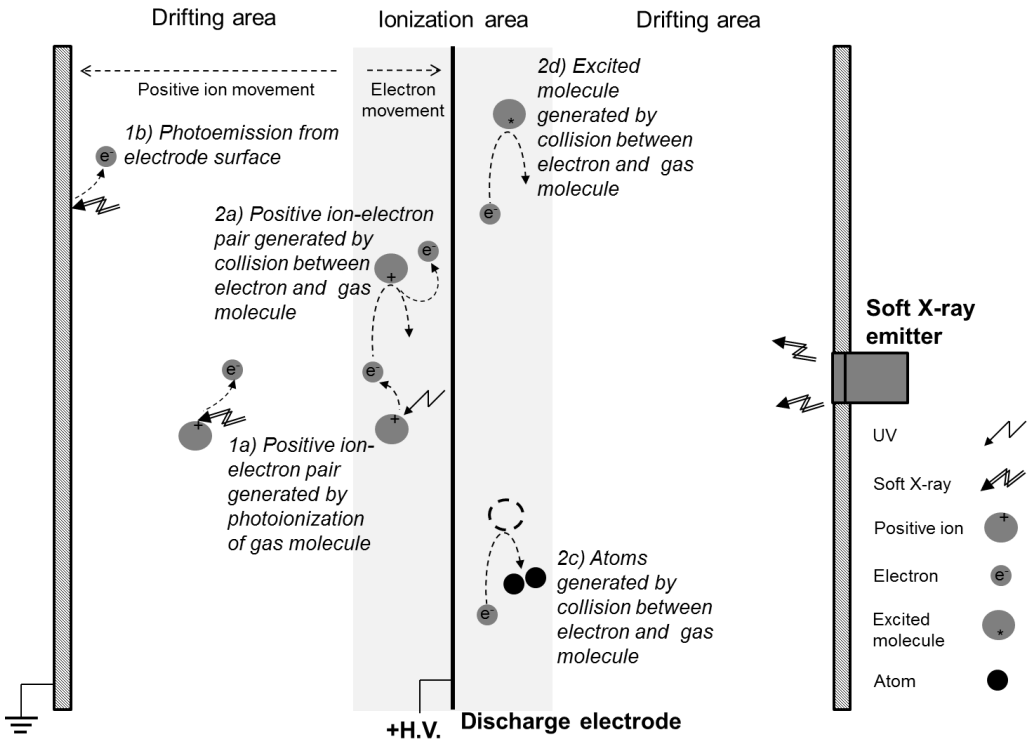

(b)

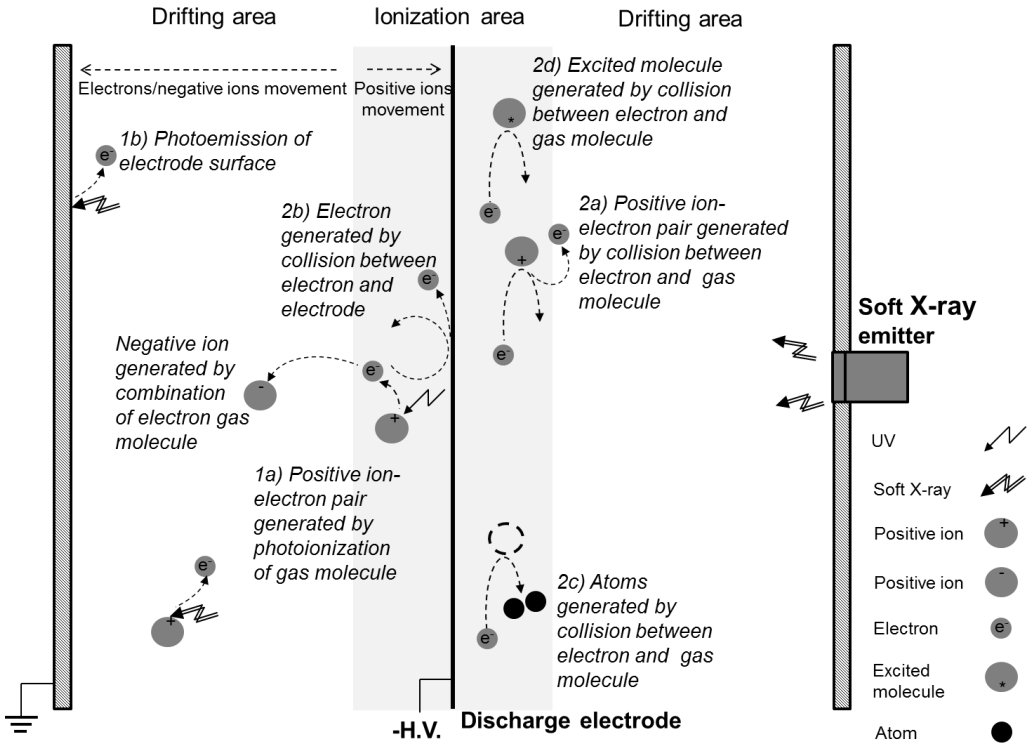

Figure 2.3 Schematic of ion and electron generation and movement in ESP coupled with soft X-rays [the serial numbers correspond to the steps discussed in the text; (a) is for positive case, and (b) is for negative case]

The O_3 generated by an ESP is an active chemical species that oxidizes mercury. O_3 generations under various voltages with soft X-ray on or off are shown in Figure 2.4. In the voltage range from -8.8 kV to +10 kV, under the same voltage, the concentration of O_3 was slightly higher when the soft X-ray was on than when it was off. However, when the voltage was between -10 kV and -8.8 kV, X-rays reduced O_3 generation. Comparing the O_3 generation with the Hg^0 conversion result in Figure 2.2, a higher O_3 concentration was obtained under -10 kV than under +10 kV; however, Hg^0 conversion was higher under +10 kV. Therefore, O_3 might not be the

most important species in oxidizing Hg^0. This conclusion matches the theoretical calculation. The reduction of Hg^0 concentration due to reactions with O_3 in the ESP was calculated using:

$$\Delta c_{Hg0,Hg0-O3} = k c_{O3}{}^{a} \bar{c}_{Hg0}{}^{b} t \tag{2.4}$$

Kinetic parameters for this reaction have been reported in the literature (k is 2.1×10^{-18} $cm^3molec^{-1}s^{-1}$, a is 1.0, and b is 0.8, Hall, 1995; k is 7.5×10^{-19} $cm^3molec^{-1}s^{-1}$, a is 1.0, and b is 1.0, Pal and Ariya, 2004). With these kinetic parameters, the estimated Hg^0 conversion efficiency due to reactions with O_3 is at least one order of magnitude lower than the Hg^0 conversion efficiencies for the experimental cases. Thus, it can be inferred that the reaction between Hg^0 and O_3 might not be the key mechanism of Hg^0 conversion, and that O radicals contribute most in Hg^0 oxidation in the system.

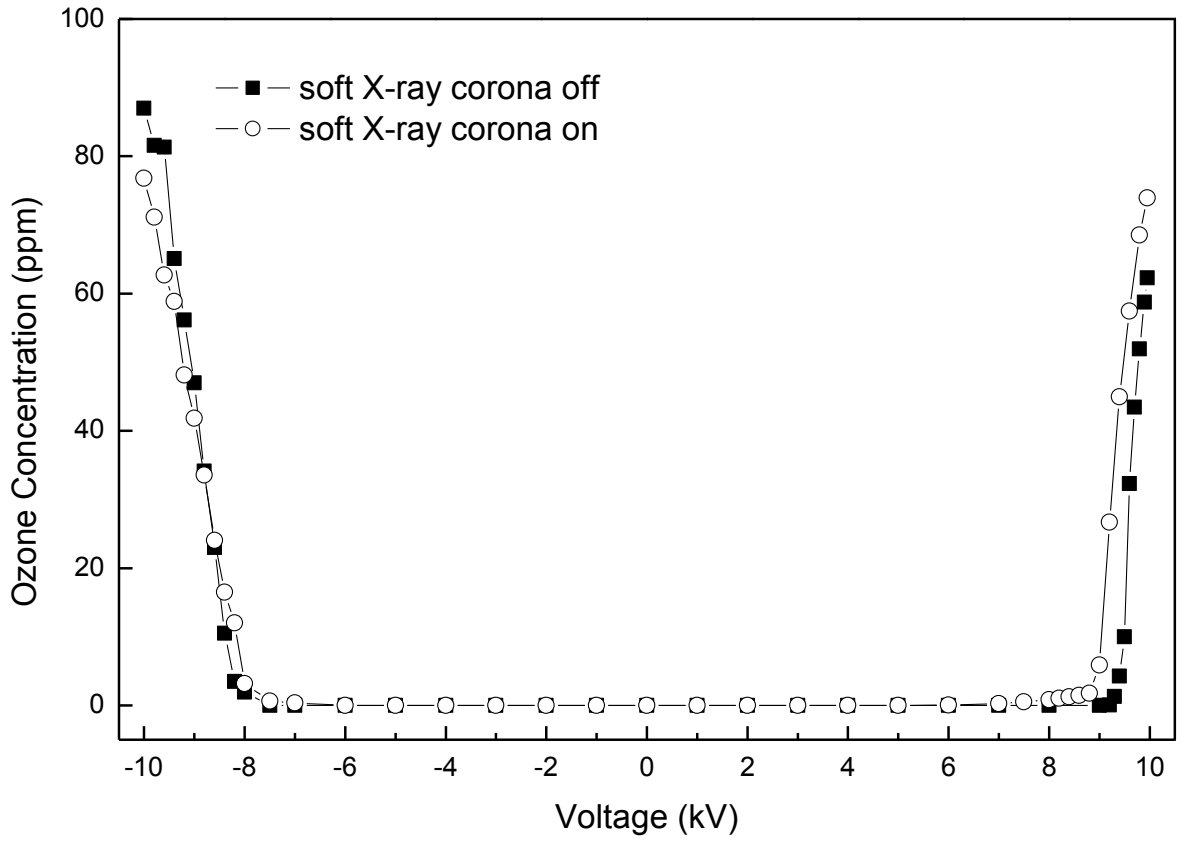

Figure 2.4 Ozone generation from ESP under base condition (0.04 lpm O_2, 0.12 lpm CO_2, 0.84 lpm N_2)

The above-mentioned results showed that a positive ESP voltage created better Hg^0 oxidation than a negative one. Hence, a voltage of +10 kV was applied to the ESP in subsequent experiments.

2.3.3 Effect of flue gas compositions

To further elucidate the mechanism, especially how gas composition determines radical formation (step 3 in the mechanism), Hg^0 conversion was measured under pure O_2, CO_2, and N_2, respectively. The Hg^0 conversions and current measurements are shown in Figure 2.5 with

simulated flue gas scenarios as reference, and O_3 generations in those cases are shown in Figure A1.4.

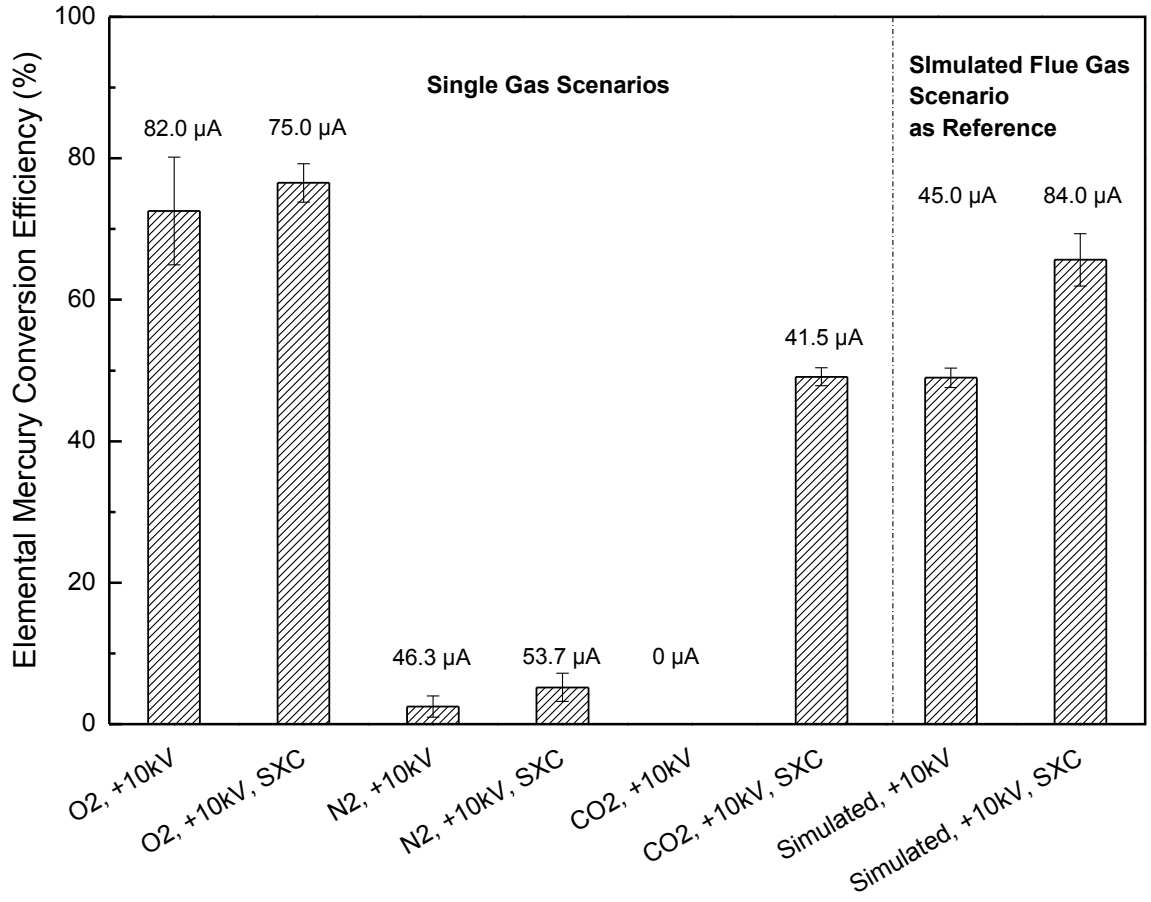

Figure 2.5 Mercury conversion efficiencies by ESP and soft X-rays under single gas environments (total flow rate: 1 lpm, ESP currents for various cases are above the bars, gas combination: 4% O_2, 12% CO_2, 84% N_2)

Under pure O_2, O and O_3 radicals were formed in the following reactions (Chen and Davidson, 2002):

$$e + O_2 \rightarrow O + O + e \tag{2.5}$$

$$O + O_2 + M \rightarrow O_3 + M \tag{2.6}$$

where M is a gas molecule. ESP currents and Hg^0 conversions are both high under ESP alone and ESP with soft X-rays. One noteworthy phenomenon is that the current was lower when the soft X-ray was on. The reason might be that electrons produced by corona discharge reached an extremely high concentration in the ionization area due to high concentration of O_2 and the drifting effect shown in Figure 2.3a, and the bipolar charging due to soft X-ray photoionization actually neutralized the electrons. However, the Hg^0 conversions were at the same level in both cases. Perhaps the radical concentrations were high enough that they were no longer limiting factors of Hg^0 oxidation reactions in both cases.

When N_2, is used, soft X-ray and UV radiations as well as high energy electrons were present in the system, but there was no source for O radicals. In this case, Hg^0 conversion was below 5%. These results verify that radicals generated from oxygen are the main cause of Hg^0 oxidation rather than direction reactions between Hg^0 molecule and high energy radiations or electrons. The slight Hg^0 conversion may be due to ionization of excited Hg atoms in the presence of N_2 (Sibata et al., 1979).

Under pure CO_2, no Hg^0 was oxidized by ESP alone, and no current was detected. This result agrees with the previous understanding that CO_2 plays a role in stabilizing the discharge process (Wang et al., 2009). However, when soft X-ray was added, a current of 41.5 μA and an Hg^0 conversion of 49.1% were reached. The main reaction involved is as follows (Skalny et al., 2008a, 2008b):

$$e + CO_2 \rightarrow e + O + CO \tag{2.7}$$

This reaction leads to generation of O radicals. However, the extent of reaction was extremely low under corona discharge alone, because the electron-impact dissociation rate of CO_2 is 4-5 orders of magnitude lower than that of O_2 (Li et al., 1995; Wang et al., 2011). On the other hand, soft X-ray ionization can generate electrons, which promote the chain reactions and eventually result in a high concentration of radicals. ESP current measurements support this mechanism. No current was observed under ESP alone. However, when soft X-rays were on, a current of 41.5 μA was observed. The Hg^0 conversion result indicates that soft X-ray enhancement has great potential in Hg^0 oxidation by ESP when high concentrations of CO_2 are present in flue gas, such as in the oxy-combustion case.

The effect of O_2 concentrations on Hg^0 oxidation by ESP and soft X-rays was also investigated in simulated flue gas (Figure A1.5). When ESP alone was used, the mercury conversion efficiency significantly increased as the oxygen concentration increased, because O_2 is the major source for generation of chemically active species. However, when ESP and soft X-rays were both applied, the Hg^0 conversion was relative stable, because CO_2 is also an important source for generation of chemically active species in this condition. The O_3 concentrations under various O_2 concentrations are shown in Figure A1.6.

2.3.4 Modeling of electron density in an ESP

Based on the above discussed mechanisms and reaction pathways, a model for predicting electron density distribution was built. The simulation results can explain why the ESP coupled with soft X-rays oxidized Hg^0 better under positive voltages than negative ones. Considering the

configuration of the ESP, a 1D axisymmetric model was used to represent a cross section of the ESP. Its schematic diagram is shown in Figure A1.7.

Shown in eq2.8-eq2.10, the drift-diffusion equation, multicomponent diffusion equations, and Gauss' Law are the governing equations for electron density, non-electron species densities, and the electric field.

$$\frac{\partial}{\partial t}(n_e) + \nabla \bullet [-n_e(\vec{\mu}_e \bullet \vec{E}) - \vec{D}_e \bullet \nabla n_e] = R_e \tag{2.8}$$

$$\rho \frac{\partial}{\partial t}(w_i) + \rho(\vec{u} \bullet \nabla) w_i = \nabla \bullet \vec{j}_i + R_i \tag{2.9}$$

$$\nabla \bullet \varepsilon_0 \vec{E} = s \tag{2.10}$$

The generation rates of species were calculated based on 12 electron impaction reactions and 11 chemical reactions (Table A1.2). The ionization rate due to soft X-ray radiation was estimated based on data from Kulkarni et al. (2002).

Electron density distributions under +10 kV and -10 kV with and without soft X-rays are shown in Figure 2.6. The number of electrons that were close to the electrode, where the electrons had higher energies, was higher for the positive voltage cases than negative voltage cases. Electrons having higher energy were more likely to trigger reactions, such as in eq2.5 and eq2.7, through which O radicals were produced. This effect can explain our experimental observation that the Hg^0 oxidation rate was higher under positive voltage. Meanwhile, with soft X-rays, the number of electrons was higher, which resulted in a higher Hg^0 oxidation rate.

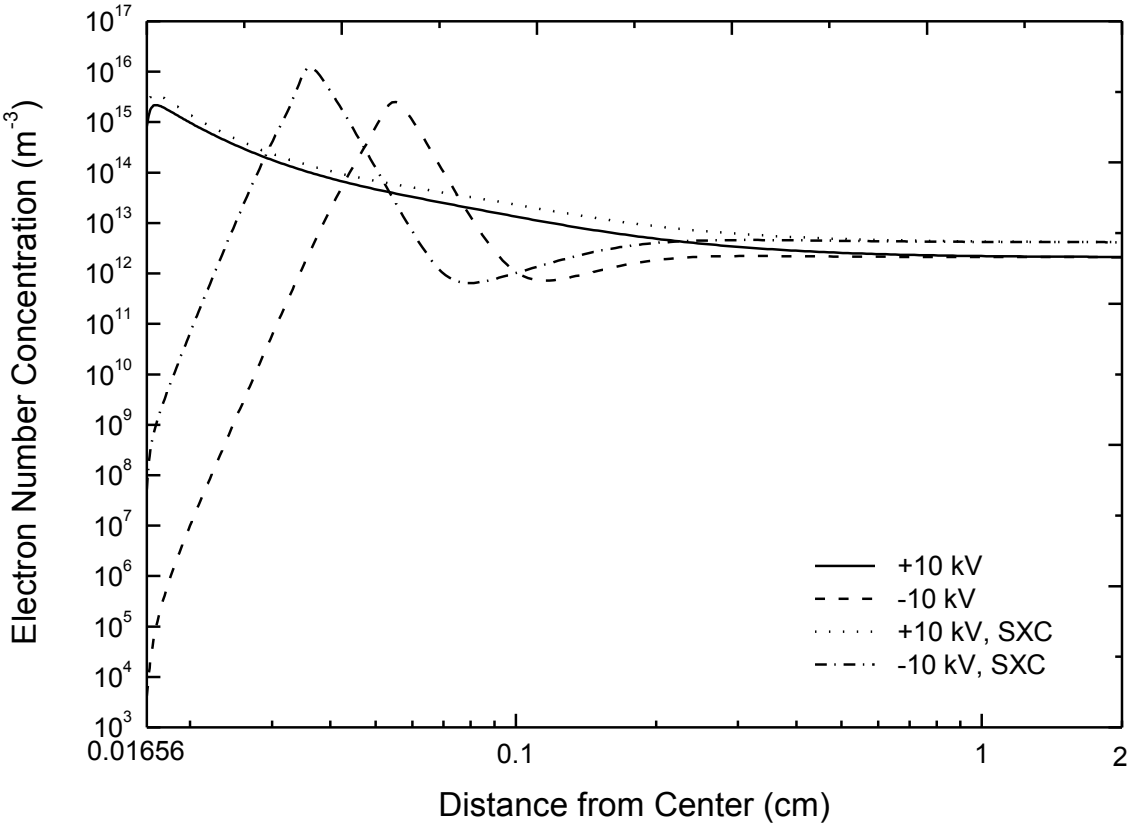

Figure 2.6 Electron density distributions in ESP at +10 kV and -10 kV, with and without soft X-rays

2.3.5 Effect of particles in flue gas

Flue gas usually contains high concentrations of particulate matter. The particles may participate in and influence the process of Hg^0 oxidation by ESP and soft X-rays in various ways. The effects of three kinds of particles were studied in this section, including SiO_2, TiO_2, and KI particles. SiO_2, a chemically inert substance, is one of the main components of fly ash particles. TiO_2 is a well-known and widely applied photocatalyst which can be activated under UV light and catalyze many reactions (Wold 1993; Wang 2011b, 2012). It has been reported that oxidation of Hg^0 in flue gas by oxygen takes place in the presence of nanostructured TiO_2

particles and UV light (Wu et al., 1998). KI particles were reported to have the ability to oxidize Hg^0 in flue gas (Li et al., 2009b).

Table 2.2 summarizes Hg^0 conversions in the ESP with particle injection. The size distributions of the particles are shown in Figure A1.8. The SiO_2 particles had no significant influence on Hg^0 conversion. The slight decrease might be due to a small amount of electrons attaching to the particles instead of participating in the chain reactions.

Table 2.2 Elemental mercury conversion efficiencies under SiO_2, TiO_2, and KI particle injection (gas combination: 0.04 lpm O_2, 0.12 lpm CO_2, 0.84 lpm N_2)

	Conversion when ESP and soft X-rays were both off	Conversion when just ESP was on	Conversion when ESP and soft X-rays were both on
SiO_2	0	53.7%±1.3%	60.3%±1.5%
TiO_2	0	14.0%±0.8%	17.3%±0.1%
KI (high concentration)	92.5%±2.2%	87.1%±2.8%	90.4%±1.1%
KI (low concentration)	19.4%±1.3%	66.1%±3.2%	70.0%±2.5%

The TiO_2 particles significantly reduced Hg^0 conversion. UV photons from corona discharge and soft X-rays had energies higher than 3.0 eV, which is the band gap of TiO_2. In this case, UV photons and soft X-rays were absorbed by TiO_2 particles, and they excited electrons from TiO_2 particles. The generated electron-hole pairs reacted with electron donors or acceptors adsorbed on the surface of TiO_2 particles (Chen and Mao, 2007; Yates, 2009). Thus, the decrease of Hg^0

conversion might be because both soft X-rays and UV light from corona discharge were partially absorbed by TiO_2 particles. As a result, the extent of gas molecule ionization was reduced, and eventually fewer radicals were produced. On the other hand, the amount of Hg^0 that absorbed on the surface of TiO_2 particles was low, so the contribution of the TiO_2 photocatalytic pathway on Hg^0 oxidation was insignificant. Overall, TiO_2 particle injection in this test reduced the Hg^0 conversion. However, it has been reported that TiO_2 particles fixed in a DBD reactor can react with corona discharge in the reactor and enhance mercury oxidation (Yang et al., 2012a; Yang et al., 2012b), which is contrary to the results of this study. The explanation is that in the specific experimental conditions of Yang et al. (2012a, 2012b) active sites containing OH functional groups were formed on the surface of TiO_2 under UV radiation, which resulted in Hg^0 oxidation.

KI particles increased the Hg^0 conversion by introducing a new pathway for Hg^0 oxidation (Li et al., 2009b):

$$O_2 + 4KI \rightarrow 2I_2 + 2K_2O \tag{2.11}$$

$$Hg + I_2 \rightarrow HgI_2 \tag{2.12}$$

Considering the corona discharge and soft X-ray radiation environment, the following reactions were likely to form I_2 radicals:

$$O + 2KI \rightarrow I_2 + K_2O \tag{2.13}$$

$$O_3 + 2KI \rightarrow I_2 + K_2O + O_2 \tag{2.14}$$

It should be noted that most of the KI particles were quickly deposited on the collection electrode of the ESP once they flew in, and the chance that they could participate in the reaction was much lower. This is evidenced by the comparison of Hg^0 conversions under different operating

conditions with a high concentration of KI particles. When the ESP and soft X-rays were off, Hg^0 conversion of 92.5% was achieved; however, when the ESP was turned on or they were both turned on, the conversion decreased by 5.4% and 2.1%. Another issue is that reaction between KI and Hg^0 at room temperature was observed in this study. However, in a previous study (Li et al., 2009b), no conversion was observed. The difference may be due to the longer residence time of the flue gas in the system in this study (30.0 sec compared to 5.8 sec).

2.3.6 Mercury oxidation in flue gas from coal combustion

In this section, mercury oxidation by ESP and soft X-rays was tested in flue gas from coal combustion in a drop-tube furnace (Figure 2.1b). The particle size distribution in the flue gas from PRB coal combustion is shown in Figure 2.7. The size distribution is typical for coal combustion (Zhuang and Biswas, 2001; Suriyawong et al., 2006; Li et al., 2009a; Wang et al., 2013b). Figure 2.7 also shows that the ESP can remove at least 99.7% of the fly ash particles. For flue gas with particles, no clear Hg^0 conversions were observed (conversion efficiencies were 1.1%±0.1% with ESP alone, and 1.5%±0.2% with both ESP and soft X-rays).

To compare the flue gas from drop-tube furnace with the simulated gas used in experiment set I; the composition of the former one is more complicated and contains water vapor, SO_2, HCl, and NO_x. Water vapor can enhance Hg^0 oxidation due to ·OH radical generation under corona discharge (Ko et al., 2008b; Wang et al, 2009; Yang et al. 2012b). SO_2 and HCl also can enhance Hg^0 conversion (Figure A1.10 and Figure A1.11). NO interferes Hg^0 oxidation because they compete with Hg^0 on reacting with oxidizing radicals (Jeong and Jurng, 2007; Ko et al., 2008a; Ko et al., 2008b; Wang et al., 2009).

Based on the above discussion and the results presented in the last section, two factors, NO and particles in the flue gas, are known to alter Hg^0 oxidation. However, Hg^0 conversions in particle-free flue gas (particles were filtered out by a HEPA filter before flying into the ESP) were still extremely low (conversion efficiencies were 0 with ESP alone, and 3.9% ±0.4% with both ESP and soft X-rays). Therefore, particles are not the main reason for the conversion reduction. NO in the flue gas is the cause of the conversion reduction.

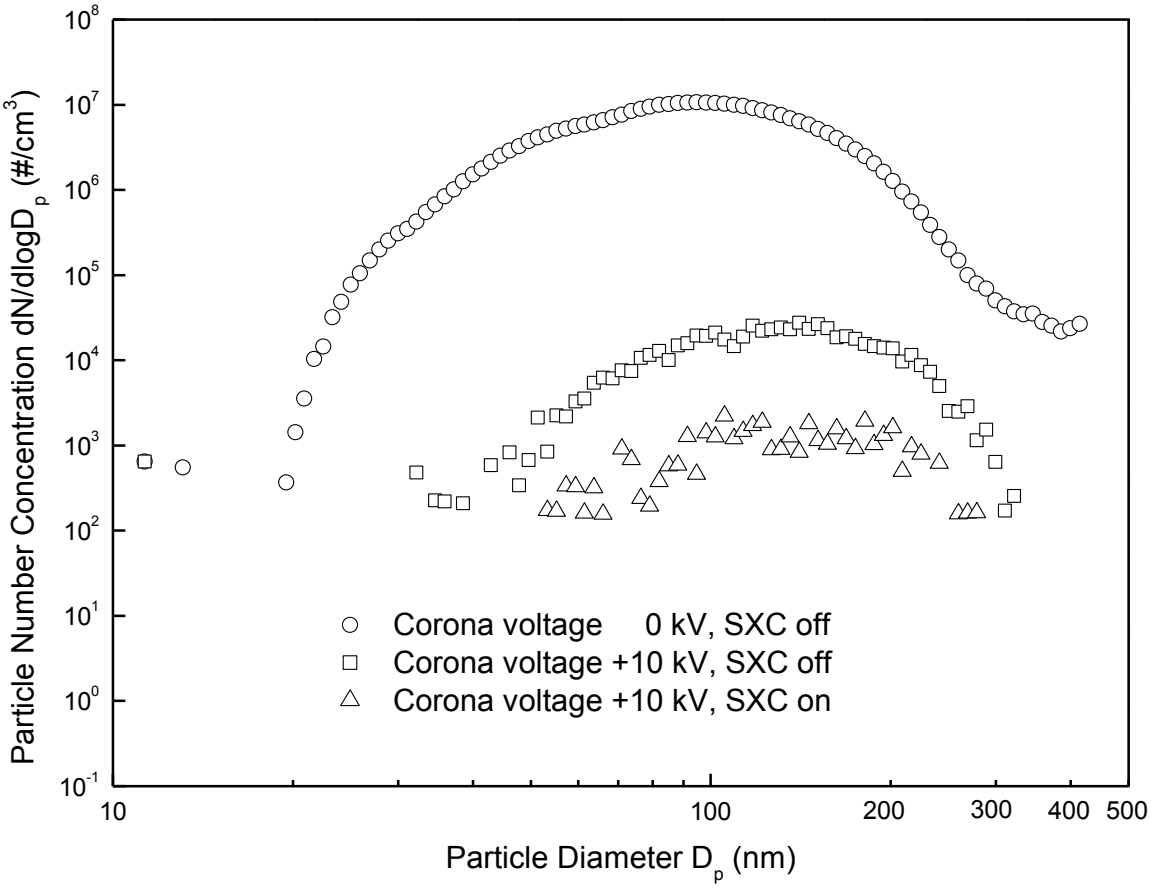

Figure 2.7 Particle size distributions of PRB coal combustion downstream of the ESP

Figure 2.8 shows the conversions in the cases where 200 ppm KI was mixed into the coal before combustion. Higher conversions were observed when the ESP and soft X-rays were turned on,

which evidences that Hg^0 can be oxidized by ESP and soft X-rays in this condition. If the Hg^0 concentration in the flue gas with ESP and soft X-rays off was used as baseline, the conversions due to ESP and to ESP with soft X-rays were 21.5% and 27.7%, respectively, which are 43.9% and 42.3% of the values for synthetic flue gas. One explanation might be that with I_2 in flue gas working as an oxidizer in the ESP, the radicals generated by the ESP and soft X-rays were in excess after the preferred reaction with NO, and they oxidized the Hg^0.

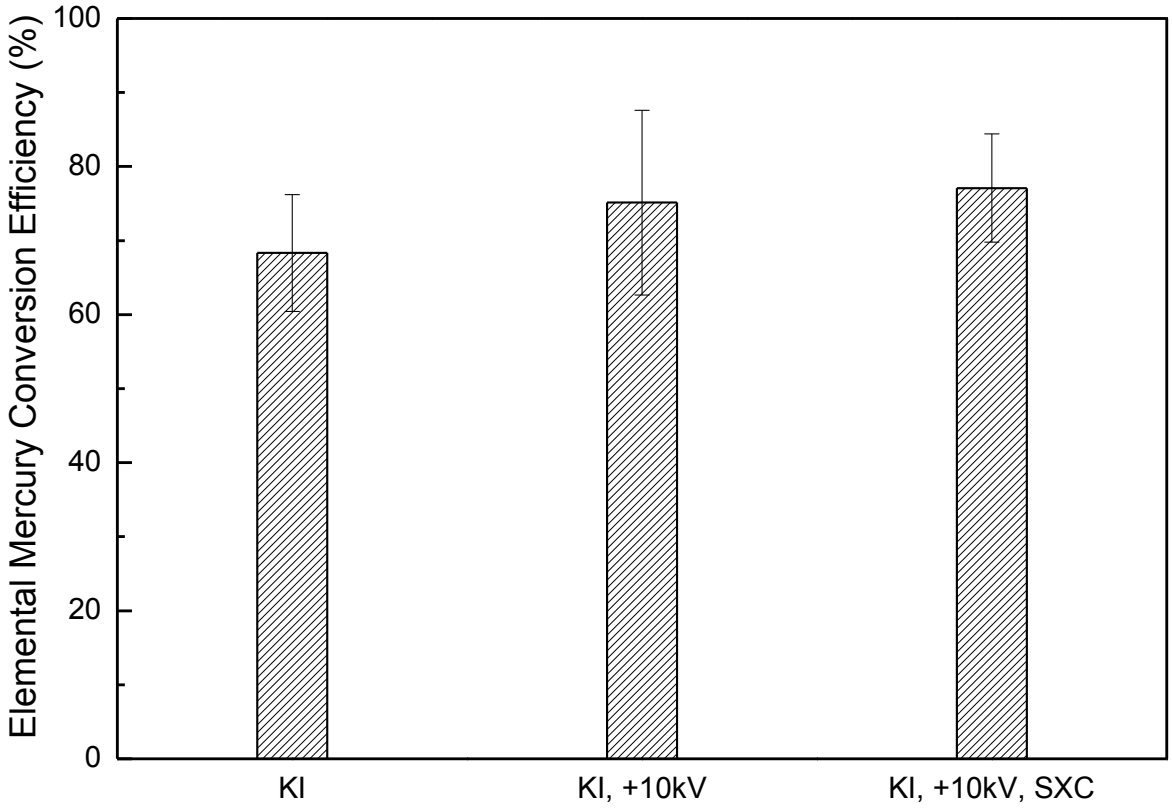

Figure 2.8 Elemental mercury conversion efficiencies by ESP and soft X-rays in practical flue gas from coal combustion, with KI addition (200 ppm KI in China S03 coal)

2.4 Conclusions

The process of Hg^0 oxidation by ESP and soft X-rays was investigated. Studies were first conducted in synthetic flue gas. Hg^0 was oxidized under +10 kV and -10 kV voltages of the ESP, and +10 kV had the better effect. Soft X-rays enhanced the oxidation. A mechanism for Hg^0 oxidation was proposed: electrons were emitted due to photoionization caused by UV radiation from corona discharge and by soft X-ray radiation in the ESP, and then they initiated chain reactions that produced electrons, intermediate species, and other products. Radicals, such as O and O_3, were produced in the chain reactions, and they oxidized Hg^0. A model simulating the plasma processes was built for predicting the electron distribution in the ESP.

Oxidation mechanisms were further demonstrated by experiments conducted under single gas environments. Especially, in pure CO_2 soft X-ray photoionization showed significant enhancement on Hg^0 oxidation. SiO_2 particles did not have a significant effect on Hg^0 oxidation process; TiO_2 particles absorbed photons from corona discharge and soft X-rays and inhibited the Hg^0 oxidation; KI particles enhanced Hg^0 oxidation, because I^- could be oxidized into I_2 radicals.

In practical flue gas from coal combustion, the effects of ESP and soft X-rays on Hg^0 oxidation were not significant, which might be due to interference from NO. With KI addition to the coal, beneficial effects of ESP and soft X-rays on Hg^0 oxidation could be observed. With the ESP voltage at +10 kV, soft X-ray enhancement, and KI addition, mercury oxidation was maximized.

2.5 Nomenclature

a = order of reaction between elemental mercury and ozone with respect to ozone

b = order of reaction between elemental mercury and ozone with respect to elemental mercury

c = concentration

$\bar{c}$ = average concentration in the ESP

Δc = change of concentration

$\vec{D}$ = diffusivity

$\vec{E}$ = intensity of electric field

$\vec{j}$ = diffusive flux vector

k = reaction rate constant

n = number concentration

R = generation rate

s = space charge density

t = time

$\vec{u}$ = mass averaged fluid velocity vector

w = mass fraction

Greek Letters

ε = permittivity

$\vec{\mu}$ = electric mobility

ρ = density

Subscripts

e = electron

$Hg0$ = elemental mercury

$Hg0-O3$ = reaction between elemental mercury and ozone

i = species i

$O3$ = ozone

off = ESP is off

on = ESP is on

0 = reference index (represent vacuum in eq10)

2.6 References

Byun, Y., K.B. Ko, M. Cho, W. Namkung, D.N. Shin, J.W. Lee, D.J. Koh, and K. T. Kim. 2008. Oxidation of elemental mercury using atmospheric pressure non-thermal plasma. *Chemosphere* 72:652-658.

Byun, Y., D.J. Koh, and D.N. Shin. 2011a. Removal mechanism of elemental mercury by using non-thermal plasma. *Chemosphere* 83:69-75.

Byun, Y., D.J. Koh, D.N. Shin, M. Cho, and W. Namkung. 2011b. Polarity effect of pulsed corona discharge for the oxidation of gaseous elemental mercury. *Chemosphere* 84:1285-1289.

Chen, J. 2002. Direct-current corona enhanced chemical reactions. Ph.D. Thesis, University of Minnesota, USA.

Chen, J., and J.H. Davidson. 2002. Ozone production in the positive DC corona discharge: Model and comparison to experiments. *Plasma Chem. Plasma P.* 22(4):495-522.

Chen, X., and S.S. Mao. 2007. Titanium dioxide nanomaterials: synthesis, properties, modifications, and applications. *Chem. Rev.* 107:2891-2959.

Chen, Z., D.P. Mannava, and V.K. Mathur. 2006. Mercury oxidization in dielectric barrier discharge plasma system. *Ind. Eng. Chem. Res.* 45:6050-6055.

Feeley, T.J., L.A. Brickett, J.T. Murphy. 2003. Evaluation of the effect of SCR NO_x control technology on mercury speciation. http://www.netl.doe.gov/technologies/coalpower/ewr/pubs/SCRHgPaperFinal030503.pdf (accessed December 21, 2013)

Fujiwara, N., Y. Fujita, K. Tomura, H. Moritomi, T. Tuji, S. Takasu, S. Niksa. 2002. Mercury transformations in the exhausts from lab-scale coal flames. *Fuel* 81:2045-2052.

Gao, Y., Z. Zhang, J. Wu, L. Duan, A. Umar, L. Sun, Z. Guo, and Q. Wang. 2013. A critical review on the heterogeneous catalytic oxidation of elemental mercury in flue gases. *Environ. Sci. Tech.* 47, 10813-10823.

Hall, B. 1995. The gas phase oxidation of elemental mercury by ozone. *Water Air Soil Poll.* 80:301-315.

Hedrick, E., T.G. Lee, P. Biswas, and Y. Zhuang. 2001. The development of iodine based impinger solutions for the efficient capture of Hg^0 using direct injection nebulization-inductively coupled plasma mass spectrometry analysis. *Environ. Sci. Eng.* 35:3764-3773.

Hogan, C.J., Jr., M.H. Lee, and P. Biswas. 2004. Capture of viral particles in soft X-ray–enhanced corona systems: charge distribution and transport characteristics. *Aerosol Sci. Tech.* 38:475-486.

Hu, C.X., J.S. Zhou, S. He, L. Zhang, J.M. Zhang, Z.Y. Luo, K.F. Cen. 2009. Influence and control of electrostatic precipitators and wet flue gas desulfurization systems on the speciation of mercury in flue gas. *J. Power Eng.* 29(4):400-404.

Jeong, J., and J. Jurng. 2007. Removal of gaseous elemental mercury by dielectric barrier discharge. *Chemosphere* 68:2007-2010.

Jiang, Y., J. An, K. Shang, D. Jiang, J. Li, N. Wu, and Y. Lu. 2013. Oxidation efficiency of elemental mercury in two DBD plasma reactors. *JPCS* 418:012118.

Kettleson, E.M., B. Ramaswami, C.J. Hogan, Jr., M.H. Lee, G.A. Statyukha, P. Biswas, and L.T. Angenent. 2009. Airborne virus capture and inactivation by an electrostatic particle collector. *Environ. Sci. Eng.* 43:5940-5946.

Kettleson, E.M., J.M. Schriewer, R.M.L. Buller, and P. Biswas. 2013. Soft-X-ray-enhanced electrostatic precipitation for protection against inhalable allergens, ultrafine particles, and microbial infections. *Appl. Environ. Microb.* 79(4):1333-1341..

Ko, B.K., Y. Byun, M. Cho, W. Namkung, D.N. Shin, D.J. Koh, and K.T. Kim. 2008a. Influence of HCl on oxidation of gaseous elemental mercury by dielectric barrier discharge process. *Chemosphere* 71:1674-1682.

Ko, B.K., Y. Byun, M. Cho, W. Namkung, I.P. Hamilton, D.N. Shin, D.J. Koh, and K.T. Kim. 2008b. Pulsed corona discharge for oxidation of gaseous elemental mercury. *Appl. Phys. Lett*. 92:251503.

Ko, B.K., Y. Byun, M. Cho, W. Namkung, I.P. Hamilton, D.N. Shin, D.J. Koh, and K.T. Kim. 2008c. Influence of gas components on the oxidation of elemental mercury by positive pulsed corona discharge. *Main Group Chem*. 7(3):191-204.

Korpiel, J.A., and R.D. Vidic. 1997. Effect of sulfur impregnation method on activated carbon uptake of gas-phase mercury. *Environ. Sci. Eng.* 31(8):2319-2325.

Kuikarni, P., N. Namiki, Y. Otani, and P. Biswas. 2002. Charging of particles in unipolar coronas irradiated by in-situ soft X-rays: enhancement of capture efficiency of ultrafine particles. *J. Aerosol Sci.* 33:1279-1296.

Li, J., W. Sun, B. Pashaie, and S.K. Dhali. 1995. Streamer discharge simulation in flue gas. *IEEE T. Plasma Sci.* 23(4):672-678.

Li, Y., A. Suriyawong, M. Daukoru, Y. Zhuang, and P. Biswas. 2009a. Measurement and capture of fine and ultrafine particles from a pilot-scale pulverized coal combustor with an electrostatic precipitator. *J. Air & Waste Manage. Assoc.* 59:553-559.

Li, Y., M. Daukoru, A. Suriyawong, and P. Biswas. 2009b. Mercury emissions control in coal combustion systems using potassium iodide: bench-scale and pilot-scale studies. *Energ. Fuel.* 23:236-243.

Liang, X., S. Jayaram, P. Looy, A. Berezin, and J.S. Chang. Pulse Corona Application for the Collection of Mercury from Flue Gas. Paper presented at 1998 IEEE International Symposium on Electrical Insulation, Arlington, VA, June 7-10, 1998.

Liang, X., P.C. Looy, S. Jayaram, A.A. Berezin, M.S. Mozes, and J.S. Chang. 2002. Mercury and other trace elements removal characteristics of DC and pulse-energized electrostatic precipitator. *IEEE T. Ind. Appl.* 38(1):69-76.

Lin, W., B. Zhang, W. Hou, Q. Zhou, and H. Yang. 2010. Enhanced oxidation of elemental mercury in simulated flue gas by non-thermal plasma. *Proc. CSEE* 30(2):72-76.

Namiki, N., K. Cho, P. Fraundorf, and P. Biswas. 2005. Tubular reactor synthesis of doped nanostructured titanium dioxide and its enhanced activation by coronas and soft X-rays. *Ind. Eng. Chem. Res.* 44:5213-5220.

Pal, B., and P.A. Ariya. 2004. Studies of ozone initiated reactions of gaseous mercury: kinetics, product studies, and atmospheric implications. *Phys. Chem. Chem. Phys.* 6:572-579.

Parker, K.R. 2003. Electrical Operation of Electrostatic Precipitators. London: The Institution of Electrical Engineers.

Qunn, R.J., M. Neville, M. Janghorbani, C.A. Mims, and A.F. Sarofim. 1982. Mineral matter and trace-element vaporization in a laboratory-pulverized coal combustion system. *Environ. Sci. Eng.* 16(11):776-781.

Richardson, C., T. Machalek, B. Marsh, S. Miller, M. Richardson, R. Chang, M. Strohfus, S. Smokey, T. Hagley, G. Juip, and R. Rosvold. Chemical addition for mercury control in flue gas derived from western coals. Joint EPRI DOE EPA Combined Utility Air Pollution Control Symposium, The Mega Symposium, Washington, D.C., May 19-22, 2003.

Sibata, A., M. Takahasi, H. Mikuni, H. Horiguchi, and S. Tsuchiya. 1979. Chemi-ionization of excited mercury atom with 253.7 nm irradiation in the presence of N_2 and CH_4. *B. Chem. Soc. Jpn.* 52(1):15-20.

Sjostrom, S., M. Durham, C.J. Bustard, and C. Martin. 2010. Activated carbon injection for mercury control: Overview. *Fuel* 89(6):1320-1322.

Skalny, J.D., S. Matejcik, J. Orszagh, R. Vladoiu, and N.J. Mason. 2008a. A study of the physical and chemical processes active in corona discharges fed by carbon dioxide. *Ozone-Sci. Eng.* 30:145-151.

Skalny, J.D., A. Stoica, J. Orszagh, R. Vladoiu, and N.J. Mason. 2008b. Positive and negative corona discharges in flowing carbon dioxide. *J. Phys. D: Appl. Phys.* 41:175211.

Suriyawong, A., M. Gamble, M.H. Lee, R. Axelbaum, and P. Biswas. 2006. Submicrometer particle formation and mercury speciation under O_2-CO_2 coal combustion. *Energ. Fuel.* 20:2357-2363.

Suriyawong, A., C.J. Hogan, Jr., J. Jiang, and P. Biswas. 2008. Charged fraction and electrostatic collection of ultrafine and submicrometer particles formed during O_2-CO_2 coal combustion. *Fuel* 87:673-682.

Suriyawong, A., M. Smallwood, Y. Li, Y. Zhuang, and P. Biswas. 2009. Mercury capture by nano-structured titanium dioxide sorbent during coal combustion: lab-scale to pilot-scale studies. *Aerosol Air Qual. Res.* 9(4):394-403.

Urabe, T., Y. Wu, T. Nagawa, and S. Masuda. 1988. Study on Hg, NO_x, SO_x behavior in municipal refuse incinerator furnace and removal of those by pulse corona discharge. *Seiso Giho* 13:12-29.

U.S. Environmental Protection Agency. 2011. Cleaner power plants. http://www.epa.gov/mats/powerplants.html (accessed July 2013).

Van Veldhuizen, E.M. 2000. Electrical Discharges for Environmental Purpose: Fundamentals and Applications. New York: Nova Science Publishers.

Wang, M., T. Zhu, H. Luo, P. Tang, and H. Li. 2009. Oxidation of gaseous elemental mercury in a high voltage discharge reactor. *J. Environ. Sci.-China* 21:1652-1657.

Wang, M., T. Zhu, H. Luo, H. Wang, and W. Fan. 2011a. Effects of reaction conditions on elemental mercury oxidation in simulated flue gas by DC nonthermal plasma. *Ind. Eng. Chem. Res.* 50:5914-5919.

Wang, M., Y. Sun, and T. Zhu. 2013a. Removal of NO_x, SO_2, and Hg from simulated flue gas by plasma–absorption hybrid system. *IEEE T. Plasma Sci.* 41(2):312-318.

Wang, W.N., J. Park, and P. Biswas. 2011b. Rapid synthesis of nanostructured Cu-TiO_2-SiO_2 composites for CO_2 photoreduction by evaporation driven self-assembly. *Catal. Sci. Tech.* 1(4):593-600.

Wang, W.N., W.J. An, B. Ramalingam, S. Mukherjee, D.M. Niedzwiedzki, S. Gangopadhyay, and P. Biswas. 2012. Size and structure matter: enhanced CO_2 photoreduction efficiency by size-resolved ultrafine Pt nanoparticles on TiO_2 single crystals. *J. Am. Chem. Soc.* 134(27):11276-11281.

Wang, X., S.M. Daukoru, S. Torkamani, W.N. Wang, and P. Biswas. 2013b. Role of exhaust gas recycle on submicrometer particle formation during oxy-coal combustion. *P. Combust. Inst.* 34:3479-3487.

Wang, Y.J., Y.F. Duan, L.G. Yang, S.L. Meng, Z.J. Huang, C.J. Wu, and Q. Wang. 2008. Experimental study on mercury removal by combined wet flue gas desulphurization with electrostatic precipitator. *Proc. CSEE* 28(29):64-69.

Wang, Z.H., S.D. Jiang, Y.Q. Zhu, J.S. Zhou, J.H. Zhou, Z.S. Li, and K.F. Cen. 2010. Investigation on elemental mercury oxidation mechanism by non-thermal plasma treament. *Fuel. Process. Technol.* 91:1395-1400.

Wold, A. 1993. Photocatalytic Properties of TiO_2. *Chem. Mater.* 5:280-283.

Worathanakul, P., P. Kongkachuichay, J.D. Noel, A. Suriyawong, D.E. Giammar, and P. Biswas. 2008. Evaluation of nanostructured sorbents in differential bed reactors for elemental mercury capture. *Environ. Eng. Sci.* 25(7):1061-1070.

Wu, C.Y., T.G. Lee, G. Tyree, E. Arar, and P. Biswas. 1998. Capture of mercury in combustion systems by in situ-generated titania particles with UV irradiation. *Environ. Eng. Sci.* 15(2):137-148.

Xie, R., Y. Duan, Y. Cao, L.C. Li, S. Kellie, W.P. Pan, J.T. Riley, K. Ho, P. Chu, and A. Metha. 2002. Mercury speciation and concentration at ESP in a 100 MWth coal-fired power plant. *Abstr. Pap. Am. Chem. S.* 224:U574.

Xu, F., Z. Luo, W. Cao, P. Wang, B. Wei, X. Gao, M. Fang, and K. Cen. 2009. Simultaneous oxidation of NO, SO_2 and Hg^0 from flue gas by pulsed corona discharge. *J. Environ. Sci.-China* 21:328-332.

Yang, H., W. Hou, H. Zhang, and L. Zhou. 2012. Oxidation of elemental mercury with non-thermal plasma coupled with photocatalyst. *J. Adv. Oxid. Technol.* 15(2):321-327.

Yang, H., H. Liu, H. Wu, and M. Wang. 2012. Photochemical removal of gaseous elemental mercury in a dielectric barrier discharge plasma reactor. *Plasma Chem. Plasma P.* 32:969-977.

Yang, L., X. Fan, D. Feng, and Y. Wang. Mercury removal characteristics of coal-fired power plants. Paper presented at 2013 Third International Conference on Intelligent System Design and Engineering Applications, Hong Kong, China, January 16-18, 2013.

Yates, J.T., Jr.. 2009. Photochemistry on TiO_2: Mechanisms behind the surface chemistry. *Surf. Sci.* 609:1605-1612.

Zhuang, Y., and P. Biswas. 2001. Submicrometer particle formation and control in a bench-scale pulverized coal combustor. *Energ. Fuel.* 15:510-516.

CHAPTER 3. SECONDARY AEROSOLS GENERATION IN AN ELECTROSTATIC PRECIPITATOR DURING FLUE GAS TREATMENT

The results of this chapter will be compiled as a paper for submission to Energy & Fuels (authors: He Jing, Xiaofei Wang, Wei-Ning Wang, Bhupesh Dhungel, Benjamin M. Kumfer, Richard L. Axelbaum, Brent J. Williams, Pratim Biswas).

Supplementary materials are available in Appendix II

Abstract

Electrostatic precipitators (ESPs) are widely used to control fly ash particulate matter in flue gas treatment for coal combustion processes. This study reports a mechanistic understanding of formation of secondary aerosols concurrenting in an ESP, secondary aerosols could be formed at the same time. The newly formed aerosols were mostly ultrafine (< 100 nm) particles, with a unimodal size distribution (GMD = 20 nm). Their chemical composition, as characterized by a HR-Tof-AMS (aerosol mass spectrometer), shows that the secondary aerosols contained high concentrations of sulfates and organics, which is very likely from sulfuric acid (H_2SO_4) and various organics. The most probable aerosol formation mechanisms are: first, H_2SO_4 vapor is produced from reactions among sulfur dioxide (SO_2), water (H_2O) in the flue gas, and the oxidizing radicals generated by the corona discharge in the ESP. Following this, H_2O-H_2SO_4 aerosols are formed through ion-induced nucleation, and grow by condensation and coagulation; concurrently, organic compounds are absorbed on the particles. The role of SO_2 concentration, the water content in the flue gas, the ESP voltage, and the flow rate on the H_2O-H_2SO_4 secondary aerosol formation was evaluated.

3.1 Introduction

Currently, 38.7% of U.S. electricity is provided by coal-fired power plants (Hankey 2015). 570,000 tons of $PM_{2.5}$ are produced annually from U.S. coal-fired power plants (Davidson et al., 2005). To control such particle emissions, electrostatic precipitators (ESPs) are effectively used, with high overall mass-based collection efficiencies exceeding 99%.

Fine (<2.5 μm) and ultrafine (<0.1 μm) aerosols have received special attention because they can penetrate into the alveolar regions of the lungs upon inhalation, and create more severe health hazards for human beings (Biswas and Wu, 2005). Thus, the fine particle capture capability of ESPs has been specifically studied on both bench-scale ESPs with synthetic particles (Yoo et al., 1997; Zhuang et al., 2000; Jing et al., 2013; Huang and Chen, 2002) and ESPs with particles and flue gas from combustion systems (McCain et al., 1975; Ylätalo and Hautanen, 1998; Suriyawong et al., 2008). Two phenomena were commonly observed. (1) A minimum collection efficiency was observed for the 0.1-1 μm size range; due to the combined effects of diffusion charging, which increases with decreased particle sizes, and field charging, which increases with increased particle sizes. (2) In the ultrafine size range below 100 nm, the collection efficiency decreased with decreasing size. A key reason for this was that the particle charging efficiency decreased dramatically as the particle size became smaller (Kulkarni et al., 2002).

However, in previous fine particles collection studies (Li et al., 2009), the important factor, new particle formation in the ESP operation process has rarely been taken into account, such formation might be the reason for the extremely high penetration in the low particle size range (below 30 nm). Theoretically, new particle formation, which can be referred to as secondary aerosol (SA) generation in this case, is possible under DC (direct current) corona discharge (the main ion generation mechanism of the ESP) in the presence of gaseous pollutants such as SO_2,

NO, and VOCs in the flue gas. Two mechanisms may contribute to particle formation. First, corona discharge in the ESP produces oxidizing radicals, such as O and O_3, in the presence of O_2 (Jing et al., 2015). These radicals may react with the aforementioned volatile compounds and produce semi- or non-volatile compounds, which further form particles through gas-solid phase partitioning (Nagato 2009). Second, ion-induced nucleation may take place under corona discharge and promote particle formation (Wilhelm et al., 2004; Sorokin et al., 2006; Nagato, 2009; Lapshin et al., 2012; Hvelplund et al., 2013). However, to the best of our knowledge, there is no report on SA particle formation in the ESP during flue gas treatment.

In this study, the SA formation in the ESP was first verified and characterized with a slip stream exhaust gas from a pilot-scale combustion system. The SA chemical composition was determined using an aerosol mass spectrometer (AMS) on a lab-scale drop-tube furnace combustion system to unravel the mechanistic pathway. Finally, the effects of ESP operating conditions, flow rate through the ESP, and gas compositions in flue gas on SA formation were evaluated on a simulated flue gas system.

3.2 Experimental Section

3.2.1 Experimental system

A bench-scale DC corona-based wire-cylinder type ESP was used and was described in previous studies (Jing et al., 2015). The ESP configuration is shown in Figure A2.1 in supporting information. The experiments were conducted on three experimental systems of different scales. The first system was a 1 MW capacity pilot-scale coal combustor with a boiler in the Advanced Coal and Energy Research Facility (ACERF) at Washington University in St. Louis (Figure 3.1a).

West Elk bituminous coal was combusted. The proximate and ultimate analyses are shown in Table A2.1. For the air-fired combustion cases, the facility was operated at 400 kW thermal power; for the oxy-combustion case, the facility was operated at 270 kW power. A slipstream of gases was drawn after the boiler, passed through a cascade impactor (1 μm cut-off size; Mark III, Pollution Control Systems Corp., Seattle, WA), and then introduced into the ESP. A scanning mobility particle sizer (SMPS, TSI, model 3080, Shoreview, MN) was used to measure the fly ash particle size distribution. In the ESP efficiency test, the particle penetration for each size was determined by:

$$\mathrm{P}(d_p) = \frac{N_{out}(d_p)}{N_{in}(d_p)}, \tag{3.1}$$

where P is the particle penetration, N_{out} and N_{in} are the particle concentrations downstream and upstream from the ESP, and d_p is the particle diameter. For direct measurement of the secondary aerosols, a HEPA (High-efficiency particulate arrestance) filter (Pall Corporation, Port Washington, NY) was placed before the ESP to remove all particles to ensure that the particles detected were from new particle formation processes. During all of the above experiments, the flow rate through the ESP was 10 LPM.

The drop-tube furnace system is shown in Figure 3.1b. The configuration and parameters have been discussed in previous papers (Wang et al., 2013a; Wang et al., 2015). Illinois No.6 coal (proximate and ultimate analyses shown in Table A2.1) was fed at a rate of 2.5 g/hr. A high-resolution time-of-flight aerosol mass spectrometer (HR-Tof-AMS, Aerodyne Research Inc, Billerica, MA) was used to analyse the SA chemical composition. In order to increase the particles size of SAs beyond the critical particle diameter required by AMS (lower size limit: 40 nm), particles were grown with water vapor in a bubbler before they entered the AMS. In the

simulated flue gas system (Figure 3.1c), air was mixed with SO_2 and water vapor to mimic the flue gas. The water vapor was introduced by passing air through a water bubbler. In both lab-scale systems, HEPA filters were placed before the ESP. The flow rate through the ESP was 15 LPM unless noted.

(a)

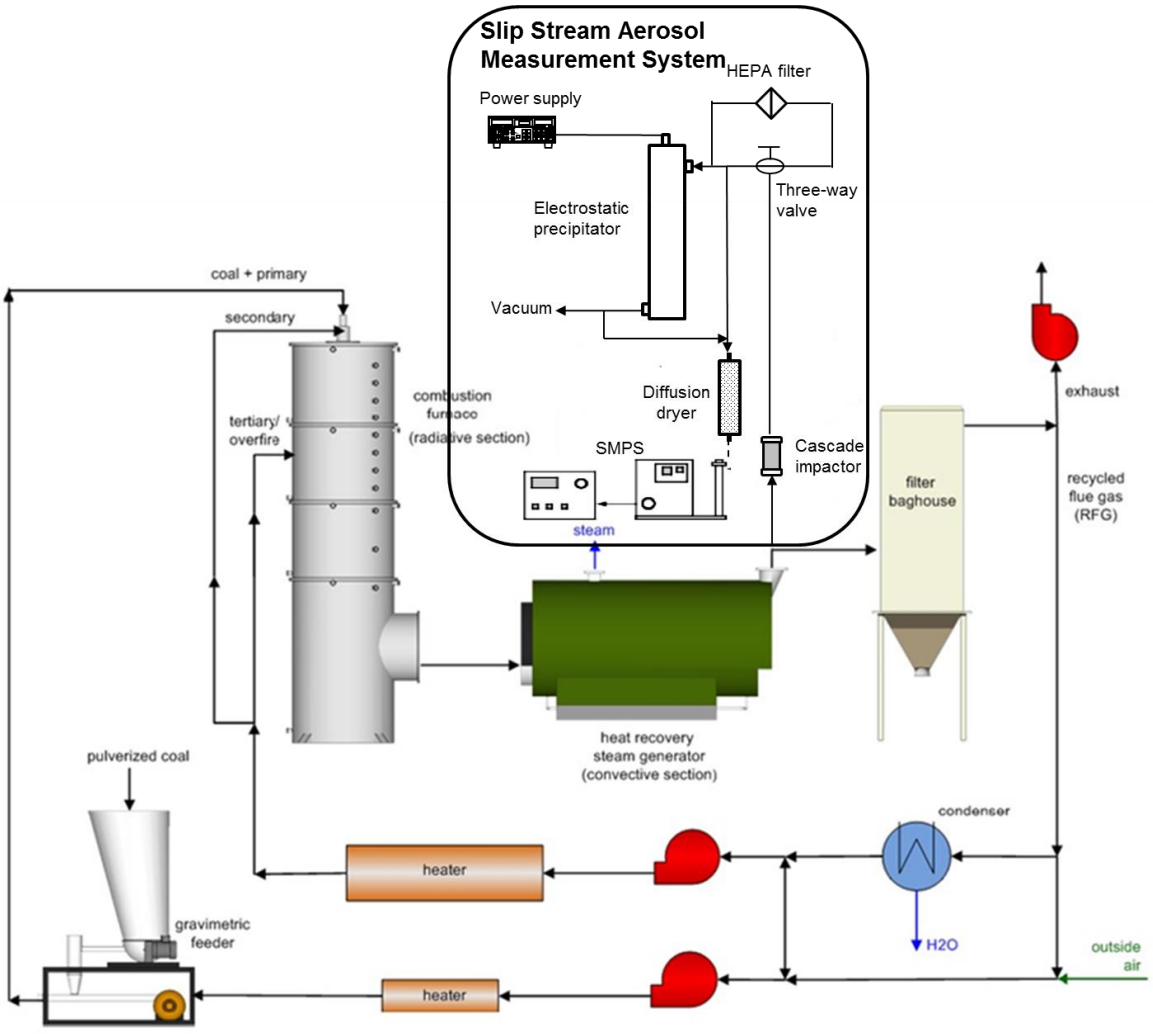

(b)

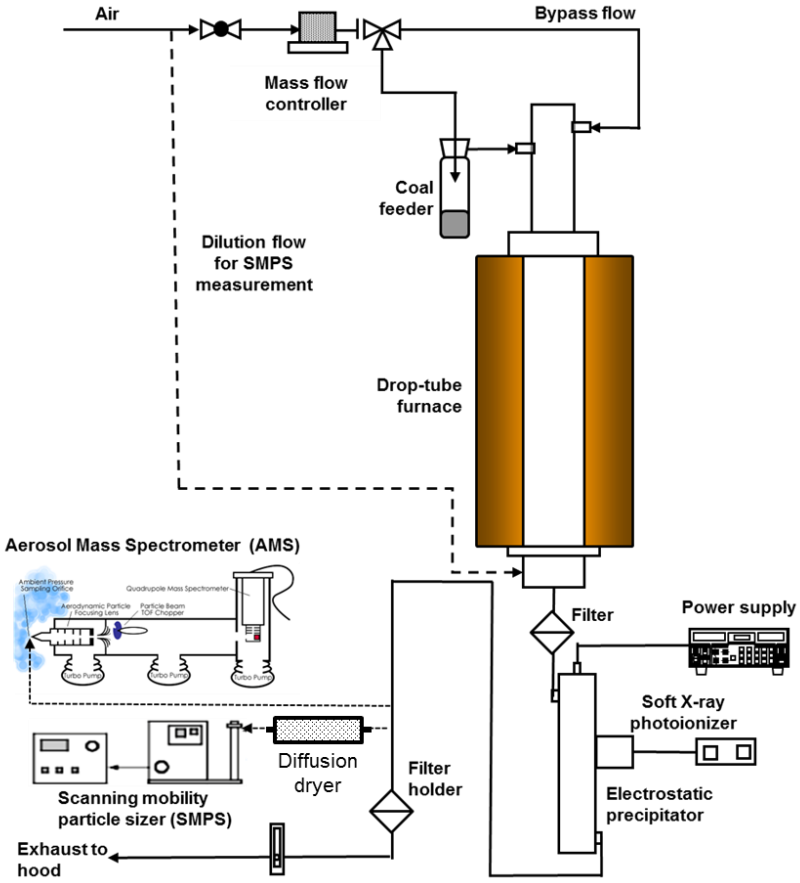

(c)

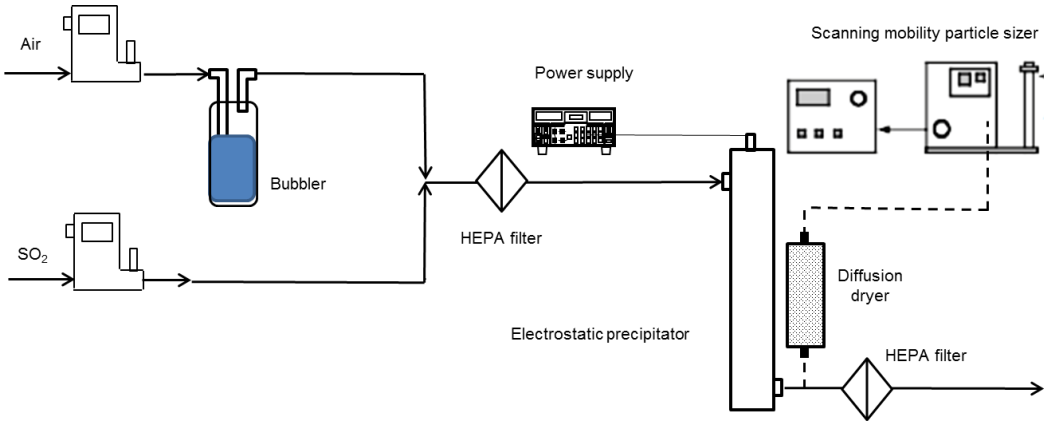

Figure 3.1 Schematic of experimental setups: (a) ACERF pilot-scale combustion system and particulate matter measurement instruments; (b) drop-tube furnace system (figure adapted from Wang et al., 2013); (c) simulated flue gas system

3.2.2 High-resolution time-of-flight aerosol mass spectrometer (HR-Tof-AMS)

In this study, a HR-Tof-AMS (Aerodyne Research Inc, Billerica, MA) was used to determine the chemical compositions of the aerosols. Aerosols were introduced into the instrument through an aerodynamic lens and focused into a narrow beam, and then the sizes of the aerosols were determined by their velocities through a time of flight chamber. After that, the particles were impacted on a 600 ^{o}C vaporizer for chemical analysis. The non-refractory portion of the particles was vaporized and immediately ionized through electron impact ionization, resulting ions were analysed by the time-of-flight mass spectrometer.

3.2.3 Experimental design

This study was conducted in three steps. In the first step, SA formation was verified in a pilot-scale setting (1 MW combustion system). The particle size distribution was characterized. Second, the chemical composition was determined on the drop-tube furnace system with AMS. Last, parameter studies were conducted to study the SA formation. The detailed experimental design is shown in Table 3.1.

Table 3.1 Summary of the experiments performed

Set	Objective	Flue gas	Measurement
I	To verify the secondary aerosol formation in ESP	Slipstream from the boiler of ACERF pilot-scale combustion system	Size distributions of secondary aerosols by SMPS
II	To characterize the chemical composition of secondary aerosols	Flue gas from coal combustion in the drop-tube furnace system	Size distributions of secondary aerosols by SMPS; Chemical compositions of secondary aerosols by AMS
II	To evaluate the effects of SO_2 concentration, water content, ESP voltage, and flow rate through ESP on the secondary aerosols formation	Gas mixture of air, SO_2, and water vapor	Size distributions of secondary aerosols by SMPS

3.3 Results and Discussion

3.3.1 Observation of SA formation and particle size distribution measurement

The fly ash particles introduced from the combustor into the ESP were submicrometer aerosols with a unimodal distribution (Figure A2.2). Such fly ash aerosol size distribution is typical for coal combustion (Zhuang and Biswas, 2001; Suriyawong et al., 2006; Wang et al., 2013b). The flue gas compositions corresponding to different runs are summarized in Table A2.2. The ESP

demonstrated high collection efficiencies for particles larger than 30 nm, with both positive and negative voltages, as shown in Figure 3.2. However, for particles smaller than 30 nm, the penetration increased dramatically as the particle size decreased, which is in agreement with the findings of Li et al. (Li et al., 2009) from a pilot-scale ESP. This penetration increase may be partially due to the decrease in the charging efficiency of ultrafine particles, especially sub-50 nm (Yoo et al., 1997; Zhuang et al., 2000; Huang and Chen, 2002; Jing et al., 2013). However, as particle size dropped below 20 nm, we observed that penetration exceeded one which could only be explained by new particle formation.

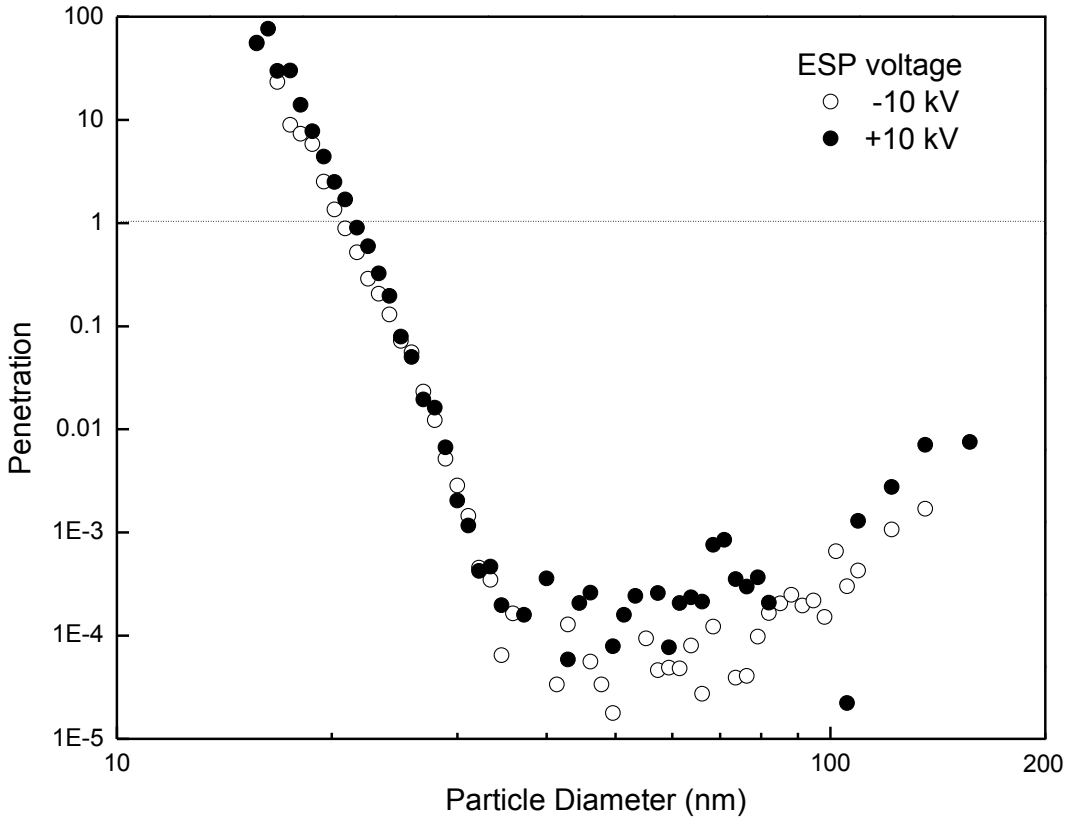

Figure 3.2 Penetrations of fly ash particles through ESP at ACERF pilot-scale system (for -10 kV and +10 kV ESP voltages)

Previously, new particle formation in ESP-type indoor air cleaners and WESPs (wet ESPs) has been reported. Waring et al. (Waring et al., 2008) observed SA generation from VOCs in an ESP-type indoor air cleaner. Recently, formation of hydrobromic and hygrochloric acid (HBr and HCl) aerosols (Sinanis et al., 2013), as well as sulfuric acid (H_2SO_4) aerosols (Mertens et al., 2014; Anderlohr et al., 2015) in a WESP have been reported. Closely related to this topic, it has been reported that corona discharge reactors can initiate reactions with SO_2 and NO to form H_2SO_4 and HNO_3 particles (Matteson et al., 1972; Kuroki et al., 2002; Mok and Nam, 2002; Dong et al., 2003), and the particles were expected to be collected in the reactors. A penetration,

P > 1, observed in this study (Figure 3.2) clearly indicates that new particles can be formed in a dry ESP and penetrate through during exhaust gas treatment.

In order to directly measure the size distribution of newly formed SAs, particles were removed with a HEPA filter before they entered the ESP. In coal-fired power plants, ESPs are usually operated under negative polarity in order to achieve higher ion concentrations and capture efficiency, so the test ESP was fixed in negative voltage mode in all following experiments. Three combustion conditions were tested ([1] air-fired with 2% O_2 in the flue gas, [2] air-fired with 4% O_2 in the flue gas, and [3] 40% O_2/60% air as oxidizer). The flue gas compositions and flow rates are summarized in Table A2.2. Figure 3.3 shows that the SAs leaving the ESP had a unimodal size distribution, which is an outcome of two competing processes, the formation of SAs and the simultaneous capture of newly formed SAs in the ESP. The SAs formed through nucleation and condensation typically has a unimodal size distribution (Hinds 1999), which greatly determined the size distribution of SAs exiting the ESP. At the same time, ESPs have lower capture efficiency for smaller particles. Previous studies have shown that the efficiency of ESPs dropped dramatically when the particle size was below 30 nm (Hogan et al., 2004). This drop could explain why in all the three studied cases with different flue gas compositions, the peak of the size distributions remained at 20 nm. It is important to note that with fly ash present, the size distribution of newly formed aerosols might be slightly different from that shown in Figure 3, because some of the secondary aerosol precursor molecules might condense on the fly ash particles instead of forming new particles.

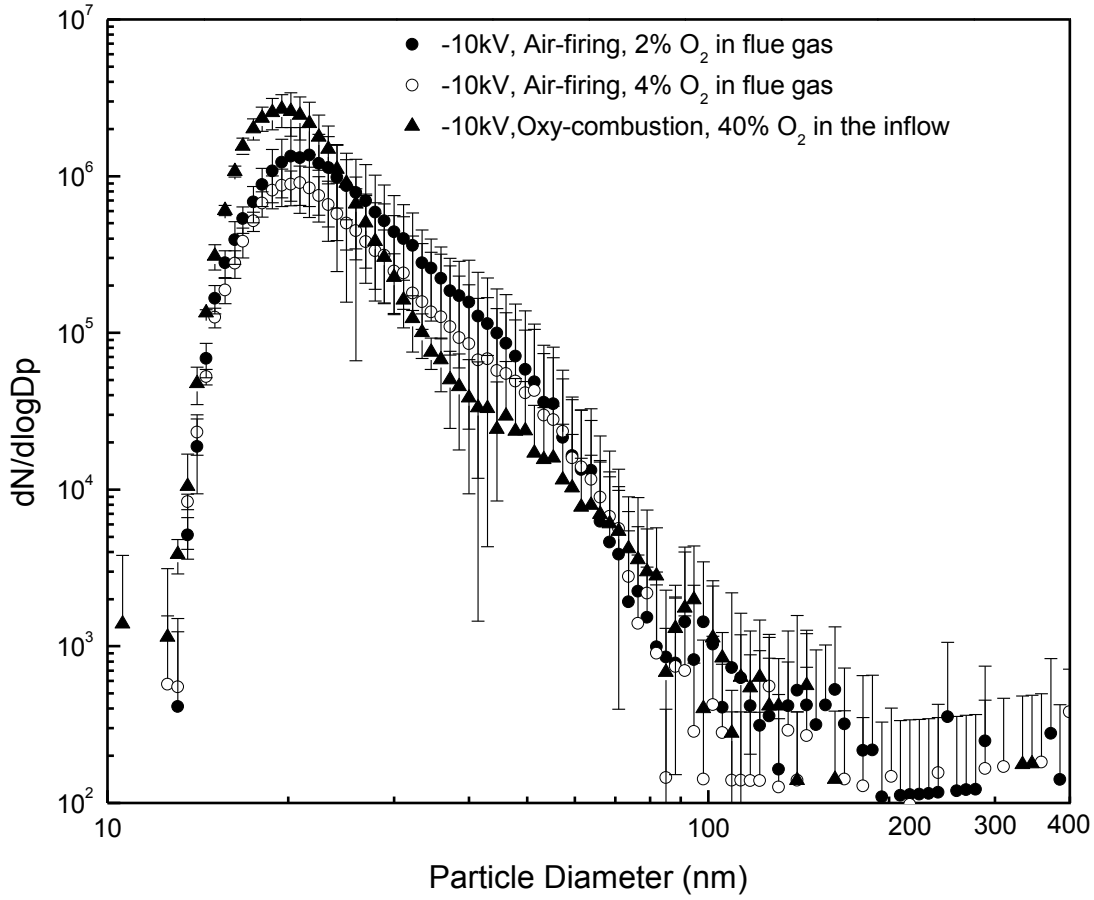

Figure 3.3 Particle size distributions of secondary aerosols formed in the ESP during flue gas treatment

3.3.2 Chemical compositions and formation mechanism of SAs

In order to measure the chemical composition of the SAs, formation in an ESP was repeated on a lab-scale drop-tube (Figure 3.1b). As in the pilot-scale system test, the SAs had a unimodal size distribution with a peak size of 22 nm (Figure A2.3). The mass spectrum of SAs is shown in Figure 3.4a. The main compositions of SAs were sulfate ions and organics.

Significant sulfate fragment peaks are observed at m/z 48 (SO^+), 64 (SO_2^+), 80 (SO_3^+), and 98 ($H_2SO_4^+$), which shows that the SAs contained a significant amount of SO_4^{2-}. Considering the compositions of the flue gas and possible reactions, as well as that there were limited ammonium or other metal cations in the particles; the main component of the SAs was expected to be sulfuric acid (H_2SO_4). To be specific, the newly formed aerosols are likely to be H_2O-H_2SO_4 aerosols (Van Dingenen and Raes, 1991). The formation of those aerosols can be divided into two steps: (1) H_2SO_4 vapor is produced from SO_2 through oxidation reactions; (2) H_2SO_4 vapor then forms H_2O-H_2SO_4 particles through gas-solid partitioning in the presence of water vapor. For step 1, the mechanism of H_2SO_4 vapor production under corona discharge is well known (Mok and Nam, 2002): (1a) The oxidizing radicals, such as O·, OH·, and O_3, are formed in the ESP under corona discharge; (1b) The radicals react with SO_2 and finally produce H_2SO_4. The key reactions for step 1b are summarized below:

$$SO_2 + O \rightarrow SO_3 \tag{3.2}$$

$$SO_2 + OH \rightarrow HSO_3 \tag{3.3}$$

$$SO_2 + O_3 \rightarrow SO_3 + O_2 \tag{3.4}$$

$$HSO_3 + OH \rightarrow H_2SO_4 \tag{3.5}$$

$$SO_3 + H_2O \rightarrow H_2SO_4 \tag{3.6}$$

In step 2, nuclei are formed through ion-induced nucleation. Ion charge reduces the nucleation barrier and the size of the critical cluster, and thus helps to form new particles more efficiently (Lovejoy et al., 2004). Based on previous studies (Nagato, 2009; Hvelplund et al., 2013), the clusters that could form in this condition include $H^+(H_2SO_4)(H_2O)_n$, $HSO_5^-(H_2O)_n$, and SO_4^-

$(H_2O)_n$. After nucleation, the aerosols grow through condensation and coagulation (Stauffer et al., 1973; Hamill 1975; Hinds 1999). The pathways discussed above are shown in Figure 5 (the right part of the schematic diagram).

In the mass spectrum of SAs (Figure 3.4a), major peaks are also observed at several m/z values, which shows the presence of organics in the particles. Especially, the peaks at m/z 44, 60, 73 indicate the presence of carboxylic acids. The peak at 57 is likely to be hydrocarbon-like fragments ($C_xH_y^+$) (Canagaratna et al., 2007). Aldehydes and alcohols (m/z 27, 29, 31, 41, 43, 55, 56, 57, 70) were also major organics in the SAs. Peaks at m/z 77 and 91 are not significant, suggesting there was almost no aromatic compounds in the SA (Ng et al., 2010; McLafferty and Tureek, 1993). A possible pathway for the formation of the organic components: start with organic vapor in the flue gas. Inside the ESP, the molecules of organic compounds are adsorbed by the sulfuric particles as they grow (physical/chemical adsorption), and as a result the SAs have a significant amount of organics. This pathway is also shown in Figure 3.5.

The evolution of the composition of organic species in the SAs is further supported by the high resolution of the AMS spectrum (Figure 3.4b). Hydrocarbon (CH)-like species were the main organic species, which suggests that it is unlikely that they were formed through oxidation and nucleation. Instead, probably H_2O-H_2SO_4 particles absorbed these organics from the gas phase directly. Other than CH-like species, $C_xH_yO^+$ and $C_xH_yO_z^+$ ion series also contribute a significant fraction to the total organics.

(a)

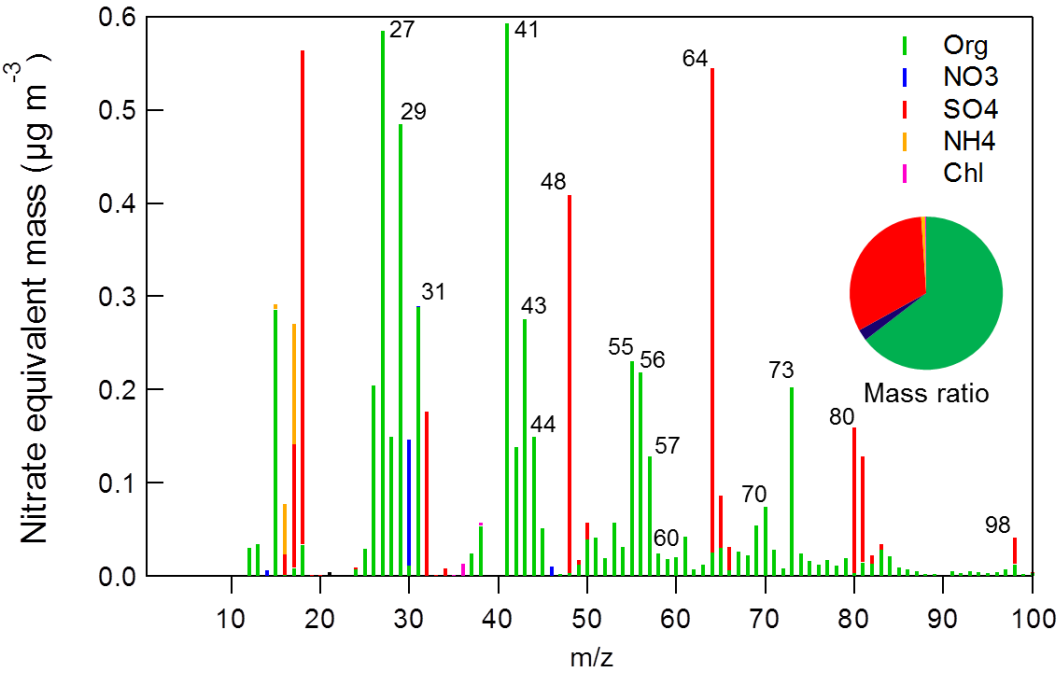

(b)

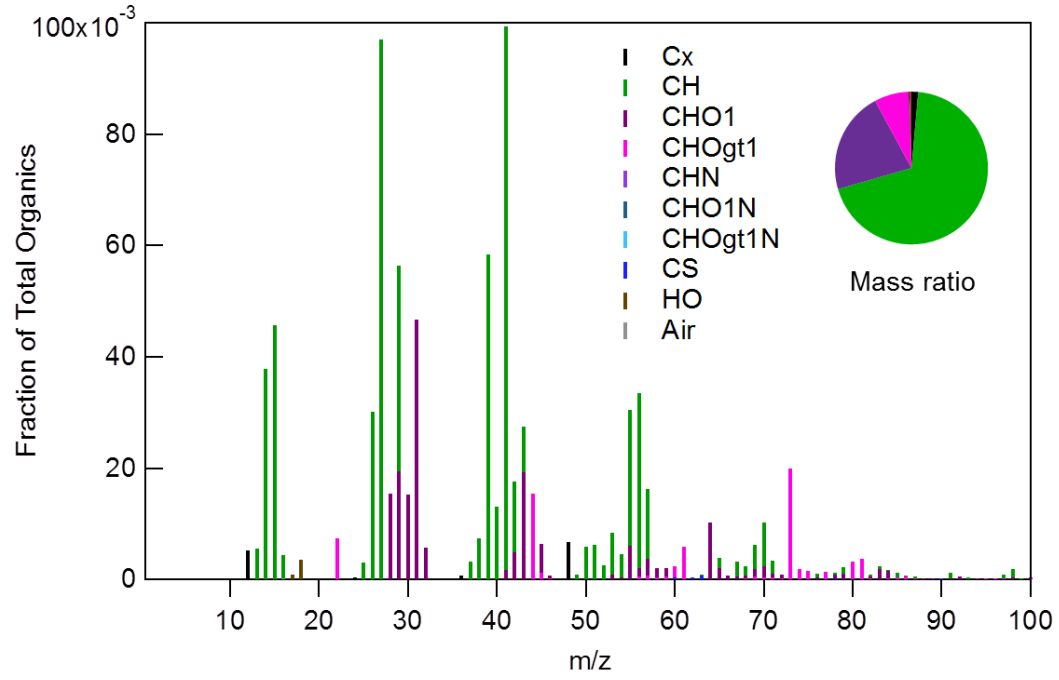

Figure 3.4 Average mass spectra for particulate matter generated in the ESP: (a) mass spectrum of secondary aerosols; (b) High resolution spectrum of organics

It should be noted that AMS measurements have also been done under control conditions: with coal feeding but with ESP off. The corresponding mass spectrum, in Figure A2.4, shows that no significant sulfate or organic chemical signals were found. This observation confirms that the SA formation was due to the corona discharge in the ESP.

Figure 3.5 is the schematic diagram of the SA formation in the ESP. Besides the mechanisms of aerosol formation discussed above, the capture of newly formed aerosols by the ESP is also taken into account. The left part of the schematic diagram shows the fate of the aerosols in the ESP. While exhaust gases go through the ESP, aerosols are formed, and then grow (process 1); simultaneously, some of the newly formed aerosols are captured by the ESP (process 2). As shown in the left part of Figure 3.5, the difference between the newly formed aerosols and the captured aerosols are the SAs that can be observed downstream of the ESP (part 3 in the left side of Figure 3.5). Similar simultaneous aerosol formation and deposition process has been well described in previous studies (Borra 2006, 2008). The aerosol formation (process 1) is governed by the kinetics of vapor phase H_2SO_4 formation and the dynamics of aerosols; while the capture of aerosols (process 2) is determined by the kinematics of the aerosols in the ESP, which is influenced the flow and electric fields, and the particle charging. To better understand the SA formation process and assist in predicting the SA emission from an ESP under practical operating conditions, the critical parameters of chemical kinetics, aerosol dynamics, and the growth dynamics of aerosols influence the whole process were investigated.

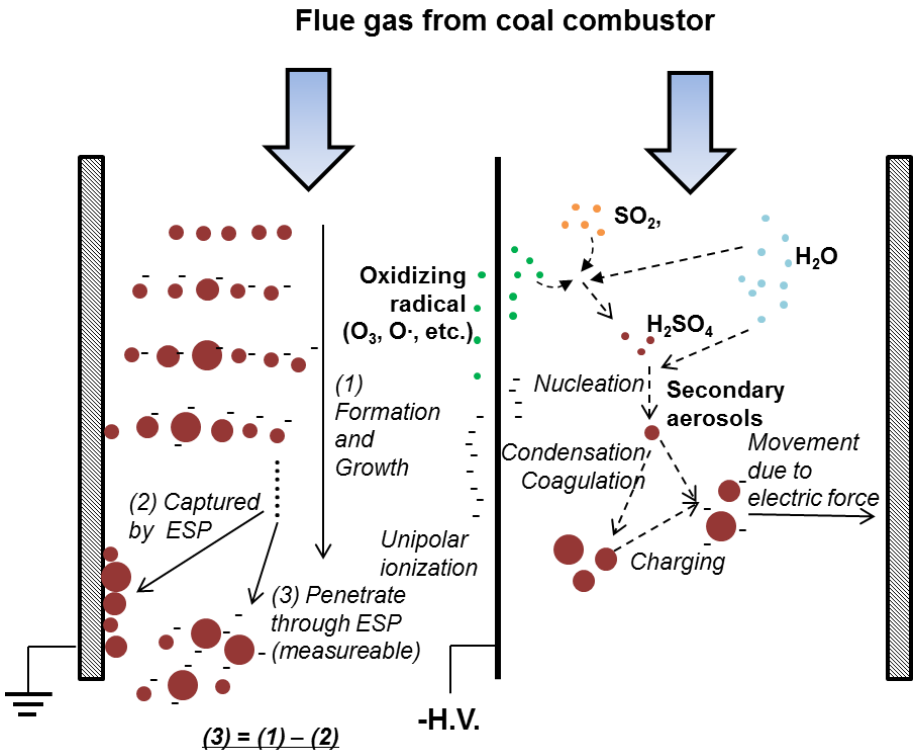

Figure 3.5 Mechanistic description of the secondary aerosol formation process in the ESP

3.3.3 Effects of SO_2 concentration, humidity, ESP voltage, and flow rate on H_2SO_4 SA formation

In the last section, it was proposed that formation of H_2O-H_2SO_4 aerosols is the key pathway of SA formation. A parametric study was performed on a simulated flue gas system to evaluate the effects of SO_2 concentration, the water content in the gas phase, the ESP voltage, and the flow rate through the ESP on H_2O-H_2SO_4 SA formation. The size distributions of SAs that exit the ESP under various conditions are shown in Figure 3.6.

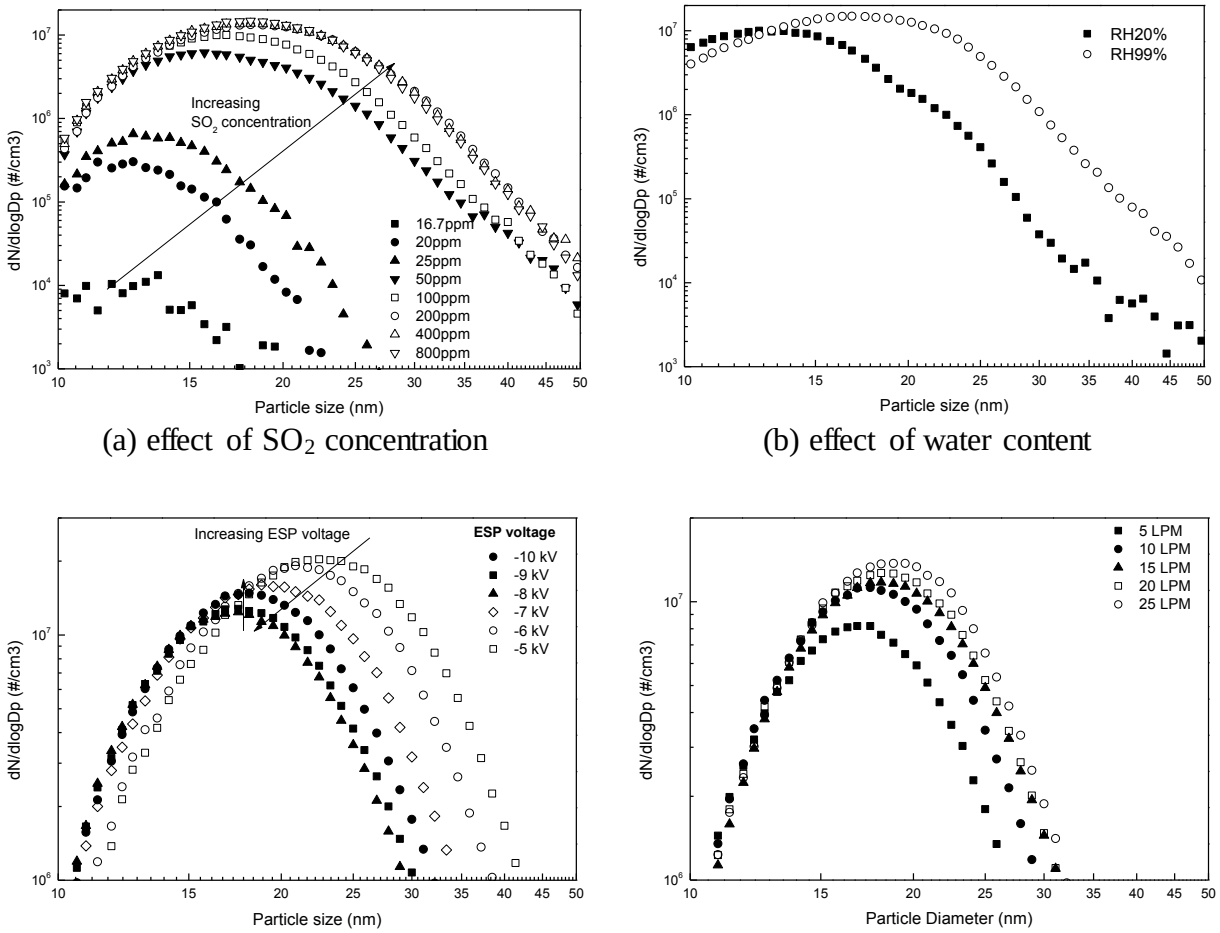

(a) effect of SO_2 concentration (b) effect of water content

(c) effect of ESP voltage (d) effect of flow rate through ESP

Figure 3.6 Size distributions of secondary aerosols under various conditions (a: SA size distributions under different SO_2 concentrations; b: SA size distributions under different water contents; c: SA size distributions under different ESP voltages; d: SA size distributions under different flow rates)

As shown in Figure 3.6a, in the SO_2 concentration range between 16.7 ppm to 200 ppm, higher SO_2 concentrations resulted in higher SA concentrations and larger particle sizes. Conversely, when the SO_2 concentration exceeded 200 ppm, the size distribution of SAs remained the same. The reactions among SO_2, oxidizing radicals, and H_2O played an important role in this set of tests. While the SO_2 concentration varied, the concentrations of H_2O and oxidizing radicals were

kept the same. When the SO_2 concentration was below 200 ppm, SO_2 was the limiting factor of those reactions; while when its concentration exceeded 200 ppm, H_2O or oxidizing radicals became the limiting factor. A similar phenomenon has been observed on other DC corona reactors (Matteson et al., 1972). In their study, when the initial SO_2 concentration was larger than 500 ppm, the SO_2 reaction rate was not influenced by the initial SO_2 concentration. In a typical coal combustor exhaust, the SO_2 concentration varies between 500 ppm (low sulfur coal) to 3000 ppm (high sulfur coal) (Lowell et al., 1971).

Water content in the flue gas promoted the formation of SAs, as shown in Figure 3.6b, because the presence of H_2O resulted in ·OH radical formation, as well as contributed in the reaction to form H_2SO_4 (eq3.6). At the same time, water molecules participate in forming the SA nuclei (Nagato 2009; Hvelplund et al., 2013) and in SA growth (Stauffer et al., 1973; Wilhelm et al., 2004; Sorokin et al., 2006), as discussed in the previous section. With increasing ESP voltage, the SA concentration and peak size first decreased (from -5 kV to -8 kV), and then increased (from –8 kV to -10 kV), as shown in Figure 3.6c. Figure 3.6d shows that at higher simulated gas flow rate, the SA concentration was higher and the peak size was larger.

ESP voltages and the gas flow rate are two factors that can influence both SA formation (process 1 in Figure 3.5) and the capture of newly formed SAs (process 2 in Figure 3.5). Higher voltage (resulted in a higher extent of ionization) promotes SA formation by increasing the ion-induced nucleation and oxidizing radical generation. However, higher voltages also enhance particle capture by increasing the particle charging efficiencies and providing a high-intensity electric field for collection. Before the voltage reached the corona initiation voltage (-8 kV in this system, as shown in Figure A2.5), gas molecule ionizations occasionally occurred. Under this condition, oxidation of SO_2, ion-induced nucleation, and consequent particle growth could happen.

However, the ion concentration is low for particle charging purposes, which made the capture of SAs more sensitive to a change in voltage. As a result, the SA concentration and peak size first decreased from -5 kV to -8 kV as the capture efficiency became higher. On the other hand, once the voltage reached the corona initiation voltage (-8 kV), the ion concentration increased dramatically. At this ion concentration level and within -8 kV to -10 kV, the particle capture efficiencies were comparable. In this case, the impact of ESP voltage on SA formation is stronger. Thus, as the voltage changed from -8 kV to -10 kV, the SA concentration and peak size increased.

Higher flow rates resulted in lower residence times for both flue gas and particles, which reduced both the SA formation and ESP capture efficiency. The impact on the ESP capture efficiency was higher. Thus, as the flow rate increased, SA concentration was higher and the peak size was larger.

3.4 Conclusions

In this study, the phenomenon of secondary aerosol formation in an ESP when treating flue gas was first demonstrated on a 1 MW scale coal combustion system. The secondary aerosol had a unimodal size distribution with a peak size of 20 nm. The chemical composition of SAs was characterized with an AMS. It was found that the aerosols generated in the ESP were a mixture of H_2SO_4, H_2O, and organics. H_2O-H_2SO_4 SAs were formed through the following pathway: (1) SO_2 in the exhaust gas was oxidized by radicals, reacted with H_2O in the ESP, and eventually formed H_2SO_4 (vapor); (2) H_2O-H_2SO_4 SAs were first formed through ion-induced nucleation; (3) SAs grew by condensation and coagulation. It is proposed that during this process, organic

compounds also were absorbed by the aerosols. Concurrently, some of the newly formed particles were captured by the ESP. The effects of SO_2 concentration, the water content in the feeding gas, the ESP voltage, and the flow rate through the ESP on H_2O-H_2SO_4 SA formation were investigated. The SA concentration and peak size increased with higher SO_2 concentrations, higher water content, and higher flow rates through ESP. With increasing ESP voltage, the SA concentration and peak size first went down (from -5 kV to -8 kV), and then increased (from –8 kV to -10 kV).

3.5 References

Anderlohr, C., L. Brachert, J. Mertens, and K. Schaber. 2015. Collection and Generation of Sulfuric Acid Aerosols in a Wet Electrostatic Precipitator. *Aerosol Sci. Tech.* 49:144-151.

Biswas, P., and C.-Y. Wu. 2005. Nanoparticles and the environment. *J. Air Waste Manag.* 55 (6):708-746.

Davidson, C.I., R.F. Phalen, and P.A. Solomon. 2005. Airborne particulate matter and human health: a review. *Aerosol Sci. Tech.* 39 (8):737-749.

Dong, L.M., Z. Wu, J.X. Yang, and X.C. Chi. 2003. Chemical kinetics model for sulfur dioxide removal in flue gas using corona discharge. Paper presented at Conference on Electrical Insulation and Dielectric Phenomena, Albuquerque, NM, USA, October 19-22, 2003.

Hamill, P. 1975. The time dependent growth of H_2O-H_2SO_4 aerosols by heteromolecular condensation. *J. Aerosol Sci.* 6(6):475-482.

Hankey, R. 2015. Electric Power Monthly with Data for January 2015. U.S. Energy Information Administration.

Hinds, W.C. 1999. Aerosol technology: properties, behavior, and measurement of airborne particles.New York: John Wiley & Sons.

Hogan, C.J., M.-H. Lee, and P. Biswas. 2004. Capture of viral particles in soft X-ray-enhanced corona systems: charge distribution and transport characteristics. *Aerosol Sci. Tech.* 38(5):475-486.

Huang, S.-H., and C.-C. Chen. 2002. Ultrafine aerosol penetration through electrostatic precipitators. *Environ. Sci. Tech.* 36(21):4625-4632.

Hvelplund, P., J.O.P. Pedersen, K. Støchkel, M.B. Enghoff, and T. Kurtén. 2013. Experimental studies of the formation of cluster ions formed by corona discharge in an atmosphere containing SO_2, NH_3, and H_2O. *Int. J. Mass Spectrom.* 341:1-6.

Jing, H., S. He, Q. Ou, T.-C. Hsiao, and D.-R. Chen. 2013. Development of a compact electrostatic nanoparticle sampler for offline aerosol characterization. *MAPAN-J. Metrol. Soc. I.* 28 (3):217-226.

Jing, H., X. Wang, W.-N. Wang, and P. Biswas. 2015. Elemental mercury oxidation in an electrostatic precipitator enhanced with in situ soft X-ray irradiation. *J. Air Waste Manag.* 65 (4):455-465.

Kuroki, T.; Takahashi, M.; Okubo, M.; Yamamoto, T. 2002. Single-stage plasma-chemical process for particulates, NO_x, and SO_x simultaneous removal. *IEEE T. Ind. Appl.* 38 (5):1204-1209.

Lapshin, V.B., A.A. Paley, A.V. Balyshev, I.A. Boldyrev, S.N. Dubtsov, and L.I. Tolpygin. 2012. Evolution of nanometer-size aerosol in dry and humid environment under the influence of corona discharge. *Atmos. Ocean. Opt.* 25(2):171-175.

Li, Y., A. Suriyawong, M. Daukoru, Y. Zhuang, and P. Biswas. 2009. Measurement and capture of fine and ultrafine particles from a pilot-scale pulverized coal combustor with an electrostatic precipitator. *J Air Waste Manag.* 59(5):553.

Matteson, M.J., H.L. Stringer, and W.L. Busbee. 1972. Corona discharge oxidation of sulfur dioxide. Environ. Sci. Tech. 6(10):895-901.

McCain, J.D., J.P. Gooch, and W.B. Smith. 1975. Results of field measurements of industrial

particulate sources and electrostatic precipitator performance. *JAPCA J. Air Waste Ma.* 25(2):117-121.

Mertens, J., C. Anderlohr, P. Rogiers, L. Brachert, P. Khakharia, E. Goetheer, and K. Schaber. 2014. A wet electrostatic precipitator (WESP) as countermeasure to mist formation in amine based carbon capture. *Int. J. Greenh. Gas Con.* 31:175-181.

Mok, Y.S., and I.-S. Nam. 2002. Modeling of pulsed corona discharge process for the removal of nitric oxide and sulfur dioxide. *Chem. Eng. J.* 85(1):87-97.

Nagato, K. 2009. Charged particle formation by the ionization of air containing sulfur dioxide. *Int. J. Mass Spectrom.* 285(1):12-18.

Sinanis, S., A. Wix, and K. Schaber. 2013. Formation of Hydrobromic and Hydrochloric Acid Aerosols in Wet Flue Gas Cleaning Processes. *Chem. Eng. Commun.* 200(6):748-763.

Sorokin, A., F. Arnold, and D. Wiedner. 2006. Formation and growth of sulfuric acid–water cluster ions: Experiments, modelling, and implications for ion-induced aerosol formation. *Atmos. Environ.* 40(11):2030-2045.

Stauffer, D., V.A. Mohnen, and C.S. Kiang. 1973. Heteromolecular condensation theory applied to particle growth. *J. of Aerosol Sci.* 4(6):461-471.

Suriyawong, A., M. Gamble, M.-H. Lee, R. Axelbaum, and P. Biswas. 2006. Submicrometer particle formation and mercury speciation under O_2-CO_2 coal combustion. *Energy. Fuel.* 20(6):2357-2363.

Suriyawong, A., C.J. Hogan, J. Jiang, and P. Biswas. 2008. Charged fraction and electrostatic collection of ultrafine and submicrometer particles formed during O_2-CO_2 coal

combustion. *Fuel* 87(6):673-682.

Van Dingenen, R., and F. Raes. 1991. Determination of the condensation accommodation coefficient of sulfuric acid on water-sulfuric acid aerosol. *Aerosol Sci. Tech.* 15(2):93-106.

Wang, X., B.J. Williams, Y. Tang, Y. Huang, L. Kong, X. Yang, and P. Biswas. 2013a. Characterization of organic aerosol produced during pulverized coal combustion in a drop tube furnace. *Atmos. Chem. Phys.* 13(21):10919-10932.

Wang, X., E. Cotter, K.N. Iyer, J. Fang, B.J. Williams, and P. Biswas. 2015. Relationship between pyrolysis products and organic aerosols formed during coal combustion. *P. Combust. Inst.* 35(2):2347-2354.

Wang, X., S.M. Daukoru, S. Torkamani, W.-N. Wang, and P. Biswas. 2013b. Role of exhaust gas recycle on submicrometer particle formation during oxy-coal combustion. *P. Combust. Inst.* 34 (2):3479-3487.

Waring, M.S., J.A. Siegel, and R.L. Corsi. 2008. Ultrafine particle removal and generation by portable air cleaners. *Atmos Environ* 42(20):5003-5014.

Wilhelm, S., S.Eichkorn, D. Wiedner, L. Pirjola, and F. Arnold. 2004. Ion-induced aerosol formation: new insights from laboratory measurements of mixed cluster ions $HSO_4^-(H_2SO_4)_a(H_2O)_w$ and $H^+(H_2SO_4)_a(H_2O)_w$. *Atmos. Environ.* 38(12):1735-1744.

Ylätalo, S.I., and J. Hautanen. 1998. Electrostatic precipitator penetration function for pulverized coal combustion. *Aerosol Sci. Tech.* 29(1):17-30.

Yoo, K.H., J.S. Lee, and M.D. Oh. 1997. Charging and collection of submicron particles in two-

stage parallel-plate electrostatic precipitators. *Aerosol Sci. Tech.* 27(3):308-323.

Zhuang, Y., and P. Biswas. 2001. Submicrometer particle formation and control in a bench-scale pulverized coal combustor. *Energ. Fuel.* 15(3):510-516.

Zhuang, Y., Y.J. Kim, T.G. Lee, and P. Biswas. 2000. Experimental and theoretical studies of ultra-fine particle behavior in electrostatic precipitators. *J. Electrostat*. 48(3):245-260.

CHAPTER 4. CAPTURE OF SUBMICROMETER PARTICLES WITH A PRESSURIZED ELECTROSTATIC PRECIPITATOR

The results of this chapter will be compiled as a paper for submission to Aerosol Science & Technology (authors: He Jing, Zhichao Li, Pratim Biswas).

Supplementary materials are available in Appendix III

Abstract

In this study, the influence of gas pressure on the performance of an electrostatic precipitator (ESP) in submirometer particle capture was investigated. The ESP was operated under 1 atm, 2 atms, and 3 atms, respectively. Current-voltage characteristics of the ESP were studied under various pressures. Fundamental study on the particle capture was performed with NaCl particles. With a similar voltage, the particle capture efficiency became lower with a higher pressure, due to a lower ion concentration in the ESP. With the same current, the particle capture efficiency became higher with a higher pressure, which was mainly determined by the transport of charged particles. A modified Deutsch-Anderson (D-A) equation was developed. The estimation particle capture efficiency results from the modified D-A equation match the NaCl capture data well. The capture of fly ash particles from a drop-tube furnace in the pressurized ESP was also studied. The charge status of the fly ash particles played an important role in this process. As a result, with the same current, the particle capture efficiency became lower with a higher pressure.

4.1 Introduction

Aiming at providing reliable and low-cost energy, advanced technologies, such as gasification (Minchener 2005), pressurized fluidized bed combustion (Schemenau 1993), and pressurized oxy-combustion (Gopan et al., 2014) are considered to be promising alternative energy generation processes. The feasibility of those systems is not just determined by the energy generation processes themselves, but also greatly depends on the performance of their ancillary equipment. Particle control equipment is one important component of those systems.

Electrostatic precipitators (ESPs) are widely used in particle control from various emission sources because of their high capture efficiency and low operation cost, and their ability of working under the extreme environment (high temperature and high pressure) have been proven (Brown and Walker, 1971; Bush et al., 1979; Rinard et al, 1987; Villot et al., 2012), which made them a good candidate of particle control equipment in gasification and pressurized combustion systems. It has been reported that corona discharge (main mechanism of ESP) can be obtained under a pressure up to 3.5 MPa and temperature up to 1700 ^{o}F (Brown and Walker, 1971). However, the capture efficiency of the ESP under high pressure and high temperature, and how the capture behaves as the pressure increases or temperature increases are not well understood. Especially, no size-dependable capture efficiency has been reported.

Among various particle size ranges, the submicrometer range (particle sizes smaller than 1μm) requires the special attention because they have more severe adverse health effect to human (Biswas and Wu, 2005). Extensive studies have been done on the capture of submicrometer particles with ESPs (under atmosphere pressure). On one hand, fundamental studies have been done on bench-scale ESPs with synthetic particles (Yoo et al., 1997; Zhuang et al., 2000; Jing et al. 2013; Huang and Chen, 2002); on the other hand, studies have been carried out on ESPs with

particles and flue gas from real combustion systems (McCain et al., 1975; Ylätalo and Hautanen, 1998; Li et al., 2009). It is of great interests how pressure influences the submicrometer particle capture capability of ESPs, which has not been investigated yet.

In this study, fundamental studies were firstly done to evaluate the effects of pressure on current-voltage (I-V) characteristics and capture efficiencies of submicrometer particles (NaCl particles) of the ESP. Afterwards, the capture of submicrometer fly ash particles with an ESP under various pressures were investigated on a pressurized drop-tube furnace system.

4.2 Experimental Section

4.2.1 Experimental system

The ESP used in this study is a bench-scale DC corona-based wire-cylinder type ESP, which has been used and described in early studies. The ESP configuration is shown in Figure A3.1. A Bertan (model 230) power supply was used to provide the high voltage for the ESP. The experiment system is shown in Figure 4.1. Two types systems were used to generate test particles. NaCl particles were generated by an atomizer (TSI model 3076). A Po-210 radioactive source was used to neutralize the charges on the NaCl particles from the atomizer, and a diffusion dryer was used to dry and remove water vapor from the particles. Fly ash particles were generated with a pressurized drop-tube furnace. The configuration and operation parameters of the furnace have been described in previous papers (Suriyawong et al. 2006; Wang et al., 2013a, 2013b, 2015). PRB (Powder River Basin) coal was used and the coal feeding rate is 1.5 g/hr. The drop-tube furnace was operated up to 3 atms in this study. An addition air flow was added to the system to adjust the total flow rate through the ESP. The current through the ESP was measured

with a microammeter meter (Simpson Model 17424). A scanning mobility particle sizer (SMPS, TSI model 3080) was used to measure the particle size distribution.

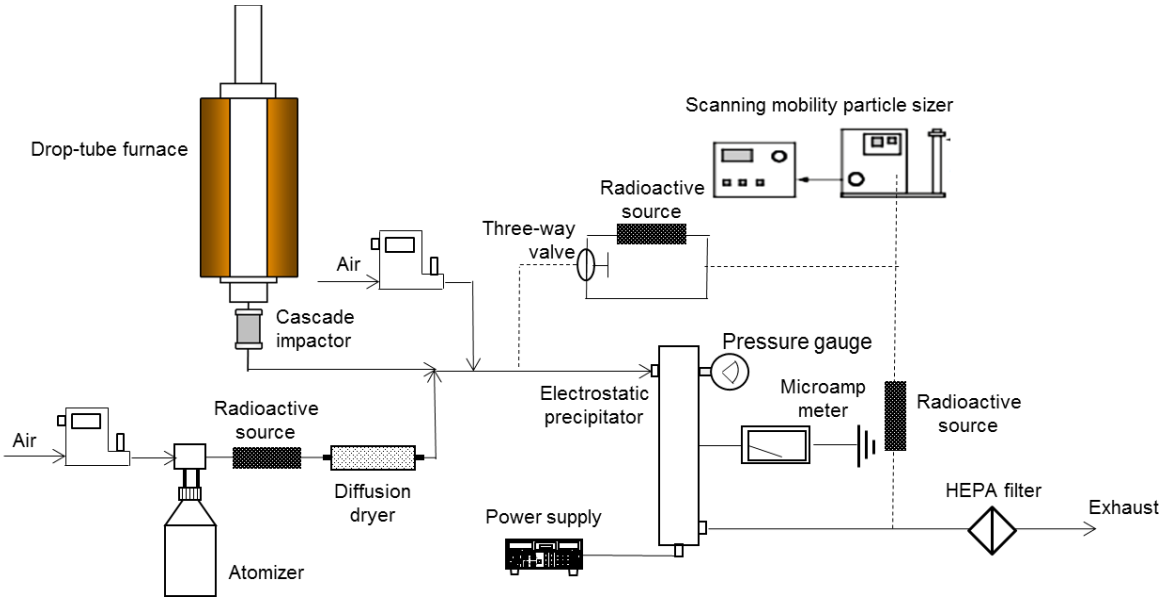

Figure 4.1 Schematic of the experimental setup

4.2.2 Calculation of particle penetration through ESP and charges on particles from the furnace

The particle penetration through the ESP for each size was determined by eq4.1:

$$\text{penetration} = \frac{N_{off}}{N_{on}} \tag{4.1}$$

where N_{off} and N_{on} are particle number concentrations downstream from the ESP for a certain size bin when the ESP was off and on, respectively.

A method adapted from Suriyawong et al. (2008) was applied to estimate the charges on the particles from the drop-tube furnace. The particles were introduced to the DMA (differential mobility analyser) of SMPS through two routes, respectively: (1) directly introduced to the DMA;

(2) passing through a Po-210 radioactive source, which gave the particles a known charge distributions, and then introduced to the DMA. The concentrations of particle penetrating through the DMA were measured with the CPC (condensation particle counter) of the SMPS. The DMA was operated under both a negative and positive applied voltage to determine the charges of particles with positive and negative charges, respectively. With the concentration measurements, a charge index can be calculated using eq4.2 to indicate the charge status of the particles:

$$I_C = \frac{N_C}{N_{Ceq}} C f_{eq1} \tag{4.2}$$

where I_C is the charge index, N_C is the number concentration of charged particles of diameter d_p, N_{Ceq} is the number concentration of charged particles of diameter d_p measured after charge neutralization, and Cf_{eq1} the equilibrium charge fraction for particles of diameter d_p with one unit charge calculated as described by Wiedensohler (Wiedensohler 1988). The physical meaning of the charge index is the charge fraction of particles with the assumption that all the particles are singly charged (with +1 or -1 unit charge). However, it should be noted that multiple charged particles (particles with the same electrical mobility with the singly charged particles of the concerned size) also contribute to this index.

4.2.3 Experimental design

In this study, the operation of the pressurized ESP was first studied fundamentally, including the study of the current-voltage characteristics (Set I) and the study of capture efficiency with NaCl particles with Boltzmann charge distributions (Set II). A modified Deutsch-Anderson equation was also developed to predict the capture efficiency of the pressurized ESP under various gas

pressures and ESP voltages (Set III). In the second step, the capture of fly ash particles from a drop-tube furnace in the pressurized ESP was investigated (Set V). In this study, the furnace was operated under the same gas pressure with the ESP for each run. To better elucidate the capture of fly ash particles, the charging status of the particles from the drop-tube furnace under various pressures were also studied (Set IV). The summary of experimental conditions is shown in Table 4.1.

Table 4.1 Summary of the experiments performed

Set	Objective	Particles	Gas compositions	ESP operation	Gas pressure	Flow rate	Measurements
I	To investigate the I-V characteristics of the ESP	N/A	Air	-20 kV to +20 kV	1 atm, 2 atms, 3 atms	15 LPM	ESP current
II	To investigate the capture efficiency of the NaCl particles	NaCl particles	Air	(1) ±16.7 kV (±12.7 kV for 1 atm); (2) ±20 μA	1 atm, 2 atms, 3 atms	15 LPM	Particle size distribution downstream the ESP when the ESP off and on respectively
III	To develop an equation to predict the performance of the pressurized ESP	N/A	N/A	N/A	N/A	N/A	N/A (data from Set II is used)
IV	To investigate the charge status of the fly ash particles from the drop-tube furnace	Fly ash particles from drop-tube furnace	Flue gas from drop-tube furnace	N/A	1 atm, 2 atms, 3 atms	8 LPM	Concentration of particles (passing through the radioactive sources or directly to the DMA) through the DMA
V	To investigate the capture efficiency of the fly ash particles	Fly ash particles from drop-tube furnace	Flue gas from drop-tube furnace	±20 μA	1 atm, 2 atms, 3 atms	25 LPM	Particle size distribution downstream the ESP when the ESP off and on respectively

4.3 Results and Discussion

4.3.1 Current-voltage characteristics of the pressurized ESP

The I-V characteristics provide the information of the corona working range, at the same time, the current also indicates the ion concentration in the ESP. Figure 4.2 shows the I-V characteristics of the studied ESP under three pressures, 1 atm, 2 atms, and 3 atms. Results show that for both the positive and negative polarities, as the pressure increased, the corona on-set voltage increased. Under the same voltage, the ESP current was lower with a higher pressure. These observations can be explained by the mechanism of the corona formation. To form the corona discharge, a certain amount of ions and electrons are needed. Most of the ions and electrons are generated from the ionization process due the impaction between the gas molecules and high energy electrons. Important to note that in order to initiate the ionization, an electron should have a kinetic energy that is above a critical value (an energy that is high enough for the electron to knock out a secondary electron from a gas molecule). With higher pressure, the mean free path inside the ESP decreases. Thus, there is a higher chance that the electron hit a gas molecule before being accelerated to have the critical kinetic energy. This hinders the ionization process (Robinson 1971). Previous studies also established an empirical relationship between the ESP onset voltage and the gas pressure in the ESP (Robinson 1967). The equation is shown in the supplemental materials.

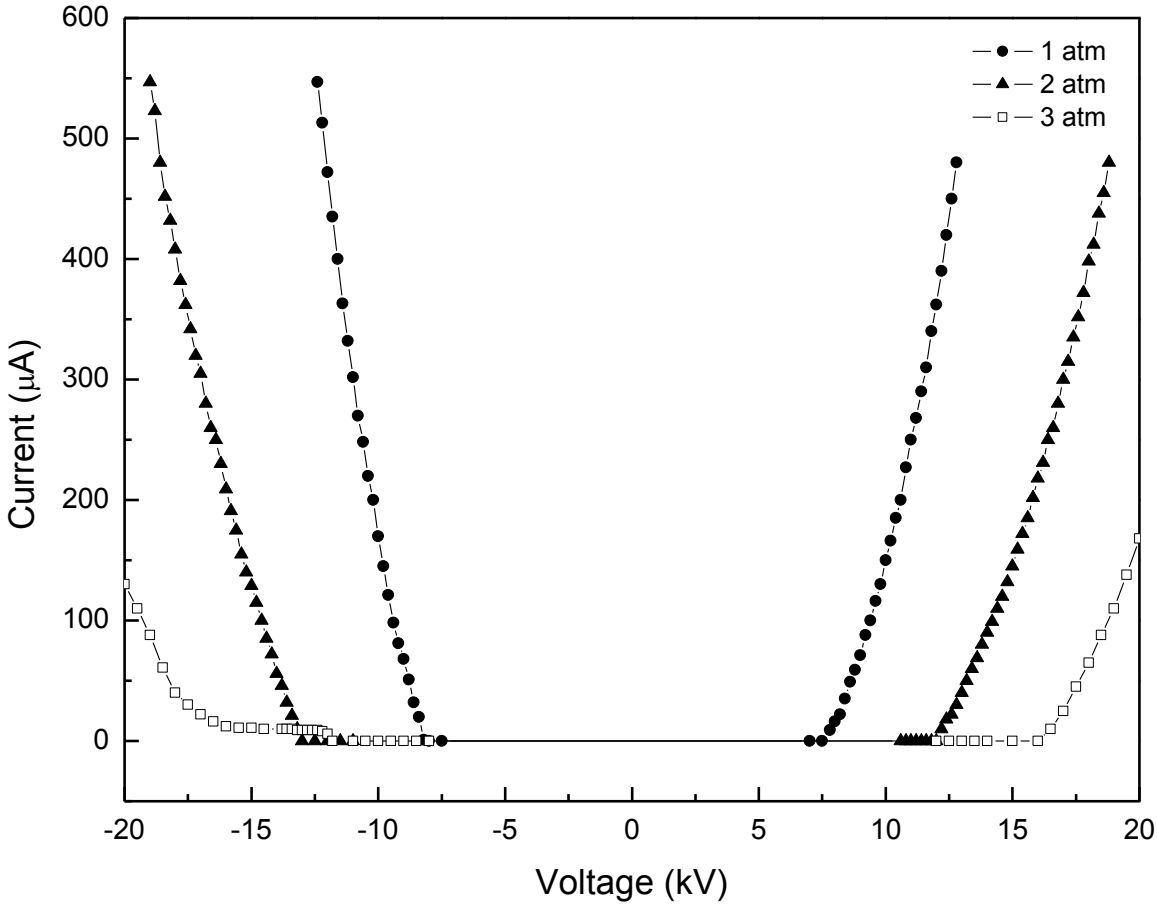

Figure 4.2 The relationship between ESP voltage and current under different gas pressures

4.3.2 Capture of the NaCl particles with a Boltzmann charge distribution

In order to perform a fundamental study on the pressurized ESP, NaCl particles generated using atomization methods were used to evaluate the capture efficiencies of the ESP. The particles passed through a Po-210 radioactive radiation source, which gave them a Boltzmann charge distribution. The size distributions of particles generated by atomization under different gas pressures are shown in Figure A3.2.

Voltage is one of the most important ESP operation parameter. Thus firstly, ESP performances under different gas pressures were compared under a similar ESP voltage (±16.7 kV for 2 atms and 3 atms cases; ±12.7 kV for 1 atm case because the maximum current output was reached). Figure 4.3 shows the particle penetrations through the ESP under various pressures. The ESP behaviors under positive and negative polarities were similar. Generally, as particles diameter increased, the particle penetration increased, because the larger particles ended up with lower electrical mobility (Jing et al., 2013). The above observation could be easily verified using the Deutsch-Anderson equation (Hinds 1999). Particle penetration increased with higher gas pressure. The reason is that: with a similar ESP voltage, the ion concentrations in the ESP decreased with higher gas pressure, which is indicated by the ESP current measurements. Lower ion concentration resulted in less particle charging (Hinds 1999), which eventually resulted in a higher particle penetration.

(a)

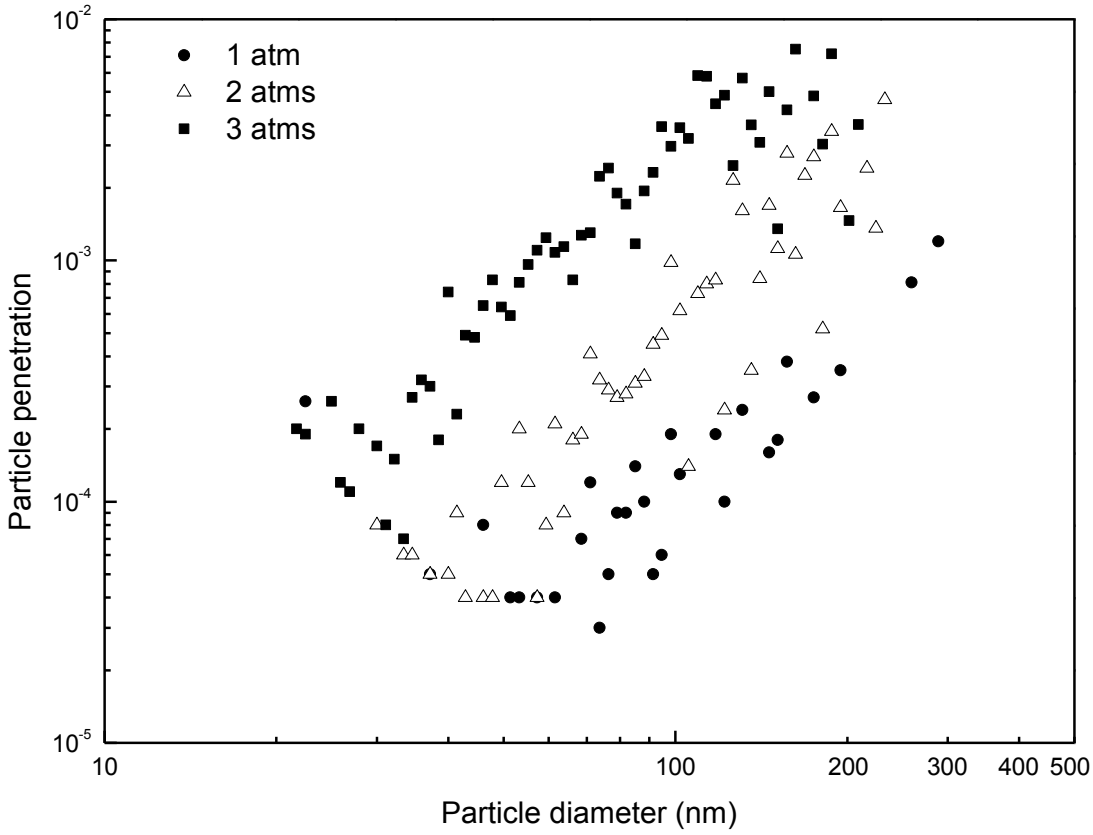
1 atm
2 atms
3 atms
Particle penetration
Particle diameter (nm)
10
100
200
300
400
500

(b)

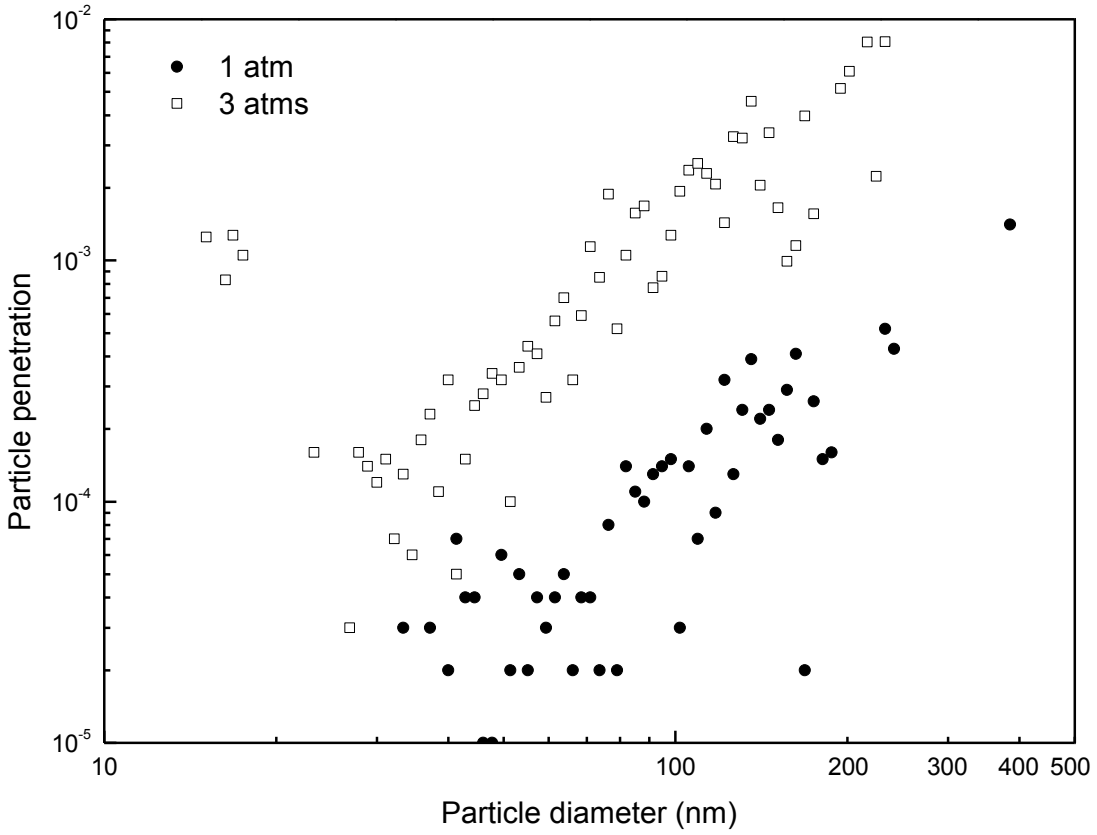

Figure 4.3 Particle penetrations through the ESP for NaCl particles of various sizes under different gas pressures: (a) negative ESP; (1 atm case: ESP voltage -12.9 kV, current -500 μA; 2 atms case: voltage -16.7 kV, current -200 μA; 3 atms case: voltage -16.7 kV, current -20 μA;) (b) positive ESP; (1 atm case: ESP voltage +12.9 kV, current +500 μA; 3 atms case: voltage +16.7 kV, current +20 μA)

To further investigate the influence of factors other than the ion concentration on the particle capture, ESP performances under different gas pressures were compared under the same current (20 μA), and it is assumed that the ion concentrations were the same in those conditions. Figure 4.4 shows the particle penetration through the ESP under 1 atm, 2 atms, and 3 atms, respectively. Similar with the results from Figure 4.3, the ESP behaviors under

positive and negative polarities were similar, and the penetration increased with particle diameter. The particle penetrations of 1 atm case were higher than those of 2 atms and 3 atms cases, and the penetrations for the latter two cases were similar. In this set of experiments, particle capture was mainly determined by the transport of the charged particles in the ESP, and this result is an outcome of the combined effect of three factors: (1) lower particle velocity along the direction of gas flow with higher pressure; (2) lower particle migration velocity to the collecting electrode with higher pressure; and (3) higher electrical field strength with higher voltage (higher gas pressure). Factor (1) and (3) enhance the particle capture with increasing gas pressure, while factor (2) weakens the particle capture with increasing gas pressure.

(a)

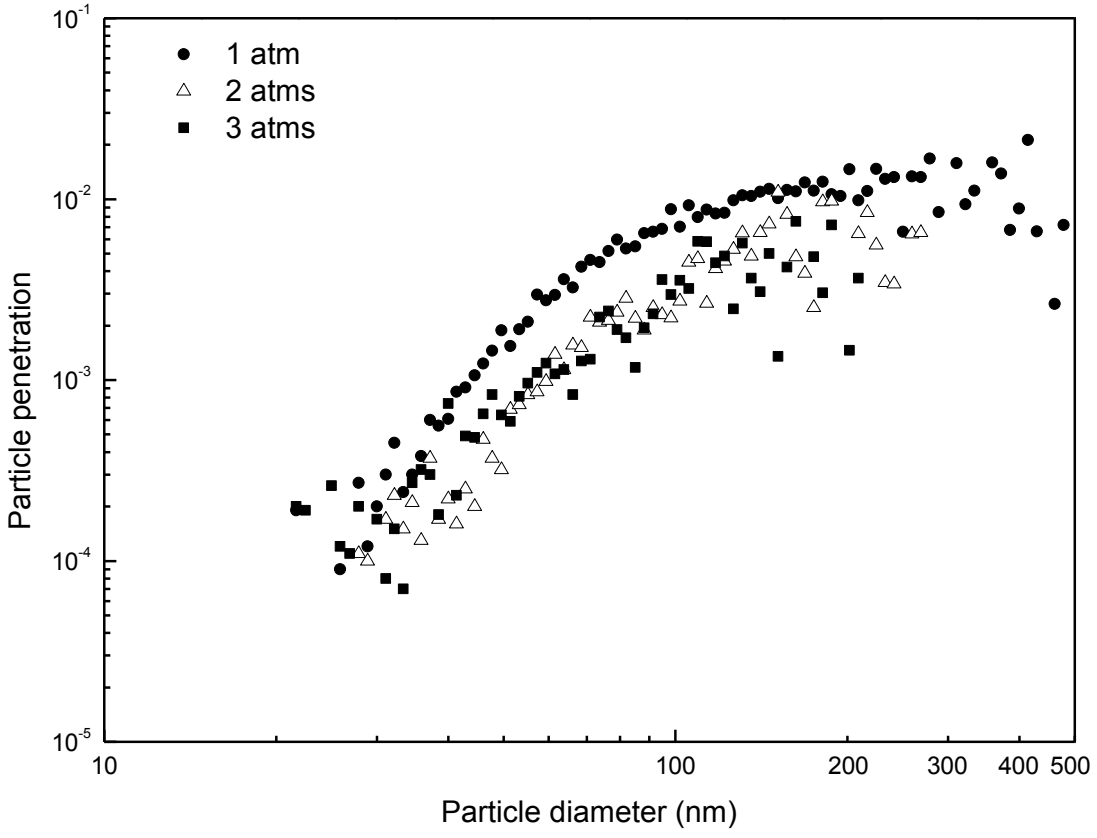

(b)

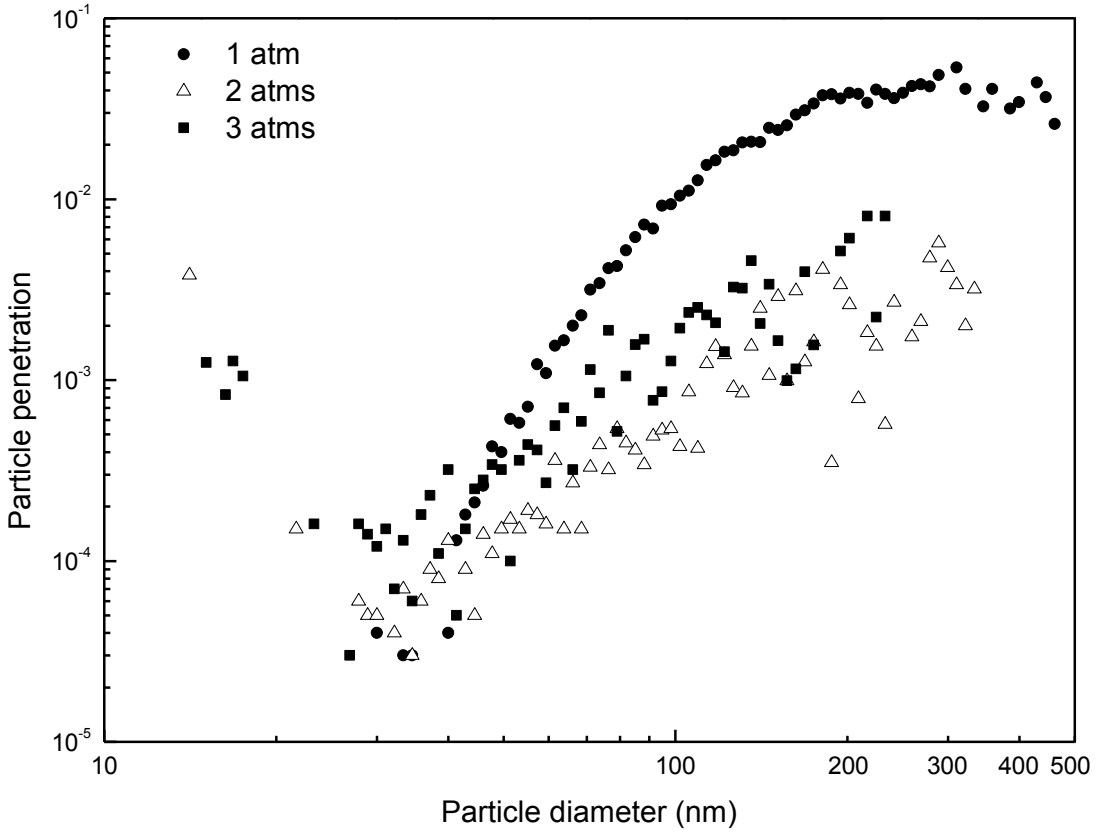

Figure 4.4 Particle penetrations through the ESP for NaCl particles of various sizes under different gas pressures but a fixed current: (a) negative ESP; (1 atm case: ESP voltage -8.9 kV, current -20 μA; 2 atms case: voltage -12.9 kV, current -20 μA; 3 atms case: voltage -16.7 kV, current -20 μA); (b) positive ESP; (1 atm case: ESP voltage +8.9 kV, current +20 μA; 2 atms case: voltage +12.9 kV, current +20 μA; 3 atms case: voltage +16.7 kV, current +20 μA)

4.3.3 Capture efficiency data fitting with modified Deutsch-Anderson equation

In order to predict the performance of the pressurized ESP under other operation conditions (gas pressure, ESP voltage, etc.), an equation or a model for particle capture efficiency estimation is needed. Deutsch-Anderson (D-A) equation (Anderson 1919) is widely used to estimate the particle capture efficiency in ESP design and analysis, and it is adapted here.

The D-A equation is as below:

$$\eta = 1 - \exp\left(-\frac{A_c v_{TE}}{Q}\right) \tag{4.3}$$

in which η is the particle capture efficiency (1 − penetration), A_c is the area of collection surface, Q is the volumetric flow rate through ESP, and v_{TE} is the particle migration velocity which is determined using eq4.4:

$$v_{TE} = \frac{neE\,C_c}{3\pi\mu\,d_p} \tag{4.4}$$

in which n is the number of elementary charge on the particle, e is the elementary charge, E is the average electric filed in the ESP, Cc is the Cunningham correction factor, μ is the viscosity of air, and d_p is the particle diameter. The number of charge on the particle is estimated following a method used in Lin et al. (2012), as shown in eq4.5:

$$n = n_{diff} + n_{field} \tag{4.5}$$

in which n_{diff} is the number of elementary charge from diffusion charging, and n_{field} is the number of elementary charge from field charging. They are calculated using Fuchs' equation (Fuchs 1947) and Moreau-Hanot equation (Pauthenier and Moreau-Hanot, 1932), respectively:

$$n_{diff} = \frac{d_p kT}{2K_E e^2} \ln\left(1 + \frac{\pi K_E d_p \bar{c}_i e^2 N_i t}{2kT}\right) \tag{4.6}$$

$$n_{field} = \left(\frac{3\varepsilon}{\varepsilon+2}\right)\left(\frac{E {d_p}^2}{4K_E e}\right)\left(\frac{\pi K_E e Z_i N_i t}{1+\pi K_E e Z_i N_i t}\right) \tag{4.7}$$

in which k is the Boltzmann constant, K_E is the constant of proportionality, $\bar{c_i}$ is the average thermal speed of the ions, N_i is the ion concentration in the ESP, t is the residence time of particles in the ESP, ε is the relative permittivity of the particle, Z_i is the mobility of the ions. The ion concentration is estimated based on the ESP current:

$$N_i = \frac{I}{A_c e Z_i E} \tag{4.8}$$

in which I is the ESP current, and the average electric field is determined based on the ESP voltage:

$$E = \frac{V}{s} \tag{4.9}$$

in which V is the ESP voltage, and s is the distance between the central wire and the tube wall. Besides, the Cunningham correction factor in eq4.4 is determined by eq4.10:

$$C_c = 1 + \frac{\lambda}{d_p}\left(2.34 + 1.05\, exp\left(-0.39\,\frac{d_p}{\lambda}\right)\right) \tag{4.10}$$

where λ is mean free path.

The relationship between the calculated values of non-dimensional group $\frac{A_c v_{TE}}{Q}$ in D-A equation and the experimental NaCl particle capture efficiency data is shown in Figure A3.3. Only the data from 1 atm case fitted with the theoretical curve well and the D-A equation could not provide satisfied estimations for 2 atms and 3atms cases. The reason is that one the assumption of the D-A equation is that the particles immediately obtain a large number of elementary charge (close to saturated charge number) once they enter the ESP. However, in

high gas pressure conditions, the particle charging is slower so larger error is introduced due to this assumption.

In order to reduce the error introduced by the assumption discussed above, the number of elementary charge on the particle used in E-A equation is modified as below:

$$n' = n\left(\frac{P}{P_0}\right)^{-1}\left(\frac{ln(I)}{ln(I_0)}\right)^{\frac{1}{2}\left(1-\frac{P}{P_0}\right)}\left(\frac{ln(V)}{ln(V_0)}\right)^{-\frac{1}{12}\left(1-\frac{P}{P_0}\right)} \tag{4.11}$$

where n' is the modified number of elementary charge on the particle, P_0 is the atmosphere pressure, I_0 is the reference ESP current, which is 20 μA here, and V_0 is the reference ESP voltage, which is 8.9 kV here. With this modified the equation, the relationship between the calculated value of the non-dimensional group and the experimental capture efficiency data are shown in Figure 4.5. The relationship follows the theoretical curve well for all cases, which indicates the modified D-A equation can be used to predict the performance of the ESP.

(a)

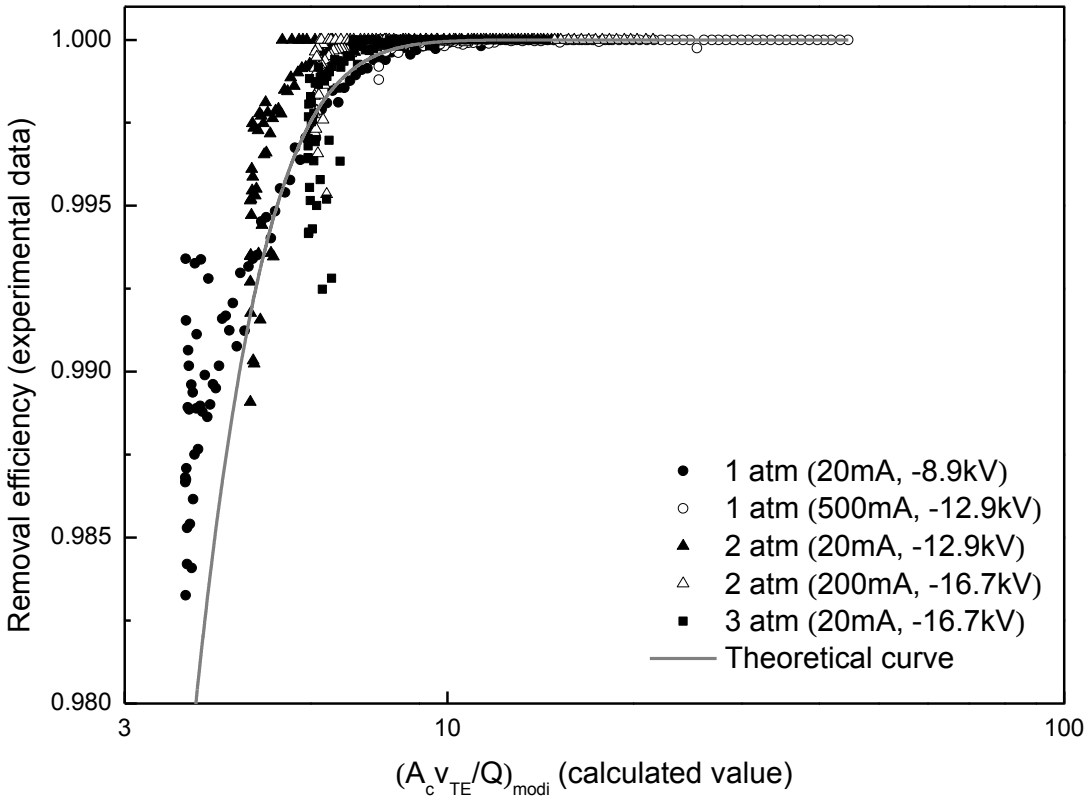
1.000
0.995
0.990
0.985
0.980
Removal efficiency (experimental data)
3
10
100
$(A_c v_{TE}/Q)_{modi}$ (calculated value)
1 atm (20mA, -8.9kV)
1 atm (500mA, -12.9kV)
2 atm (20mA, -12.9kV)
2 atm (200mA, -16.7kV)
3 atm (20mA, -16.7kV)
Theoretical curve

(b)

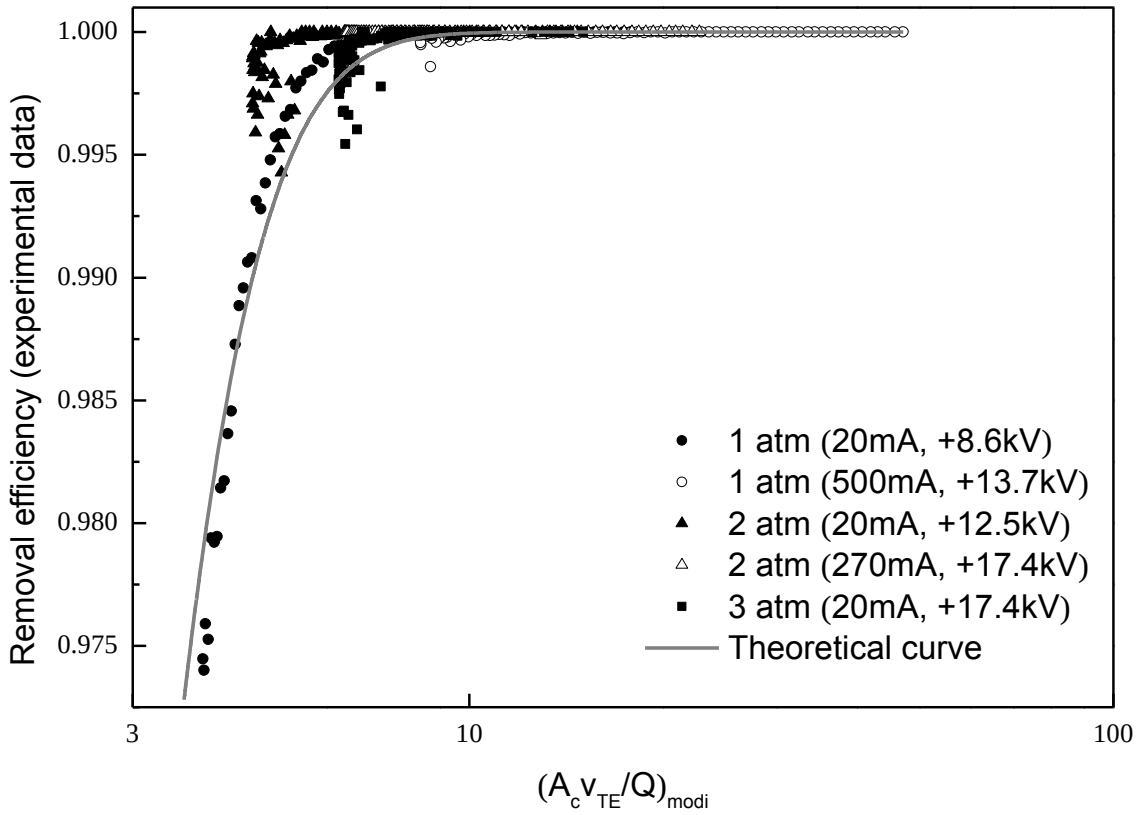

Figure 4.5 The relationship between measured NaCl particle removal efficiencies and the calculated values of the non-dimensional group from the modified Deutsch-Anderson equation: (a) negative polarity; (b) positive polarity

With the modified capture efficiency estimation equation, the relationship between particle penetration and the ESP voltage under different pressures were analyzed, as shown in Figure A3.4.

4.3.4 Characterization of fly ash particle charging status

In order to evaluate the performance of pressurized ESP in an actual combustion conditions, a drop-tube furnace system was used to generate fly ash particles to test the ESP. The fly ash

particle size distributions were shown in Figure A3.4. Because the initial charging status of particles (fraction of charged particles, number of charges on the particles, etc.) could influence how many of them would penetrate the ESP, a characterization of the charging status is needed.

In this section, the charging statuses of fly ash particles from the drop-tube furnace operated under various gas pressures were discussed. A charge index was used to indicate the charging status, and it was calculated based on the method described in the experimental section. The charge indices of the particles with diameters of 20 nm, 30 nm, 40 nm, 60 nm, 100 nm, 200 nm for the 1 atm, 2 atm, and 3 atms conditions are shown in Figure 4.6. The indices of the smaller particle diameters (20 nm, 30 nm) under 3 atms (positive) case are higher than 1, which is strong evidence that part of fly ash particles were multiply and positively charged under the 3 atms combustion. It is also highly possible that in 3 atms case the chance that the fly ash were multiply charged was higher. Considering the main charging mechanism of the particles inside the drop-tube furnace is diffusion charging (Burtscher et al., 1986; Burtscher 1992), it also means that the charge fraction of particles from the 3 atms combustion was higher.

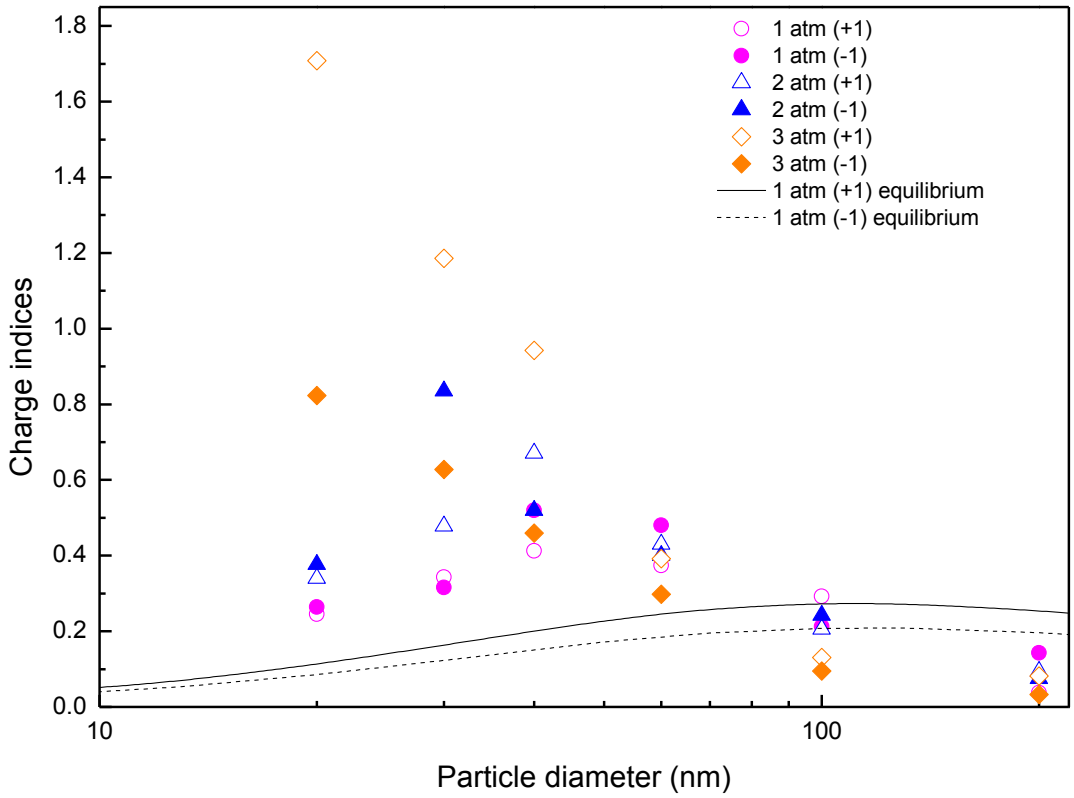

Figure 4.6 Charge indices of particles of various sizes under 1 atm, 2 atms, and 3 atms

Based on the above discussion, it is hypothesized that with a higher gas pressure in the coal combustor, for the particles of each size the charge fraction and number of the average charge on the particles are both larger when the particles exit the combustor. This hypothesis is correct theoretically. With a higher gas pressure, the residence time of the submicrometer particles in the drop-tube furnace is higher, which results in both a larger charge fraction and a larger number of the average charge based on the theory of diffusion charging (Hinds 1999). A longer residence time also enhances the direct thermoionization and photoionization of particles, which contribute in increasing the charge fraction and number of charge as well although their effects are secondary to the diffusion charging (Burtscher 1992). At the same time, the results that with a higher gas pressure the charge indices for smaller particles (20

nm, 30 nm, and 40 nm) are larger, and those for larger particles (60 nm, 100 nm, 200 nm) are smaller (Figure 5) also support the hypothesis that with higher gas pressure in the combustor, the particles exiting the combustor have a larger chance to be multiply charged.

4.3.5 Capture of fly ash particles from the pressurized ESP

In the fly ash particle capture study, the absolute value of the ESP current was kept the same (+20 μA for positive polarity case and -20 μA for negative polarity case). The particle penetration for various gas pressures are shown in Figure 4.7. For the negative ESP case (Figure 4.7a), the penetration still increased with the particle size. However, the particle penetration was higher for a higher gas pressure, which is exactly opposite with the conclusion drawn from the second test of experiment set II (results shown in Figure 4.4), in which the ESP operation was almost the same as in the test of this section (currents were the same; voltages were slightly different because the gas compositions affected the I-V characteristics). The reason might be that the charging status played an important role here. In the NaCl particle test, all the particles were with a Boltzmann charge distribution, however, in the fly ash particle test, the charging statuses varied for studies with different gas pressure. From the discussion of the previous section, it is very likely that there were a higher percentage of multiply positively charged particles from combustion under higher gas pressure. Those multiply charged particles caused an overall higher penetration.

(a)

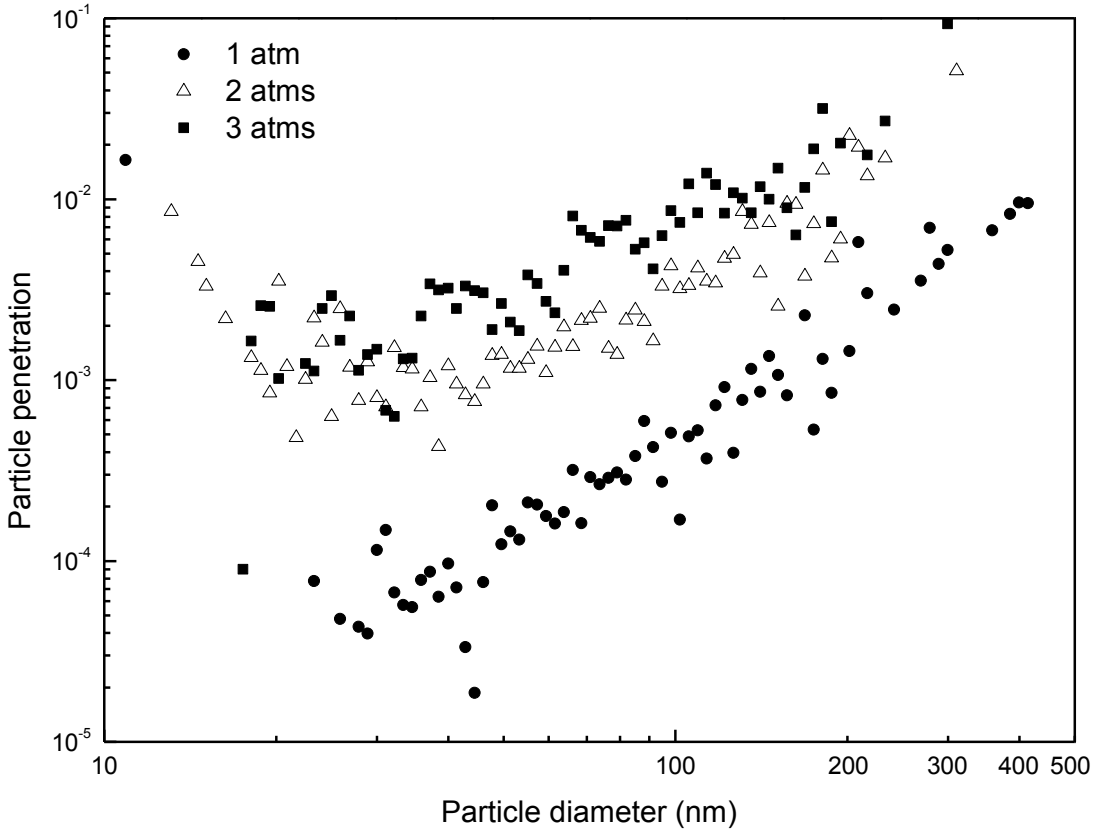
1 atm
2 atms
3 atms
Particle penetration
Particle diameter (nm)
10
100
200
300
400
500

(b)

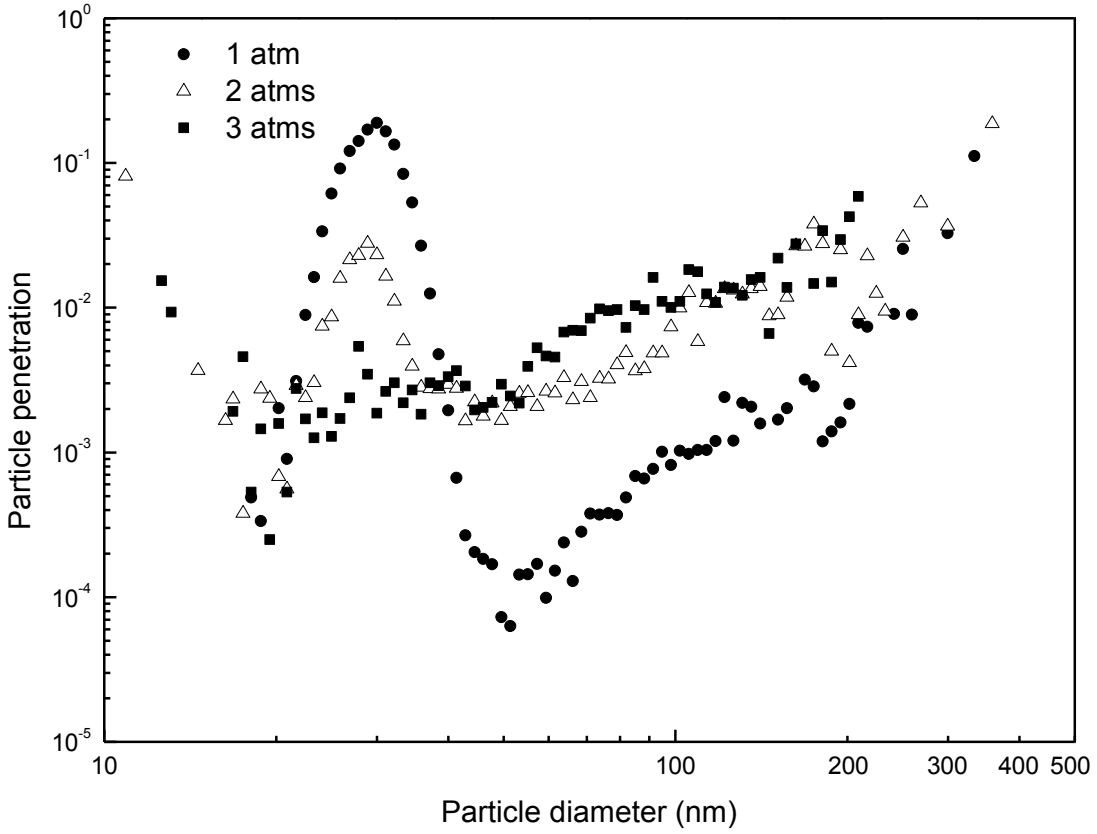

Figure 4.7 Particle penetrations through the ESP for fly ash particles of various sizes under different gas pressures: (a) negative ESP; (1 atm case: ESP voltage -8.6 kV, current -20 μA; 2 atms case: voltage -12.8 kV, current -20 μA; 3 atms case: voltage -15.7 kV, current -20 μA;) (b) positive ESP; (1 atm case: ESP voltage +8.3 kV, current +20 μA; 2 atms case: voltage +13.2 kV, current +20 μA; 3 atms case: voltage +16.8 kV, current +20 μA)

For the positive ESP case (Figure 4.7b), there was a peak at 30 nm for each of the three penetration curves, which is because the formation of secondary H_2SO_4-H_2O aerosols, a result of the oxidation reaction of SO_2 from the flue gas, and following nucleation, condensation, and coagulation inside the ESP. The formation of secondary aerosols in the ESP has been well discussed in another paper. The reason why the particle formation was not

observed in the negative case is that negative ESP has higher capture efficiency for the concerned particles than positive ESP. The secondary particle penetration of the 1 atm case was higher than that of the 2 atms case, and the penetration of the 3 atms case was even lower. This might be because higher residence time in the ESP resulted in higher capture efficiency of the secondary aerosols. Other than the secondary formation and penetration, the penetration curves of the positive ESP cases had the same pattern with those of negative ESP cases. Important to noted that the voltages that provided the ±20 μA currents in this section were slightly different with those in the second test of experiment set II (results shown in Figure 4), which might be due to the minor change in the gas composition.

4.4 Conclusions

In this study, the effect of gas pressure on the performance of an ESP was examined. The corona on-set voltage increased with the gas pressure, and under the same voltage, the ESP current was lower with higher gas pressure, because the higher gas density hindered the ionization process. Effect of gas pressure on the submicrometer particle capture in the ESP was firstly with NaCl particles. Under a similar operating voltage, particle penetration was lower for a lower gas pressure due to that the ion concentration was higher with lower gas pressure. To investigate the effect of factors other than ion concentration, the ESP current was fixed. With the same current, the particle penetration was higher for a lower gas pressure, which was an outcome of the combined effect of higher particle velocity along the gas flow, higher particle migration velocity, and lower electrical field strength.

A modified Deutsch-Anderson equation, which accounts for all the factors discussed above, was developed to predict the particle capture efficiency in the pressurized ESP. The estimations from the modified D-A equation matched the experimental results of NaCl particle capture well.

To investigate the capture of fly ash particles in the pressurized ESP, a drop-tube furnace was used to generate fly ash particles. With higher gas pressure, the particles from the furnace tended to have higher charge fraction and average number of charge, which made the penetration of fly ash particles through the ESP increased with increasing gas pressure under the same ESP current.

4.5 References

Anderson, E. 1919. Unpublished rept. Los Angeles, CA: Western Precipitation Co.

Biswas, P., and C.-Y. Wu. 2005. Nanoparticles and the environment. *J. Air Waste Manage.* 55(6):708-746.

Brown, R.F., and A.B. Walker. 1971. Feasibility demonstration of electrostatic precipitation at 1700 F. *JAPCA J. Air Waste Ma.* 21(10):617-620.

Burtscher, H., A. Reis, and A. Schmidt-Ott. 1986. Particle charge in combustion aerosols. *J. Aerosol Sci.* 17(1):47-51.

Burtscher, H. 1992. Measurement and characteristics of combustion aerosols with special consideration of photoelectric charging and charging by flame ions. *J. Aerosol Sci.* 23(6):549-595.

Bush, J.R., P.L. Feldman, and M. Robinson. 1979. High temperature, high pressure electrostatic precipitation. *JAPCA J. Air Waste Ma.* 29(4):365-371.

Fuchs, N.A. 1947. The Charges on the Particles of Aerocolloids. *Izv. Akad. Nauk. SSSR. Ser. Geogr. Geofiz.* 11:341-348.

Gopan, A., B.M. Kumfer, J. Phillips, D. Thimsen, R. Smith, and R.L. Axelbaum. 2014. Process design and performance analysis of a Staged, Pressurized Oxy-Combustion (SPOC) power plant for carbon capture. *Appl. Energ.* 125:179-188.

Hinds, W.C. 1999. Aerosol technology: properties, behavior, and measurement of airborne particles. New York: John Wiley & Sons.

Huang, S.-H., and C.-C. Chen. 2002. Ultrafine aerosol penetration through electrostatic precipitators. *Environ. Sci. Tech.* 36(21):4625-4632.

Jing, H., S. He, Q. Ou, T.-C. Hsiao, and D.-R. Chen. 2013. Development of a Compact Electrostatic Nanoparticle Sampler for Offline Aerosol Characterization. *Mapan-J. Metrol. Soc. I.* 28(3):217-226.

Li, Y., A. Suriyawong, M. Daukoru, Y. Zhuang, and P. Biswas. 2009. Measurement and capture of fine and ultrafine particles from a pilot-scale pulverized coal combustor with an electrostatic precipitator. *J. Air Waste Manag.* 59(5):553.

Lin, G.Y., Chen, T.M., Tsai, C.J. 2012 A Modified Deutsch-Anderson Equation for Predicting the Nanoparticle Collection Efficiency of Electrostatic Precipitators. *Aerosol Air Qual. Res.* 12:697-706.

McCain, J.D., J.P. Gooch, and W.B. Smith. 1975. Results of field measurements of industrial particulate sources and electrostatic precipitator performance. *JAPCA J. Air Waste Ma.* 25(2):117-121.

Minchener, A.J. 2005. Coal gasification for advanced power generation. *Fuel* 84(17):2222-2235.

Pauthenier, M., and M. Moreau-Hanot. 1932. Charging of Spherical Particles in an Ionizing Field. *J. Phys. Radium* 3:590-613.

Rinard, G., D.E. Rugg, and T. Yamamoto. 1987. High-temperature high-pressure electrostatic precipitator electrical characterization and collection efficiency. *IEEE T. Ind. Appl.* (1):114-119.

Robinson, M. 1967. The corona threshold for coaxial cylinders in air at high pressures. *IEEE T. Power Ap. Syst.* (2):185-189.

Robinson, M. 1971. Electrostatic precipitation. In *Air pollution control*. New York: John Wiley.

Schemenau, W. 1993 Pressurized fluidized-bed combustion is advanced coal usage for electricity-genericity-generation with operational experience. *Brennstoff-Warme-Kraft* 45 (1-2):23-26.

Suriyawong, A., M. Gamble, M.-H. Lee, R. Axelbaum, and P. Biswas. 2006. Submicrometer particle formation and mercury speciation under O_2-CO_2 coal combustion. *Energ. Fuel.* 20(6):2357-2363.

Suriyawong, A., C.J. Hogan, J. Jiang, and P. Biswas. 2008. Charged fraction and electrostatic collection of ultrafine and submicrometer particles formed during O_2-CO_2 coal combustion. *Fuel* 87(6):673-682.

Villot, A., Y. Gonthier, E. Gonze, A. Bernis, S. Ravel, M. Grateau, and J. Guillaudeau. 2012. Separation of particles from syngas at high-temperatures with an electrostatic precipitator. *Sep. Purif. Technol.* 92:181-190.

Wang, X., B.J. Williams, Y. Tang, Y. Huang, L. Kong, X. Yang, and P. Biswas. 2013a. Characterization of organic aerosol produced during pulverized coal combustion in a drop tube furnace. *Atmos. Chem. Phys.* 13(21):10919-10932.

Wang, X., E. Cotter, K.N. Iyer, J. Fang, B.J. Williams, and P. Biswas. 2015. Relationship

between pyrolysis products and organic aerosols formed during coal combustion. *P. Combust. Inst.* 35(2):2347-2354.

Wang, X., S.M. Daukoru, S. Torkamani, W.-N. Wang, and P. Biswas. 2013. Role of exhaust gas recycle on submicrometer particle formation during oxy-coal combustion. *P. Combust. Inst.* 34(2):3479-3487.

Wiedensohler, A. 1988. An approximation of the bipolar charge distribution for particles in the submicron size range. *J. Aerosol Sci.* 19(3):387-389.

Ylätalo, S.I., and J. Hautanen. 1998. Electrostatic precipitator penetration function for pulverized coal combustion. *Aerosol Sci. Tech.* 29(1):17-30.

Yoo, K.H., J.S.Lee, and M.D. Oh. 1997. Charging and collection of submicron particles in two-stage parallel-plate electrostatic precipitators. *Aerosol Sci. Tech.* 27(3):308-323.

Zhuang, Y., Y.J. Kim, T.G. Lee, and P. Biswas. 2000. Experimental and theoretical studies of ultra-fine particle behavior in electrostatic precipitators. *J Electrostat* 48(3):245-260.

CHAPTER 5. DEVELOPMENT OF A COMPACT ELECTROSTATIC NANOPARTICLE SAMPLER FOR OFFLINE AEROSOL CHARACTERIZATION

The results of this chapter has been published in Jing, H.; He, S.; Ou, Q.; Hsiao, T.C.; Chen, D.R., Development of a Compact Electrostatic Nanoparticle Sampler for Offline Aerosol Characterization. Journal of Metrology Society of India (JMSI), 2013, 28, 217-226

Abstract

A compact electrostatic nanoparticle sampler has been developed to support the offline analysis of nanoparticles via electron microscopy. The basic operational principle of the sampler is to electrically charge particles by mixing nanoparticles and unipolar ions produced by DC corona discharge, and then electrostatically collecting charged particles. A parametric study was first performed to identify the optimal operating condition of the sampler: a total flow rate (i.e., the sum of the particle and ion carrier flow rates) of 1.0 lpm, an aerosol/ion carrier flow rate ratio of 1.0, and a collection voltage of 4.5 kV. Under the above condition, the sampler achieved a collection efficiency of more than 90% for particles ranging from 50 to 500 nm. The effect of particle material on the sampler's performance was also studied. The prototype had lower collection efficiencies for oleic acid particles than for sodium chloride (NaCl) particles in the size range from 50 to 150 nm, while achieving a comparable efficiency in the size range large than 150 nm. The effect of particle diameter, particle material, and total flow rate on the sampler's collection efficiency is explained by the particle charging data, i.e., charging efficiencies and mean charges per particle.

5.1 Introduction

For two reasons, much attention has recently been given to investigation of particles in the nanometer size range. First, nanoparticles have been reported in exhausts of various combustion sources, chemical processes, and aerosol reactors (Kaupplnen and Pakkanen, 1990; Biswas and Wu, 2005). Such nanosized particulates are considered environmental pollution because of the potential toxicity attributed to their small size and large surface area (Warheit 2004). Secondly, nanoparticles are considered as building blocks for nanotechnology and are widely utilized, such as in biomedical, optical, and electronic applications (Katz and Willner, 2004; Al-Jamal and Kostarelos, 2007). Most of the nanoparticles mentioned above are airborne. For either the pollution control or industrial applications, they must be well characterized.

To characterize the physical properties of airborne nanoparticles, a scanning mobility particle sizer (SMPS) (Wang and Flagan, 1990) has been developed to measure the size distribution of particles in the submicrometer range. A nanoparticle surface area monitor (NSAM) for *in situ* measurement of the surface area of nanoparticles deposited in certain regions of human lungs has also been built (Shin et al., 2007). However, some features of nanoparticles, such as their morphology and chemical composition, cannot be measured online by these instruments. Nanoparticles' morphology is an important feature as it can significantly influence their transport behaviour and functions. Real-world nanoparticles are mostly in agglomerate form because of the high number concentration of nanoparticles produced in various sources. Nanoparticle morphology is best investigated via offline electron microscopy (Ito et al., 2004;

Liu 2005). In offline characterization, particles first need to be collected and then analysed offline by instruments such as scanning/transmission electron microscopes (SEM/TEM).

Several nanoparticle samplers for supporting electron microscopy are commercially available. The TEM sampler offered by FHNW (Fachhochschule Nordwestschweiz) shares a similar configuration with that designed by Dixkens and Fissan (Dixkens and Fissan, 1999), including a unipolar diffusion charging component and an electrostatic deposition component. However, it has limited collection efficiency ranging from 11% for 20 nm particles to 3% for 320 nm particles (Fierz et al., 2007). The operation of the nanometer aerosol sampler (NAS; TSI Model 3089) is based on the electrostatic precipitation principle. It has been successfully applied in studying atmospheric aerosols (Hinkley et al., 2008; Barone and Zhu, 2008). However, the TSI sampler is commercialized as an accessary to SMPSs, requiring sampled particles to be electrically charged prior to entering the sampler (Li et al., 2010). Moreover, the samplers are portable but not especially compact (FHNW TEM sampler: 35 cm × 25 cm × 15 cm, and NAS: 20.3 cm × 25.6 cm × 22.8 cm, respectively). The design of the ESPnano Model 100 (DASH Connector Technology, Inc.) is also basically an electrostatic precipitator in the "point-to-plate" configuration, in which particles are charged and collected at the same time. The ESPnano can efficiently collect nanoparticles on a TEM grid and is compact enough for use for studying nanoparticles in work environments (Miller et al., 2010). However, for a sampler using the "point-to-plate" design, aerosol contacts with the high energy zone of a corona discharge, which is not recommended in practice (Stommel and Riebel, 2005).

The corona charger is the key component of a sampler. Recent studies on chargers have provided supports to the development of new samplers. The corona ionizer developed by Hernandez-Sierra et al. (2011) can achieve charging efficiencies of 30% for 10 nm particles under both positive and negative coronas. The unipolar corona charger developed by Laschober et al. (2006) can yield three to five times of singly charged particles compared to bipolar charging under optimal corona settings.

A compact nanoparticle sampler based on the principles of DC corona charging and electrostatic precipitation is proposed in this study. The proposed sampler can be easily applied in collecting nanoparticles for SEM/TEM and EDX (energy-dispersive X-ray spectroscopy) analysis. Various experiments were conducted to evaluate and optimize the performance of this prototype sampler. The effects of operational parameters, including the total flow rate, aerosol/ion carrier flow rate ratio, and collection voltage, were first investigated by using the particle collection efficiency as an index. The obtained results were also used to determine the optimal working parameters for the sampler. The percentage of particles deposited on different surfaces in the sampler was then characterized. The results from this deposition experiment gave an accurate value for the percentage of particles actually captured on the collection surface of the SEM stub in the proposed sampler. Finally, to better understand the sampler's performance in real-world applications, the collection efficiency curves in the optimal operation were characterized for both solid and liquid particles as well as PSL standard particles.

5.2 Sampler Design

A schematic diagram of the compact electrostatic sampler is shown in Figure 5.1. It consists of two chambers: one for particle charging and the other for particle collection. The particle charging chamber in the configuration is the same as that used in the NSAM (Shin et al. 2007). To produce unipolar ions, a pointed corona needle is used in the discharge compartment, physically separated from the charging zone. Unipolar ions are then transported by an ion carrier flow (free of particles) to the particle charging zone. By using clean air as the ion carrier flow, the corona tip is well protected (i.e., free of contamination) for long-term operation. The carrier flow and sampled aerosol stream are well mixed in the particle charging zone via the opposing flow arrangement, and particles acquire electrical charges during the mixing. The particles are then carried to the collection chamber, in which a SEM stub is placed and electrically insulated from the ground. Within the electrically grounded collection chamber wall, the electrified SEM stub is the collection stage of the sampler. Several TEM grids can be fixed on the SEM stub if needed. Particles not collected finally follow the total flow (i.e, the sum of the aerosol and ion carrier flows) and exit the sampler via the outlet. Thus, two gas flows are inputs to the sampler (one an ion carrier flow and the other an aerosol flow) while only one gas flow exits the particle collection chamber. To operate the prototype sampler, two high voltage supplies are needed (one for corona discharge and the other for charged particle collection).

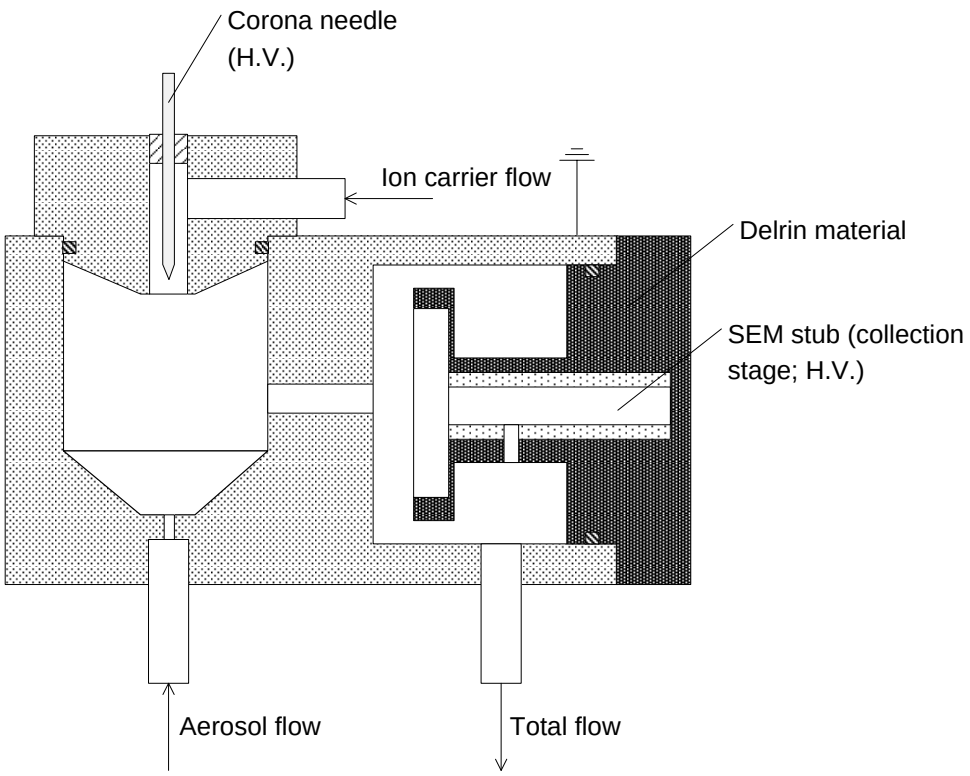

Figure 5.1 Schematic diagram of prototype compact electrostatic sampler

5.3 Experimental Setup and Data Analysis

5.3.1 Experimental setup

Figure 2 is a schematic diagram of the experimental setup for evaluating the electrostatic nanoparticle sampler. The sampler was tested with laboratory generated particles ranging from 10 nm to 1000 nm (i.e., 10 nm to 500 nm for NaCl particles, 60 nm to 500 nm for oleic acid particles, 100 nm to 1000 nm for PSL particles, and 60 nm to 400 nm for fluorescent sodium particles). Monodisperse NaCl and oleic acid test particles in the sizes ranging from 60 nm to 500 nm were produced and selected by atomization-DMA (differential mobility analyzer)-classification (Liu and Pui, 1974). To obtain particles with diameters less than 60

nm, monodisperse NaCl particles were generated by evaporation-condensation-DMA-classification (Scheibel and Porstendörfer, 1983). Monodisperse PSL particles were dispersed in air by spraying the PSL particle suspension (prepared from the dilution of concentrated PSL particle suspensions purchased from Duke Scientific Corporation). Then they were classified in a DMA. After the DMA classification, all the classified particles were electrically charged. Particles with a steady-state charge distribution were obtained by passing DMA-classified particles through a Po^{210} charge neutralizer. Electrically neutral particles were further obtained by passing particles with a steady-state charge distribution through a homemade electrostatic particle precipitator.

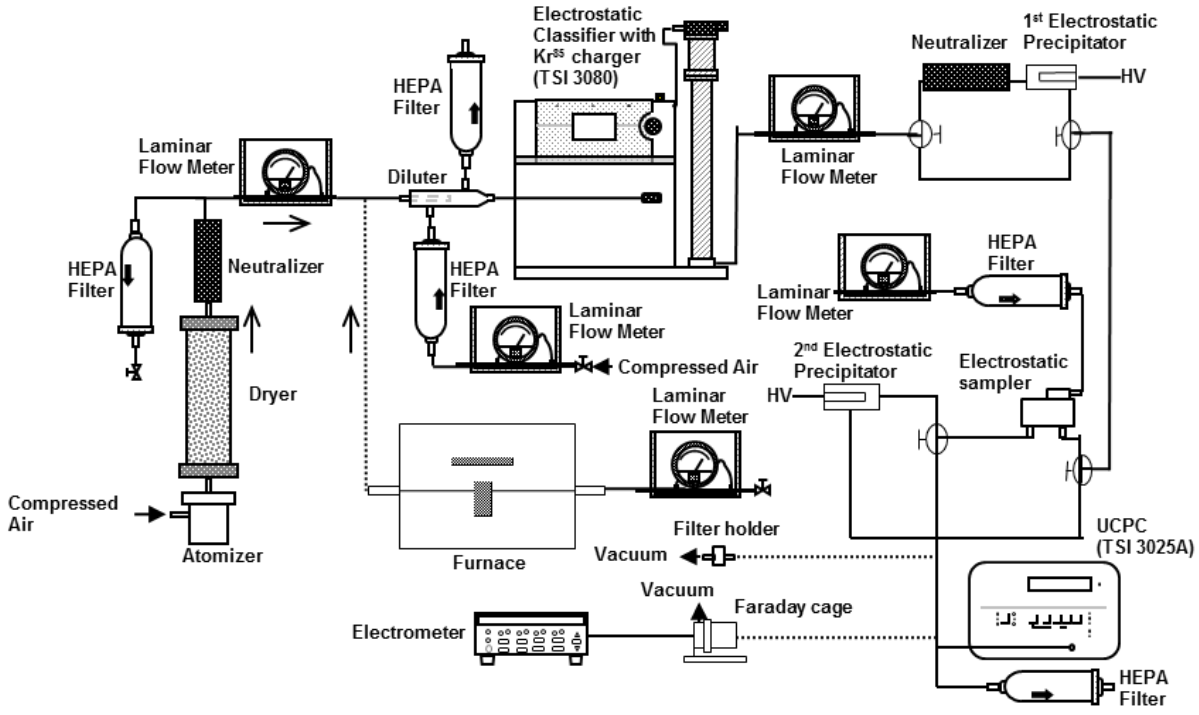

Figure 5.2 Experiment setup for the charger evaluation, measurement of particle collection efficiency, and the fluorescence experiments

To measure the charge fraction of particles, a second electrostatic precipitator was applied to remove the charged portion of particles exiting the particle charging chamber. The number

concentrations of particles upstream and downstream of the sampler were measured by a UCPC (TSI Model 3025) operated in low flow mode (i.e., 0.3 lpm). The electrical charges on particles after the particle charging chamber were measured with a sensitive electrometer (Keithley Model 6514) connected to a homemade aerosol Faraday cage.

In this investigation the voltage applied on the corona needle was set at 2.7 kV in order to obtain an operational current of 2.0 A. The particle collection voltage was varied from 1.5 to 4.5 kV in order to find the optimal collection voltage for the sampler. The ion carrier and aerosol flow rates were varied from 0.33 to 1.50 lpm.

Fluorescence experiments were performed to characterize the percentage of particles actually collected on the collection surface of the stage and other surfaces inside the sampler. Monodisperse fluorescent sodium test particles were produced by the same technique used to produce monodisperse NaCl particles. The spray solutions were prepared by dissolving fluorescent sodium salt (Uranine; Sigma-Aldrich) in iso-propanol (CHROMASOLV® Plus, for HPLC, 99.9%; Sigma-Aldrich**)**. A filter holder with HEPA (high-efficiency particulate air) filter medium was placed downstream of the sampler to collect particles in the exit stream. A brief summary of the procedure in this part of experiment is given in the section 5.3.2c.

5.3.2 Experimental procedure and data analysis

(a) Measuring the particle collection efficiency of the sampler

The collection efficiency of the sampler at a specific particle size was calculated by eq5.1:

$$\text{Collection efficiency} = 1 - \frac{N_1}{N_2} \tag{5.1}$$

where N_1 and N_2 were the measured particle number concentrations downstream from the sampler when particle charging was on and the collection voltage was off.

(b) Measuring the charging efficiency and average charge of the particles in the sampler

The intrinsic particle charging efficiency of the charger for a given size was calculated by the method of Romay and Pui (1992), using eq5.2:

$$\text{Intrinsic charge efficiency} = 1 - \frac{N_3}{N_4} \tag{5.2}$$

where N_3 and N_4 are the particle number concentrations measured downstream from the second electrostatic precipitator with the applied voltage turned on and off, respectively. Note that, in this part of experiment, the particle charging of the sampler was on, and the collection stage voltage was off.

The extrinsic charging efficiency for particles of a specific size was evaluated using the method described by Chen and Pui (1999):

$$\text{Extrinsic charge efficiency} = 1 - \frac{N_5 - N_3 / P_{ec}}{N_6} \tag{5.3}$$

where N_5 and N_6 are the particle number concentration measured downstream and upstream of the sampler, respectively. P_{ec} is the penetration of neutral particles through the 2nd

electrostatic precipitator. The voltage applied to the corona needle was on, and the particle collection voltage was off.

The average charge of the particles was calculated by eq5.4:

$$\text{Average charge} = \frac{I_6 / e}{N_6 \times Q} \tag{5.4}$$

where I_6 is the aerosol current measured downstream from the sampler by the aerosol Faraday cage electrometer, Q was the flow rate sampled into the cage electrometer; and e was the elementary charge, 1.60×10^{-19}C. In this measurement, the voltage on the corona needle was on and the voltage to the collection stage was off.

(c) Determining the percentage of particles deposited at various surfaces in the sampler

Fluorescence experiments were performed to investigate the percentage of particles deposited on various surfaces in the sampler. The detailed procedure for the experiments can be found in the literature, such as the work of Chen and Pui (1995). Monodisperse fluorescent sodium particles were the test particles. Each experimental run took two hours. After each run, particles deposited on various surfaces in the sampler were recovered by multiple wiping with cotton swabs wetted with aqueous solutions of 0.001 N NH_4OH and then immersed in beakers with 25 ml of the same solution. The solutions were then measured by a fluorometer (Modulus Luminometer, Turner BioSystems). The fluorescence of each beaker solution represented the mass of particles deposited at the designated surface in the sampler.

The percentage of particles of a given size on each designated surface was then calculated by eq5.5:

$$\text{Percentage of particles depositing on the surface } i = \frac{A_i}{\sum_{j=1}^{n} A_j} \qquad (5.5)$$

where A_i is the fluorescence of the beaker solution containing the particles recovered from the surface i in the sampler, and n was the total number of inner surfaces studied.

5.4 Results and Discussion

5.4.1 Optimization of the sampler performance

(a) The effect of particles' pre-charge condition and the particle charging

DMA-classified NaCl particles were selected as test particles to evaluate the particle charging performance of the sampler, measured for particles having either neutralized or steady-state charge distributions. The test operational conditions were 0.5 lpm aerosol flow, 0.5 lpm ion carrier flow, and 4.5 kV for collection stage voltage. Figure 5.3 shows the particle collection efficiency of the sampler when challenged with electrically neutral particles or particles having steady-state charge distribution. It should be noted that the particle size in the figure referred to the equivalent mobility size diameter, and this applies to the following figures. In general, for particles having either pre-charge conditions, the efficiency of the sampler increased as the particle size increased. The figure further evidences that the difference in collection efficiencies for both pre-charge conditions are minor, ranging from 0.1% to 5.4% when the particle size was varied from 50 to 500 nm. To better simulate typical conditions,

particles with a steady-state charge distribution were selected for the following collection efficiency test.

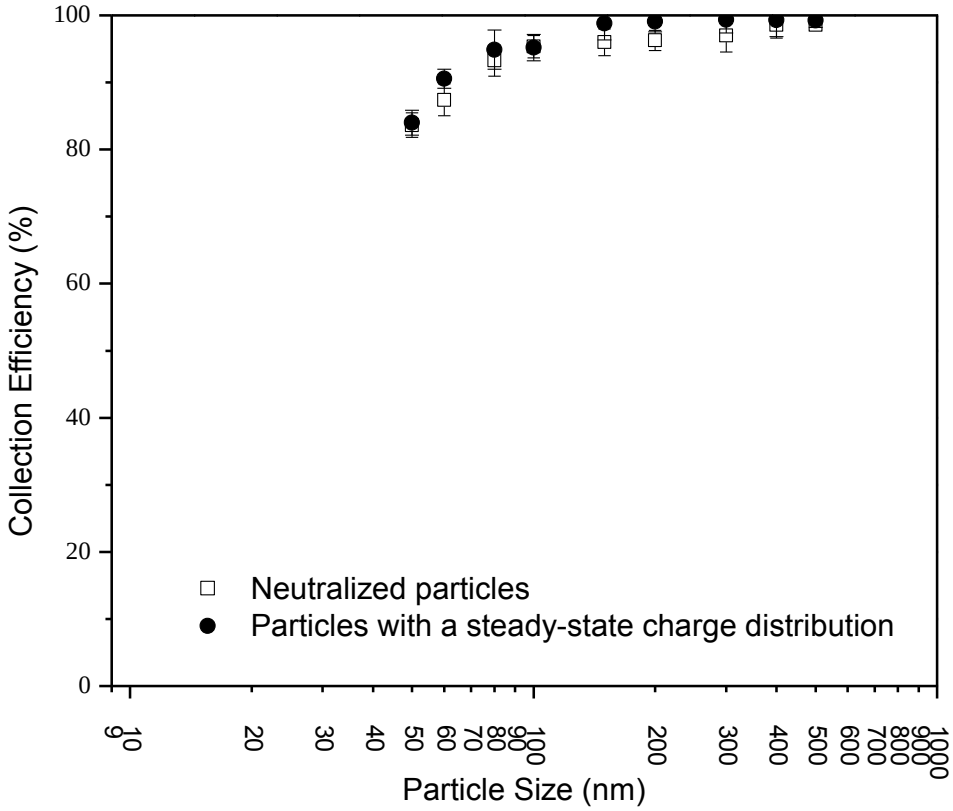

Figure 5.3 Collection efficiencies of neutralized and steady-state charge distribution NaCl particles (aerosol/ion carrier flow rate ratio of 1.0; total flow rate of 1 lpm; collection stage voltage of 4.5 kV)

The particle charging performance was further evaluated to better understand the observed trend in particle collection efficiency. Figure 5.4 shows the measured intrinsic and extrinsic efficiencies of particle charging in the sampler at an aerosol/ion carrier flow rate ratio of 1.0 and a total flow rate of 1 lpm. The collection stage voltage was off. It is evident that both charging efficiencies increased as the particle size increased, and the efficiencies reached

close to 100% at a particle size of 160nm. Such an increasing trend in the charging efficiency was also observed in the evaluation of corona-based particle chargers (Kruis and Fissan 2001, Qi et al. 2007, Li and Chen 2011). The figure also shows that the intrinsic and extrinsic particle charging efficiencies of the sampler were close for a given particle size. The difference between two charging efficiencies was less than 4% except for the case of 10 nm particles, indicating that particle loss in the charging chamber of the sampler is negligible for the size range of interest.

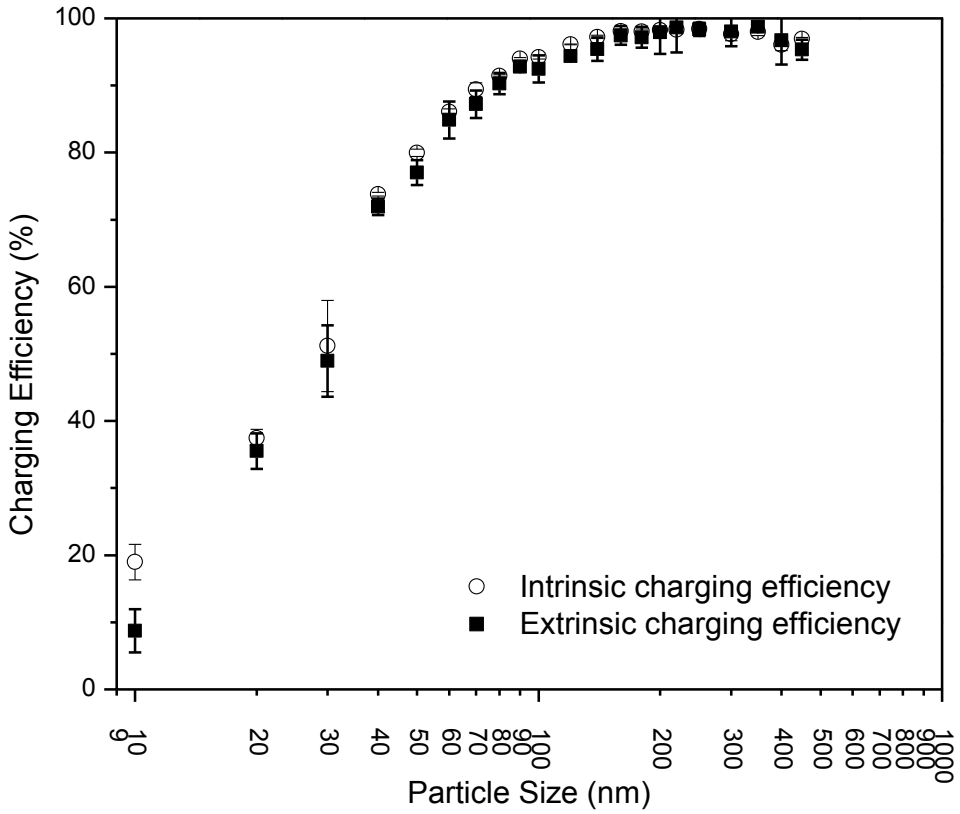

Figure 5.4 Intrinsic and extrinsic charging efficiencies of NaCl particles (aerosol/ion carrier flow rate ratio of 1.0; total flow rate of 1 lpm)

(b) Effect of aerosol and ion carrier flow rate ratio

In this part of test, the total flow rate and the collection stage voltage were kept at 1.0 lpm and 4.5 kV, respectively. Figure 5.5 shows the particle collection efficiencies of the sampler at the various flow rate ratios. The efficiency remained nearly the same when the ion carrier flow rate was higher than the aerosol flow, but collection efficiency was lower when the aerosol flow rate was higher than the ion carrier flow rate (i.e., an aerosol/ion carrier rate ratio of 3.0), especially for the particles smaller than 100 nm. The above observation can be explained as follows: When the aerosol flow was dominant, more particles were carried into the sampler while fewer ions were carried out by the low ion carrier flow, leading to low particle charging efficiency. Compared with those for other test flow rate ratio cases, it reduced particle collection efficiencies by 4.1% to 9.2% for particles ranging from 60 nm to 100 nm. The effect was not significant for particles larger than 100 nm, because the ion concentration remained sufficient to charge such relatively large particles. The efficiency of particle charging in the sampler (as shown in Figure 5.4) was 92.5% to 99.0% for particles larger than 100 nm in diameter. It can further be expected that the sampler collection efficiencies of particles with the sizes larger than 100 nm would decrease if the flow rate ratio was further increased.

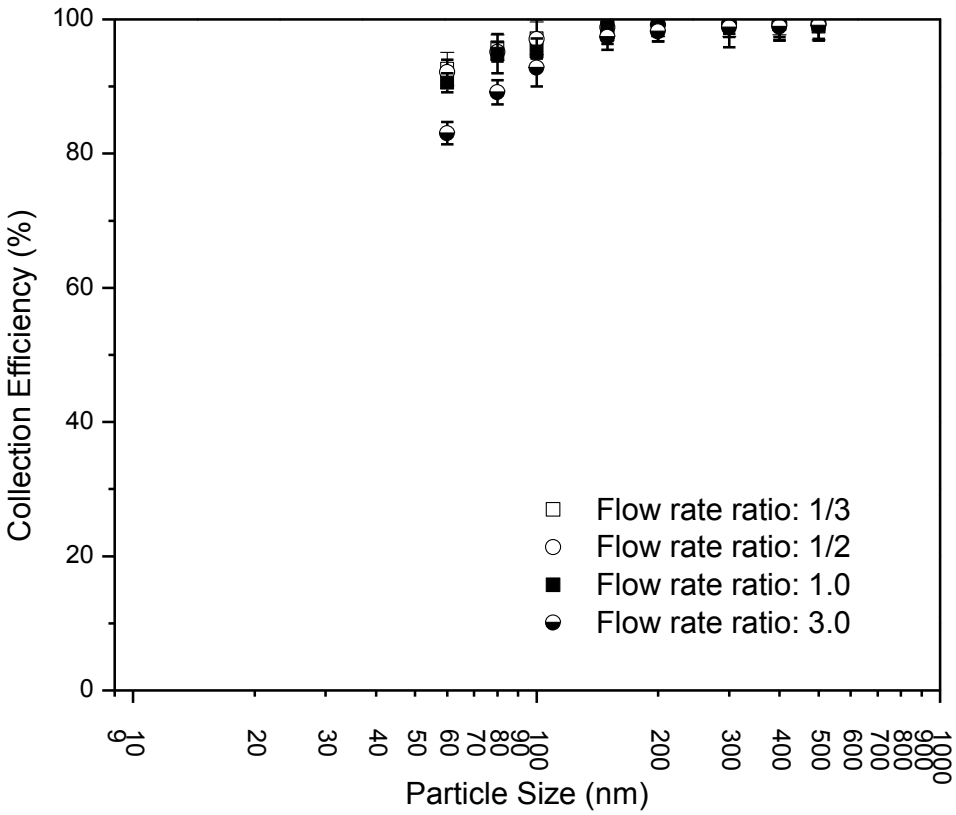

Figure 5.5 Collection efficiencies of NaCl particles at different aerosol/ion carrier flow rate ratio (total flow rate of 1 lpm; collection stage voltage of 4.5 kV)

(c) Effect of total flow rate

The effect of total flow rate (i.e., the sum of the aerosol and ion carrier flow rates) on the sampler performance was investigated at an aerosol/ion carrier flow rate ratio of 1.0 and collection stage voltage of 4.5 V. Figure 5.6 shows the collection efficiencies of the sampler operated at total flow rates of 1.0, 2.0, and 3.0 lpm. Over the entire test particle size range, the particle collection efficiency decreased as the total flow rate increased. This observation is attributed to the reduction of residence time for particle charging and collection in the

sampler as total flow rate increased (Hinds 1999). In single stage electrostatic precipitator, particles flow through the charging and precipitation zone in high intensity electrical field. Under the influence of the electric field, charged particles drift toward the collection stage/substrate. High aerosol flow velocity results in a quick passage through the precipitation zone, and consequently a short drifting distance and lower collection efficiency. Moreover, for particles larger than 100 nm in diameter, the collection efficiency of the studied sampler slightly decreased as the particle size increased, especially for the case of 3 lpm total flow rate. The above observation is attributed to the shorter time for particle charging and lower charges on large particles (leading to the reduction of particle electrical mobility) as compared to those at low total flow rates.

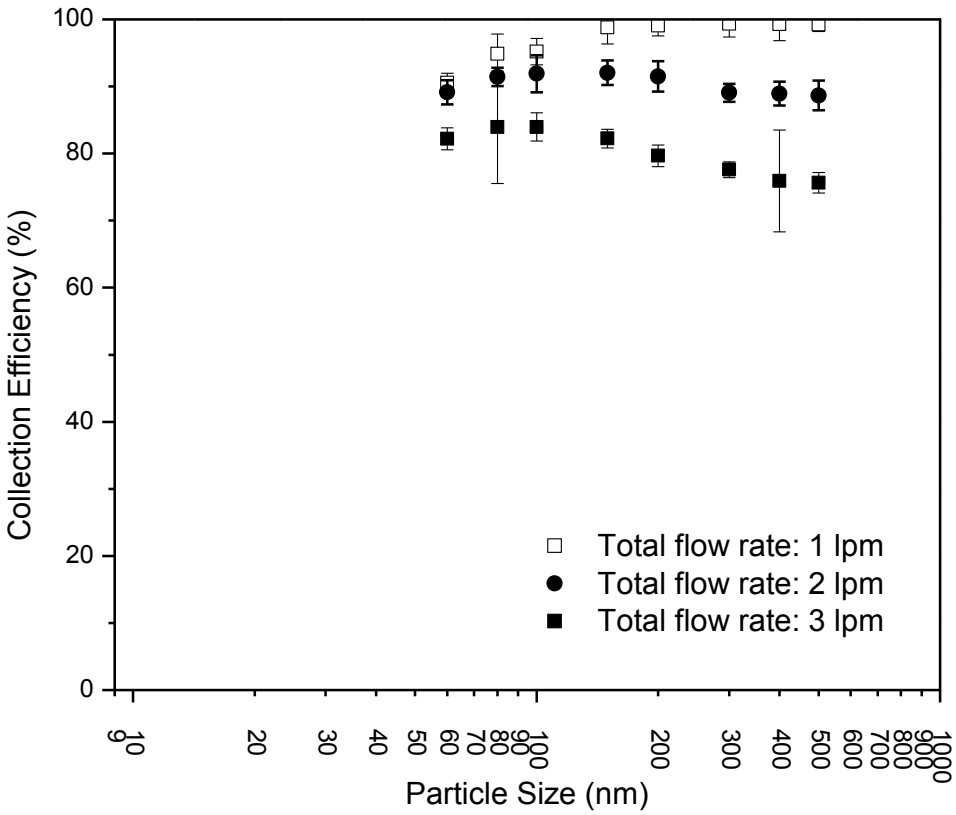

Figure 5.6 Collection efficiencies of NaCl particles at different total flow rates (aerosol/ion carrier flow rate ratio of 1.0; collection stage voltage of 4.5 kV)

(d) Effect of collection voltage

The effect of collection voltage on the sampler was studied at an aerosol/ion carrier flow rate ratio of 1.0 and total flow rate of 3 lpm. The 3 lpm total flow rate was selected because the particle charging time and the residence time of particles in the collection chamber were limited, leading to more noticeable variation in the sampler collection efficiency when the collection stage voltage was varied. Figure 5.7 gives the efficiency at the collection stage for 1.5, 3.0, and 4.5 kV. Accordingly, the electric field intensities between the aerosol inlet of the

collection chamber and the front surface of the collection stage were 9.4 kV/cm, 18.9 kV/cm, and 28.3 kV/cm. The figure shows that the collection efficiency decreased as the collection voltage decreased, over the entire tested particle size range. The above result is expected because the weak electrical field at the low collection stage voltage setting resulted in shorter drifting distance of charged particles, leading to less collection efficiency.

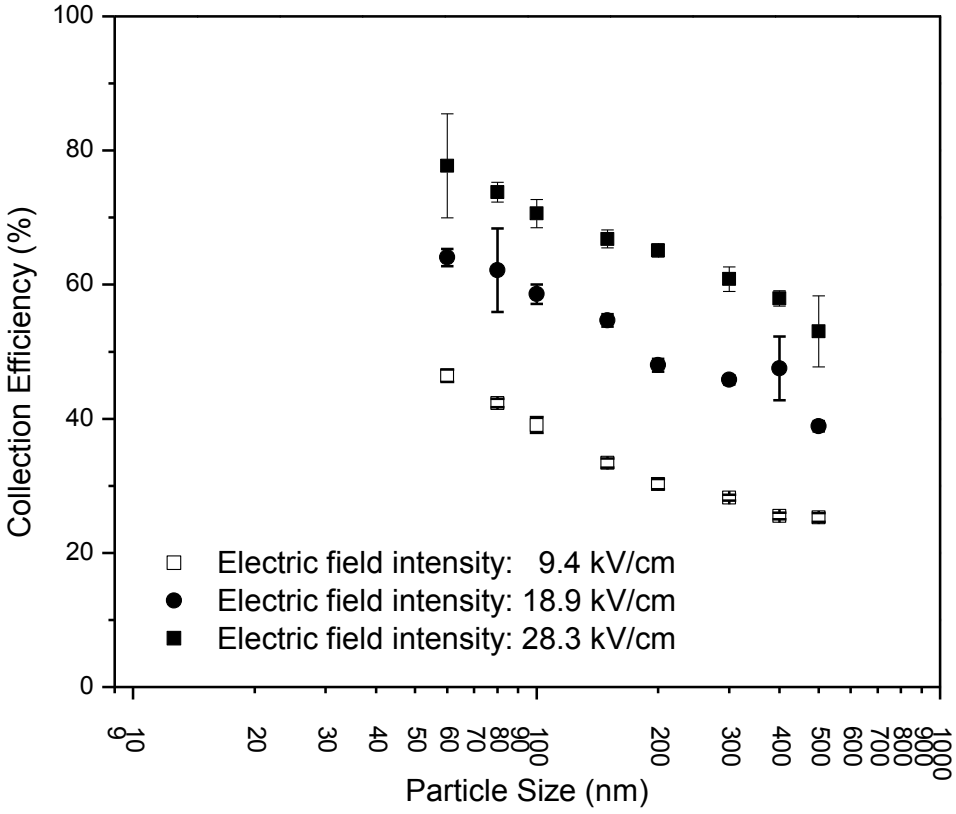

Figure 5.7 Collection efficiencies of NaCl particles at different collection stage voltages (aerosol/ion carrier flow rate ratio of 1.0; total flow rate of 3 lpm)

Figure 5.7 also shows that the particle collection efficiency decreased as the particle diameter increased for a given collection stage voltage. The electrical mobility of particles was reduced

as their sizes increased. Figure 8a gives the measured average charges on particles varying from 10 to 500 nm, at a 1.0 aerosol/ion carrier flow rate ratio and 1 lpm total flow rate. Figure 8b provides the calculated electrical mobility of particles based on the average charges measured for a given size (Hinds 1999). The electrical mobility of particles decreased significantly as the particle diameter increased. The low electrical mobility of large particles requires high electrical field intensity in order to precipitate them, thus there is less particle deposition on the collection stage.

(a)

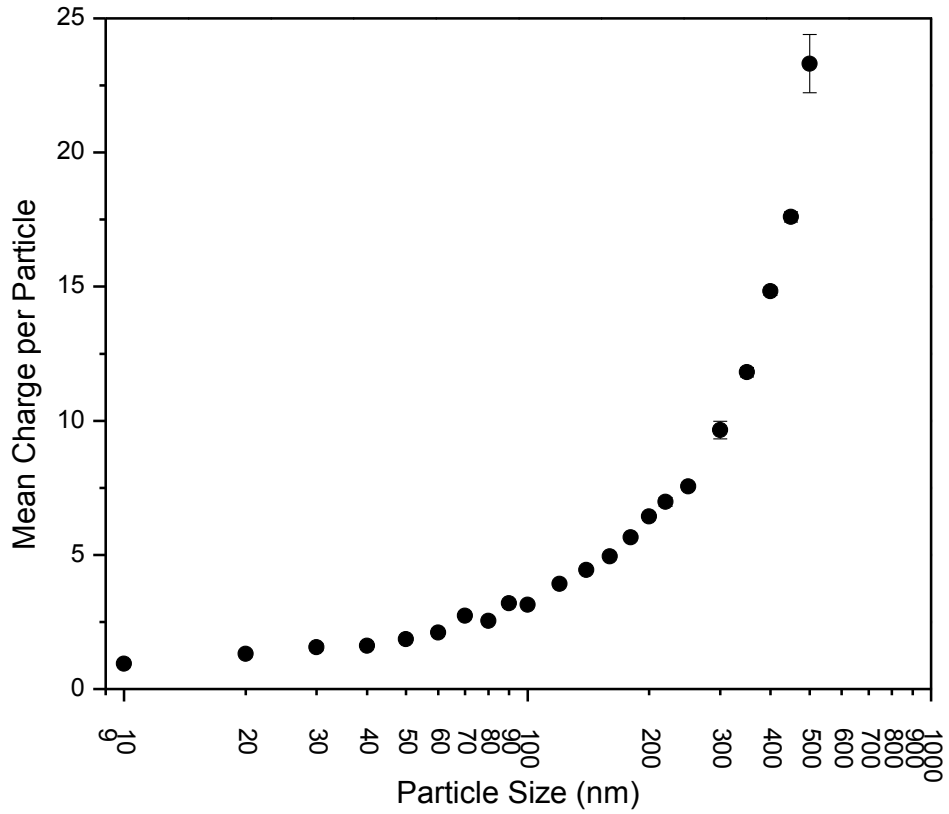

(b)

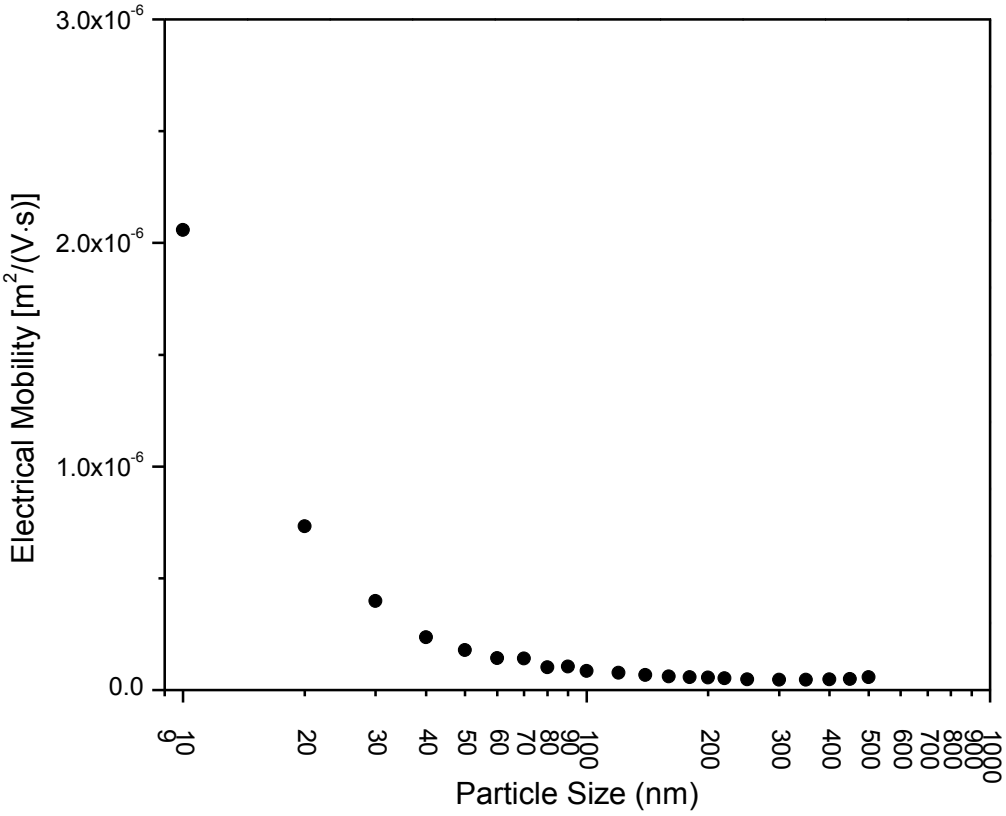

Figure 5.8 (a) Collection efficiencies of NaCl particles at different collection stage voltages; (b) Electrical mobility of NaCl particle (aerosol/ion carrier flow rate ratio of 1.0; total flow rate of 1 lpm)

(e) Optimal operational conditions of the studied sampler

Based on the data present above, we concluded that the prototype sampler achieved the highest particle collection efficiency at a total flow rate of 1.0 lpm (with the aerosol/ion carrier flow rate ratio of 1.0) and a collection stage voltage of 4.5 kV.

5.4.2 Particle deposition in the sampler

Fluorescence experiments were performed to characterize the percentage of particles deposited on various surfaces inside the sampler as a function of particle size. The results of these experiments are given in Figure 5.9, indicating that 57% to 78% of the particles deposited on the front surface of the collection stage (i.e., the SEM stub) for particles with the diameters varying from 60 nm to 400 nm.

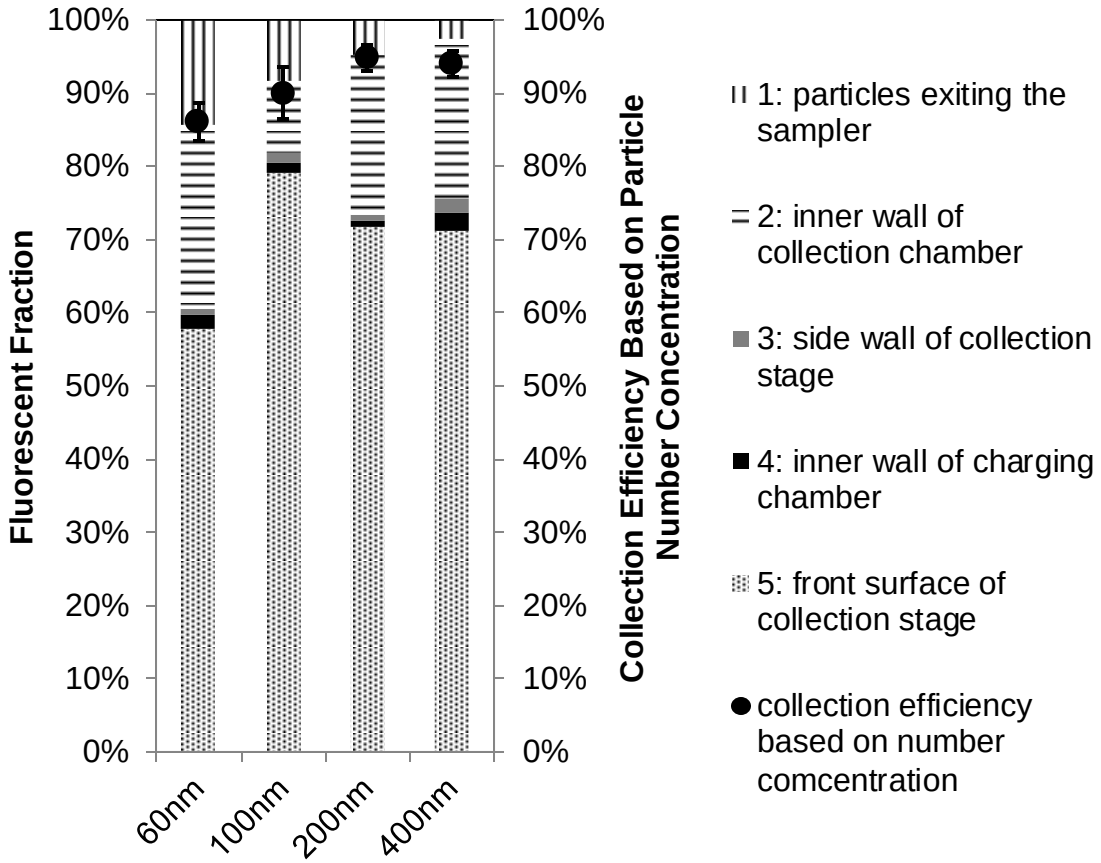

Figure 5.9 Particle deposition in the sampler

In addition to the collection surface of the SEM stub, noticeable particle deposition occurred on the inner surface of the collection chamber (9.8% to 25.2%). After entering the collection chamber, particles that were not deposited on the collection surface of the SEM stub moved outward to the stub edge, turned 90^{o} and moved through the annular gap at the stub's outer

edge prior to exiting. The sharp flow turn generally resulted in flow recirculation at the corner, facilitating particle deposition on the inner wall of collection chamber.

Note that particles that escaped from the sampler were collected on the HEPA filter in each experimental run. By fluorescence measurement, between 4.7 to 12.2% of particles in test sizes of 400, 200, 100, and 60 nm were not collected by the sampler. This set of data is consistent with the calculated penetration of particles with designated particle sizes (based on particle number concentration measurement). The calculated penetration data are also presented in Figure 5.9 for the reference.

5.4.3 Effect of particle material

To investigate the effect of particle material on the particle collection efficiency, oleic acid particles and PSL particles were selected. PSL particles were used because they are standard research particles (Gombocz et al., 1987; Li and Lindsay, 1991). The collection efficiency measurements are shown in Figure 5.10. The collection efficiency data for NaCl particles under the optimal operation condition is also given in the same plot for comparison. As discussed previously, the collection efficiency of NaCl particles increased as the particle size increased, due to the increase in charging efficiency. The sampler had more than 90% collection efficiency for particles larger than 60 nm. Similarly, the sampler had a collection efficiency higher than 90% for PSL particles with diameters varying from 100 to 900 nm.

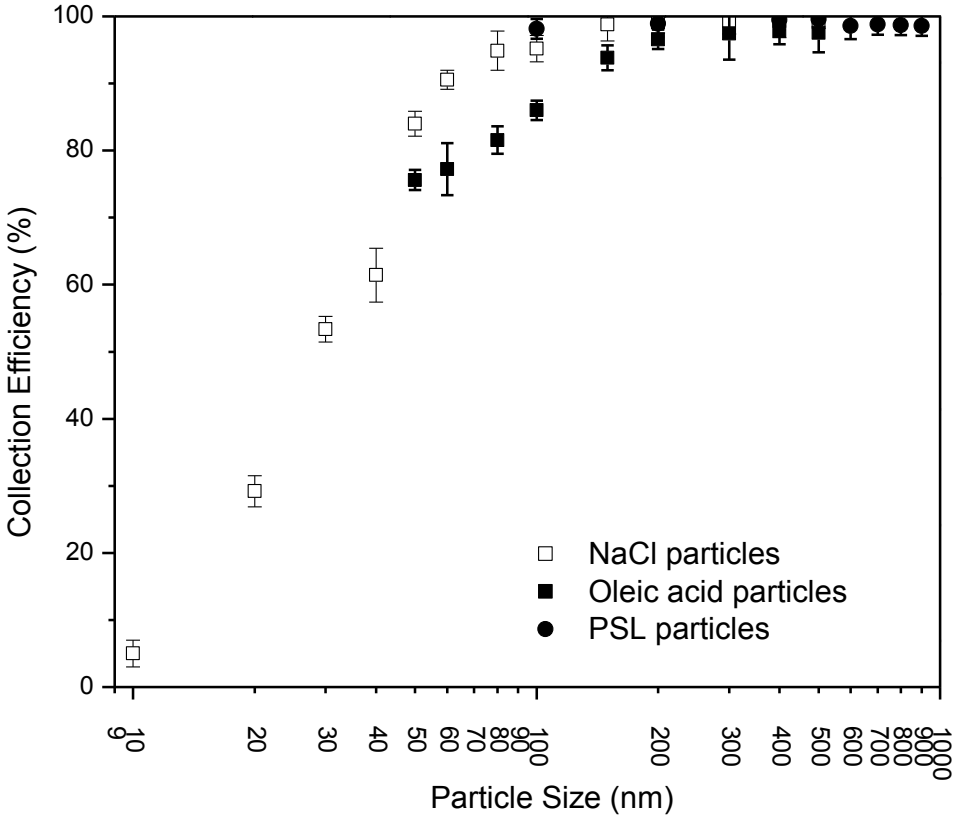

Figure 5.10 Collection efficiencies of NaCl particles, oleic acid particles and PSL particles (aerosol/ion carrier flow rate ratio of 1.0; total flow rate of 1 lpm; collection stage voltage of 4.5 kV)

For oleic acid particles, the collection efficiency of the sampler increased, as the particle size increased as expected. However, the efficiency was higher than 90% at sizes larger than 150 nm, a higher value than those for the cases of NaCl and PSL particles. The collection efficiencies for oleic acid particles were in general lower than those for NaCl particles in the particle size range from 50 to 150 nm.

The trend of a collection efficiency increase with increasing particle size, and the low collection efficiency for oleic acid particles as compared to the cases of NaCl and PSL

particles ranging from 50 to 150 nm can both be explained by the charging efficiency and average charges on particles (shown in Figure 5.11). For comparison, the data for NaCl particles are also re-plotted. The increasing trend of the collection efficiency is due to the increase of charging efficiency with increasing particle size. However, the charging efficiency of an oleic acid particle is lower than that of a NaCl particle in the same size range (shown in Figure 5.11a).

(a)

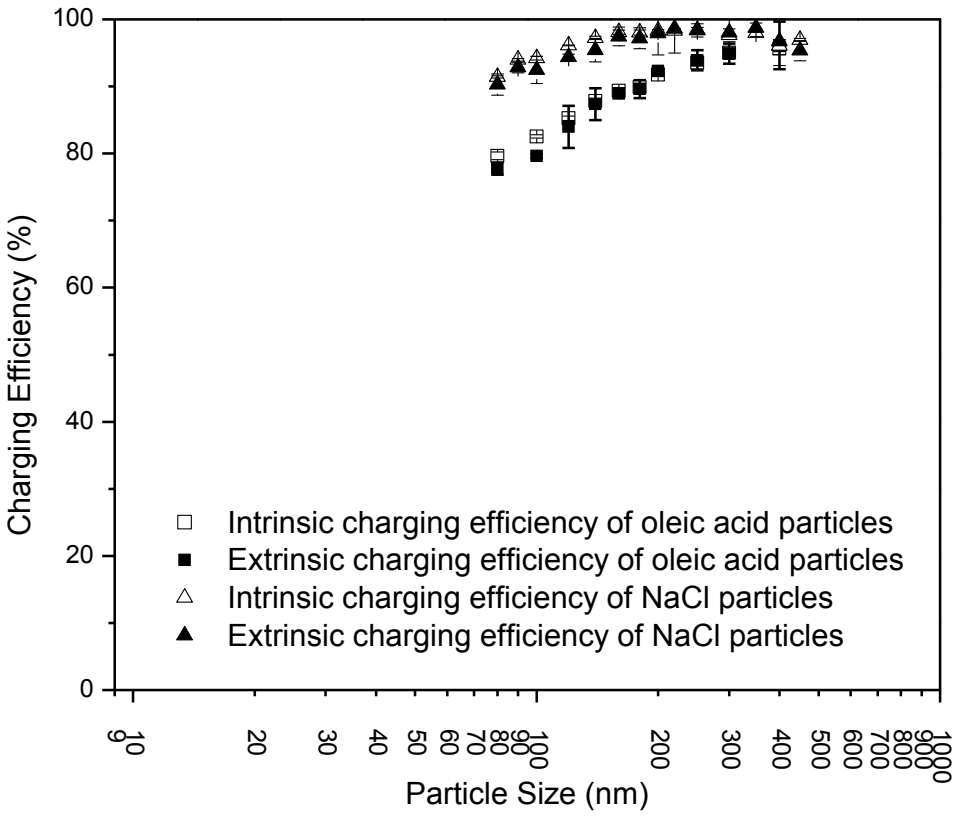

(b)

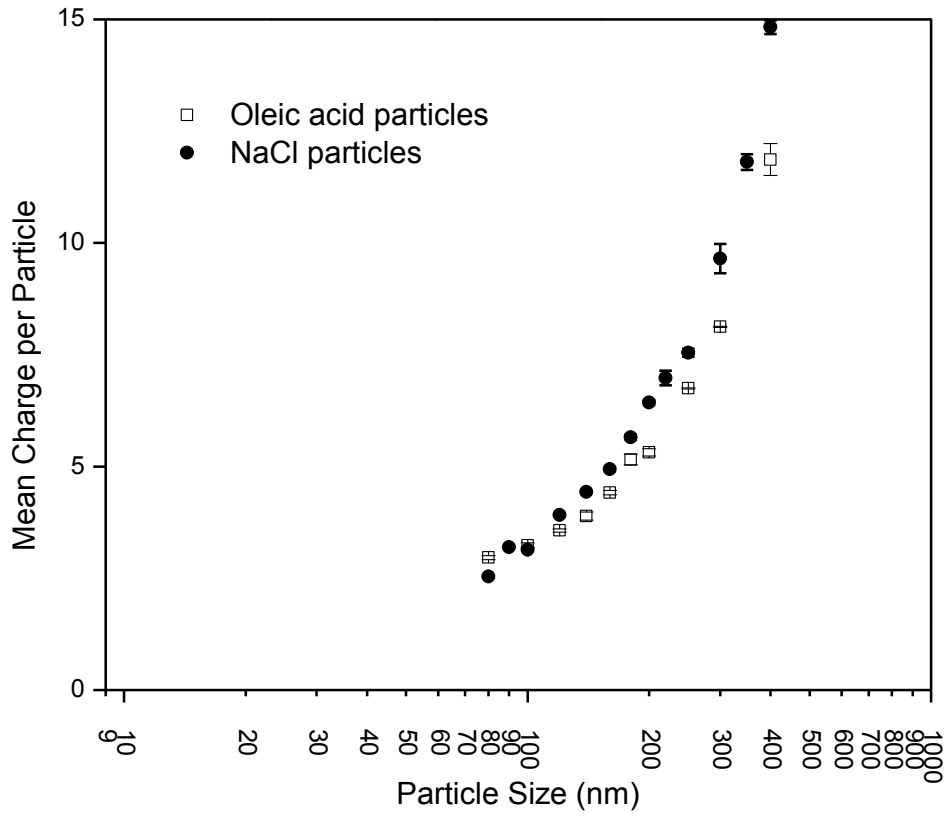

Figure 5.11 (a) Intrinsic and extrinsic charging efficiencies of oleic acid particles and NaCl particles; (b) Average charges of oleic acid particles and NaCl particles (aerosol/ion carrier flow rate ratio of 1.0; total flow rate of 1 lpm)

As shown in Figure 5.11b, the average charges on oleic acid particles are close to those on NaCl particles in the same diameters. Consistent with the finding of Shin et al. (2009), particles made of materials with different dielectric constants had similar mean charge per particle values in unipolar diffusion charging. The similar mean charges per particle for NaCl and oleic acid particles resulted in similar transport behavior in the collection chamber of the studied sampler.

5.5 Conclusions

An electrostatic nanoparticle sampler in a compact package has been developed for offline analysis of nanoparticles via electron microscopy. The prototype sampler basically consists of two chambers: one chamber is for particle charging and the other for particle collection. For charging particles, unipolar ions are produced in a separate compartment via DC corona discharge and carried to the particle charging chamber via a particle-free gas flow. The charging process prevents the corona needle (especially the needle tip) from becoming contaminated by particles. Particles are sampled into the charging chamber of the prototype via the inlet and electrically charged by mixing them with an ion carrier flow (in an opposing flow arrangement). After the electrical charging, particles are directed into the collection chamber via a straight nozzle connecting the two chambers. A nozzle-to-plate configuration is used in the collection chamber for collecting charged particles on the collection stage (i.e., the SEM stub) by a separate electrical field established between the nozzle and collection stage. Particles that escape collection exit the sampler through the outlet.

A parametric study, including the effect of total flow rate, the ratio of the aerosol/ion carrier flow rates, and collection voltage, was performed to optimize the performance of the prototype. The collection efficiency of lab-generated NaCl particles with sizes from 50 nm to 500 nm was measured in this part of the study. The optimal working conditions for the prototype were found to be a total flow rate of 1.0 lpm, an aerosol/ion carrier flow rate ratio of 1.0, and a collection voltage of 4.5 kV. Under the above working conditions, the particle collection efficiency of the sampler varied from 90.5% to 99.3% for particles in the sizes ranging from 50 to 500 nm. Because of the increase in charging efficiency, the particle

collection efficiency of the sampler in general increased as the particle diameter increased. It was further found that, at a total flow rate higher than 3.0 lpm, the sampler's collection efficiency showed a decreasing trend as the particle diameter increased, because of the decrease in particle electrical mobility and particle residence time in the particle charging chamber.

Fluorescence experiments were also performed to characterize the percentage of particles actually collected on the collection stage of the sampler. It was concluded that 57% to 78% of fluorescent sodium particles ranging from 60 to 400 nm were collected on the front surface of the collection stage (i.e., the SEM stub). The remaining particles were either deposited on the inner wall of the collection chamber or exited the sampler.

Monodisperse PSL and oleic acid particles were used to investigate the effect of particle material on the sampler performance. High collection efficiencies of 98.1% to 99.6% for PSL particles with sizes from 100 nm to 900 nm were obtained. For oleic acid particles ranging from 50 to 150 nm, the sampler had lower collection efficiencies (from 75.6% to 93.8%) than for NaCl particles in the same size range. The sampler had comparable collection efficiency (from 96.7% to 97.7%) for oleic acid and NaCl particles larger than 150 nm. The above observation was attributed to the lower charging efficiency for oleic acid particles in the size range from 50 nm to 150 nm and the comparable charging efficiency in the size range from 150 nm to 500 nm, when compared with that in the case of NaCl particles. It was further found that the prototype had a collection efficiency ranging from 5.0% to 83.1% for 10 to 50 nm NaCl particles. For particles in all three test materials, the collection efficiency of the sampler in general increased as the particle diameter increased. This result can be explained

by the low charging efficiency of single digit nanoparticles and the increase of the charging efficiency as the particle size increases.

5.6 References

Al-Jamal, W.T., and K. Kostarelos. 2007. Liposome Nanoparticle Hybrids for Multimodal Diagnostic and Therapeutic Applications. *Nanomedicine* 2:85-98.

Barone, T.L., and Y. Zhu. 2008. The Morphology of Ultrafine Particles on and near Major Freeways. *Atmos. Environ.* 42:6749-6758.

Biswas, P., and C.-Y. Wu. 2005. Nanoparticles and the environment. *J. Air Waste Manage.* 55(6):708-746.

Chen, D.-R., and D.Y.H. Pui. 1995. Numerical and Experimental Studies of Particle Deposition in a Tube with Conical Contraction-Laminar Flow Regime. *J. Aerosol Sci.* 26:563-574.

Chen, D.-R., and D.Y.H. Pui. 1999. A High Efficiency, High Throughput Unipolar Aerosol Charger for Nanoparticles. *J. Nanopart. Res.* 1:115-126.

Dixkens, J., and H. Fissan. 1999. Development of an Electrostatic Precipitator for Off-Line Particle Analysis. *Aerosol Sci. Tech.* 30:438-453.

Fierz, M., R. Kaegi, and H. Burtscher. 2007. Theoretical and Experimental Evaluation of a Portable Electrostatic TEM Sampler. *Aerosol Sci. Tech.* 41:520-528.

Gombocz, E., D. Tietz, S.S. Hurtt, and A. Chrambach. 1987. Polystyrene Latex Particles as Size Standards in Quantitative Agarose Gel Electrophoresis: Application to Three Plant Viruses. *Electrophoresis* 8:261-271.

Hernandez-Sierra, A., F.J. Alguacil, and M. Alonso. 2011. Unipolar Charging of Nanometer

Aerosol Particles in a Corona Ionizer. *J. Aerosol Sci.* 34:733-745.

Hinds, W.C. 1999. Aerosol technology: properties, behavior, and measurement of airborne particles. New York: John Wiley & Sons.

Hinkley, J.T., H.A. Bridgman, B.J.P. Buhre, R.P. Gupta, P.F. Nelson and T.F. Wall. 2008. Semi-Quantitative Characterisation of Ambient Ultrafine Aerosols Resulting from Emissions of Coal Fired Power Stations. *Sci. Total Environ.* 391:104-113.

Ito, K., L. Sun, M.A. Bevan, and R.M. Crooks. 2004. Comparison of Nanoparticle Size and Electrophoretic Mobility Measurements Using a Carbon-Nanotube-Based Coulter Counter, Dynamic Light Scattering, Transmission Electron Microscopy, and Phase Analysis Light Scattering. *Langmuir* 20:6940-6945.

Katz, E., and I. Willner. 2004. Integrated Nanoparticle–Biomolecule Hybrid Systems: Synthesis, Properties, and Applications. *Angew. Chem. Int. Ed.* 43:6042-6108.

Kaupplnen, E.I., and T.A. Pakkanen, 1990. Coal Combustion Aerosols: A Field Study. *Environ. Sci. Tech.* 24:1811-1818.

Kruis, F.E., and H. Fissan. 2001. Nanoparticle Charging in a Twin Hewitt Charger. *J. Nanopart. Res.* 3:39-50.

Laschober, C., S.L. Kaufman, G. Reischl, G. Allmaier, and W.W. Szymanski. 2006. Comparison between an Unipolar Corona Charger and a Polonium-Based Bipolar Neutralizer for the Analysis of Nanosized Particles and Biopolymers. *J. Nanosci. Nanotechno.* 6:1474-1481.

Li, L., and D.-R. Chen. 2011. Performance Study of a DC-Corona-Based Particle Charger for Charge Conditioning. *J. Aerosol Sci.* 42:87-99.

Li, Y., and S.M. Lindsay. 1991. Polystyrene Latex Particles as a Size Calibration for the Atomic Force Microscope. *Rev. Sci. Instrum.* 62:2630-2633.

Li, C., S. Liu, and Y. Zhu. 2010. Determining Ultrafine Particle Collection Efficiency in a Nanometer Aerosol Sampler. *Aerosol Sci. Tech.* 44:1027-1041.

Liu, J. 2005. Scanning Transmission Electron Microscopy and Its Application to the Study of Nanoparticles and Nanoparticle Systems. *J. Electron Microsc.* 54:251-278.

Liu, B.Y.H., and D.Y.H. Pui. 1974. A Submicron Aerosol Standard and the Primary, Absolute Calibration of the Condensation Nuclei Counter. *J. Colloid Interface Sci.* 47:155-171.

Miller, A., F. Garrett, G. King, and C. Sunderman. 2010. A Handheld Electrostatic Precipitator for Sampling Airborne Particles and Nanoparticles. *Aerosol Sci. Tech.* 44:417-427.

Qi, C., D.-R. Chen, and D.Y.H. Pui. 2007. Experimental Study of a New Corona-Based Unipolar Aerosol Charger. *J. Aerosol Sci.* 38:775-792.

Romay, F.J., and D.Y.H. Pui. 1992. On the Combination Coefficient of Positive Ions with Ultrafine Neutral Particles in the Transition and Free-Molecule Regimes. *Aerosol Sci. Tech.* 17:134–147.

H.G., Scheibel, and J. Porstendörfer. 1983. Generation of Monodisperse Ag- and NaCl-

Aerosols with Particle Diameters between 2 and 300 nm. *J. Aerosol Sci.* 14:113-126.

Shin, W.G., D.Y.H. Pui, H. Fissan, S. Neumann, and A. Trampe. 2007. Calibration and Numerical Simulation of Nanoparticle Surface Area Monitor (TSI Model 3550 NSAM). *J. Nanopart. Res.* 9:61-69.

Shin, W.G., C. Qi, J. Wang, H. Fissan, and D.Y.H. Pui. 2009. The Effect of Dielectric Constant of Materials on Unipolar Diffusion Charging of Nanoparticles. *J. Aerosol Sci.* 40:463-468.

Stommel, Y.G., and U. Riebel. 2005. A Corona-Discharge-Based Aerosol Neutralizer Designed for Use with the SMPS-System. *J. Electrostat.* 63:917-921.

Wang, S.C., and R.C. Flagan. 1990. Scanning Electrical Mobility Spectrometer. *Aerosol Sci. Tech.* 13:230-240.

Warheit, D.B. 2004. Nanoparticles: Health Impacts. *Mater. Today* 7:32-35.

CHAPTER 6. CHARACTERIZATION OF SUBMICROMETER PARTICLES FROM SAWDUST/COAL CO-FIRING IN A DROP-TUBE FURNACE

The results of this chapter will be compiled as a paper for submission to Bioresource Technology (authors: He Jing, Xiaofei Wang, Sijia Li, Brent J. Williams, and Pratim Biswas).

Abstract

Co-firing of coal with biomass for electricity generation is a promising alternative of coal combustion, considering its economic and environmental benefits. However, many aspects of co-firing are still not well known, for example, the fine particle formation from co-firing. In this study, the submicrometer particles from co-firing of coal with sawdust in a drop-tube furnace were studied. Particle size distributions, elemental compositions, and organic compositions of particles were analyzed in detail. Results show that coal contributed more in the submicrometer particle formation than sawdust. With higher amount of sawdust in the blended fuel, there were less fine particles generated. It was also found that high sulfur coal resulted in more particle formations during the co-firing, which subsequently resulted in more organics in the particles. Higher combustion temperature promoted the submicrometer particle formation and also resulted in higher organic concentrations in the particles. With higher moisture content in the sawdust, the total number concentration of particles decreased, however, the particle growth was enhanced and the particle concentrations in the size range of 80 nm to 500 nm increased. The organic particle concentration was also higher with higher moisture, indicating that most of the organics were in the larger particles (> 80 nm).

6.1 Introduction

Pulverized coal combustion is a major source for electricity generation in U.S.. In 2014, 38.7% of the electricity is provided by coal-fired power plants (Hankey 2015). Meanwhile, coal combustion has a significant environmental impact due to its pollution emissions. In order to control the air pollution emissions, recently USEPA has finalized several rules and standards to reduce power plant emissions, including Cross-State Air Pollution Rule (CSAPR) aiming to reduce SO_2 emissions by 73% and NO_x emissions by 54% from 2005 levels in the CSAPR region, and Mercury and Air Toxics Standards (MATS), which will result in reducing 90% of mercury emissions, 88% of acid gas emissions, 41% of SO_2 emissions beyond the reductions expected from CSAPR, as well as reduction of non-mercury metals and dioxins and furans emissions. Nowadays, CO_2, the primary greenhouse gas, is considered as a gas pollutant as well. Fossil fuel-fired power plants are the largest source of U.S. CO_2 emissions. In order to reduce the CO_2 emissions, currently EPA is also developing carbon pollution standards for power plants under the Clean Air Act.

Co-firing of coal and biomass for electric generation is an attractive biomass-to-energy approach because of its economic and environmental benefits. It has been demonstrated, tested, and proved in all boiler types commonly used by electric utilities (Dai et al., 2008; Sami et al., 2001). Co-firing can help reduce the pollutant emissions. Firstly, most biomass fuels have low sulfur contents; besides, alkaline ash from biomass combustion can capture SO_2, so co-firing generates less SO_2 than coal combustion. Secondly, most of the nitrogen in biomass is converted into NH radicals, which reacts with NO; meanwhile, woody biomass contains lower amount of nitrogen than coal, thus, co-firing reduces NO_x emissions. It will

reduce the mercury emissions as well due to the low mercury content in the biomass. Moreover, biomass is considered CO_2-neutral, so co-firing directly reduces CO_2 emissions from power plants (Saidur et al., 2011; Sami et al., 2001; Williams et al., 2012).

As other fossil fuel combustion process, co-firing also generates fly ash particles. Among them, the submicrometer particles are of special interests because they could penetrate into the alveolar regions of the lungs upon inhalation, thus have more significant adverse health effects (Biswas and Wu, 2005). Previously researches have been done on characterization of submicrometer particles from co-firing of coal with orujillo (Jiménez and Ballester, 2005), switchgrass (Blevins and Cauley, 2005), rice husk (Chao et al., 2008; Mantananont et al., 2012), bamboo (Chao et al., 2008), and bagasse (Mantananont et al., 2012). However, more studies are needed, because the compositions of different types of biomass vary (Sami et al., 2001; Dai et al., 2008; Williams et al., 2012; Saidur et al., 2011) and it will influence the physical and chemical properties of the emitted submicrometer ash particles. Among the previous studies, only one has looked into the chemical composition of submicrometer ash particles (Jiménez and Ballester, 2005). Moreover, the organic composition of submicrometer particles has not been investigated.

Sawdust is a major by-product of cutting, grinding, drilling, sanding, or pulverizing wood. Its abundance and heat value (commonly 8440-18991 kj/kg) (Bartok 2004) make sawdust a good biomass candidate for the co-firing. It has been proven experimentally that co-firing of coal and sawdust may have lower NO_x emission than the dedicated coal combustion (Skeen et al., 2010), as well as less SO_2 (Kazagic and Smajevic, 2009; Zuwala and Sciazko, 2010) and CO (Zuwala and Sciazko, 2010) emission. Besides, the sawdust could enhance ignition

characteristics of low rank coals (Gani et al., 2005). Furthermore, an investigation shows that co-firing of coal with pine-sawdust did not have operational problems due to slagging and fouling (Abreu et al., 2010). Sawdust may be a good option as biomass fuel in the co-firing with coal in the future and currently studies on improve the co-firing performance is undergoing (Sarkar et al., 2014). Considering the potential developments and applications of co-firing of coal with sawdust, the study on submicrometer particles from this co-combustion process is urgently needed.

In this study, the submicrometer particles from coal/sawdust co-firing in a drop-tube furnace were characterized, including the particle size distribution, elemental analysis, and organic composition analysis. Both low sulfur and high sulfur content coals were used. The effects of combustion temperature and moisture content in sawdust on the particle formation were also studied.

6.2 Experimental Section

6.2.1 Drop-tube furnace system

The drop-tube furnace system for coal/sawdust combustion is shown in Figure 6.1. The drop-tube furnace consists of a furnace (Lindberg/Blue M Model HTF55342C, ThermoElectron Corp., USA) and an alumina tube (5.72 cm ID, 121.92 cm long) inside it. The coal/sawdust blend was fed by a coal feeder with a mass flow rate of 2.5 g/hr. A total of 3 LPM of air was introduced into the furnace as oxidizer, in which 0.5 LPM of air passed through the coal feeder and carried the coal/sawdust blend, and the other 2.5 LPM was introduced directly into

the furnace. Downstream the furnace, 5 LPM air was introduced to dilute the flue gas. A cascade impactor (Mark III, Pollution Control System Corp, Seattle, WA) was used to remove the particles with diameter larger than 1 μm.

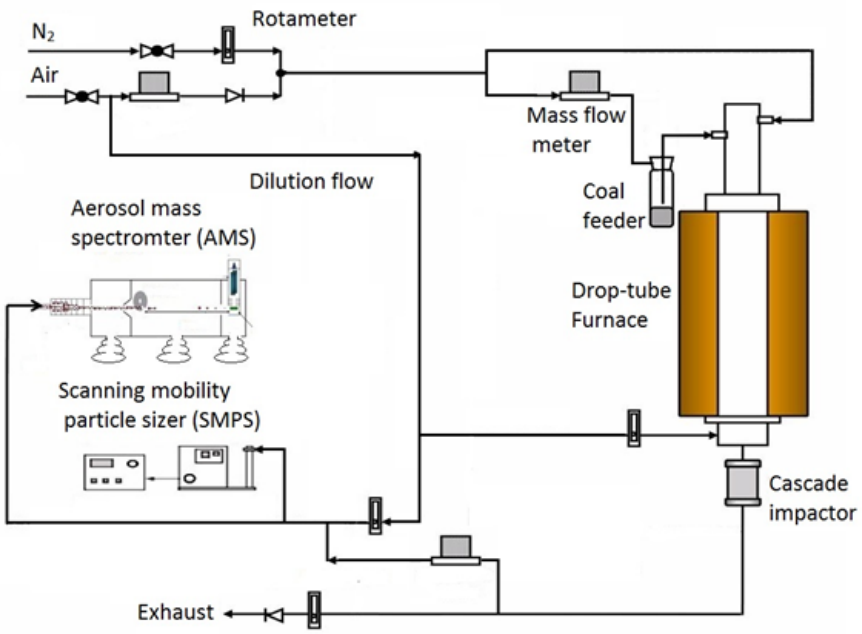

Figure 6.1 Schematic of the drop-tube furnace system and particulate matter measurement instruments

6.2.2 Particle characterization methods

The on-line instruments are also shown in Figure 6.1. The size distributions of submicrometer fly ash particles were measured with a scanning mobility particle sizer (SMPS, TSI Inc., Shoreview, MN, USA). For elemental analysis, the particle samples were collected on Teflon filters and then analyzed with X-ray fluorescence (XRF) offline.

A high-resolution time-of-flight aerosol mass spectrometer (HR-Tof-AMS, Aerodyne Research, MA) was used to characterize the organic compositions of particles. Its operation

mechanism can be summarized as: during the measurements, particles were introduced in the instrument through an aerodynamic lens, which focus the particles into a narrow beam, and the sizes of particles were determined by their velocities across a time of flight chamber at the exit of the lens. The particles were then impacted on a 600 ^{o}C vaporizer where their non-fraction fraction got vaporized. After that, the vapors were immediately ionized with electron impact ionization and analyzed by time-of-flight mass spectrometry. More detailed description of this instrument could be found in previous reports (Allan et al., 2003; Canagaratna et al., 2007; DeCarlo et al., 2006; Jimenez et al. 2003).

6.2.3 Properties of coal and sawdust

Two types of coal are used in this study, including the PRB (Powder River Basin) sub-bituminous coal and Illinois No.6 high sulfur bituminous coal. The proximate and ultimate analysis of coal and sawdust are shown in Table 6.1. The coal and biomass were pulverized into particles with sizes smaller than 45 μm before use. For the blends samples, the coal and sawdust were well mixed with a shaker before use.

Table 6.1 Proximate and ultimate analysis of coals and sawdust

	Illinois No. 6 coal	PRB coal	Sawdust
Proximate analysis (%wt)			
Volatile matter[1]	42	48.3	81.1
Fixed carbon[1]	48	42.9	16.55
Ash[1]	10	8.0	1.03
Moisture[2]	13.5	27.7	9.0
Ultimate analysis (%wt)			
Carbon	71	67.3	49.55
Nitrogen	1.3	0.96	0.16
Hydrogen	5	4.58	5.70
Oxygen	9.13	19.9	N/A
Sulfur	3.47	0.57	0.023
Chlorine	0.11	0.01	N/A
Fluorine	N/A	0.796	N/A

[1]Dry weight basis

[2]As-received basis

6.2.4 Experimental design

This study was conducted in four parts. Firstly, the chemical compositions and size distributions of submicrometer particles from PRB coal/sawdust co-firing were characterized; then, Illinois No.6 coal was used instead of PRB coal to investigate the effect of using a high

sulfur coal on particle formation during co-firing; thirdly, size distributions and organic compositions of particles generated under three different combustion temperatures were compared to study the temperature effect; lastly, the effect of moisture content in the sawdust on submicrometer particle formation was evaluated. The detailed experimental design is shown in Table 6.2. The selected blend ratios were 15% biomass and 30% biomass because they are in the best range for blended coal/biomass fuel in terms of maximum energy output with minimum pollutant emissions (Chao et al., 2008).

Table 6.2 Summary of experimental conditions

Set	Objective	Fuel	Moisture content in sawdust	Furnace set temperature	Measurements
I	To characterize the submicrometer particles from co-firing in general	PRB coal/sawdust (0/100, 70/30, 85/15, 100/0)	0	1376 K	Particle size distribution (SMPS); elemental analysis (XRF); organics concentrations (AMS)
II	To evaluate the effect of sulfur in coal on submicrometer particle formation	Illinois No.6 coal/sawdust (0/100, 70/30, 85/15, 100/0)	0	1376 K	SMPS; AMS
III	To evaluate the effect of combustion temperature on submicrometer particle formation	PRB coal/sawdust (85/15)	0	1376 K; 1326 K; 1276 K	SMPS; AMS
IV	To evaluate the effect of combustion temperature on submicrometer particle formation	PRB coal/sawdust (85/15)	0, 20%, 40%	1376 K	SMPS; AMS

6.3 Results and Discussion

6.3.1 Characterization of submicormeter particle formation from PRB coal/sawdust co-firing

The size distributions of submicrometer particles from co-firing (15% sawdust and 30% sawdust), dedicated PRB coal combustion, and sawdust combustion are shown in Figure 6.2a. They all had a unimodal distribution, because they were formed through a pathway of nucleation/condensation of volatilized mineral matter. This pathway is well-known for coal combustion (Flagan 1978; Xu et al., 2011; Zhuang and Biswas, 2001; Suriyawong et al., 2006; Wang et al., 2013a), and there is a general agreement on the fact that the formation of fine particles from biomass combustion follows the same pathway (Bryers 1996, Jiménez and Ballester 2005). The size distribution of 15% sawdust case had a peak at 43 nm, and the peak size of the distribution of 30% sawdust case was 53 nm. Generally, with increasing sawdust content in the fuel, fewer particles were formed. It indicates that there were less volatilized minerals in sawdust than in PRB coal (Xu et al., 2011). Elemental analysis results in Figure 6.2b are also good support to this point. The elemental composition of the fine particles from co-firing was similar to that of the particles from coal combustion, and particles from co-firing did not have high alkaline metal content (calcium and potassium from the sawdust combustion) as particles from biomass combustion. Thus, coal was the main contributor of submicrometer particles in this case.

(a)

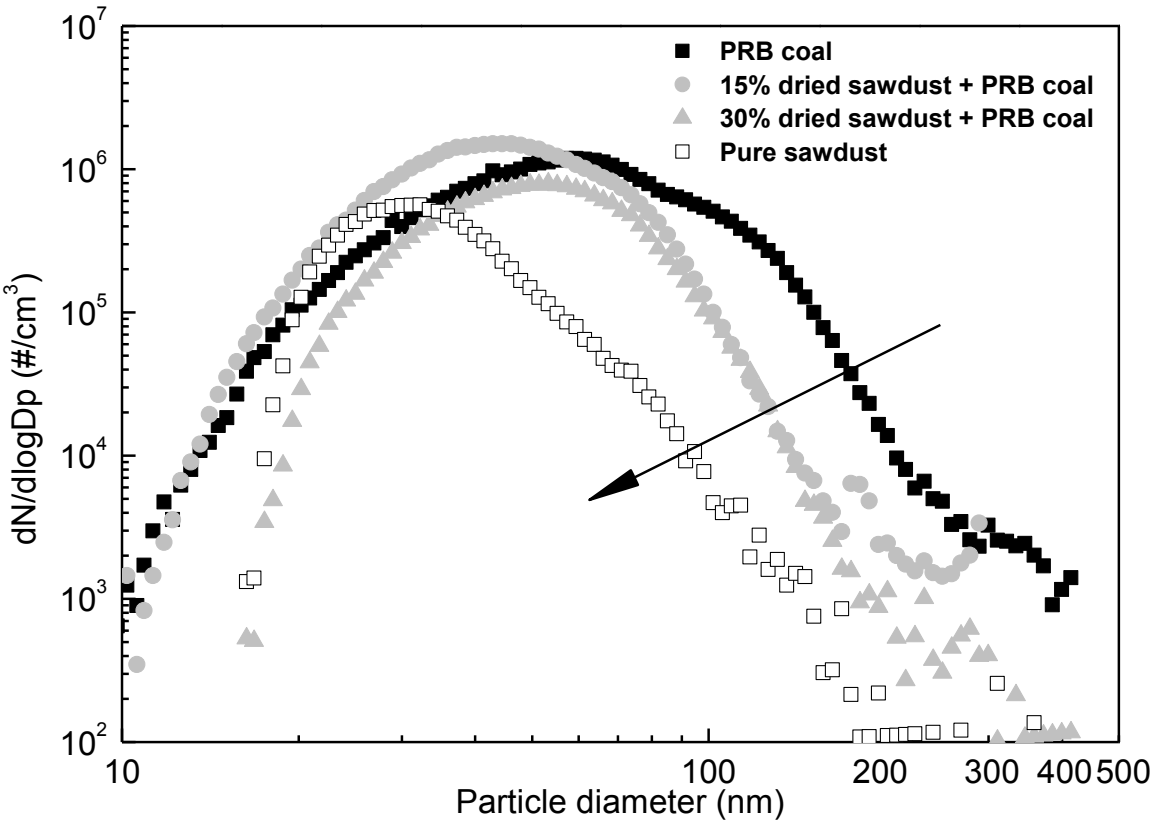
PRB coal
15% dried sawdust + PRB coal
30% dried sawdust + PRB coal
Pure sawdust
dN/dlogDp (#/cm3)
Particle diameter (nm)
10
100
200
300
400
500

(b)

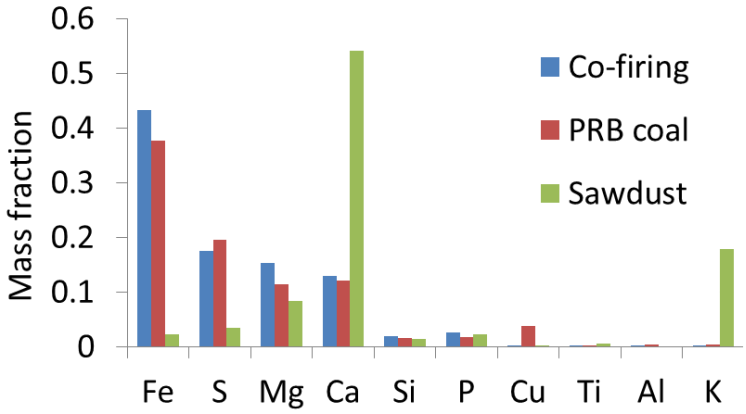
Co-firing
PRB coal
Sawdust
Mass fraction
0.6
0.5
0.4
0.3
0.2
0.1
0
Fe
S
Mg
Ca
Si
P
Cu
Ti
Al
K

(c)

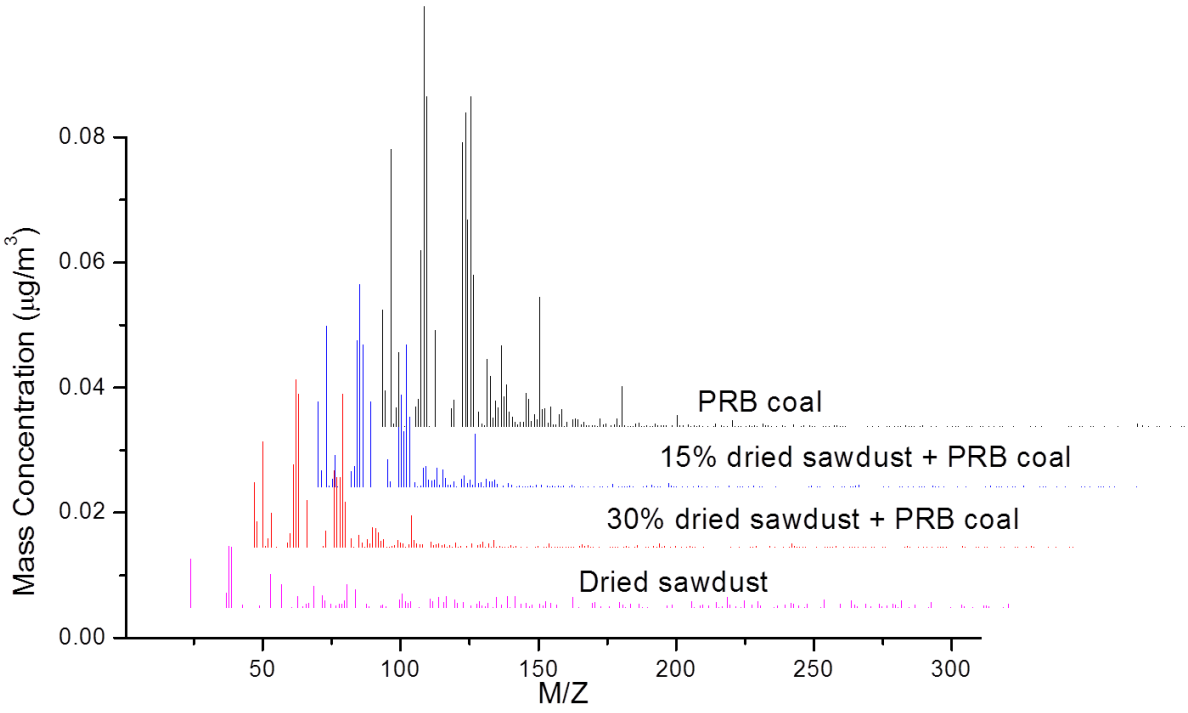

Figure 6.2 Characterizations of particles from co-firing of PRB coal with sawdust, dedicated coal and sawdust combustion: (a) size distribution; (b) elemental analysis; (c) average mass spectrum

In previous co-firing studies, it was found that orujillo, rice husk, and bamboo contributed more than coal in submicrometer formation (Jiménez and Ballester, 2005; Chao et al., 2008); switchgrass combustion dominated the particles formation in the range between 10 nm to 150 nm (Blevins and Cauley, 2005). Compared to them, the sawdust used in this study is a better biofuel for co-firing application in terms of submicrometer particle emissions. Moreover, the proximate analysis in Table 6.1 shows that the sawdust has a very low ash content, which results in low total ash production.

Although the main components of submicrometer particles are inorganic substances (Linak and Wendt, 1994; Jiménez and Ballester, 2005), it has been found that there are organics in fine particles from both biomass combustion (Hays et al., 2002) and pulverized coal combustion (Wang et al., 2013b; Wang et al., 2015). The currently proposed mechanism organic aerosol formation from coal combustion is shown in Figure 1.2. Coal combustion usually occurs in three steps: (a) pyrolysis of coal; (b) burning of tar; and (c) burning of char (Warnatz 2006). A small fraction of organic volatiles from coal pyrolysis are not oxidized or just partially oxidized and absorbed by the inorganic ash particles, resulting in presence of organic parts in the submicrometer particles (Wang et al., 2013b; Wang et al. 2015). The organic aerosol formation from biomass combustion is expected to occur in the same route.

The AMS organic mass spectra of submicrometer particles from co-firing, and dedicated PRB coal and sawdust combustion are shown in Figure 6.2c. Many significant organic peaks (such as m/z 43, 44, 55, 57, and 69) are observed from the co-firing samples. The large peak at m/z 44 indicates the presence of carboxylic acids, and the peak at m/z 69 indicates aromatic compounds (Dall'Osto and Harrison, 2012). They are two major organic compounds in the submicrometer particles from co-firing. With higher sawdust mixing ratio, organic concentration is lower. It seems contradictory to the fact that sawdust has much higher volatile matter (VM) content than PRB coal. However, the reaction characteristics time of VM played a more important role than VM concentration here, which resulted in a reduction of particle organic concentration when sawdust mixing ratio increased. The VM combustion time scale in biomass was in the order of a few milliseconds while coal took a few seconds to finish the combustion (Sami et al., 2001). Thus the VM from sawdust will be combusted

more completely than VM form coal during the same residence time (~62.6 seconds for the studied drop-tube furnace system). Previous study has also showed that biomass could reduce the PAH concentration in the fly ash particles (Chao et al., 2008).

6.3.2 Characterization of submicormeter particle formation from Illinois No.6 coal/sawdust co-firing

In this section, Illinois No.6 coal was used in the co-firing with sawdust to investigate the effect of sulfur content in coal on submicrometer particles formation during co-firing. The particle size distributions for the cases in Illinois No.6 coal co-firing study are shown in Figure 6.3a. The particle concentrations from co-firing were much higher than when PRB coal was used (Figure 6.2a), because Illinois No.6 coal has a higher sulfur content (3.47% compared to 0.57% in PRB coal, as shown in Table 6.1) and the combustion produced a large amount of sulfate particles. When PRB coal was used, the concentration of particles from co-firing was much lower than that from dedicated coal combustion for the 80 nm to 500 nm size range. However, in the Illinois No.6 coal cases, particle concentrations in that range were almost the same for co-firing and dedicated coal combustion. Previous studies have hinted that the relatively increase of particle concentrations from co-firing resulted from the reaction between the alkali metal species and SO_2 in the flue gas (Christensen et al., 1998; Christensen and Livbjerg, 2000; Iisa et al., 1999; Jiménez and Ballester, 2005). Burning of high sulfur Illinois No.6 coal resulted in high SO_2 concentration. The high SO_2 concentration resulted in higher extent sulfation reactions of alkali chlorides and hydroxides (calcium and potassium species in the sawdust case), which were mainly from sawdust.

(a)

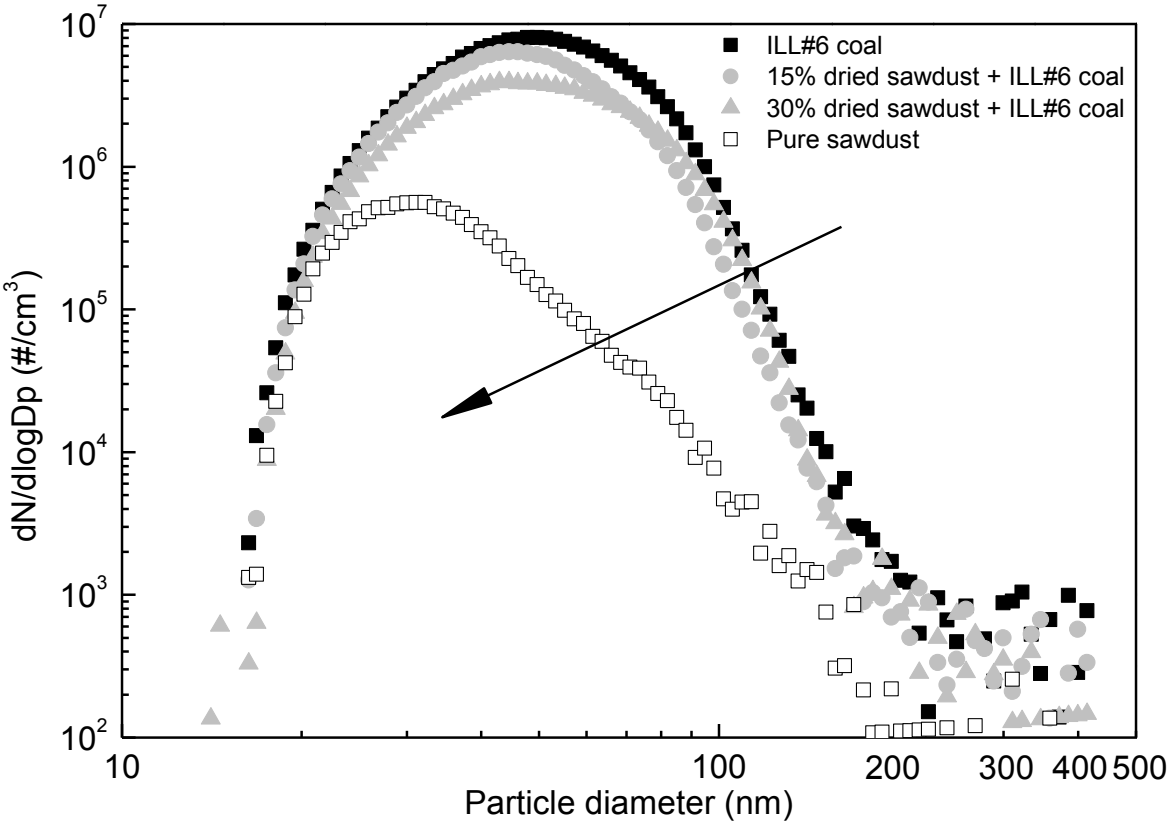
ILL#6 coal
15% dried sawdust + ILL#6 coal
30% dried sawdust + ILL#6 coal
Pure sawdust
dN/dlogDp (#/cm3)
Particle diameter (nm)
10^7
10^6
10^5
10^4
10^3
10^2
10
100
200
300
400
500

(b)

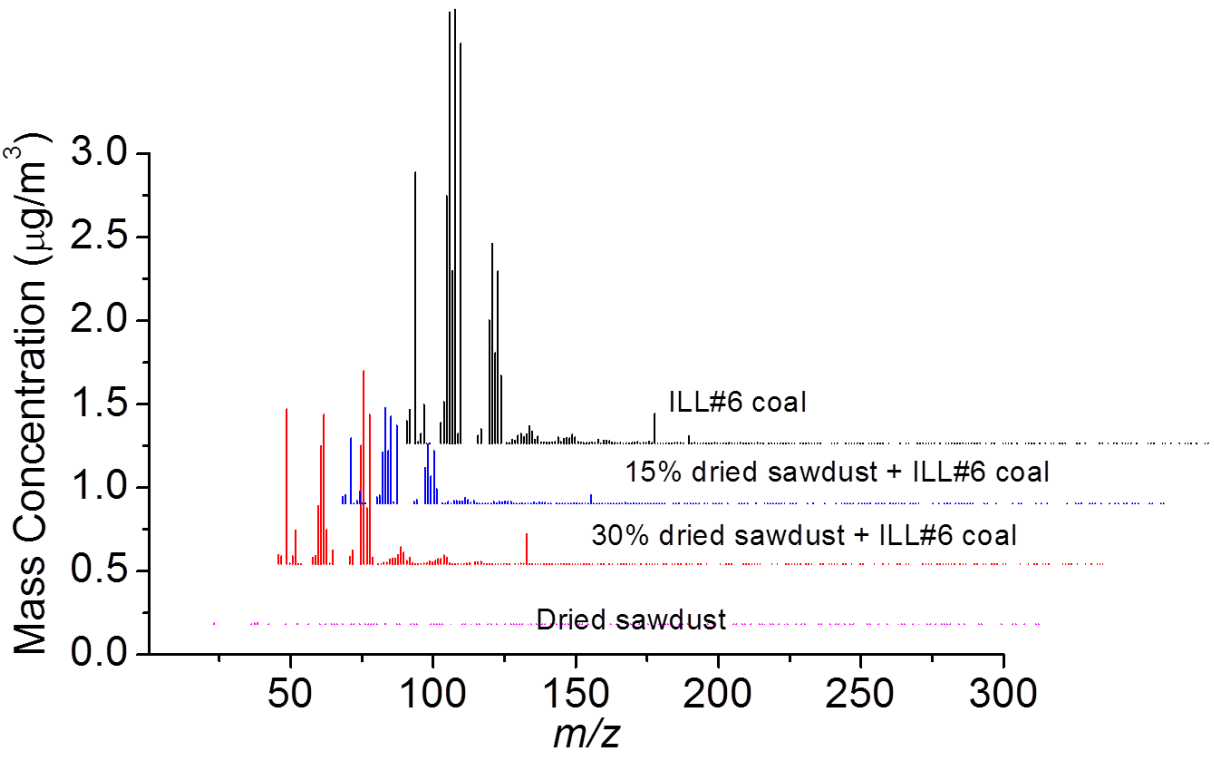

Figure 6.3 Characterizations of particles from co-firing of Illinois No.6 coal with sawdust, dedicated coal and sawdust combustion: (a) size distribution; (b) average mass spectrum

The organic particle concentrations from sawdust/Illinois No.6 co-firing (Figure 6.3b) were much higher than those from sawdust/PRB coal co-firing (Figure 6.2c) as well (almost two orders of magnitudes higher). This is because the organic particle formation is closely correlated with the inorganic particle formation, as shown in Figure 1.2. Firstly, total surface area of particles, which is determined by the total amount of inorganic compositions in the particles, greatly influences how much volatile organics absorbs on the particles; secondly, the inorganic compounds in the particles can protect organics in the particles from further oxidation (Wang et al., 2013b; Wang et al., 2015). Thus higher amount of inorganic particles from co-firing of sawdust/Illinois No.6 resulted in a high concentration of organic aerosols.

The concentrations of organics from co-firing were still lower than those from the dedicated coal combustion. However, unlike in the co-firing of PRB coal with sawdust (Figure 6.2c), more organic aerosols were formed in the 30% sawdust case than in the 15% sawdust case. It is hypothesized that submicrometer particles grew more rapidly in the co-firing of Illinois No.6 coal with sawdust, which provided better protection to organic matters that were absorbed on the particles and prevent them from being further oxidized; in the 30% sawdust case, more VM was generated and absorbed on the particles, which led to a higher organic concentrations in the particles from the co-combustion.

6.3.3 Effects of temperature on submicrometer particles formation during co-firing

In order to evaluate the effect of combustion temperature on particle formation, 15% sawdust and 85% PRB coal were co-fired under 1276 K, 1326 K, and 1376 K, respectively. Figure 6.4a shows that with lower combustion temperature, particle formation was suppressed, because lower temperature resulted in less quantity of metal species that were volatilized, which subsequently engendered less fine particle formation (Zhang et al., 2006; Zhang et al., 2007; Sui et al. 2007).

(a)

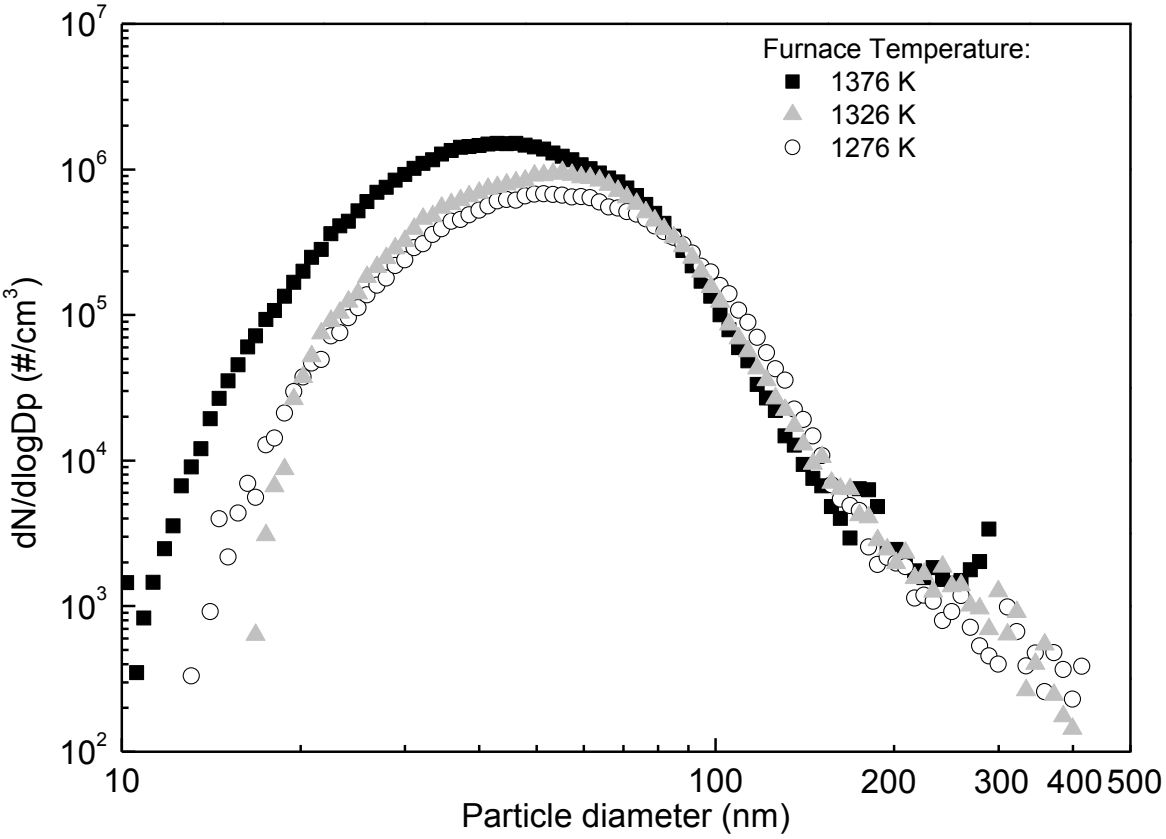
Furnace Temperature:
1376 K
1326 K
1276 K
dN/dlogDp (#/cm3)
Particle diameter (nm)
10
100
200
300
400
500

(b)

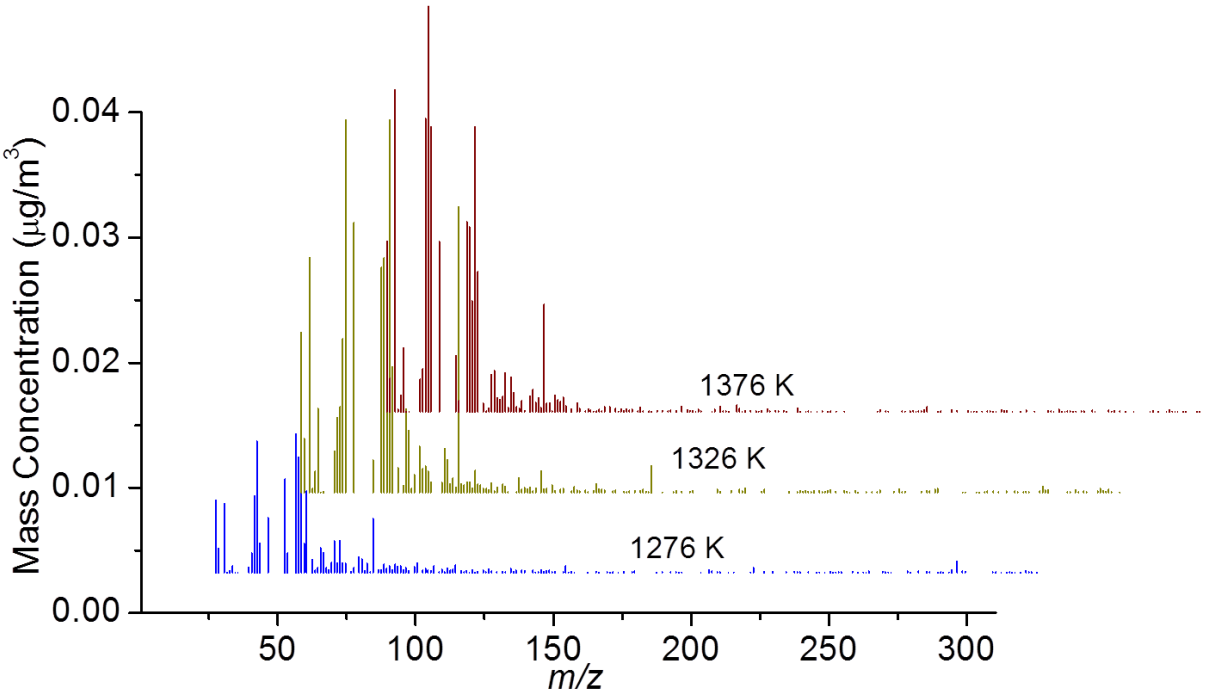

Figure 6.4 Characterizations of particles from co-firing of PRB coal with sawdust (mass ratio: 85/15) under various temperatures: (a) size distribution; (b) average mass spectrum

Influenced by the suppressed formation of fine particles, the concentration of organics in particles decreased under lower temperature, as shown in Figure 6.4b. It should be noted that a lower combustion temperature also slows down oxidation of VM, which results in an increase of organic concentration. However, the AMS mass spectra results indicate that this factor was less important than the influence of total fine particle formation in this case.

6.3.4 Effects of moisture in the sawdust on submicrometer particle formation during co-firing

Typically fresh biomass contains significant amount of moisture, present as bound and free water, and even after considerable drying the moisture content can still be high (eg. 15-20%

for woods) (Williams et al., 2012). Biomass moisture content plays a significant role in the combustion process. In this section, the effect of moisture in the sawdust on fine particle formation was evaluated.

The size distributions of fine particles from co-firing with sawdust with different moisture contents are shown in Figure 6.5a. Particle concentrations were higher in no moisture case for 10 nm to 80 nm particles, while for particles larger than 80 nm particles, the number concentrations were higher in 20% and 40% moisture case than in no moisture case. Two factors may contribute to this result. Firstly, with high moisture content, part of the heat was transferred to the latent heat of vaporization during combustion and hence overall temperature was reduced (Chao et al., 2008), which resulted in less vaporization of metal species from the fuel (Zhang et al., 2006; Zhang et al., 2007; Sui et al., 2007). This explains why the total particle number concentration and peak concentration were much lower in the high moisture cases than in 0% moisture content case. Secondly, high moisture content in the sawdust caused high water content in the gas phase. The water vapor could low down the energy barrier to convert vapors of metal species into submicrometer particles, thus greatly enhance the growth of nuclei (Kulmala and Laaksonen, 1990). This factor resulted in a shift of particle size distribution to the larger particle side with more moisture content, as shown in Figure 5a. The size distributions were similar for 20% and 40% moisture cases. It may be because an equilibrium condition was researched.

(a)

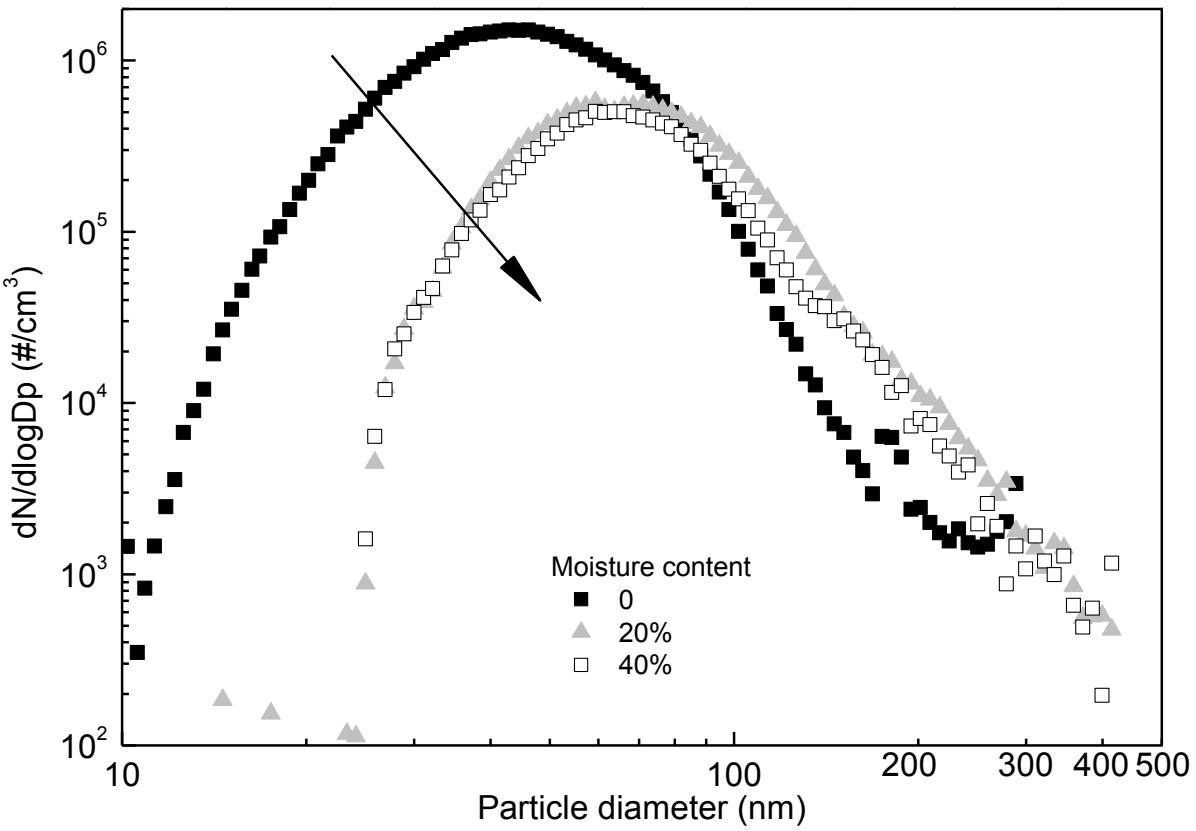

(b)

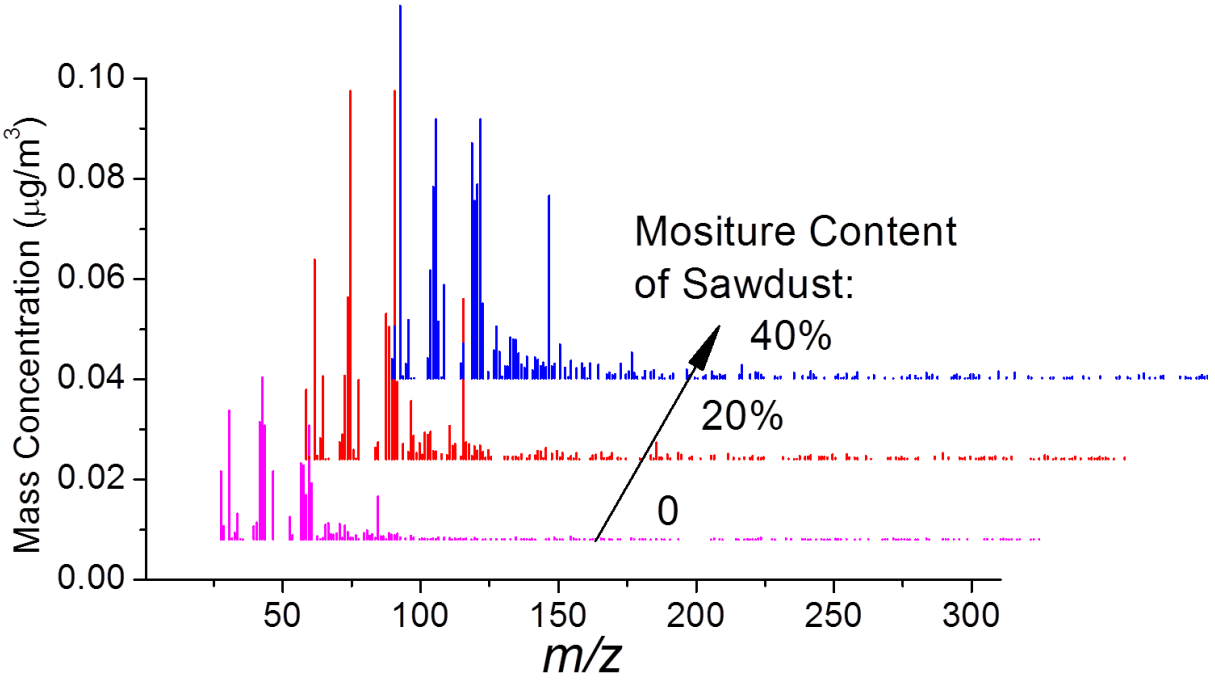

Figure 6.5 Characterizations of particles from co-firing of PRB coal with sawdust (mass ratio: 85/15) under various sawdust moisture contents: (a) size distribution; (b) average mass spectrum

Figure 6.5b shows that when moisture content increased, the organic mass concentration increased as well. Comparing this result with the size distributions in Figure 6.5a, we could imply that larger particles played a more important role in the formation of organic particles.

6.4 Conclusions

In this study, the size distributions and chemical compositions of submicrometer particles from co-firing of sawdust and coal in a drop-tube furnace were studied, with a focus on elucidating the formation of the organic part of those fine particles. The fine particles had a

unimodal size distribution, implying a formation pathway of nucleation/condensation of volatilized mineral matter. With higher amount of sawdust in the blended fuel, there were less fine particles generated. At the same time, particles from co-firing had an elemental composition more similar to that of particles from coal combustion. It indicates that the sawdust contributed less in submicrometer particle formation since the sawdust had lower content of volatilized mineral. AMS analysis shows that carboxylic acids and aromatic compounds were two major organic compounds in the submicrometer particles from co-firing. With higher sawdust mixing ratio in the fuel, the organic concentrations were lower, due to a smaller reaction characteristics time of volatile matters from sawdust.

With higher sulfur content in the coal, the concentration of fine particles increased because of formation of sulfates. This increase also promoted the organic particle formations due to an increase of organic absorption on the particles and better protection of organics from being oxidized. Higher combustion temperature resulted in high concentrations of submicrometer particles and organics. Higher moisture content resulted in lower overall particle concentrations but a higher organic particle concentration, which may be related with the higher particle concentrations in the larger (> 80 nm) particle size range.

6.5 References

Abreu, P., C. Casaca, and M. Costa. 2010. Ash deposition during the co-firing of bituminous coal with pine sawdust and olive stones in a laboratory furnace. *Fuel* 89(12):4040-4048.

Allan, J.D., J.L. Jimenez, P.I. Williams, M.R. Alfarra, K.N. Bower, J.T. Jayne, H. Coe, and D.R. Worsnop. 2003. Quantitative sampling using an Aerodyne aerosol mass spectrometer 1. Techniques of data interpretation and error analysis. *J. Geophys. Res. Atmos.* 108(D3).

Bartok, J.W. 2004. Approximate Heating Value of Common Fuels. University of Connecticut, USA.

Biswas, P., and C.-Y. Wu. 2005. Nanoparticles and the environment. *J. Air Waste Manag.* 55 (6):708-746.

Blevins, L.G., and T.H. Cauley. 2005. Fine particulate formation during switchgrass/coal cofiring. *J. Eng. Gas Turb. Power* 127(3):457-463.

Bryers, R.W. 1996. Fireside slagging, fouling, and high-temperature corrosion of heat-transfer surface due to impurities in steam-raising fuels. *Prog. Energ. Combust.* 22(1):29-120.

Canagaratna, M.R., J.T. Jayne, J.L. Jimenez, J.D. Allan, M.R. Alfarra, Q. Zhang, T.B. Onasch, F. Drewnick, H. Coe, and A. Middlebrook. 2007. Chemical and microphysical characterization of ambient aerosols with the aerodyne aerosol mass

spectrometer. *Mass Spectrom. Rev*. 26(2):185-222.

Chao, C.Y.H., P.C.W. Kwong, J.H. Wang, C.W. Cheung, and G. Kendall. 2008. Co-firing coal with rice husk and bamboo and the impact on particulate matters and associated polycyclic aromatic hydrocarbon emissions. *Bioresource Technol.* 99(1):83-93.

Christensen, K.A., and H. Livbjerg. 2000. A plug flow model for chemical reactions and aerosol nucleation and growth in an alkali-containing flue gas. *Aerosol Sci. Tech.* 33(6):470-489.

Christensen, K.A., M. Stenholm, and H. Livbjerg. 1998. The formation of submicron aerosol particles, HCl and SO_2 in straw-fired boilers. *J. Aerosol Sci.* 29(4):421-444.

Dai, J., S. Sokhansanj, J.R. Grace, X. Bi, C.J. Lim, and S. Melin. 2008. Overview and some issues related to co−firing biomass and coal. *Can. J. Chem. Eng.* 86(3):367-386.

Dall'Osto, M., and R.M. Harrison. 2012. Urban organic aerosols measured by single particle mass spectrometry in the megacity of London. *Atmos. Chem. Phys.* 12(9):4127-4142.

DeCarlo, P.F., J.R. Kimmel, A. Trimborn, M.J. Northway, J.T. Jayne, A.C. Aiken, M. Gonin, K. Fuhrer, T. Horvath, and K.S. Docherty. 2006. Field-deployable, high-resolution, time-of-flight aerosol mass spectrometer. *Anal. Chem.* 78(24):8281-8289.

Flagan, R.C., and S.K. Friedlander. 1978. Particle formation in pulverized coal combustion-a review. In *Recent Developments in Aerosol Science*, edited by David T Shaw. New York: Wiley.

Gani, A., K. Morishita, K. Nishikawa, and I. Naruse. 2005. Characteristics of co-combustion

of low-rank coal with biomass. *Energ. Fuel.* 19(4):1652-1659.

Hankey, R. 2015. Electric Power Monthly with Data for January 2015. U.S. Energy Information Administration.

Hays, M.D., C.D. Geron, K.J. Linna, N.D. Smith, and J.J. Schauer. 2002. Speciation of gas-phase and fine particle emissions from burning of foliar fuels. *Environ. Sci. Tech.* 36(11):2281-2295.

Iisa, K., Y. Lu, and K. Salmenoja. 1999. Sulfation of potassium chloride at combustion conditions. *Energ. Fuel.* 13(6):1184-1190.

Jimenez, J.L., J.T. Jayne, Q. Shi, C.E. Kolb, D.R. Worsnop, I. Yourshaw, J.H. Seinfeld, R.C. Flagan, X. Zhang, and K.A. Smith. 2003. Ambient aerosol sampling using the aerodyne aerosol mass spectrometer. *J. Geophys. Res. Atmos.* 108(D7).

Jiménez, S., and J. Ballester. 2005. Effect of co-firing on the properties of submicron aerosols from biomass combustion. *P. Combust. Inst.* 30(2):2965-2972.

Kazagic, A., and I. Smajevic. 2009. Synergy effects of co-firing wooden biomass with Bosnian coal. *Energy* 34(5):699-707.

Kulmala, M., and A. Laaksonen. 1990. Binary nucleation of water-sulfuric acid system: Comparison of classical theories with different H_2SO_4 saturation vapor pressures. *J. Chem. Phys.* 93(1):696-701.

Linak, W.P., and J.O.L. Wendt. 1994. Trace metal transformation mechanisms during coal combustion. *Fuel Process. Technol.* 39(1):173-198.

Mantananont, N., S. Garivait, and S. Patumsawad. 2012. Characterisation of Particulate Matter Emitted from Cofiring of Lignite and Agricultural Residues in a Fixed-Bed Combustor. *Scientific World J.* 2012:702451.

Saidur, R., E.A. Abdelaziz, A. Demirbas, M.S. Hossain, and S. Mekhilef. 2011. A review on biomass as a fuel for boilers. *Renew. Sust. Energ. Rev.* 15(5):2262-2289.

Sami, M., K. Annamalai, and M. Wooldridge. 2001. Co-firing of coal and biomass fuel blends. *Prog. Energ. Combust.* 27(2):171-214.

Sarkar, P., S.G. Sahu, A. Mukherjee, M. Kumar, A.K. Adak, N. Chakraborty, and S. Biswas. 2014. Co-combustion studies for potential application of sawdust or its low temperature char as co-fuel with coal. *Appl. Therm. Eng.* 63(2):616-623.

Skeen, S.A., B.M. Kumfer, and R.L. Axelbaum. 2010. Nitric oxide emissions during coal and coal/biomass combustion under air-fired and oxy-fuel conditions. *Energ. Fuel.* 24(8):4144-4152.

Sui, J.C., M.H. Xu, Y.G. Du, Y. Liu, and G.Z. Yin. 2007. Emission characteristics and elemental partitioning of submicron particulate matter during combustion of pulverised bituminous coal. *J. Energy Inst.* 80(1):22-28.

Suriyawong, A., M. Gamble, M.-H. Lee, R. Axelbaum, and P. Biswas. 2006. Submicrometer particle formation and mercury speciation under O_2-CO_2 coal combustion. *Energ. Fuel.* 20(6):2357-2363.

Wang, X., S.M. Daukoru, S. Torkamani, W.-N. Wang, and P. Biswas. 2013a. Role of exhaust

gas recycle on submicrometer particle formation during oxy-coal combustion. *P. Combust. Inst.* 34(2):3479-3487.

Wang, X., B.J. Williams, Y. Tang, Y. Huang, L. Kong, X. Yang, and P. Biswas. 2013b. Characterization of organic aerosol produced during pulverized coal combustion in a drop tube furnace. *Atmos. Chem. Phys.* 13(21):10919-10932.

Wang, X., E. Cotter, K.N. Iyer, J. Fang, B.J. Williams, and P. Biswas. 2015. Relationship between pyrolysis products and organic aerosols formed during coal combustion. *P. Combust. Inst.* 35(2):2347-2354.

Warnatz, J., U. Maas, and R.W. Dibble. 2006. *Combustion: Physical and Chemical Fundamentals, Modeling and Simulation, Experiments, Pollutant Formation*. 4th ed. Berlin: Springer.

Williams, A., J.M. Jones, L. Ma, and M. Pourkashanian. 2012. Pollutants from the combustion of solid biomass fuels. *Prog. Energ. Combust.* 38(2):113-137.

Xu, M., D. Yu, H. Yao, X. Liu, and Y. Qiao. 2011. Coal combustion-generated aerosols: Formation and properties. *P. Combust. Inst.* 33(1):1681-1697.

Zhang, L., M. Masui, H. Mizukoshi, Y. Ninomiya, and C. Kanaoka. 2007. Formation of submicron particulates (PM_1) from the oxygen-enriched combustion of dried sewage sludge and their properties. *Energ. Fuel.* 21(1):88-98.

Zhang, L., Y. Ninomiya, and T. Yamashita. 2006. Formation of submicron particulate matter (PM_1) during coal combustion and influence of reaction temperature. *Fuel*

85(10):1446-1457.

Zhuang, Y., and P. Biswas. 2001. Submicrometer particle formation and control in a bench-scale pulverized coal combustor. *Energ. Fuel.* 15(3):510-516.

Zuwala, J., and M. Sciazko. 2010. Full-scale co-firing trial tests of sawdust and bio-waste in pulverized coal-fired 230t/h steam boiler. *Biomass Bioenerg.* 34(8):1165-1174.

CHAPTER 7. CONCLUSIONS

The major findings of this study are summarized in the following sections. Some future work related with this study is discussed in the last section.

7.1 Elemental mercury oxidation in an electrostatic precipitator enhanced with in situ soft X-ray irradiation (Chapter 2)

The DC corona based ESP can oxidize elemental mercury (under ±10 kV in the studied ESP), and soft X-ray irradiation can enhance this process. The proposed mechanism is: electrons were emitted due to photoionization caused by UV radiation from corona discharge and by soft X-ray radiation in the ESP, and then they initiated chain reactions that produced electrons, intermediate species, and other products. Radicals, such as ·O and O_3, were produced in the chain reactions, and they oxidized Hg^0. Positive ESP worked better in oxidizing Hg^0 due to the presence of more high energy electrons. The enhancement was more significant when the O_2 concentration was low.

Particles may influence the performance of this methodology, depending on the chemical properties of particles. SiO_2 particles did not have a significant effect on Hg^0 oxidation process; TiO_2 particles absorbed inhibited the Hg^0 oxidation; KI particles enhanced Hg^0 oxidation. The NO in the practical flue gas totally inhibited the Hg^0 oxidation, and with addition of KI in the coal, the oxidation by ESP with soft X-rays was partially restored.

7.2 Secondary aerosols generation in an electrostatic precipitator during flue gas treatment (Chapter 3)

Secondary aerosols may be formed in the ESP during flue gas treatment. In this study, the secondary aerosols were found to be H_2O-H_2SO_4 aerosols with a unimodal size distribution and a peak size of 20 nm. They were formed through the following pathway: (1) SO_2 in the flue gas was oxidized by the oxidizing radicals, reacted with H_2O in the ESP, and eventually formed H_2SO_4 (vapor); (2) H_2O-H_2SO_4 SAs were firstly formed through ion-induced nucleation; (3) SAs grew through condensation and nucleation. At the same time, part of the newly formed aerosols were captured by the ESP.

The SA concentration and peak size increased with higher SO_2 concentration, higher water content and higher flow rate through ESP. With the ESP voltage increasing, the SA concentration and peak size firstly went down (from -5 kV to -8 kV), and then increased (from -8 kV to -10 kV).

7.3 Capture of submicrometer particles with a pressurized electrostatic precipitator (Chapter 4)

In the pressurized ESP, the corona on-set voltage increased with the gas pressure, and under the same voltage, the ESP current was lower with higher gas pressure, because the higher gas density hindered the ionization process. Under a similar operating voltage, the penetration of submicrometer NaCl particle was lower for a lower gas pressure due to the increasing ion concentration with decreasing gas pressure. With the same current, the NaCl particle

penetration was higher for a lower gas pressure, which was an outcome of the combined effect of higher particle velocity along the gas flow, higher particle migration velocity, and lower electrical filed strength.

A modified Deutsch-Anderson equation, which accounts for all the factors discussed above, was developed to predict the particle capture efficiency in the pressurized ESP. The estimations from the modified D-A equation matched the experimental results of NaCl particle capture well.

In the fly ash particle capture test, pressurized ESP is under the same gas pressure with the coal combustor. With a higher gas pressure in the coal combustor (longer residence time), the particles had higher charge fraction and average number of charge. This charging status greatly influenced the particle penetration through the pressurized ESP. As a result, under the same current, the particle penetration increased with the gas pressure.

7.4 Development of a compact electrostatic nanoparticle sampler for offline aerosol characterization (Chapter 5)

A nanoparticle sampler with a configuration of two-stage ESP was developed. Its optimal working conditions were found to be a total flow rate of 1.0 lpm, an aerosol/ion carrier flow rate ratio of 1.0, and a collection voltage of 4.5 kV. Particle collection efficiency increased with the particle diameter due to the change of particle charging efficiency. Under the optimized conditions, collection efficiencies over 90% were achieved with for NaCl particles with the sizes ranging from 50 to 500 nm. For the size ranging from 60 nm to 400 nm, 57% to

78% of the particles were collected on the SEM stub in the sampler. The collection efficiency depended on the material of the particles. The collection efficiencies of oleic acid particles were lower than those of NaCl particles in the size range from 50 to 150 nm, due to lower charging efficiencies of oleic acid particles.

7.5 Characterization of submicrometer particles from sawdust/coal co-firing in a drop-tube furnace (Chapter 6)

The fine particles from co-firing of coal with sawdust had a unimodal size distribution, implying a major formation pathway of nucleation/condensation of volatilized mineral matter. With higher amount of sawdust in the blended fuel, there were less fine particles generated. Particles from co-firing had an elemental composition more similar to that of particles from coal combustion. It indicates that the sawdust had lower content of volatilized mineral and thus contributed less in submicrometer particle formation. Carboxylic acids and aromatic compounds were two major organic compounds in the submicrometer particles. With higher sawdust mixing ratio in the fuel, the organic concentrations were lower, due to a smaller reaction characteristics time of volatile matters from sawdust.

With higher sulfur content in the coal, the concentration of fine particles increased because of formation of sulfates. This increase also promoted the organic particle formations due to an increase of organic absorption on the particles and better protection of organics from being oxidized. Higher combustion temperature resulted in high concentrations of submicrometer particles and organics. Higher moisture content resulted in lower overall particle

concentrations but higher particle concentrations in the size range between 80 nm to 500 nm. The organic particle concentration was also higher with higher moisture, indicating that most of the organics were in the larger particles (> 80 nm).

7.6 Future work

This study can be expanded in the following directions.

The soft X-ray enhanced ESP showed high mercury oxidation efficiency in the lab test. It will be interesting and beneficial to test this methodology on a pilot-scale or full-scale coal combustion system, and do modification on the device accordingly and eventually make it applicable to practical coal combustion system.

The secondary aerosol formation has been well studied here. Future work can be put on developing strategies to prevent the formation of secondary aerosols or control the secondary aerosols. Besides, further study can also be conducted on developing model to predict the concentration and size distribution of secondary aerosols from ESP. Previous studies have been on modeling the H_2SO_4 concentration in the corona discharge reactor, modeling the H_2SO_4-H_2O aerosol formations, and modeling the particle collection efficiencies of the ESP. By combining those three models, we could obtain a model to predict the formation of secondary aerosols.

A good fundamental study has been done on the pressurized ESP. However, in order to support the practical application, the performance of this ESP under higher gas pressure (10 atms) and various gas compositions should be studied. Moreover, the pressurized ESP should

be tested on a pilot-scale or full-scale coal combustion system. At the time, the gas pressure influences the ionization, particle charging, and particle transport processes in the ESP simultaneously, and it is difficult to evaluate the combined effect. To better analyze the pressurized ESP, numerical study is needed. A coupled model can be established to simulate ionization, particle charging, and particle transport processes, which will benefit this research a lot.

The electrostatic particle sampler has high collection efficiency of the submicrometer particles. A further study may be done to investigate the flow pattern in the sampler, which can help in suggesting modification of the sampler to reduce the particle loss on the surface other than the top of the SEM stub.

The formation of the submicrometer particles was well studied here and it was proposed that organic matters were mixed with the inorganic matters. It will be interesting to know how the organics mix with inorganics. High resolution TEM can be used to perform this observation. It will also be interesting to measure the VOC concentrations and speciation in the flue gas and investigate the relationship between the VOC and organic matters in the particles.

APPENDIX I. SUPPORTING MATERIALS FOR CHAPTER 2

-- Elemental Mercury Oxidation in an Electrostatic Precipitator Enhanced with In Situ Soft X-ray Irradiation

Configuration of the electrostatic precipitator

Figure A1.1 shows the details of the ESP. The case of the ESP was made of PVC. The aerosol inlet was placed at the upper end, and the outlet was placed at the lower end. The discharge electrode was a 0.323 mm diameter stainless steel wire placed in the center. The collecting electrode was a tube enclosed by the PVC case. It was also made of stainless steel, and was 25.4 cm in length and 4.8 cm in diameter. Excess length of the discharge electrode was sheathed using an insulating material. The X-rays from the photoionizer entered the system through a circular hole (1.7 cm in diameter) in the middle of the collecting electrode and the PVC case. A thin polyamide film (Kapton® 30HN, DuPont Corp., 30 μm thick) was used to keep the ESP system airtight. The penetrability of soft X-rays through the polyamide film was estimated to be about 90%.

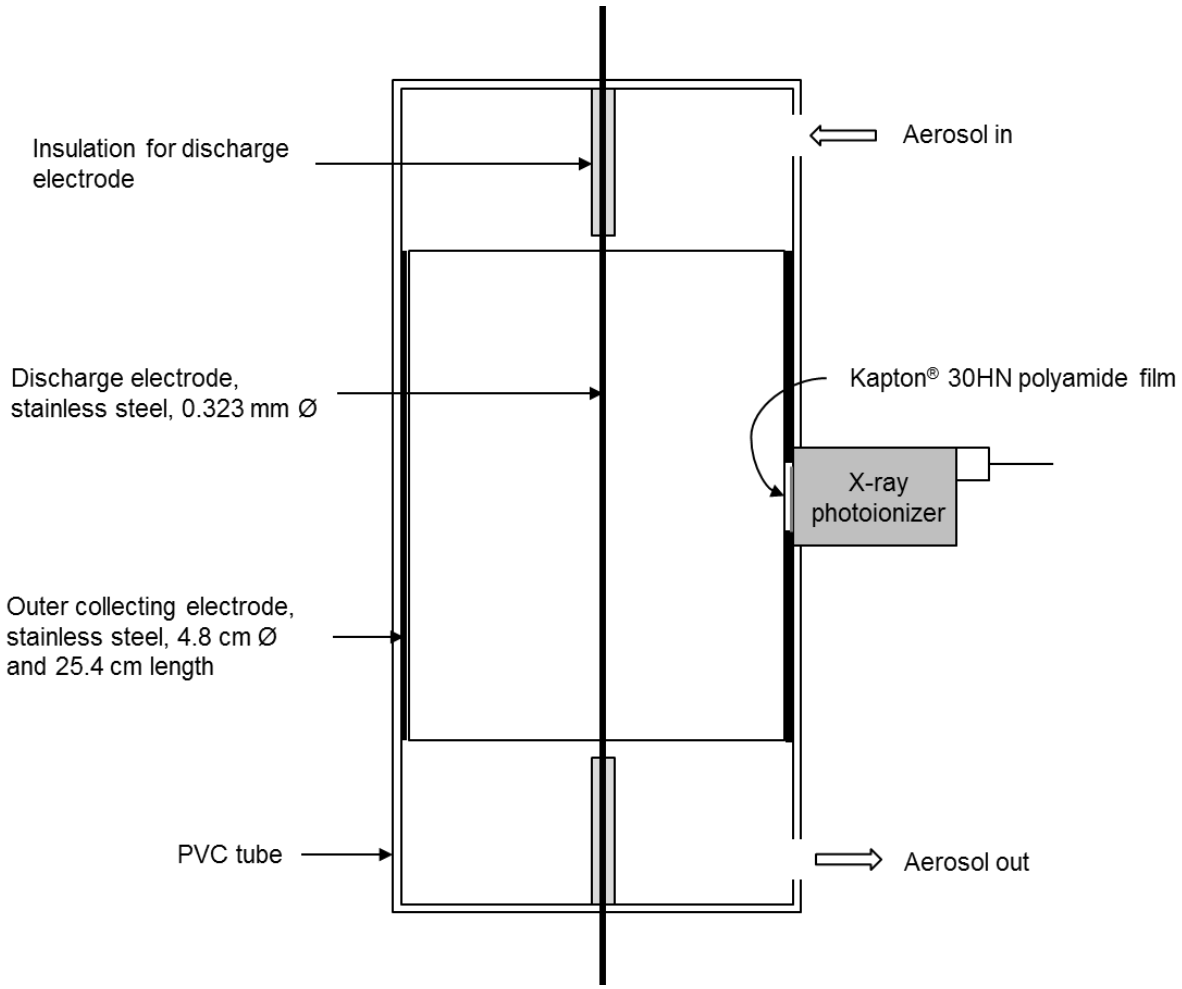

Figure A1.1 Configuration of studied electrostatic precipitator

Analysis of coals

Table A1.1 Analysis of PRB coal and Chinese S03

Coal name	Proximate Analysis				Ultimate Analysis				$Q_{net,d}$	Hg	ASTM
	$Moisture_{ad}$	Ash_d	VM_d	FC_d	S_d	C_d	H_d	O_d	MJ/kg	ppb	Rank
PRB	27.70	8.00	48.30	42.90	0.57	67.30	4.58	19.92	28.04	50	Sub-bit.
S03	0.71	26.43	16.06	57.51	2.30	62.6	3.23	4.59	24.67	489	Sub-bit.

VM – Volatile Matter; FC – Fixed Carbon; ad – air-dried; d - dry

V-I characteristics curve

By comparing the conversions in Figure 2 with the voltage-current (V-I) characteristics in Figure A1.2, it is found that on either the positive side or negative side, high conversions were reached when the currents were high, such as at +10 kV and -10 kV. In contrast, low conversions were related to low currents. The corona discharge did not reach or just reached the inception voltage at -8 kV, 0 kV, +8 kV. This result matches the understanding that for ESP the current conducting mechanisms are fundamentally interconnected with chemical processes (Thomson, 1893). Besides, current was always higher with soft X-rays.

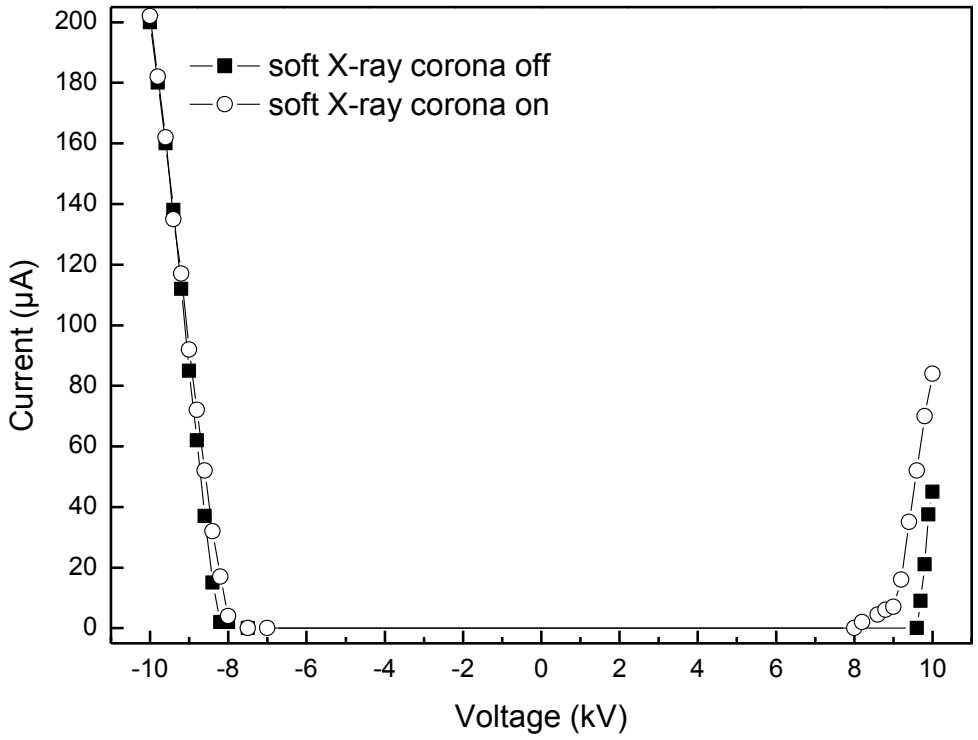

Figure A1.2 Current-voltage characteristics of ESP under base condition (0.04 lpm O_2, 0.12 lpm CO_2, 0.84 lpm N_2)

Mercury speciation

Figure A1.3 shows the mercury speciation after treatment with ESP alone at +10 kV voltage and with ESP coupled with soft X-rays. The speciation patterns for those two cases were similar, which indicates the same mechanism. Only 5.8%-10.4% oxidized Hg escaped from the ESP. The other oxidized mercury might have deposited on the inner surface of ESP in the form of HgO(s),

which has been observed in Hg^0 oxidation by dielectric barrier discharge (Byun et al., 2011).

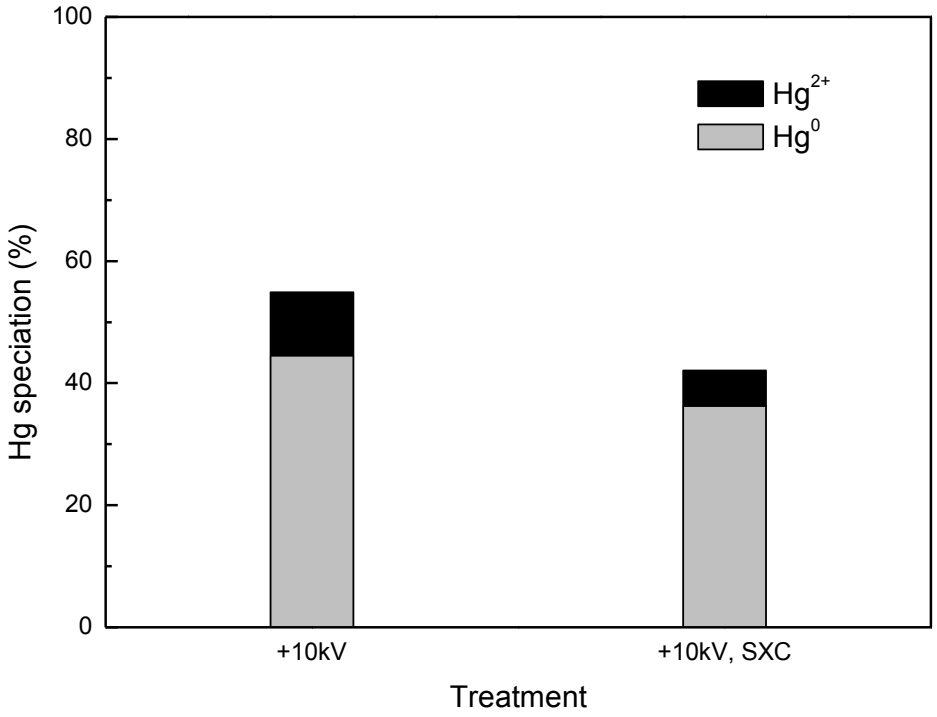

Figure A1.3 Mercury speciation of mercury treated by ESP and soft X-rays (gas combination: 0.04 lpm O_2, 0.12 lpm CO_2, 0.84 lpm N_2)

Ozone generation by the ESP in pure N_2, CO_2, or O_2 environments

Ozone generation by the ESP in pure N_2, CO_2, or O_2 is shown in Figure A1.4. In the pure CO_2 case, similar to the current measurements, no O_3 generation was observed under ESP alone. However, when soft X-rays were on, O_3 generation was observed. Under pure O_2, soft X-rays also showed an effect on reducing O_3 generation.

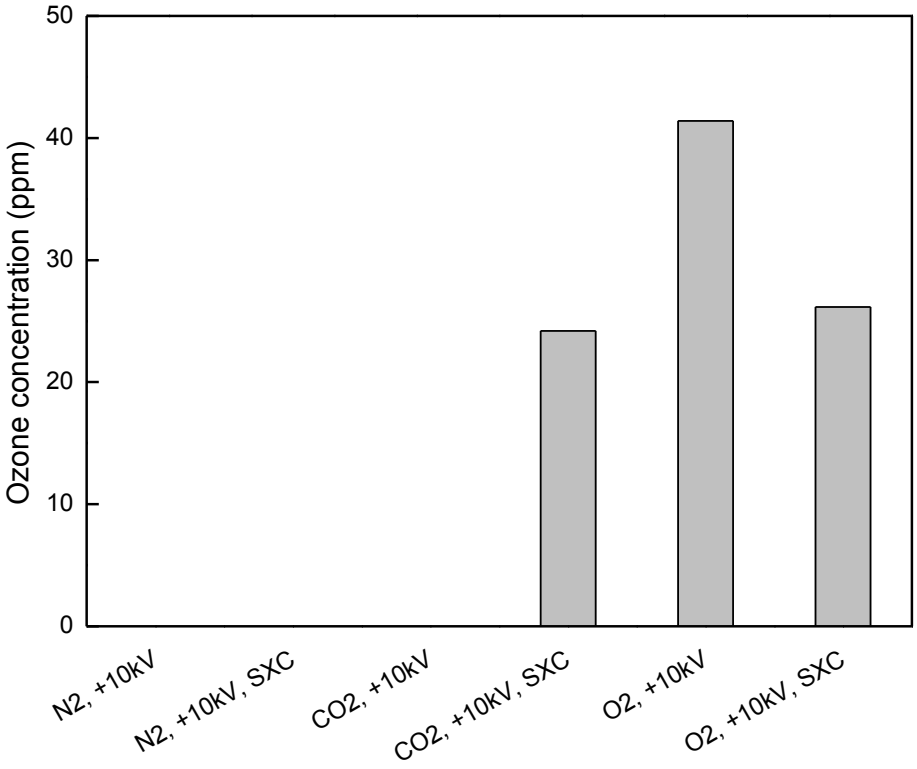

Figure A1.4 Ozone concentrations downstream of ESP in pure N_2, CO_2, or O_2

Effects of O_2 concentrations

Depending on the coal feeding rate and efficiency of the combustion, the O_2 composition in flue gas varies. To investigate the performance of ESP and soft X-rays on Hg^0 oxidation under those varying conditions, Hg^0 conversion was measured under O_2 percentages at 0%, 2%, 4%, and 6%, with the CO_2 percentage fixed to 12% and the rest balanced with N_2. Results are shown in Figure A1.5. When ESP alone was used, the mercury conversion increased from 9.0% to 64.4% as the oxygen concentration increased. This is because O_2 is an important source for generation of chemically active species. On the other hand, when ESP and soft X-rays were both applied, the

Hg^0 conversion was relative stable and varied just between 67.1% and 77.1%. Soft X-ray photoionization significantly enhanced the production of electrons and led to a very high electron concentration, which resulted in high production of radicals, even in the case when the O_2 concentration was low. The O_3 concentration measurements are shown in Figure A1.6. Based on the discussion for single gas studies, the possible explanation why Hg^0 could still be achieved under 88% N_2 and 12% CO_2 condition is: CO_2 were the sources of O, and electrons and excited N_2 from ionization of N_2 accelerate the generation of O and O_3.

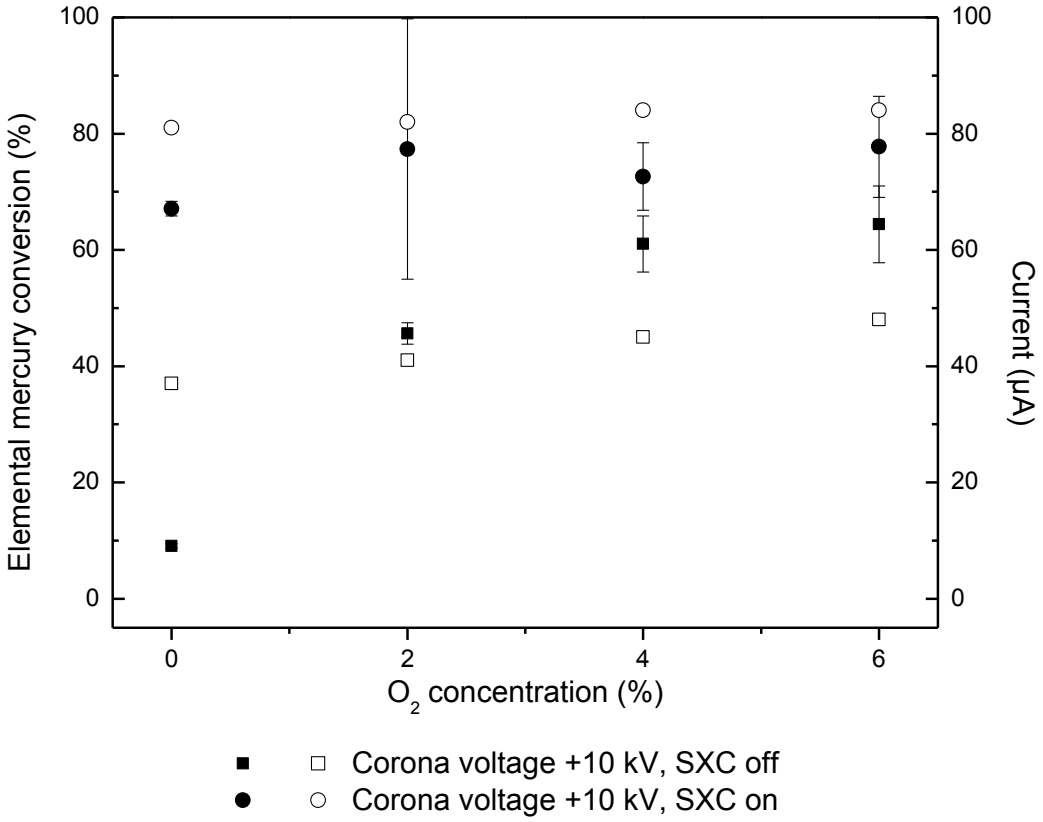

Figure A1.5 Elemental mercury conversions under various O_2 concentrations (solid symbol, mercury conversion; open symbol, current) (total flow rate: 1 lpm; CO_2 flow rate: 0.12 lpm; balanced with N_2)

Ozone generation by ESP under various O_2 concentrations

O_3 concentration measurements are shown in Figure A1.6. The O_3 concentration increased with the increase of O_2 percentage, when ESP alone was on; while under ESP and soft X-rays together, the O_3 concentration remained between 73.5 ppm and 75 ppm with various O_2 percentages.

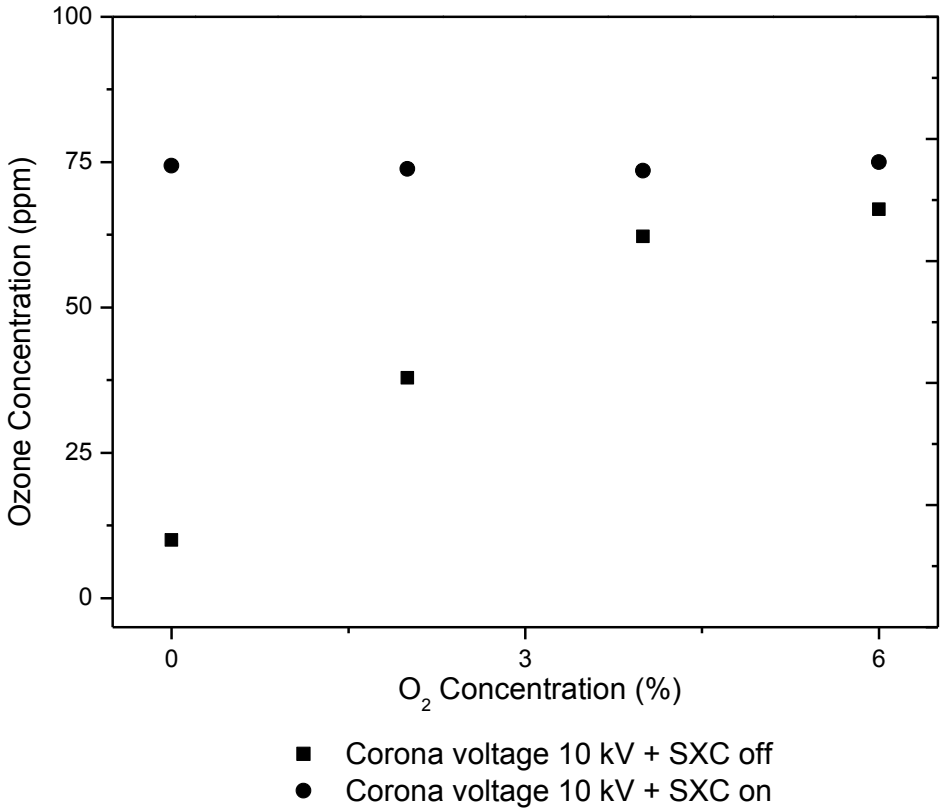

Figure A1.6 Ozone concentrations downstream of the ESP under various O_2 concentrations

Modeling of electrons distribution in the ESP

In this model, a cross section of our lab-scale ESP was studied, as shown in Figure A1.7. Considering that the cross section is axisymmetric, the simulation domain was simplified into an interval.

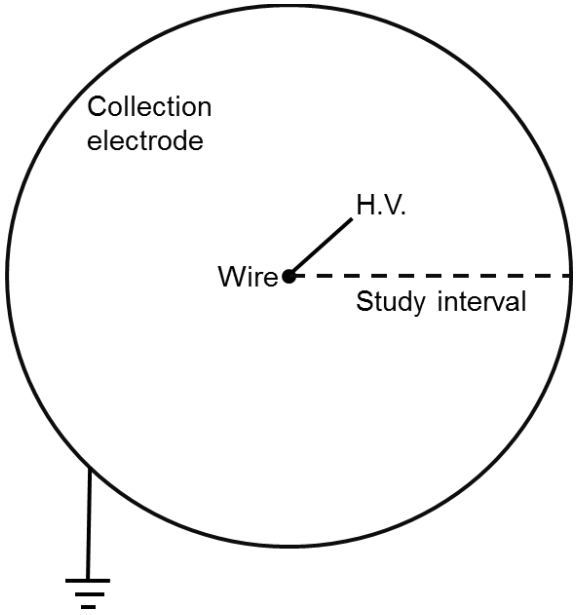

Figure A1.7 Model geometry (cross section of ESP)

The electron impact reactions and chemical reactions considered in this model were summarized in Table A1.2. The rate constants of chemical reactions were obtained from Mikoviny et al. (2004) and Wu et al. (2012)

Table A1.2 Summary of electron-impact reaction and chemical reactions in the model

Reaction	Reaction rate constant
$e + CO_2 \rightarrow e + CO + O$	-*
$e + CO_2 \rightarrow O^- + CO$	-
$e + CO_2 \rightarrow 2e$	-
$e + N_2 \rightarrow 2e + N_2^+$	-
$e + O_2 \rightarrow e + 2O$	-
$e + 2O_2 \rightarrow O_2 + O_2^-$	-
$e + O_2 \rightarrow O_2^-$	-
$e + O_2 \rightarrow 2e + O_2^+$	-
$e + O_3 \rightarrow O_2 + O^-$	-
$e + O_3 \rightarrow O + O_2^-$	-
$2CO_2 + O^- \rightarrow CO_2 + CO_3^-$	32616360 $m^6/(s \cdot mol^2)$
$2CO_2 + O_2^- \rightarrow CO_2 + CO_4^-$	3624040 $m^6/(s \cdot mol^2)$
$O + 2O_2 \rightarrow O_3 + O_2$	212 $m^6/(s \cdot mol^2)$
$O + O_2 + CO_2 \rightarrow O_3 + CO_2$	656 $m^6/(s \cdot mol^2)$
$2O + CO_2 \rightarrow O_2 + CO_2$	3769 $m^6/(s \cdot mol^2)$
$O + CO + CO_2 \rightarrow 2CO_2$	3.97 $m^6/(s \cdot mol^2)$
$O_2 + N_2^+ \rightarrow N_2 + O_2^+$	36146745 $m^3/(s \cdot mol)$
$O_2 + O_2^+ + O_2^- \rightarrow 3O_2$	7.25E10 $m^6/(s \cdot mol^2)$

$N_2 + O_2^+ + O_2^- \rightarrow 2O_2 + N_2$	7.25E10 $m^6/(s \cdot mol^2)$
$CO_2 + O_2^+ + O_2^- \rightarrow 2O_2 + CO_2$	7.25E10 $m^6/(s \cdot mol^2)$
$O + O_2 + N_2 \rightarrow O_3 + N_2$	90.6 $m^6/(s \cdot mol^2)$

*Reaction rates of electron-impact reactions were calculated based on the impact cross section data. The data was from electron database LXcat.

Size distributions of injected SiO_2, TiO_2, and KI particles

Figure A1.8 shows the particle size distribution (PSD) at the ESP outlet under three different operations: 1) ESP and soft X-ray both off, 2) ESP on and soft X-ray off, and 3) ESP and soft X-ray both on. The PSD under the first situation indicates the PSD upstream of the ESP during all the tests. Comparing the PSDs under the four particle feeding conditions showed they all had typical atomization single-modal distribution patterns. The total number concentrations and peak sizes of the four cases (SiO_2, TiO_2, low concentration KI, and high concentration KI) were comparable, respectively. Total number concentrations in the four cases were 2.94×10^5 #/cm^3, 2.12×10^5 #/cm^3, 4.01×10^5 #/cm^3, and 2.36×10^6 #/cm^3, successively. Their mean sizes were 127.5 nm, 134.2 nm, 54.8 nm, and 71.7 nm. PSDs under the second and third operating conditions show that the ESP removed at least 99.1% of the particles.

(a)

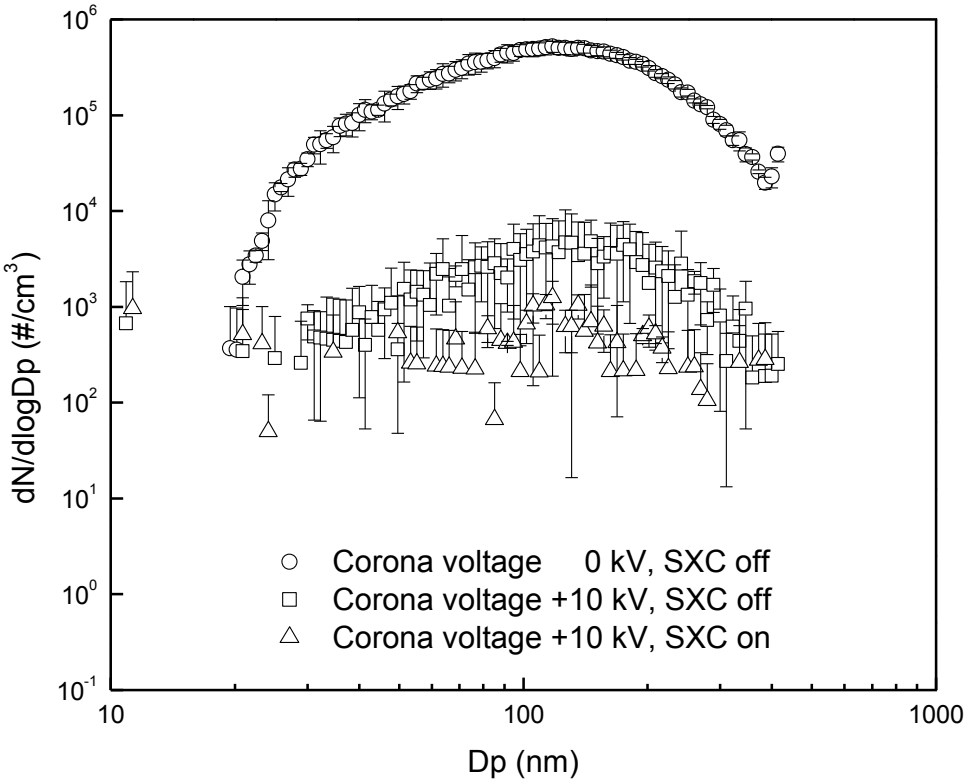
dN/dlogDp (#/cm3)
Dp (nm)
Corona voltage 0 kV, SXC off
Corona voltage +10 kV, SXC off
Corona voltage +10 kV, SXC on

(b)

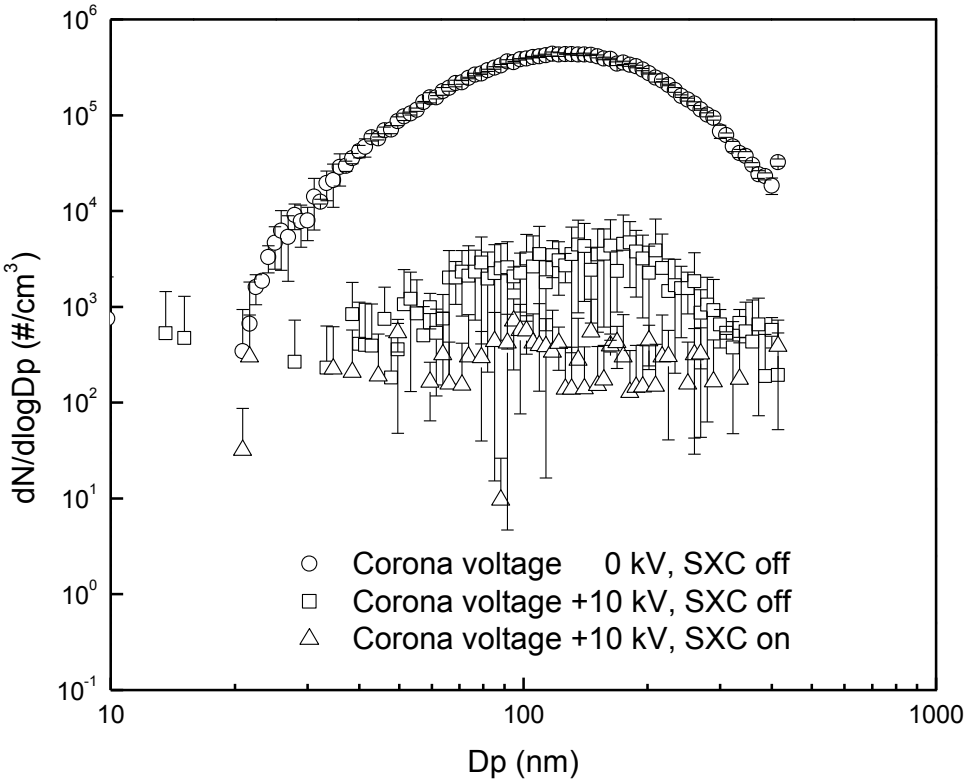
dN/dlogDp (#/cm3)
Dp (nm)
Corona voltage 0 kV, SXC off
Corona voltage +10 kV, SXC off
Corona voltage +10 kV, SXC on

(c)

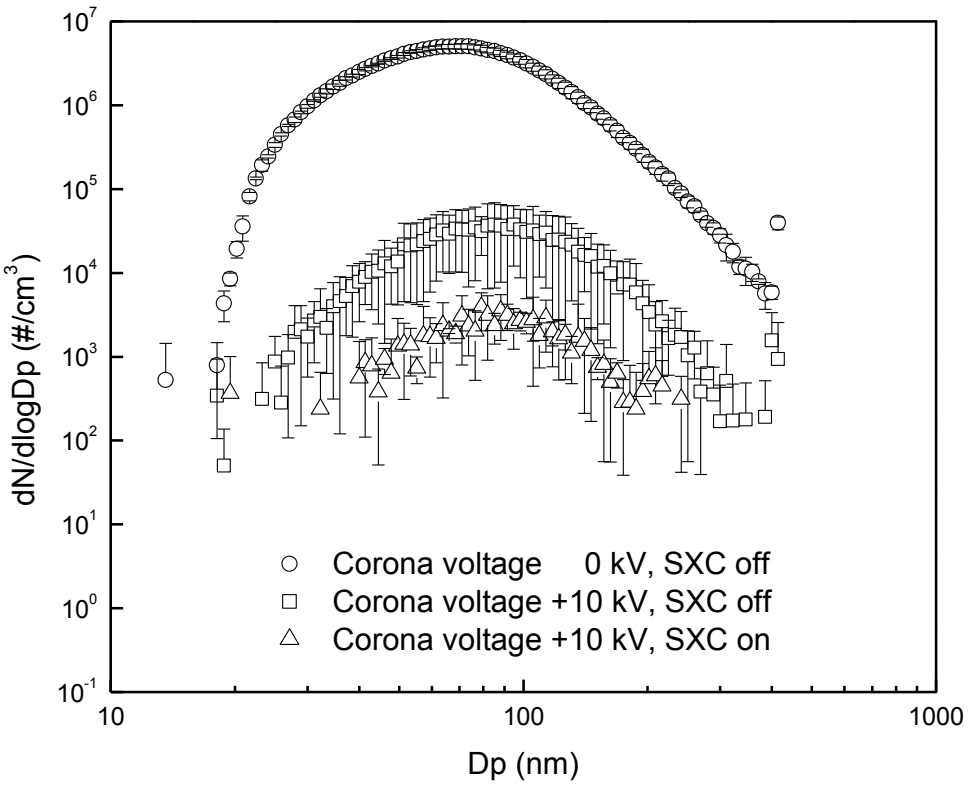
dN/dlogDp (#/cm3)
Dp (nm)
Corona voltage 0 kV, SXC off
Corona voltage +10 kV, SXC off
Corona voltage +10 kV, SXC on

(d)

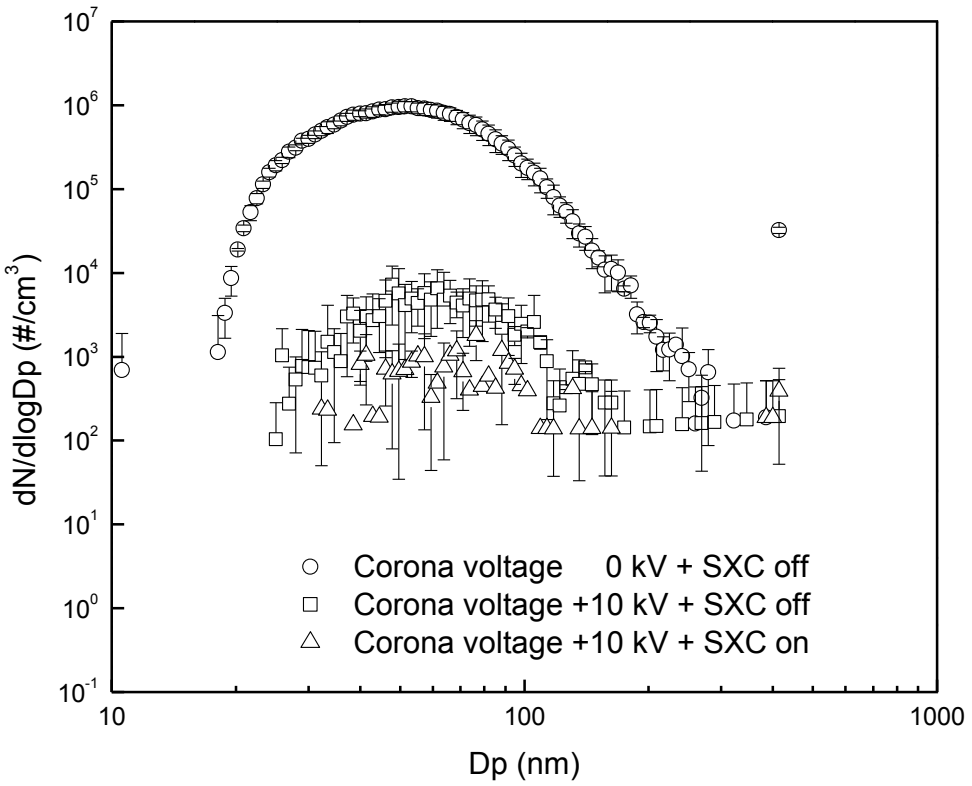

Figure A1.8 Particle size distributions of SiO2 particles downstream of the ESP: (a) SiO_2; (b) TiO_2; (c) KI (high concentration case, 189.0 ppm atomization solution); (d) KI (low concentration case, 18.9 ppm atomization solution)

Effect of gas residence time on the mercury oxidation efficiency

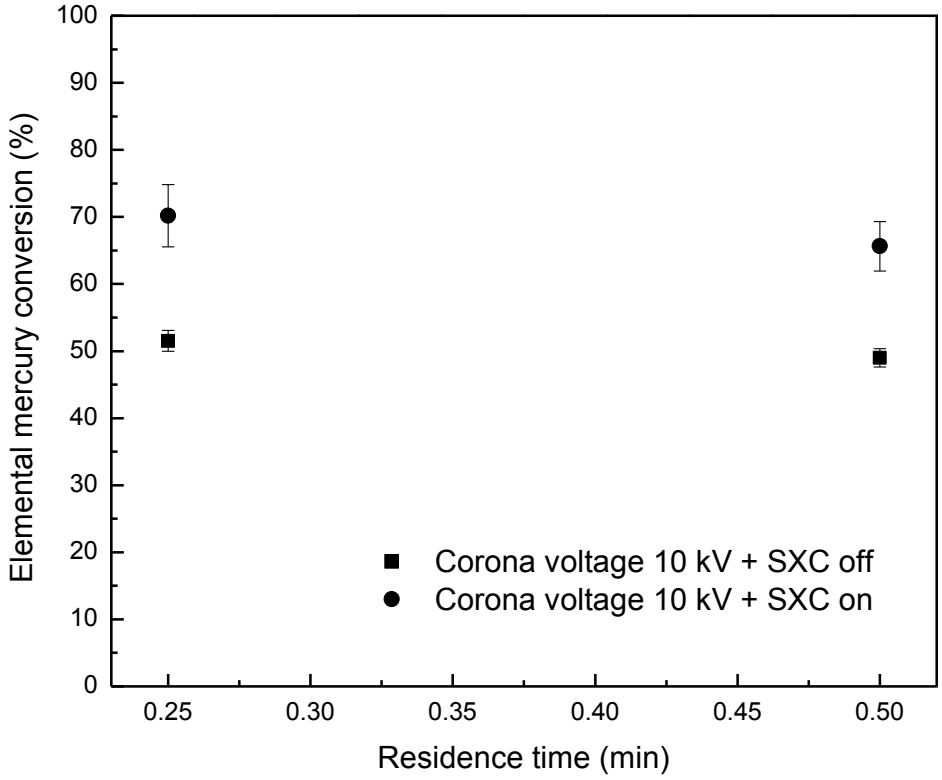

Figure A1.9 Elemental mercury conversions under two different residence time

Effects of HCl and SO_2 Concentrations in Flue Gas

HCl and SO_2 are usually present in flue gas. The effects of those gases are discussed in this section. The flow rates of O_2, N_2, and CO_2 were kept at 0.04 lpm, 0.84 lpm, and 0.12 lpm, respectively. Figure A1.10 shows the effect of HCl. With 10 ppm HCl in the flue gas, Hg^0 conversions of 98.5% and 99.2% were achieved under ESP alone and ESP coupled with soft X-rays, respectively. The enhancement can be explained by two mechanisms. First, HCl can

directly react with Hg^0 even without corona discharge, as seen in the result in Figure A1.7. This result is consistent with previous observations in coal combustion systems (Hall et al., 1991; Zhou et al., 2007). The proposed overall reaction equation for this process is (Hall et al., 1991):

$$2Hg + 4HCl + O_2 \rightarrow 2HgCl_2 + 2H_2O \quad \text{(A1.1)}$$

Moreover, with the electrons generated by ESP and soft X-rays, generation of radicals like Cl and Cl_2 was enhanced. Radicals were formed following these reactions (Ko et al., 2008a; Ko et al., 2008b):

$$e + HCl \rightarrow e + H + Cl \quad \text{(A1.2)}$$

$$N_2^* + HCl \rightarrow H + Cl + N_2 \quad \text{(A1.3)}$$

$$H + HCl \rightarrow H_2 + Cl \quad \text{(A1.4)}$$

$$Cl + Cl + M \rightarrow Cl_2 + M \quad \text{(A1.5)}$$

The Cl and Cl_2 radicals can oxidize Hg^0; the related reactions are shown below (Zhou et al., 2007; Ko et al., 2008a; Ko et al., 2008b):

$$Hg^0 + Cl + M \rightarrow HgCl + M \quad \text{(A1.6)}$$

$$HgCl + Cl + M \rightarrow HgCl_2 + M \quad \text{(A1.7)}$$

$$Hg^0 + Cl_2 \rightarrow HgCl + Cl \quad \text{(A1.8)}$$

$$HgCl + Cl_2 \rightarrow HgCl_2 + Cl \quad \text{(A1.9)}$$

$$Hg^0 + Cl_2 \rightarrow HgCl_2 \quad \text{(A1.10)}$$

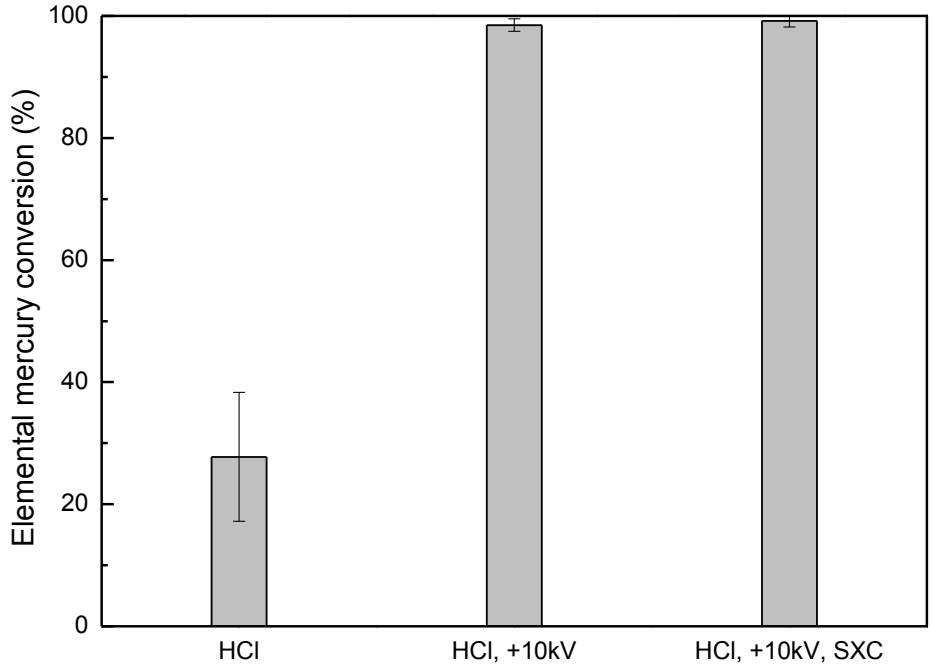

Figure A1.10 Elemental mercury conversions with HCl in flue gas (gas combination: 0.04 lpm O_2, 0.12 lpm CO_2, 0.84 lpm N_2, 10 ppm HCl)

Figure A1.11 shows that SO_2 significantly enhanced Hg^0 conversion for both ESP alone and ESP coupled with soft X-rays. Conversions of 88.9% and 92.6% were achieved for ESP alone and ESP coupled with soft X-rays, respectively, under 800 ppm SO_2. The enhancement was likely due to the following pathway (Wang et al., 2010):

$$SO_2 + O \rightarrow SO_3 \quad \text{(A1.11)}$$

$$Hg^0 + SO_3 + O \rightarrow HgSO_4 \quad \text{(A1.12)}$$

This additional pathway speeded up Hg^0 conversion, compared to the case without SO_2 injection. The stoichiometric molar ratio of Hg^0 and SO_2 in the oxidation process is 1:1. However, the SO_2 molar concentration in the study condition was more than thousand times higher than the Hg^0 concentration, and the SO_2 oxidation was highly promoted in the corona discharge environment (Mizuno et al., 1986). As a result, sufficient SO_3 was generated to participate in the Hg^0 oxidation process.

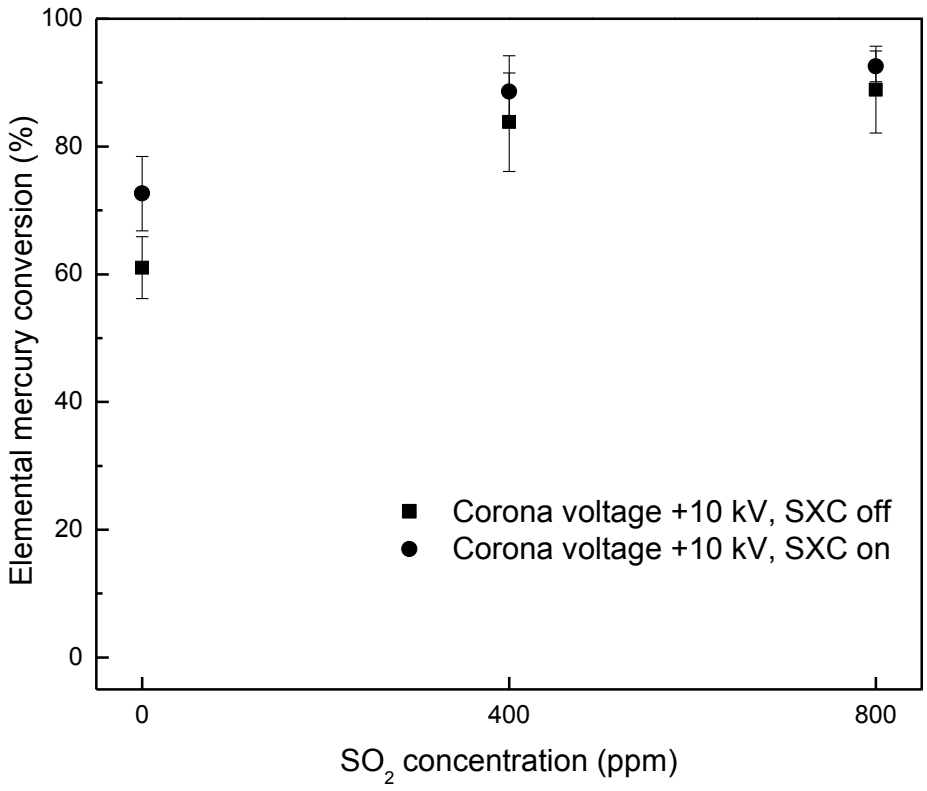

Figure A1.11 Elemental mercury conversions with SO_2 in flue gas (gas combination: 0.04 lpm O_2, 0.12 lpm CO_2, 0.84 lpm N_2)

Reference

Byun, Y., D.J. Koh, and D.N. Shin. 2011a. Removal mechanism of elemental mercury by using non-thermal plasma. *Chemosphere* 83:69-75. doi: 10.1016/j.chemosphere.2010.12.003.

Hall, B., P. Schager, K. Tomura, and O. Lindqvist. 1991. Chemical reactions of mercury in combustion flue gases. Water Air Soil Poll. 56(1):3-14. doi: 10.1007/BF00342256.

Hedrick, E., T.G. Lee, P. Biswas, and Y. Zhuang. 2001. The development of iodine based impinger solutions for the efficient capture of Hg^0 using direct injection nebulization-inductively coupled plasma mass spectrometry analysis. *Environ. Sci. Eng*. 35:3764-3773. doi: 10.1021/es010648r.

Ko, B.K., Y. Byun, M. Cho, W. Namkung, D.N. Shin, D.J. Koh, and K.T. Kim. 2008a. Influence of HCl on oxidation of gaseous elemental mercury by dielectric barrier discharge process. Chemosphere. 71:1674-1682. doi: 10.1016/j.chemosphere.2008.01.015.

Ko, B.K., Y. Byun, M. Cho, W. Namkung, I.P. Hamilton, D.N. Shin, D.J. Koh, and K.T. Kim. 2008b. Pulsed corona discharge for oxidation of gaseous elemental mercury. Appl. Phys. Lett. 92:251503. doi: 10.1063/1.2952496.

Mikoviny, T., M. Kocan, S. Matejcik, N.J. Mason, and J.D. Skalny. 2004. Experimental study of negative corona discharge in pure carbon dioxide and its mixtures with oxygen. *J. Phys. D: Appl. Phys.* 37:64-73. doi: 10.1088/0022-3727/37/1/011.

Mizuno, A., J.S. Clements, and R.H. Davis. 1986. A method for the removal of sulfur dioxide from exhaust gas utilizing pulsed streamer corona for electron energization. IEEE T. Ind. Appl. 22(3):516-522. doi: 10.1109/TIA.1986.4504752.

Thomson, J.J. 1893. Recent Researches in Electricity and Magnetism. London: Oxford Univ. Press.

Wang, Z.H., S.D. Jiang, Y.Q. Zhu, J.S. Zhou, J.H. Zhou, Z.S. Li, and K.F. Cen. 2010. Investigation on elemental mercury oxidation mechanism by non-thermal plasma treament. *Fuel. Process. Technol.* 91:1395-1400. doi: 10.1016/j.fuproc.2010.05.012.

Wu, F., R. Liao, X. Liu, F. Yang, L. Yang, Z. Zhou, and Y. Luo. Numerical simulation of DC positive corona discharge under atmospheric environment. Paper presented at 2012 International Conference on High Voltage Engineering and Application, Shanghai, China, September 17-20, 2012.

Zhou, J., Z. Luo, C. Hu, and K. Cen. 2007. Factors impacting gaseous mercury speciation in postcombustion. Energ. Fuel. 21:491-495. doi: 10.1021/ef060406i.

APPENDIX II. SUPPORTING MATERIALS FOR CHAPTER 3

-- Secondary Aerosols Generation in Electrostatic Precipitator during Flue Gas Treatment

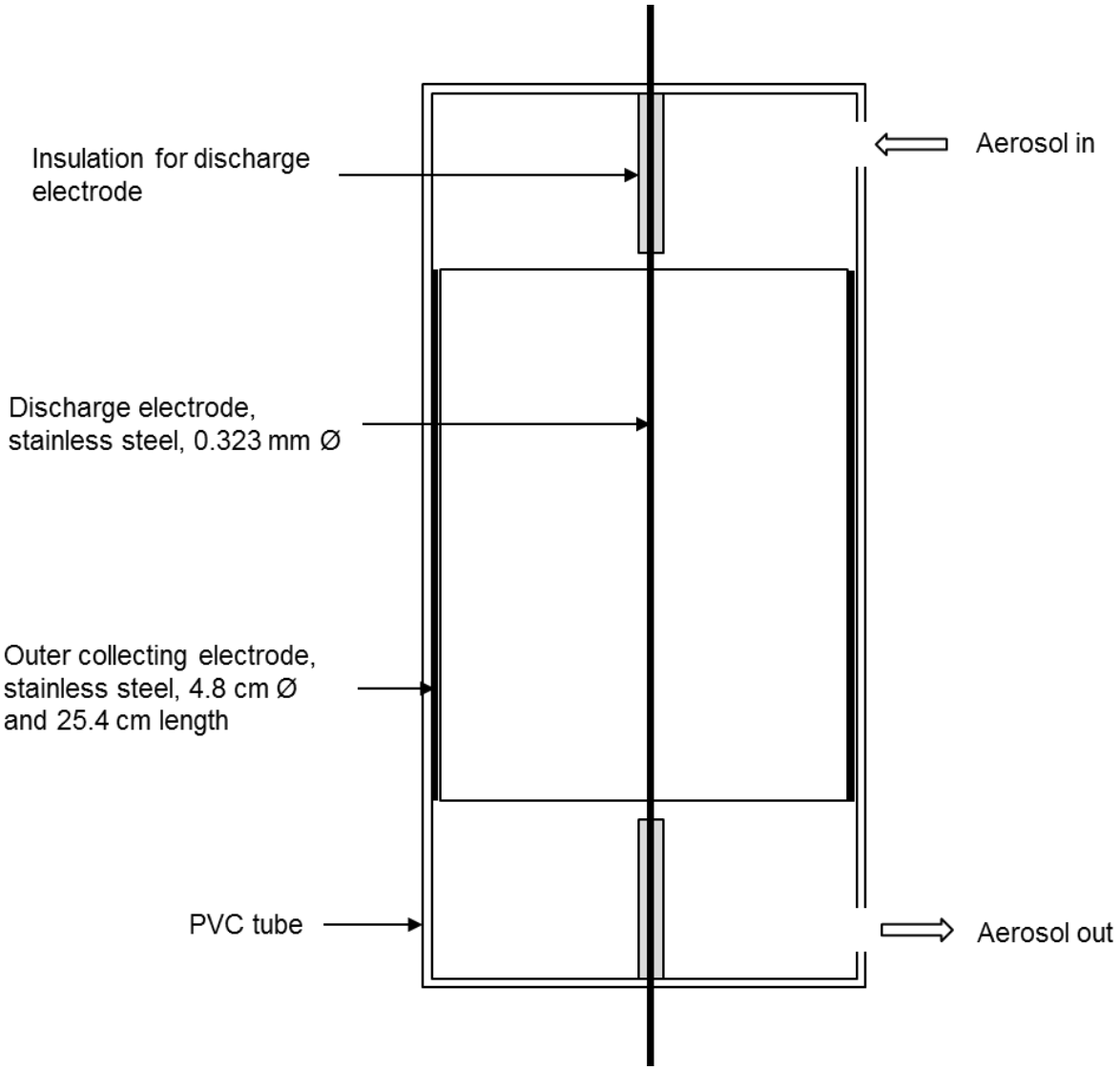

Figure A2.1 Configuration of the studied ESP

Table A2.1 Proximate and ultimate analysis of coals and sawdust

	West Elk coal	Illinois No. 6 coal
Proximate analysis (%wt)		
Volatile matter[1]	38.9	42
Fixed carbon[1]	51.4	48
Ash[1]	9.5	10
Moisture[2]	10.43	13.5
Ultimate analysis (%wt)		
Carbon	74.14	71
Nitrogen	1.53	1.3
Hydrogen	5.08	5
Oxygen	9.27	9.13
Sulfur	0.52	3.47
Chlorine	0.012	0.11

[1]Dry weight basis

[2]As-received basis

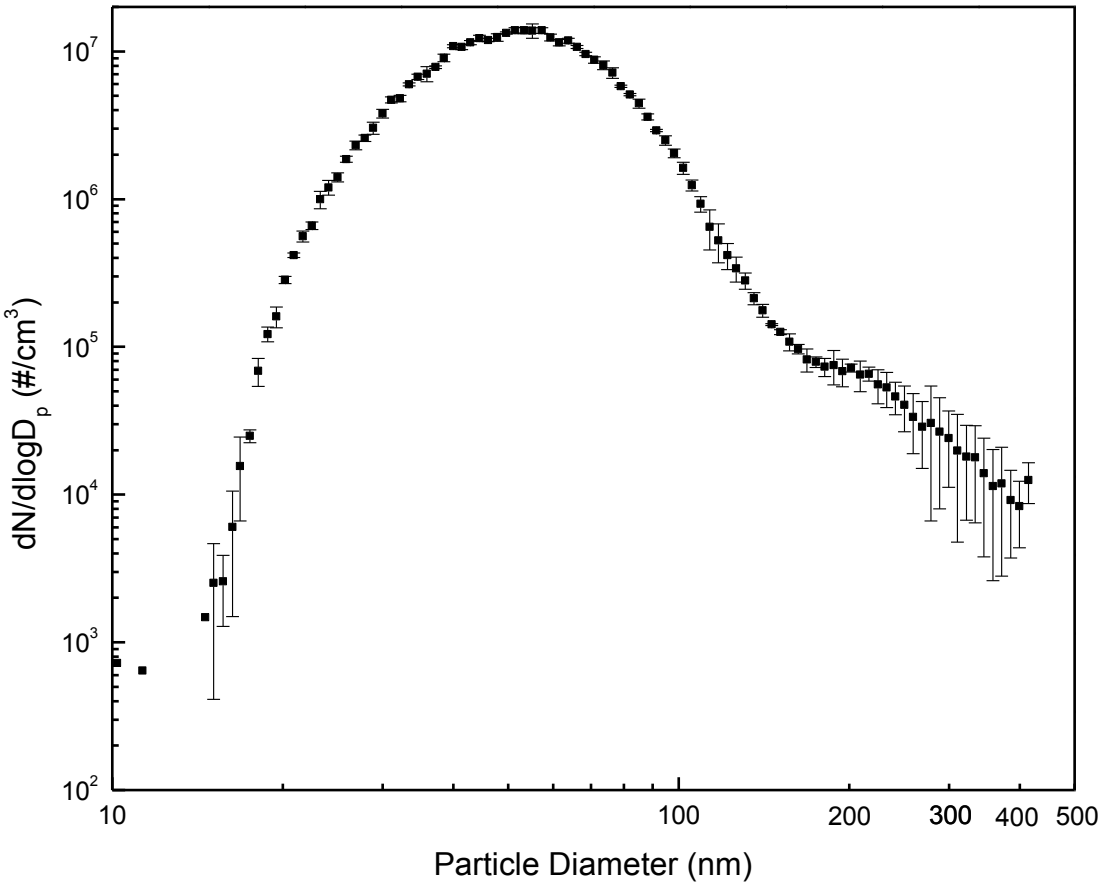

Figure A2.2 Size distribution of the fly ash particles that challenged the studied ESP (ACERF system, 6% O_2 in the flue gas)

Table A2.2 Flue gas compositions of the studied cases

Case	O_2	CO_2	H_2O[a]	SO_2
-10 kV, 6% O_2 (Figure 3.2)	5.8%	14.9%	0.37%	
+10 kV, 6% O_2 (Figure 3.2)	5.8%	14.9%	0.37%	
-10 kV, 2% O_2 (Figure 3.3)	1.7%	17.9%	0.47%	~248 ppm
-10 kV, 4% O_2 (Figure 3.3)	4.2%	14.4%	0.41%	
-10 kV, Oxy-combustion (Figure 3.3)	13%	14.2%	0.47%	

[a]Estimated based on ultimate analysis of coal

[b]Average concentration along the experiments

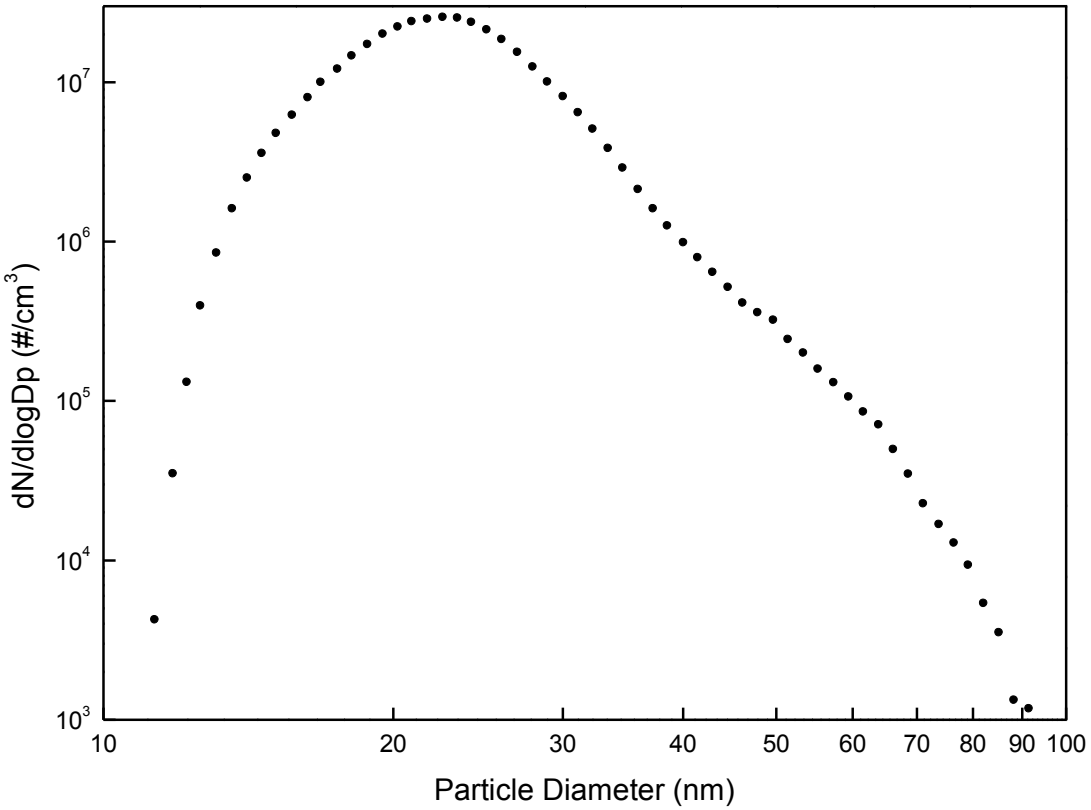

Figure A2.3 Size distribution of the secondary aerosols in the drop-tube furnace system (ESP voltage -10 kV)

(a)

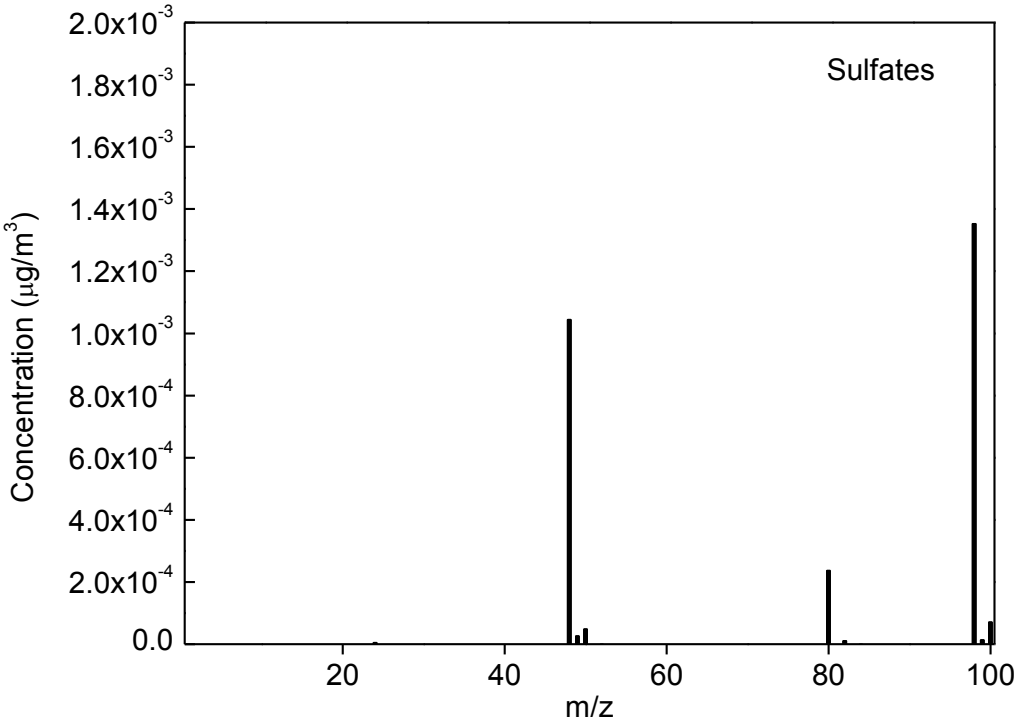

(b)

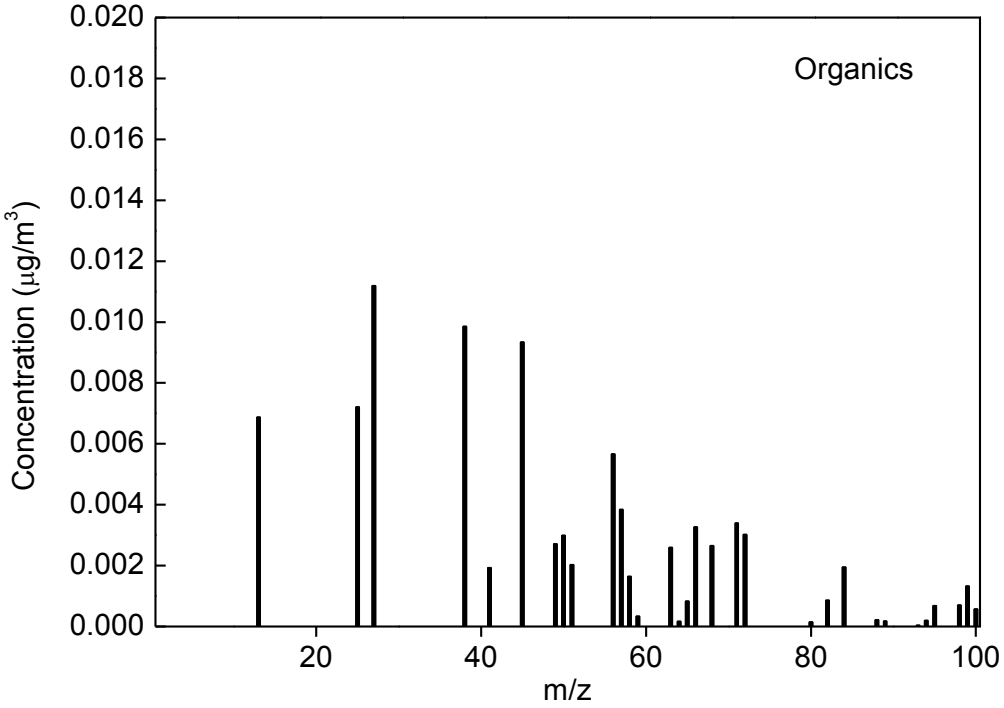

Figure A2.4 Average mass spectra of aerosols downstream ESP with coal feeding but with ESP off: (a) mass spectrum of sulfates; (b) mass spectrum of organics

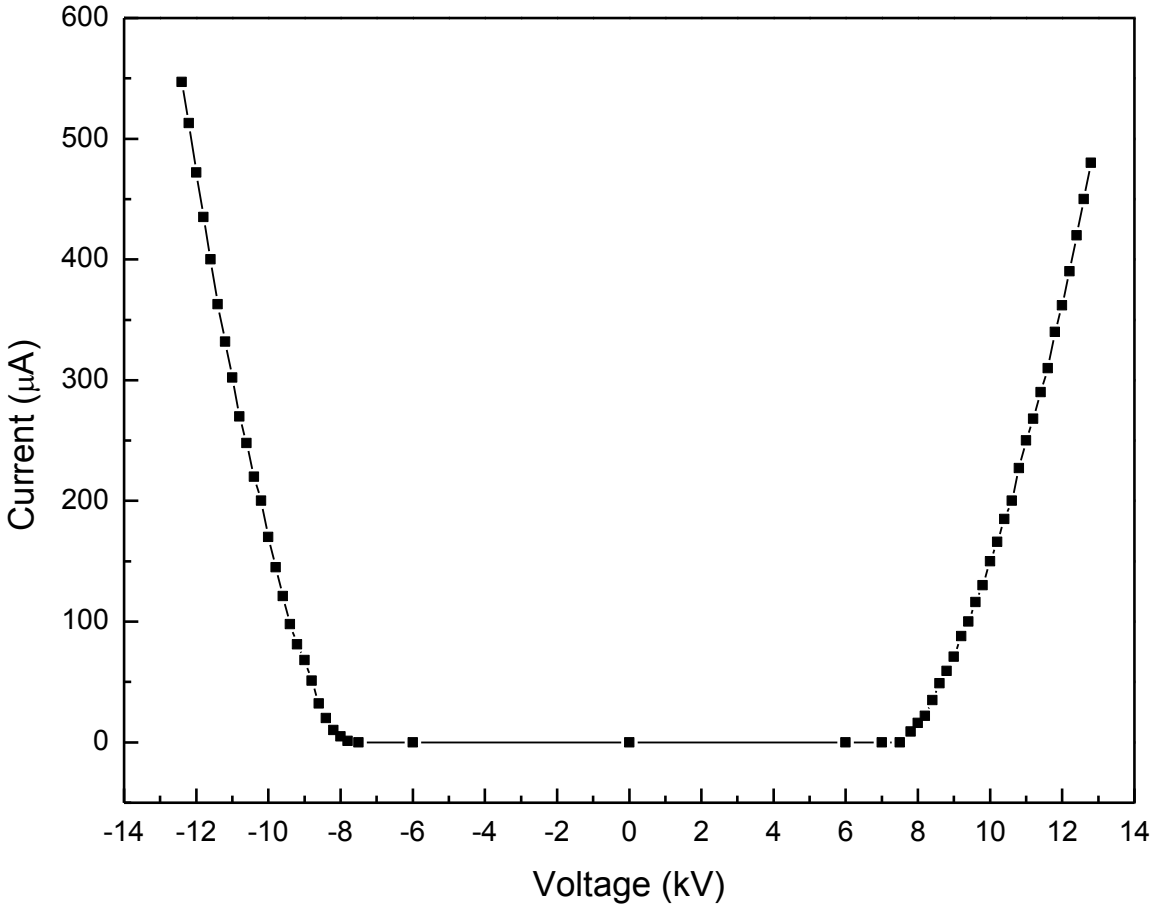

Figure A2.5 Current-voltage characteristics of the studied ESP (using air as feeding gas)

APPENDIX III. SUPPORTING MATERIALS FOR CHAPTER 4

-- Capture of Submicrometer Particles with a Pressurized Electrostatic Precipitator

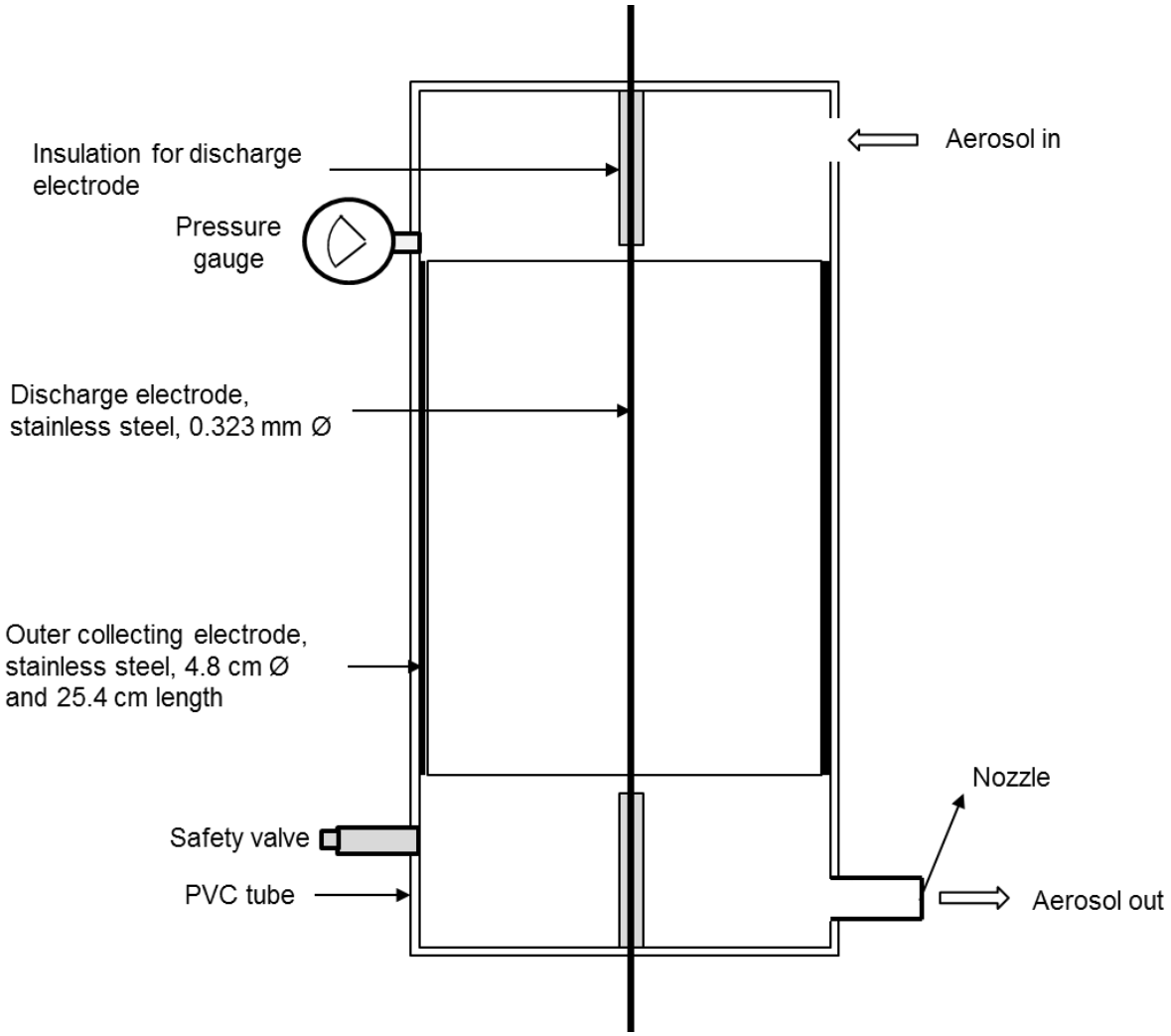

Figure A3.1 Configuration of the studied ESP

$$\frac{E_C}{\delta'} = A_g + \frac{B_g}{(r_0\delta')^{1/2}} \quad \text{(A3.1)}$$

in which

E_C --- corona on-set field

δ' --- relative gas density (relative gas pressure)

A_g, B_g --- constants that are related with the gas type

r_0 --- radius of the discharge wire

$$E_c = \frac{V_C}{r_0 \ln(r_1/r_0)} \quad \text{(A3.2)}$$

in which

V_C --- corona on-set voltage

r_1 --- radius of the collection tube

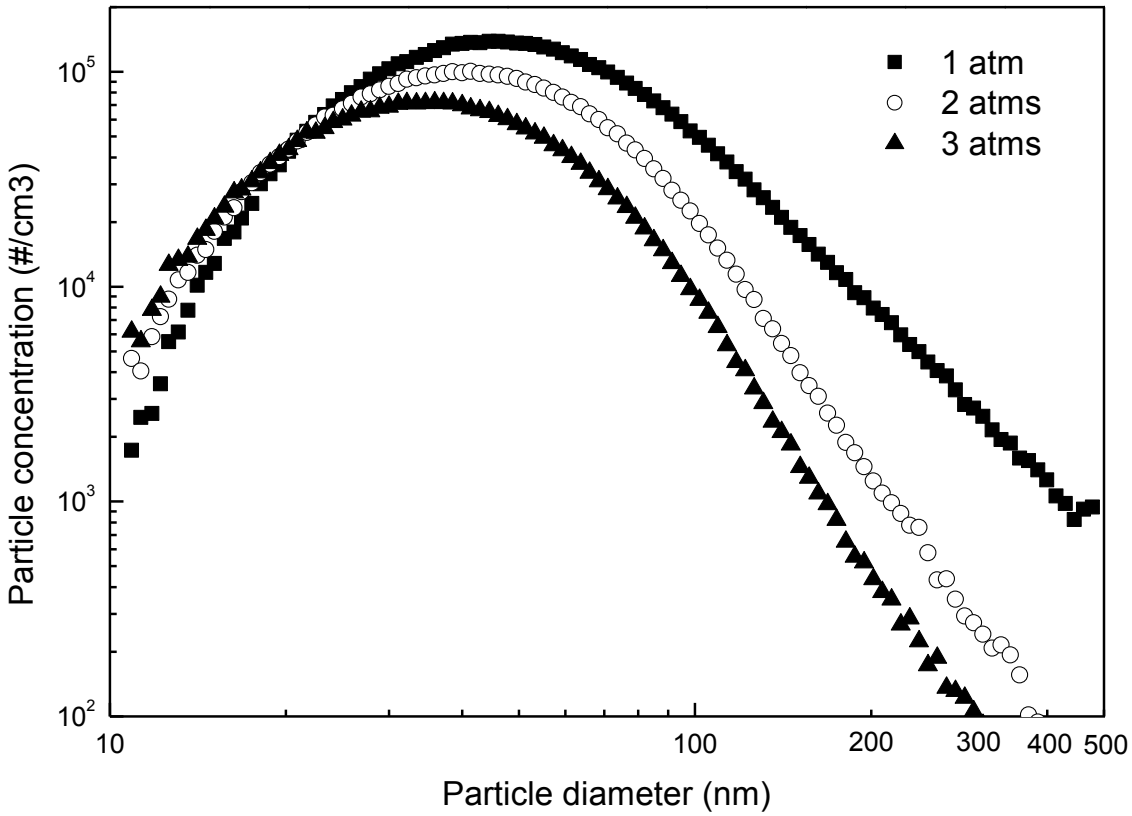

Figure A3.2 Size distribution of the NaCl particles generated using atomizer under various pressures

(a)

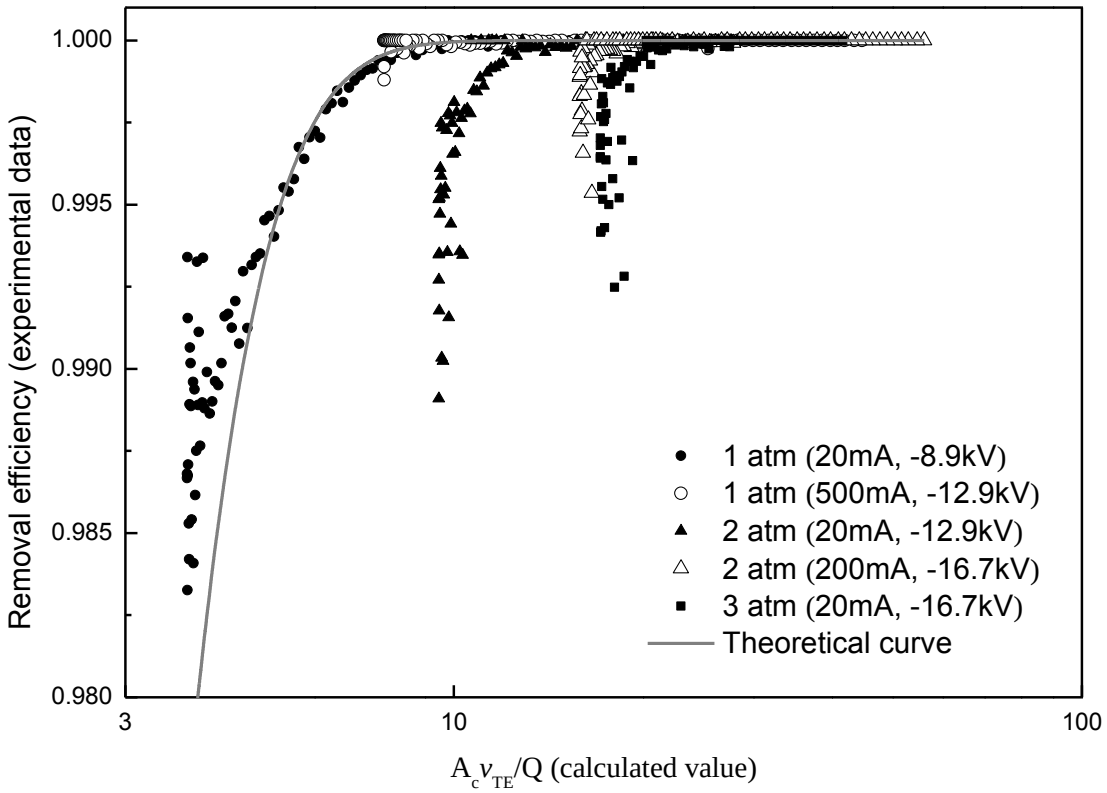
Removal efficiency (experimental data)
1.000
0.995
0.990
0.985
0.980
3
10
100
$A_c v_{TE}/Q$ (calculated value)
1 atm (20mA, -8.9kV)
1 atm (500mA, -12.9kV)
2 atm (20mA, -12.9kV)
2 atm (200mA, -16.7kV)
3 atm (20mA, -16.7kV)
Theoretical curve

(b)

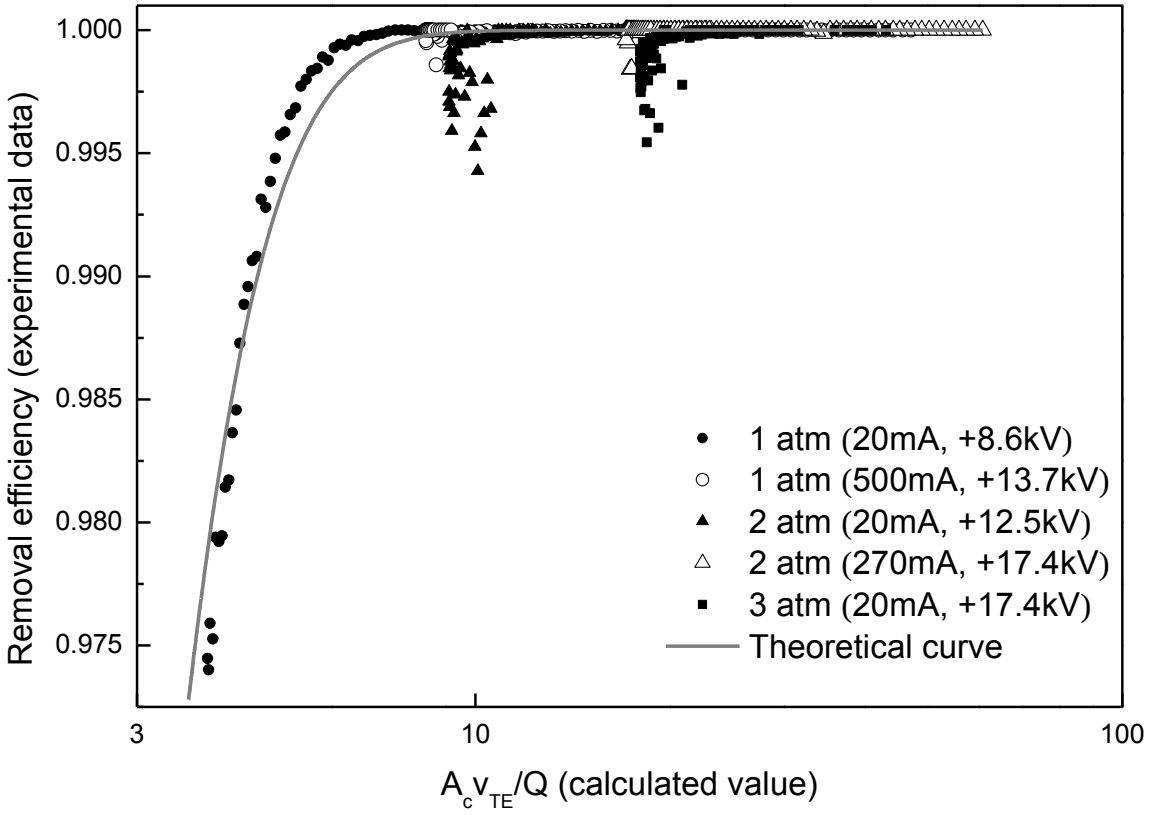

Figure A3.3 The relationship between measured NaCl particle removal efficiencies and the calculated values of the non-dimensional group from Deutsch-Anderson equation: (a) negative polarity; (b) positive polarity

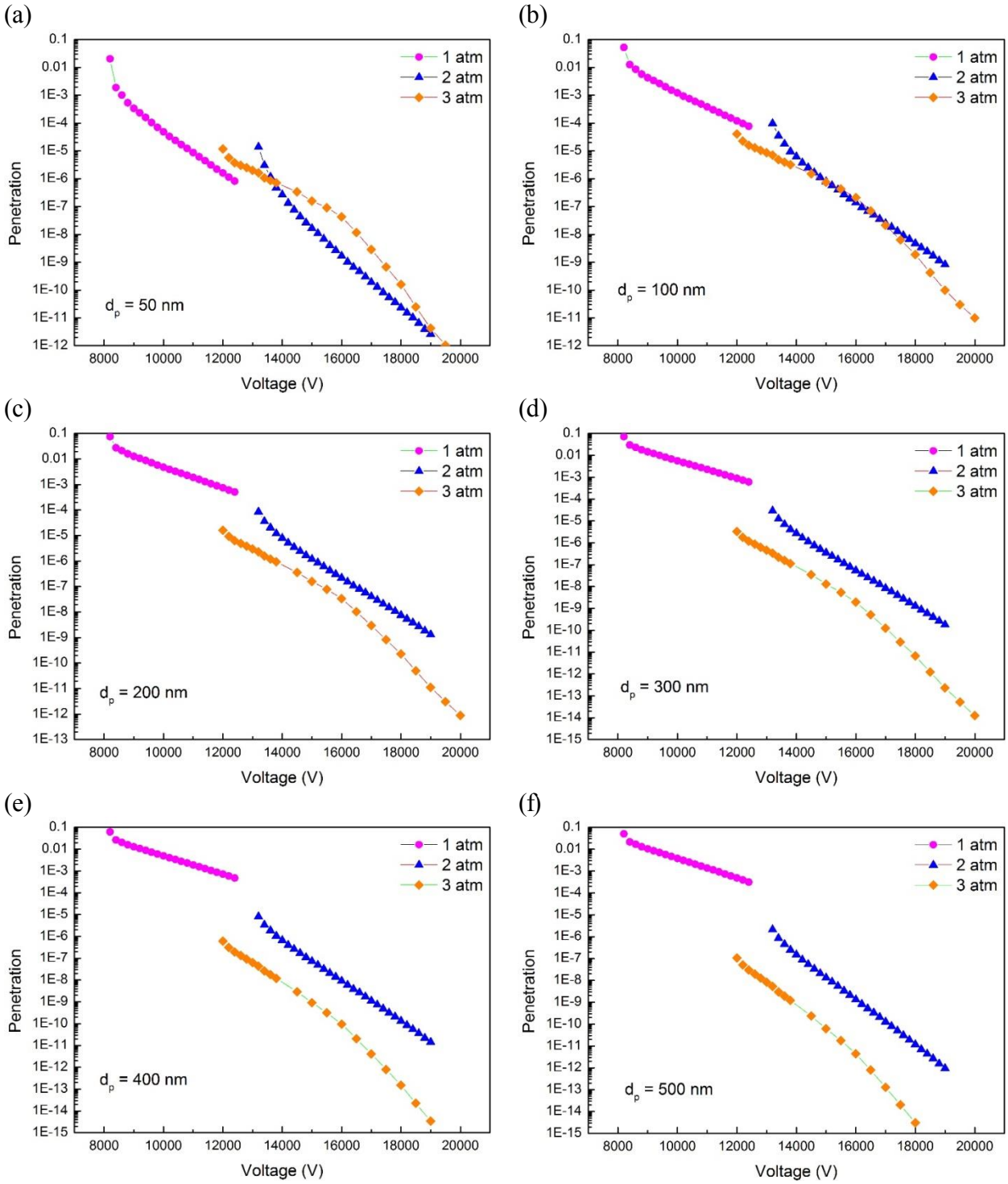

Figure A3.4 Relations between calculated penetration and voltage under different pressures (d_p = 50, 100, 200, 300, 400, 500 nm, positive polarity case)

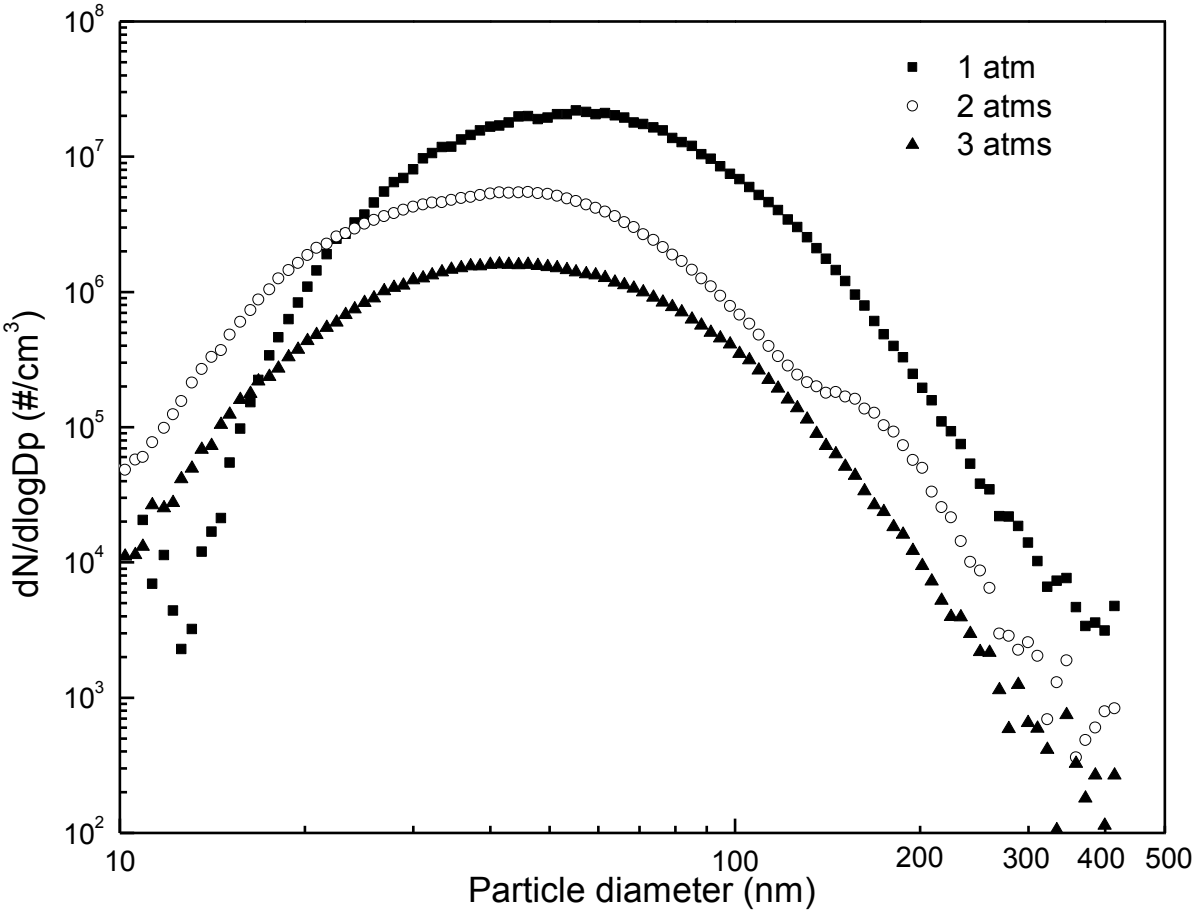

Figure A3.5 Size distribution of the fly ash particles from the drop-tube furnace under various pressures

APPENDIX IV. SUPPORTING INFORMATION ON DETERMINATION OF THE DESIGN PARAMETERS OF THE LAB-SCALE ESP

Here we compare the lab-scale ESP used in this study with a typical full-scale ESP, in order to justify the representative of the lab-scale ESP. Table A4.1 compares their average electrical field strengths and current densities.

Table A4.1 Comparison of the average electrical field strengths and current densities between the lab-scale ESP and a typical full-scale ESP

ESP scale	Average electrical field strength	Current density
Full-scale	70 kV/20 cm = 3.50 kV/cm	10 kV/2.4 cm = 4.16 kV/cm
Lab-scale	~860 μA/m^2	50 μA/0.038 m^2 = 1306 μA/m^2

The table shows that the field strengths and current densities of the two scales of ESP are comparable. Based on eq4.4-eq4.8, we could see that the particle migration velocities for a certain particle diameter are almost the same for the two scales of ESPs.

To further discuss whether the lab-scale ESP can represent the particle capture in a real ESP, we use the below scale-down term, because it equals to the ratio between the particle travel time and particle settling time:

$$Scale - down\ term = \frac{v_{TE} L}{v_{flow} H} = \frac{t_{travel}}{t_{settle}} \quad \text{(A4.1)}$$

The key parameters and scale-down terms of the two ESPs are shown in Table A4.2.

Table A4.2 Key parameters and scale-down terms of the lab-scale ESP and full-scale ESP

Parameters	**Value for a typical full-scale ESP**	**Value for the lab-scale ESP**
Migration velocity v_{TE}	Almost the same for two ESPs	
Length of collection board L	12 m	25.4 cm
Gap between boards H	20 cm	2.4 cm
Flow velocity v_{flow}	1.2 m/s	0.138 m/s
Scale-down term $\frac{v_{TE}L}{v_{flow}H}$	$50v_{TE}$	$77v_{TE}$

The above results show that the two ESPs are comparable, so it is valid to use the lab-scale ESP to represent a real ESP. The typical parameters of the real ESP are obtained from the materials of 2015 Neundorfer precipitator tutorial.

APPENDIX V. LIST OF PAPERS AND PRESENTATIONS

PAPERS

1. **Jing, H.**; Wang, X.; Wang, W.N.; Biswas, P., Elemental Mercury Oxidation in an Electrostatic Precipitator Enhanced with In Situ Soft X-ray Irradiation. *Journal of the Air & Waste Management Association*, 2015, 65, 455-465.

2. **Jing, H.**; He, S.; Ou, Q.; Hsiao, T.C.; Chen, D.R., Development of a Compact Electrostatic Nanoparticle Sampler for Offline Aerosol Characterization. *Journal of Metrology Society of India*, 2013, 28, 217-226.

3. **Jing, H.**; Wang, X.; Wang, W.N.; Dhungel, B.; Kumfer, B.M.; Axelbaum, R.L.; Williams, B.J.; Biswas, P., Secondary Aerosols Generation in an Electrostatic Precipitator during Flue Gas Treatment. *To be submitted*

4. **Jing, H.**; Wang, X.; Li, S.; Williams, B.J.; Biswas, P., Characterization of Submicrometer Particles from Sawdust/Coal Co-Firing in a Drop-Tube Furnace. *To be submitted*

5. Wang, Y.; Li, J.; **Jing, H.**; Zhang, Q.; Jiang, J.; Biswas, P., Laboratory evaluation and calibration of three low-cost particle sensors for particulate matter measurement. *Aerosol Science & Technology*, 2015, 49(11), 1063-1077.

6. Yeh, H.W.; **Jing, H.**; Chen, D.R., Formulation hydrophobicity on *in vitro* drug release of crizotinib-loaded PLGA nanoparticles. *Letters in Applied NanoBioScience*, 2015, 4, 247-250.

7. Fang, M.; Chen, C.; Guan, J.; Chen, D.R.; **Jing, H.**, Oppositely charged twin-head electrospray: a general strategy for building Janus particles with controlled structures. *Nanoscale*, 2013, 5, 2055-2064.

8. Wang, Y.; **Jing, H.**; Mehta, V.; Welter, G.J.; Giammar, D.E., Impact of galvanic corrosion on lead release from aged lead service lines. *Water Research*, 2012, 46, 5049-5060.

9. Wang, X.; **Jing, H.**; Dhungel, B.; Wang, W. N.; Kumfer, B. M; Axelbaum, R. L.; Biswas, P., Characterization of Organic and Black Carbon Aerosols from Coal Combustion: An Experimental Study in a 1 Megawatt Pilot Scale Coal Combustor. *To be submitted to Energy & Fuels*

10. Wang, X.; Wang, H.; Huang, Y.; **Jing, H.**; Wang, W. N.; Cui, W.; Williams, B. J.; Yang, X.; Biswas, P., Evidence for A New Source of Nitrogen-Containing Organic Aerosol: Combustion of High Sulfur Content Coal. *To be submitted to Environmental Science & Technology Letters*

11. Li, Z; **Jing, H.**; Biswas, P, Capture of Submicrometer Particles with a Pressurized Electrostatic Precipitator. *In preparation*

SELECTED PRESENTATIONS

1. 2014 AIChE Annual Meeting, Atlanta, Georgia, Platform presentation, 2014

- *Elemental Mercury Oxidation in an Electrostatic Precipitator with In-Situ Soft X-rays*

2. Invited talk at Peking University, Beijing, China, 2014

- *Formation of Fine Particles during Coal Combustion and Capture of Mercury from the Combustion Exhaust*

3. 2014 A&WMA Conference & Exhibition, Long Beach, California, Platform presentation, 2014

- *Elemental Mercury Oxidation in an Electrostatic Precipitator with In-Situ Soft X-rays*

4. 2014 A&WMA Conference & Exhibition, Long Beach, California, Platform presentation, 2014

- *Capture of Submicrometer Particles from Air-Fired and Oxy- Coal Combustion by a Soft X-Ray Enhanced Electrostatic Precipitator*

5. 10th IEA CCC MEC Meeting, Clearwater, Florida, Platform presentation, 2014

- *Novel Methodologies for Mercury Removal in Coal Combustors*

6. American Association for Aerosol Research 31th Annual Conference, Minneapolis, Minnesota, 2012

- *Experimental Evaluation of a Compact Nanoparticle Sampler*

7. 7th asian aerosol conference, Xi'an, China, 2011

- *Fundamental Study of a Compact Electrostatic Nanoparticle Sampler*

APPENDIX VI. LIST OF COURSES TAKEN

Course Code	Title	Credits	Grade
E33 501	Transport Phenomena in Energy, Environmental, and Chemical Engineering	3	A
E35 501	Mathematics of Modern Engineering I	3	A
E63 518	Aerosol Science and Technology	3	A
E33 503	Kinetics and Reaction Engineering Principles	3	B
E35 517	Partial Differential Equations	3	B+
E63 563	Measurement Techniques for Particle Characterization	3	A
E37 5410	Fluid Dynamics I	3	B
E33 544	Multiphase Flow	3	A
E63 592A	Advanced Topics in Aerosol Science and Engineering	3	A
E37 5412	Computational Fluid Dynamics	3	B